University of Kentucky Doctoral Dissertations

Graduate School

2007

INVESTIGATION OF THE ASSEMBLY OF SURFACTANTS AT THE SOLID-LIQID INTERFACE FOR ADSORPTION AND MATERIALS APPLICATIONS

Rong Xing
University of Kentucky, rxing2@uky.edu

ABSTRACT OF DISSERTATION

Rong Xing

The Graduate School

University of Kentucky

2007

INVESTIGATION OF THE ASSEMBLY OF SURFACTANTS AT THE
SOLID-LIQID INTERFACE FOR ADSORPTION AND
MATERIALS APPLICATIONS

ABSTRACT OF DISSERTATION

A dissertation submitted in partial fulfillment of
the requirements for the degree of Doctor of Philosophy
in the College of Engineering at the University of Kentucky

By

Rong Xing

Lexington, Kentucky

Director: Dr. Stephen E. Rankin, Professor of

Lexington, Kentucky

2007

ABSTRACT OF DISSERTATION

INVESTIGATION OF THE ASSEMBLY
OF SURFACTANTS AT THE SOLID-LIQID INTERFACE
FOR ADSORPTION AND MATERIALS TEMPLATING APPLICATIONS

This dissertation addresses two topics associated with the assembly of surfactants at the solid-liquid interface for adsorption and materials synthesis. The first is the adsorption of an anionic fluorinated surfactant, tetraethylammonium perfluorooctylsulfonate (TEA-FOS), at the solid/liquid interface. Attenuated total reflection Fourier transform infrared spectroscopy is used to study the adsorption kinetics and average orientation of surfactants at the hydroxylated germanium surface. Atomic force microscopy provides complementary images of the adsorbed layer structure on mica. The adsorption follows unusual three-stage kinetics in which the rate of adsorption starts fast, slows as the surface becomes crowded, and then (surprisingly) accelerates due to nucleation of a heterogeneous multilayer structure. These fast-slow-fast three stage adsorption kinetics are observed for a wide range of concentrations at pH 6, and the rates of the three stages are modulated by pH and salt by tuning electrostatic interactions among surfactants, counterions, and the surface. The results suggest that tetraethylammonium mediates interactions between surfactants and with negatively charged surfaces. The dichroism measurements and AFM are consistent with a mechanism in which TEA-FOS first forms an incomplete layer with chains oriented randomly or somewhat parallel to the surface, followed by formation of flattened multilayer clusters with the chains oriented somewhat normal to the substrate. The second topic is the sol-gel synthesis of mesoporous silica materials using dual surfactant templates. Studies of templating with mixed cetyltrimethylammonium bromide and octyl-

beta-D-glucopyranoside surfactants shows that the ternary phase diagram of surfactants in water can be used to predict mesoporous materials structure, and that vapor-phase ammonia treatments can either stabilize the structure or induce swelling by the Maillard reaction. Studies of sol-gel reaction-induced precipitation with demixed hydrocarbon and fluorocarbon cationic surfactant micelles show a wide variety of pore structures. A number of synthesis parameters are adjusted to tune the pore structure, for instance to adjust the size and populations of bimodal mesopores. Selective swelling of the two surfactants by liphophilic and fluorophilic solvents is observed. Finally, protein-accessible hollow spherical silica particles with mesoporous shells are reported. The methods for engineering mesoporous materials reported here have potential applications in adsorption, controlled drug delivery and for catalysis.

KEYWORDS: Surfactant Assembly, Adsorption, Sol-Gel Reaction, Solid-Liquid Interface, Bimodal Mesopores, Organic/Inorganic Hybrid Materials

Rong Xing
_____

06/08/2007
_____

INVESTIGATION OF THE ASSEMBLY OF
SURFACTANTS AT THE SOLID-LIQID INTERFACE
FOR ADSORPTION AND MATERIALS TEMPLATING APPLICATIONS

By

Rong Xing

<div style="text-align:right">

Stephen E. Rankin
_____

Director of Dissertation

Dr. Barbara L. Knutson
_____

Director of Graduate Studies

06/08/2007
_____

</div>

RULES FOR THE USE OF DISSERTATIONS

Unpublished dissertations submitted for the Doctor's degree and deposited in the University of Kentucky Library are as a rule open for inspection, but are to be used only with due regard to the rights of the authors.

Bibliographical references may be noted, but quotations or summaries of parts may be published only with the permission of the author, and with the usual scholarly acknowledgments.

Extensive copying or publication of the dissertation in whole or in part also requires the consent of the Dean of the Graduate School of the University of Kentucky.

A library that borrows this dissertation for use by its patrons is expected to secure the signature of each user.

Name   Date

DISSERTATION

Rong Xing

The Graduate School

University of Kentucky

2007

INVESTIGATION OF THE ASSEMBLY OF
SURFACTANTS AT THE SOLID-LIQID INTERFACE
FOR ADSORPTION AND MATERIALS TEMPLATING APPLICATIONS

DISSERTATION

A dissertation submitted in partial fulfillment of
the requirements for the degree of Doctor of Philosophy
in the College of Engineering at the University of Kentucky

By

Rong Xing

Lexington, Kentucky

Director: Dr. Stephen E. Rankin, Professor of

Lexington, Kentucky

2007

ACKNOWLEDGMENTS

First and foremost I would like to thank my research supervisor and committee chairman, Professor Stephen E. Rankin, for letting me join his research group and for providing the opportunity to work on the interesting projects, and his patient guidance, encouragement and support that he gave me throughout my research studies. I greatly acknowledge his help and suggestions not only in my research, but also outside the academy. Without his continuous support, I could not complete my research work, and the following dissertation would not exist.

I would like to thank my committee members, Professor B. Knutson, Professor P. M. Bummer, Professor J. Z. Hilt and Professor F. Ladipo for the useful discussions and spending time reading my dissertation. Professor B. Knutson and her group members gave me help for access to some facilities in their lab. Professor P. M. Bummer was always helpful whenever needed. My appreciation is also expressed to an earlier committee member Prof. L. S. Penn.

I would like to thank Professor H. J. Lehmler for providing the cationic pyridinium-based fluorinated surfactants used for materials synthesis in chapters 7 and 8. I thank Professor K. Anderson for allowing access to polarized optical microscope for the phase studies in chapter 6. I thank Professor B. Hinds for allowing access to plasma instruments. I thank Mrs. M. G. Engle for assisting me in using scanning confocal fluorescence microscope. I thank Dr. A. Dozier and Mr. L. A. Rice for assisting me and sharing their invaluable experience in using electron microscopy (SEM and TEM). I thank Mr. H. Francis for training and access to the XRD instruments in the Kentucky Geological Survey. I want to thank Mr. G. Spiggle for training and assistance with AFM and sputtering instruments in the Center for Nanoscale Science and Technology.

I would like to thank all members in my research group for being good friends that I could count on them in every way. In particular, I want to thank Dr. B. Tan for his help when I first joined the group.

Finally, I am deeply grateful to my wife Wenqin Shen for her love and support. I want to thank my mom and dad for their continuous support and sacrifice. I hope that the choices I have made and the things I have accomplished would have made my dead mother proud. This dissertation is devoted to all people who care about me.

TABLE OF CONTENTS

LIST OF FIGURES

xvi

LIST OF SCHEMES

Chapter 1. An Overview of Surfactant Adsorption Kinetics and Molecular Orientation at the Solid-Liquid Interface

1.1 Introduction

The aggregation behavior of surfactant molecules in bulk solution has been thoroughly studied using a variety of techniques ranging from indirect methods such as surface tension and rheology measurements to direct scattering, molecular probe, and cryo-TEM studies.[1,2] Micelle formation in bulk solution is fairly well understood, and the effects of variables such as surfactant structure, headgroup charge, counterions, and salts can be explained. At interfaces, however, the phase behavior is influenced by surfactant-surface and solvent-surface interactions that alter the aggregation behavior of the surfactants. The ongoing wide-ranging industrial application of surfactant at the solid-liquid interface necessitates a more complete understanding of surfactant self-assembly and adsorption at the solid-liquid interface than is currently available.

Rather than investigating the adsorption isotherms of surfactants at interfaces using traditional techniques such as zeta potential measurements, recent research has focused on measuring surfactant adsorption kinetics and molecular orientation in an effort to control the physical and chemical processes at the molecular level. Reaction kinetics are important from a practical point of view, but also provide insights into the interactions occurring at the solid surface. Understanding molecular orientation also provides insights into surfactant aggregate structure, a subject important not only for traditional application such as cleaning, but also for the synthesis of mesoscopic organic/inorganic hybrid materials with controlled phase structure. Both topics will be discussed in this dissertation, and here we introduce the first topic: studies of surfactant aggregation at solid-liquid interfaces.

A survey of available analytical methods leads to the conclusion that polarized attenuated total reflection Fourier transform infrared spectroscopy (ATR-FTIR) and atomic force microscopy (AFM) are good techniques for in-situ studies of interfacial phenomena. ATR-FTIR is a non-invasive technique that allows one to readily acquire information not only about surface coverage, but also about the orientation of adsorbed surfactants and the kinetics of adsorption. Recent research on the nature of evanescence provides us with the basis to interpret ATR-FTIR spectra at a multilayer

interface[3,4]. AFM provides direct qualitative information about the layer structure of adsorbed surfactants comparable to the information available from cryo-TEM studies in bulk micellar solutions. The advantage of AFM is that if done carefully, it can be performed in-situ to allow direct imaging of solvated structures and how they evolve.

The objective of the first part of this dissertation is to comprehensively investigate the extent of surface coverage and the microstructure of self-assembled fluorinated surfactants at the solid/liquid interface using ATR-FTIR. AFM is used as a complementary tool for morphological study of adsorbed surfactant layers to support our understanding of the surface aggregation mechanism. In this chapter, we briefly survey relevant literature about surfactant adsorption and then discuss the basis for interpreting our experimental studies in chapter 2 and chapter 3. Chapter 4 will present an introduction to surfactant templating of metal oxides and will be followed by several chapters addressing the synthesis of mesoporous materials using mixtures of surfactants.

1.2 Literature review

1.2.1 Generalities about surfactant

Surfactant molecules consist of a covalently bound combination of a hydrophilic part (usually called the headgroup) and a hydrophobic part (usually called the tail due to its length). The strength of the repulsive forces between the headgroups and the strength of the attraction between tails are among the factors that determine the preferred shape of surfactant molecules, and therefore the shape and size of aggregates they form. Because they possess significant non-polar character, individual surfactant molecules are sparingly soluble in water. Above the critical micelle concentration (CMC), surfactant molecules self-assemble into aggregates called micelles so as to shield their hydrophobic tails from the water (thereby releasing the structured hydration water that surrounds the free surfactants). A simple theory due to Israelachvili relates the geometry of the molecule to the shape of the aggregates that are formed[5]. The surfactant parameter S justifies the formation of a specific aggregate shape. The value of S is defined as $\upsilon/(\alpha_0 \ell_{hc})$, where ℓ_{hc} and υ stand for the hydrophobic chain length and hydrophobic chain volume, respectively, and α_0 is the optimal headgroup area[5]. These parameters explain the effects on micelle structure not

2

only of surfactant structure but also of solvents, co-surfactants and counter-ions. In addition, the parameter S can be reasonably used to predict the shape of the aggregates formed as shown in Figure 1.1.

Surfactants are classified according to the nature of their polar head and their hydrophobic tail. The charge of the headgroup determines whether a surfactant is anionic, cationic, or amphoteric (zwitterionic). Most surfactants have hydrophobic tails that consist of one or two hydrocarbon chains, but a special class of surfactants has fluorocarbon chain tails.

Fluorinated surfactants are an unusual family of surfactants that is being used in a growing number of applications ranging from emulsion polymerization of fluorinated polymers to pulmonary drug delivery. They are characterized by very strong intramolecular C-F bonds and very weak intermolecular interactions due to the large electronegativity of the fluorine atom. They are not only hydrophobic, but also lipophobic. Compared with their hydrogenated counterparts, fluorocarbon chains are stiffer and bulkier, which favors a large packing parameter for a carbon chain of a given length. When dissolved in solution, fluorinated surfactants tend to form highly stable and well organized films, bilayers, vesicles, cylinders and tubules[6].

Because they assemble more easily, fluorinated surfactants can form micelles with shorter chains compared to the corresponding hydrogenated surfactants. The rule of thumb is that the CMC of a fluorinated surfactant is roughly equal to that of hydrogenated surfactant with a tail that is 50 % longer. Moreover, new formulations of fluorinated surfactants/solvent system have been identified in recent years, which show that they have potential for a broad range of applications, including nonaqueous cleaning[7], material synthesis[8], and pulmonary drug delivery.[9]

1.2.2 Surfactants at the solid/liquid interface

1.2.2.1 Critical Surface Aggregation Concentration

As in bulk solutions, surfactants at interfaces also can assemble to form different aggregates. The influence of the surface is not well known yet. Most of models of adsorption have been based on laterally uniform layers, and non-uniform structures such as bilayer clusters or micelles have been treated more rarely.[10,11] The critical surface aggregation concentration (CSAC) is the surface analogue of the CMC in bulk

solution. In most situations, surfactants will begin to self-assemble at the solid/liquid interface at concentrations between 60 % and 80 % of the CMC [12,13].

1.2.2.2 Surface Aggregate Characterization

AFM is often used to characterize surface aggregation of surfactants. The advantage of AFM is the ability to acquire 3D structural information. Aggregation numbers, aggregate shape, micelle size and even surface excess values can be estimated from AFM images[14]. Table 1.2 summarizes the types of studies that have been reported previously. Using AFM, Manne et al.[15] demonstrated the variety of structures formed by surfactants adsorbed onto hydrophilic and hydrophobic surfaces. Several adsorbed surfactant layers showed periodic, in-plane structure ranging from regular micelles to cylinders with long range periodicity as illustrated in Figure 1.2. Liu and Ducker[19] showed that aggregates of tetradecyltrimethylammonium bromide ($C_{14}TABr$) and cetyltrimethylammonium bromide ($C_{16}TABr$) are spherical in solution and relatively unperturbed by adsorption to silica, while those of octadecyltrimethylammonium ($C_{18}TBr$) and eiconsanyltrimethylammonium bromide ($C_{20}TBr$) are spherical in solution but flat on silica. They concluded that the surfactants often form less-curved aggregates on solid substrates than in solution, and longer alkyl chains tend to form even flat structures on silica and mica. AFM studies of adsorbed surfactant layer structures at solid/liquid interfaces have been reviewed by Warr et al.[23] Neutron reflectivity studies provide depth-revolved composition information that is complementary to AFM images. Rennie[24] and Mcdermott[25] studied aggregation of trimethylammonium surfactants, and found evidence for formation of surface aggregates with headgroups concentrated in two planes, at the silica surface and facing the aqueous solution, respectively. The hydrocarbon tails were sandwiched between the two headgroup layers. Bromide counter ions were found concentrated near the ammonium head groups. Figure 1.3 illustrates these conclusions. While neutron reflectivity provides unique composition profiles, we choose to use AFM in this dissertation because it provides information about lateral structure that is not available by another technique.

1.2.3 Role of ATR-FTIR in surface analysis

Traditional surface analytical techniques require the solid to be removed from solution, washed and subjected to ultra-high vacuum prior to analysis[26]. This has undesired consequence of potentially changing the surface characteristics of the solid under investigation. While such ex situ methods can provide insights about the nature of a surface, the investigated surface is often quite different with the original surface of interest. It is obviously more desirable to probe a surface in situ, in order to gain an accurate picture of the solid surface. ATR-FTIR is one of the few techniques currently available to researchers wishing to explore solid/liquid interfacial phenomena in situ. This investigative technique has proved to be a useful tool for the study of adsorption and aggregate structure at the solid/liquid interface. Information regarding the quantity and nature of adsorbed species can be readily acquired.

1.2.4 Adsorption and molecular orientation of surfactant at the solid/liquid interface

ATR-FTIR is a very powerful and easily applied technique for the determination of surface excess and orientation of adsorbed surfactant molecules at the solid/liquid interface. Under proper conditions, IR radiation passing through a high refractive index crystal is totally internally reflected. However, a small amount of radiation emanates from the external surface of the crystal as an evanescent wave. When an infrared adsorbing sample is brought into contact with the crystal surface, the intensity of the evanescent wave is attenuated, which give rise to the ATR "absorbance" spectrum. Calibration of high refractive index crystal used for ATR (the internal reflection element, or IRE) allows the determination of surface excess of adsorbed molecules,[27,28] and under the correct conditions, the orientation of adsorbed molecules can be quantified[29].

Extending standard ATR-FTIR by polarization allows determination of the molecular orientation of adsorbed surfactants. Polarization of the internally reflected beam results in an evanescent wave that has its electric field amplitude oscillating in either the plane of incidence (P polarization) or in the direction normal to the plane of incidence (S polarization). Based on linear dichroism theory, comparison of the absorbance under P and S polarization allows the determination of the orientation with

respect to the surface of the transition moment giving rise to a specific IR band. Singh et al.[30] investigated the structure of self-assembled dodecyltrimethylammonium bromide ($C_{12}TAB$) surfactant layers on the silica surface using ATR-FTIR, to understand the structural transitions taking place at the silica/solution interface. They showed that a transition to randomly-organized spherical aggregates appears to take place at concentration below the CMC, directly from hemi-micelles and without the formation of bilayers. This structural transition is summarized by the schematic shown in Figure 1.4. Naivandt et al.[31] determined the average orientation of the methylene tail of surfactant CTAB adsorbed onto solid silica. The equilibrium orientation was measured over the pH range from 2-10. It was found that the equilibrium orientation of surfactant was larger at higher pH values owing to an increase in the packing density with increasing surface excess. The evolution of the orientation of the surfactant at the interface was monitored at a pH of 9.2. During initial stage of adsorption, there was no preferred orientation of the surfactant, but as the surface excess increased with time, the surfactant rapidly began to orient in a direction more normal to the surface.

Polarized ATR-FTIR has been successfully applied for the determination of molecular orientation of adsorbed layers at the solid/liquid interface in a number of systems[32-34]. However, few in situ attempts have been made to study the self-assembly behavior of fluorinated surfactants at the solid/liquid interface. Specific examples of the application of ATR-FTIR for the characterization of fluorocarbon layers will be discussed in chapter 2, but only after equilibrium has been reached. Because of the special properties of fluorinated surfactants mentioned above, we expect to observe self-assembly behavior of fluorinated surfactants at the solid/liquid interface that may differ from that of hydrocarbon surfactants, which motivates the in-situ investigation of fluorinated surfactant adsorption in chapters 2 and 3. Because it plays a crucial role in the interpretation of the results in those chapters, we describe here the theory used to interpret ATR-FTIR and AFM results.

1.3 Theory of ATR-FTIR

1.3.1 Principles of total attenuated reflection spectroscopy

ATR-FTIR, developed by Harrick[35], is a type of internal reflection spectroscopy in which the sample is placed in contact with an internal reflection element (IRE) of

high refractive index, as shown in Figure 1.5. Infrared radiation is focused onto the edge of the IRE, reflected through the IRE, and then directed to a detector. ATR-FTIR can be used to measure refractive index, surface excess, spectral identity and molecular orientation in situ at the solid/liquid interface.

1.3.2 IRE material

A wide variety of materials are commercially available for use as IREs. The more common ones include zinc selenide, germanium, silicon, quartz etc. Choice of IRE material depends on many factors, such as the spectral range of interest, the nature of the solvent, solution pH, the physical and chemical properties of the crystal materials available, and their respective cost. Table 1.1[36] shows a range of materials considered for use as IREs. In our case, we selected germanium because it provides an oxidized and hydroxylated surface similar to that of silicon, but unlike silicon it has a spectral range large enough to allow us to observe fluorocarbon bands (near 1152 cm^{-1} and 1244 cm^{-1}). Other metal oxide IREs (ZrO_2 and Al_2O_3) would be suitable substrates, but they are not readily available from a commercial supplier. The other IRE materials are either inert (e.g. diamond) or have significantly different surface chemistry (e.g. ZnSe).

1.3.3 Quantitative determination of surface excess from unpolarized ATR spectra

At the solid/liquid interface, the surface excess is defined as the difference between the amount of surfactants actually present in the system, and the amount that would be present (in a reference system) if the bulk concentration in the adjoining phases were maintained up to a chosen geometrical dividing surface. The method of calculation used to quantify the ATR results was developed by Tompkins[37]. In our system, we assume that the contribution of bulk solution to the surface excess is far less than the actual adsorbed surfactant amount on the Ge surface. This technique can be understood based on the illustration of the experiment in Figure 1.6., where anionic fluorinated surfactant tetraethylammonium perfluorooctylsulfonate (TEA-FOS) is used as an example.

When an electromagnetic wave approaches the interface form a denser medium (refractive index n_1) to a rarer medium (refractive index n_2) at an appropriate angle, total internal refection takes place. For this to occur, the angle of incidence must be greater than the critical angle defined by the following equation:

$$\theta > \theta_C = \arcsin(n_{21}) \qquad (1.1)$$

where n_{21} refers to the refractive index ratio $n_{21} = n_2/n_1$. A total internal reflection sets up a standing wave pattern due to interface of incoming and the outgoing wave. The standing wave amplitude pattern is shown in Figure 1.7, which shows a sinusoidal dependence of the electric filed amplitude in the denser medium and exponentially decreasing amplitude in the rarer medium. The exponential drop off of the amplitude, E, can be described by the expression:

$$E = E_0 e^{-z/d_p} \qquad (1.2)$$

where E_o is the value of the amplitude at the interface ($z = 0$), and d_p is penetration depth at which the amplitude, E, has decreased to 1/e of its value at the surface. The penetration depth is defined in the equation given by Harrick[35]:

$$d_p = \frac{\lambda}{2\pi n_1 [\sin^2 \theta - (n_2/n_1)^2]^{1/2}} \qquad (1.3)$$

where θ is the incident angle and λ is wavelength of incident beam. The interaction of the evanescent wave with the absorbing rarer medium causes a loss of reflection. Reflectivity is defined as the ratio of the reflected light intensity, I_R, to the intensity of the incident light I_0.

$$R = I_R / I_0 \qquad (1.4)$$

If reflection losses are negligible, the conventional transmission follows a simple exponential law $I_T / I_0 = e^{-\alpha d}$, where I_T is the transmitted light intensity, d is the film thickness and α is the absorption coefficient. For low absorption, i.e. $\alpha d < 0.1$, this is approximated as $I_T / I_0 \approx 1 - \alpha d$. Similarly, for internal reflection, the reflectivity of the bulk material can be written as:

$$R = 1 - \alpha d_e \qquad (1.5)$$

where d_e is effective thickness. In order to calculate d_e, we use the bulk material approximation, given by Harrick, which assume that the rarer medium is much thicker

than the penetration depth of the evanescent wave. With this assumption, d_e is given by[35]:

$$d_e = \frac{n_{21}}{\cos\theta}\int_0^\infty E^2 dz = \frac{n_{21}E_0^2 d_p}{2\cos\theta} \qquad (1.6)$$

This value is polarization dependent. If the absorbance per reflection is calculated based on the modulation of the evanescent wave using the absorption coefficient:

$$\frac{A_t}{N} = \frac{n_{21}E_0^2}{\cos\theta}\int_0^\infty \alpha e^{-2z/d_p} dz \qquad (1.7)$$

where N is number of total internal reflection. Considering that the absorption coefficient includes the effect of both concentration and molecular identity, $\alpha = C(z)\varepsilon$. Then,

$$\frac{A_t}{N} = \frac{n_{21}E_0^2}{\cos\theta}\int_0^\infty C(z)\varepsilon e^{-2z/d_p} dz \qquad (1.8)$$

The calculation of the surface excess is based on the assumption of a step-like concentration profile at the solid/liquid interface with this functional form:

$$C(z) = \begin{cases} C_b + C_i\,(0 < z < t) \\ C_b\,(t < z < \infty) \end{cases} \qquad (1.9)$$

where $C(z)$ is concentration as a function of distance z from the interface and t is the thickness of adsorbed layer. Subscripts i and b denote the interface and bulk, respectively (C_i is the excess surfactant per unit area). Substituting d_p, d_e and the step function to equation (1.8), we obtain the following equation after integration:

$$\frac{A_t}{N\varepsilon} = C_b d_e + (\frac{2d_e}{d_p})(C_i t) \qquad (1.10)$$

which relates the total absorption measured to the bulk solution concentration and the surface excess, $\Gamma_i = C_i t$. This equation will be used to calculate surface excess values in chapter 2 and 3.

1.3.4 Quantitative determination of molecular orientation by polarized ATR spectra

The molecular orientation of surfactant molecules at the solid/liquid interface can be determined by linear dichroism spectroscopy. The linear dichroic ratio (LD) is a key parameter in the analysis of the molecular orientation within adsorbed surfactant films, and is determined as the ratio of the absorbances of IR beams polarized perpendicular (A_s) and parallel (A_p) to the plane of incidence. Thus,

$$LD = \frac{A_s}{A_p} = \frac{ATE}{ATM} \qquad (1.11)$$

where A is the integrated intensity (band area), TE is the transverse electric or perpendicular filed (= E_y), and TM is the transverse magnetic or parallel filed (= E_x+E_z). E_x, E_y and E_z are the components of the evanescent wave in the x, y, z directions, respectively, at the evanescent interface. E_y is perpendicular to the plane of incidence and parallel to the surface. E_x is parallel to the plane of incidence and parallel to the surface. E_z is parallel to the plane of incidence and perpendicular to the surface. At the solid/liquid interface, the electric filed amplitude in the three Cartesian directions can be calculated using the equations give by Harrick[35].

$$
\begin{aligned}
E_x &= \frac{2\cos\theta(\sin^2\theta - n_{21}^2)^{1/2}}{(1-n_{21}^2)^{1/2}[(1+n_{21}^2)\sin^2\theta - n_{21}^2]^{1/2}} \\[1em]
E_y &= \frac{2\cos\theta}{(1-n_{21}^2)^{1/2}} \qquad\qquad (1.12) \\[1em]
E_z &= \frac{2\sin\theta\cos\theta}{(1-n_{21}^2)^{1/2}[(1+n_{21}^2)\sin^2\theta - n_{21}^2]^{1/2}}
\end{aligned}
$$

These equations are valid for a two-phase system, which is a good approximation when the thickness of the adsorbed film on the IRE is negligible compared to the penetration depth d_p.

The laboratory Cartesian coordinates (X, Y and Z axes) are shown in Figure 1.8. The X and Y axes are parallel to the surface of the IRE and the Z axis is perpendicular to the surface. That is, S-polarized radiation is orientated with its electric vector in the y direction, while P-polarized radiation lies in the OXZ plane (the plane of incidence), at 45° with each of the two axes. In this description, we presume that a chain axis, which can be used to represent molecular orientation, is defined. The absorbance measured, A, is proportional to the square of the scalar product of the electric field

vector of the evanescent wave $\vec{E}$, and the transition dipole moment of the absorbed film, $\vec{M}$.

$$A \propto (\vec{E} \bullet \vec{M})^2 \qquad (1.13)$$

This equation can be expressed in term of three experimental axes, as

$$A \propto (E_x M_x + E_y M_y + E_z M_z)^2 \qquad (1.14)$$

where M_i is the component of absorption transition moment. The absorbance due to S-polarized and P-polarized radiation can thus be calculated separately. The value for A_x, A_y and A_z will depend on the model of the adsorbed layer structure used. Haller and Ulman[38] have used a model with fixed angle of the chain from the normal to the surface. Zbinder[39] proposed a model which considers a uniaxial symmetric distribution of the transition dipole moment $\vec{M}$ about the bond axis of the chain with fixed angle α between $\vec{M}$ and c, and a uniaxial symmetric distribution of the c axis about the Z axis, with a fixed angle γ between the c and Z axes. The uniaxial model is more appropriate for our experiment, because there is no external force which causes the absorbed surfactant to orient preferentially in either of the in-plane direction during the measurement.

Formulas for dichroism based on a uniaxial model were first developed by Frey and Tamm[40]. Consider an adsorbed surfactant having a vibrational mode with its TM parallel to the director, which is inclined to the surface normal at an angle γ. After averaging A_x, A_y and A_z through rotation about the c and Z axes, we can obtain:

$$A_x = KE_x^2 |M|^2 \sin^2 \gamma$$
$$A_z = 2KE_z^2 |M|^2 \cos^2 \gamma \qquad (1.15)$$
$$A_y = KE_y^2 |M|^2 \sin^2 \gamma$$

where K is a constant. It is seen that absorpiton in the x direction is identical with absorption in the y direction due to the uniaxial nature of the sample. Therefore, the LD ratio is given by

$$LD = \frac{A_s}{A_p} = \frac{E_y^2 \sin^2 \gamma}{E_x^2 \sin^2 \gamma + 2E_z^2 \cos^2 \gamma} \qquad (1.16)$$

11

$$\gamma = \tan^{-1}\left(\frac{2LDE_z^2}{E_y^2 - LDE_x^2}\right)^{1/2} \qquad (1.17)$$

For a random array of molecules and a given band, molecular TM vectors are equally distributed about the axes:

$$LD = \frac{A_s}{A_p} = \frac{E_y^2}{E_x^2 + E_z^2} \qquad (1.18)$$

Consider a vibrational model in the same absorbed surfactant, having its TM at 90° to the molecular director. Assuming a free rotation about the director, the expression for dichroism is obtained as follows:

$$LD = \frac{A_s}{A_p} = \frac{E_y^2(1 + \cos^2\gamma)}{E_x^2(1 + \cos^2\gamma) + 2E_z^2\sin^2\gamma} \qquad (1.19)$$

$$\gamma = \arcsin\left(\frac{2(E_y^2 - LDE_x^2)}{2LDE_z^2 + E_y^2 - LDE_x^2}\right)^{1/2} \qquad (1.20)$$

Generalizing this relationship for any angle between the TM and the molecular vector gives the following expression:

$$LD = \left(\frac{E_y^2}{E_x^2 + 2E_z^2\left(\frac{2}{2\sin^2\alpha + (2\cos^2\alpha)(\sin^2\gamma) - (\sin^2\alpha)(\sin^2\gamma)} - 1\right)}\right) \qquad (1.21)$$

1.4 Theory of AFM

AFM (also called scanning force microscopy), developed by Binnig, Rohrer, and Weibel[41] in 1986, is a valuable tool for the study of surface topography. Figure1.9 schematically shows the basic principles of the AFM technique. Briefly, a laser beam is focused on a cantilever which reflects it toward a detector. The detector monitors the deflection of the cantilever by sensing the position of the reflected beam. There are three primary modes of AFM: contact, tapping, and non-contact. Contact mode AFM operates by scanning a tip attached to the end of a cantilever across the sample surface. The change in cantilever deflection is monitored by a split photodiode detector. A

feedback loop maintains a constant deflection between the cantilever and the sample by vertically moving the scanner at each (x, y) position to maintain a "setpoint" deflection. The distance the scanner moves vertically at each position is stored by the computer to form the topographic image of the sample surface. Tapping mode AFM operates by scanning a tip attached to the end of an oscillating cantilever across the sample surface. The cantilever is oscillated at or a little below its resonance frequency with an amplitude ranging typically from 20 nm to 100 nm. The tip lightly 'taps' on the sample surface during scanning by contacting the sample surface at the bottom of each oscillation. The feedback loop maintains a constant oscillation amplitude by maintaining a constant root-mean-square (RMS) signal as acquired by the detector. The vertical position of the scanner at each (x, y) position required to maintain a constant "setpoint" amplitude is stored by the computer to form the topographic images of the sample surface. Non-contact AFM operation is similar to tapping mode except that the tip does not contact the sample surface, but instead oscillates above the surface during scanning[42].

Manne et al.[43,44], for the first time, imaged saturated surfactant adsorbed layers at the solid-liquid interface by using AFM. Hydrophilic mica and silica and hydrophobic graphite are usually selected as model substrate for AFM study, since clean, flat surfaces are easily prepared. AFM measurements of layers at the solid-liquid interface can be conducted ex situ or in situ. Each type of study has its advantages and disadvantages. For in situ studies, we can follow the real time adsorption kinetics and specific regions of the sample surface, but the quality of images obtained is generally worse than that obtained under ambient conditions. For ex situ studies, we can capture images of samples with fast adsorption kinetics by quenching the sample, but the quality and quantity of adsorbed surfactants may be different from that present in situ at the solid/liquid interface.

There are many factors affecting the adsorption kinetics and molecular orientation of surfactants at the solid/liquid interface. AFM provides a simple and effective way to study these factors. For example, Ducker and Lamont[22] studied the salt effect on the ordering of lithium perfluorooctylsufonate (LiFOS) at the graphite/solution interface using in situ AFM. They observed that LiFOS molecules adsorb in periodic structure, and

the period decreases on addition of salt. Lai, et al.[45] investigated the effect of solution pH on adsorption isotherms of perfluorocarboxylic acids and their salts on aluminum oxide, and found that lower pH in solution causes the adsorption rate to reach a maximum at bilayer coverage. The following two chapters of this dissertation address some of the key aspects associated with adsorption behavior and structural arrangement of fluorinated surfactants at the solid/liquid interface. In chapter 2, we present the concentration effect of TEAFOS surfactant on unusual three stage adsorption kinetics and multilayer formation. In chapter 3, other important factors, namely solution pH and ionic strength, are further investigated based on the FTIR-ATR and AFM techniques. The remainder of the dissertation will focus on using interactions between surfactants and polymerizing metal alkoxides precursors to direct their assembly into ordered mesophases and mesoporous materials.

Table 1.1. Optical and physical properties of IRE materials.[36]

Material	Useful range,cm^{-1} (transmission)	Refractive index at 1000 cm^{-1}
Zinc selenide (ZnSe)	20,000-454	2.2
Zinc sulphide (ZnS)	17,000-720	2.2
Cadmium telluride (CdTe)	20,000-360	2.67
AMTIR[a]	11,000-625	2.5
Barium Fluoride (BaF$_2$)	50,000-740	1.42
Calcium Fluoride (CaF$_2$)	50,000-1,025	1.4
Cesium Iodide (CsI)	40,000-200	1.74
KRS-5[b]	20,000-250	2.37
Chalcogenide (AsSeTe Glass)	4,000-900	2.8
Germanium (Ge)	5,500-475	4.0
Potassium Bromide (KBr)	40,000-400	1.52
Quartz (SiO$_2$)	25,000-2,200	1.4
Sodium Chloride (NaCl)	40,000-625	1.49
Silver Chloride (AgCl)	25,000-360	1.98
Silicon (Si)	8,300-660&360-70	3.4
Cubic zirconinm (ZrO$_2$)	25,000-1600	2.15
Diamond (C)	45,000-2500	2.37
Sapphire (Al$_2$O$_3$)	50000-1525	1.5

[a]AMTIR: infrared glass made from germanium, arsenic and selenium
[b]Thallium Bromide-Iodide

Table 1.2. A summary of representative atomic force microscopy studies for different surfactant systems

Surfactant system	Solid surface	AFM mode	Force curve shown ?	Features observed	Ref
$C_{14}TAB$	silica			spherical micelles	15
	mica	contact	no	meandering stripes	
	graphite			parallel stripes	
Gemini surfactant'12 -2-12'	mica	contact	yes	flat bilayers	16
$C_{16}TAB$	mcia	contact	yes	discrete patches to cylindrical aggregates as conc. increases	17
$C_{12}E_3$	graphite	tapping and soft-contact	yes	stripe-like pattern	18
M(D'E8)M				stripe-like pattern	
$C_{18}TAB$	silica	soft-	yes	flat	19
	mica			flat	
	graphite	contact		hemicylinders	
$C_{20}TAB$	silica	soft-	yes	flat	19
	mica			flat	
	graphite	contact		hemicylinders	
HFDePC	mica	contact	no	parallel cylinders	20
TPC				meandering cylinders	
$TEC_{14}Cl$				spherical micelles	
CPC				parallel cylinders	
$C_{18}S + C_9FH$	mica	contact	no	mixed monolayers (hexagonal +linear domains)	21
LiFOS	graphite	contact	no	hemicylinders	22

$C_{14}TAB$: tetradecyltrimethylammonium bromide
'12-2-12': 1,2,-bis(n-dodecyldimethylammonium) ethane dibromide
$C_{16}TAB$: cetyltrimethylammonium bromide
$C_{12}E_3$: tri(ethylene oxide) dodecyl ether
$C_{18}TAB$: octadecyltrimethylammonium bromide
$C_{20}TAB$: eiconsanyltrimethylammonium bromide
M(D'E8)M: trisiloxane surfactant $(CH_3)_3SiO_2(CH_3)(CH2)_3(OCH_2CH_2)_8OH$
HFDePC: 1H, 1H, 2H, 2H-perfluorodecylpyridinium chloride
TPC: tetradecylpyridinium chloride
$TEC_{14}Cl$: tetradecyltriethylammonium chloride
CPC: cetylpyridinium chloride
$C_{18}S$: sodium octadecanesulfonate
C_9FH: perfluorononanoic acid

Aggregate shape
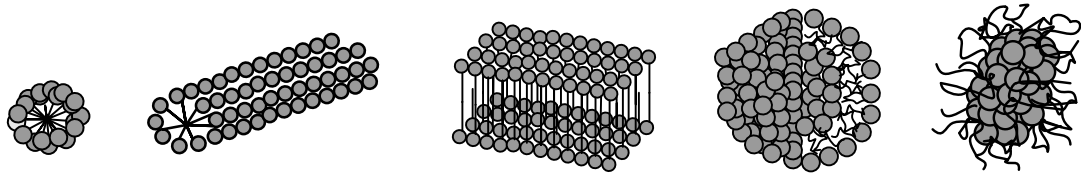
Packing Parameter

$S \le 0.33$ $1/3 < S \le 0.5$ $S = 1$ $1/2 < S \le 1$ $S > 1$

(a)   (b)   (c)   (d)   (e)

Figure 1.1. Example of surfactant aggregates as a function of packing parameter: (a) spherical shaped micelle; (b) cylindrical micelle; (c) lamellar micelle; (d) vesicular micelle; (e) inverted micelle.
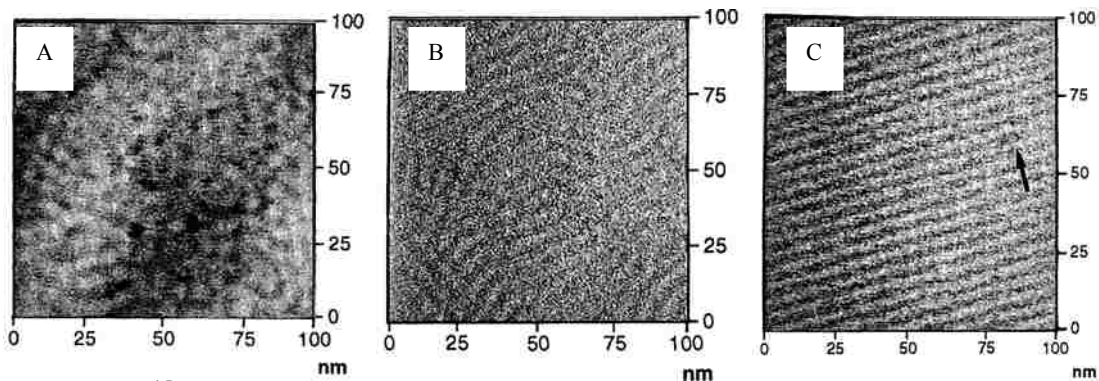
Figure 1.2.[15] AFM images of cationic surfactant $C_{14}TAB$ on solid surface from 7 mM (twice the CMC) aqueous solution (100 nm ×100 nm). A. Surfactant aggregates on silica at pH 2.9, showing spherical micelles spaced at 7.0 ± 0.9 nm. B. Surfactant aggregates on mica, showing meandering stripes spaced 5.3 ± 0.3 nm. C. Surfactant aggregates on graphite, showing parallel stripes spaced at 4.7 ± 0.3 nm. The arrow indicates a symmetry direction of the underlying lattice as determined by lattice scans. Reprinted with permission from *Prog. Colloid Polym. Sci.* **1997**, 103, 226. Copyright ©1997 with permission from Springer.
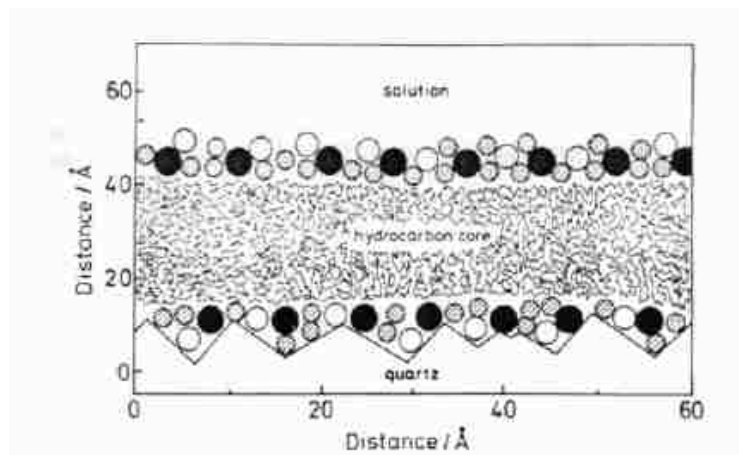
Figure 1.3.[24] Structure of adsorbed C_{16}TABr at the silica water interface from bromide to silica. The solid circles represent the headgroup of $N^+(CH_3)_4$, the open circles the counterions Br$^-$, and the shaded circles the water molecules. Reprinted with permission from *Langmuir* **1990**, 6, 1031. Copyright 1990 American Chemical Society.
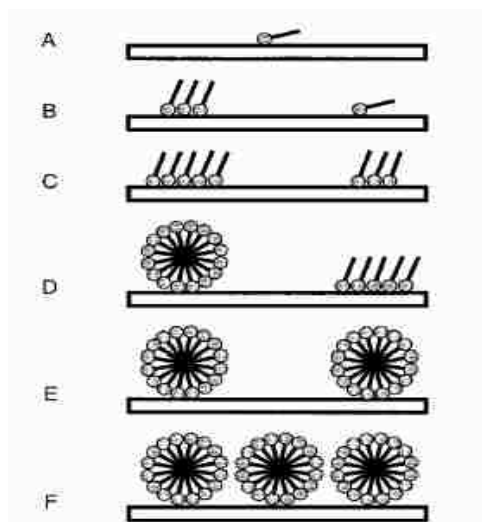
Figure 1.4.[30] Schematic representation of the proposed self assembled surfactant films at concentrations corresponding to: (A) individual surfactant adsorption, (B) low concentration of hemi-micelles on the surface, (C) higher concentration of hemi-micelles on the surface, (D) hemi-micelles and spherical surfactant aggregates formed because of increased surfactant adsorption and transition of some hemi-micelles to spherical aggregates, (E) randomly oriented spherical aggregates at onset of steric repulsive forces, and (F) surface fully covered with randomly oriented spherical aggregates. Reprinted with permission from *Langmuir* **2001**, 17, 468. Copyright 2001 American Chemical Society.
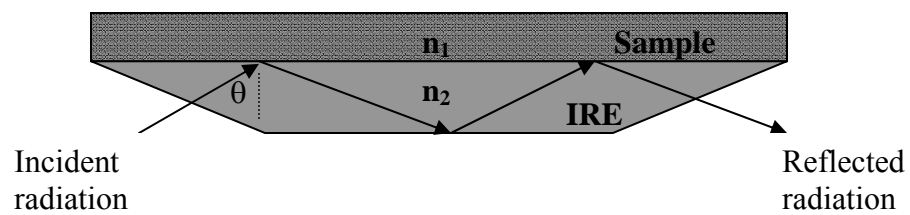
Figure 1.5. Schematic diagram of horizontal ATR accessory
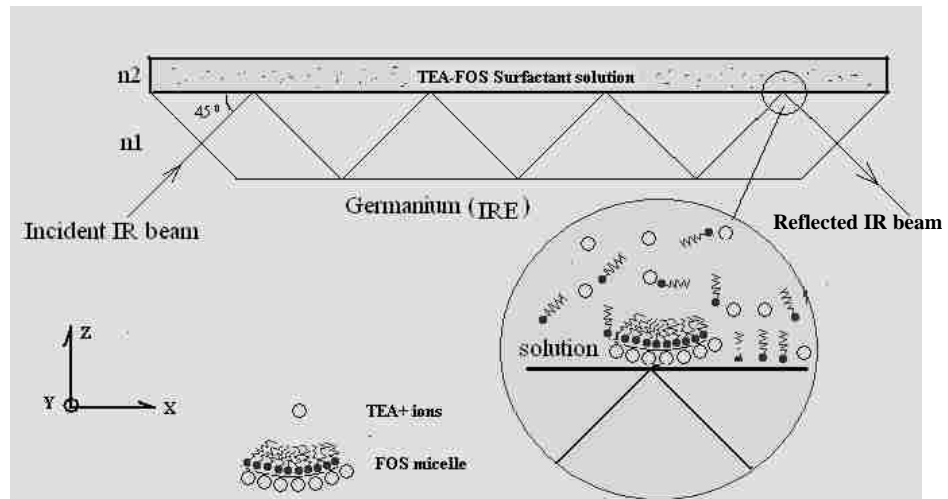
Figure 1.6. Schematic description of the evanescent field created at each reflection in an IRE of Ge.

$$\cos(\frac{2\pi z}{\lambda} + \phi)$$

E_0

n_1

d_p

n_2

Z
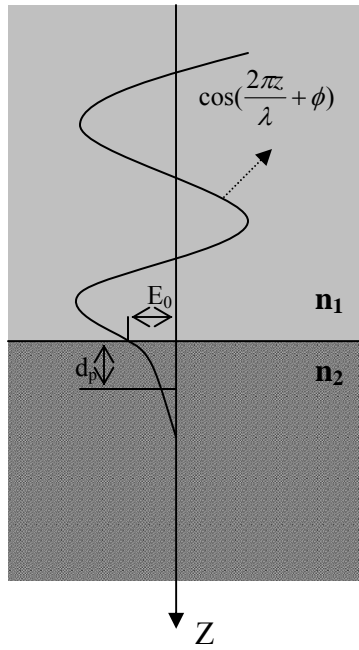
Figure 1.7. Standing-wave amplitude near a totally reflecting interface
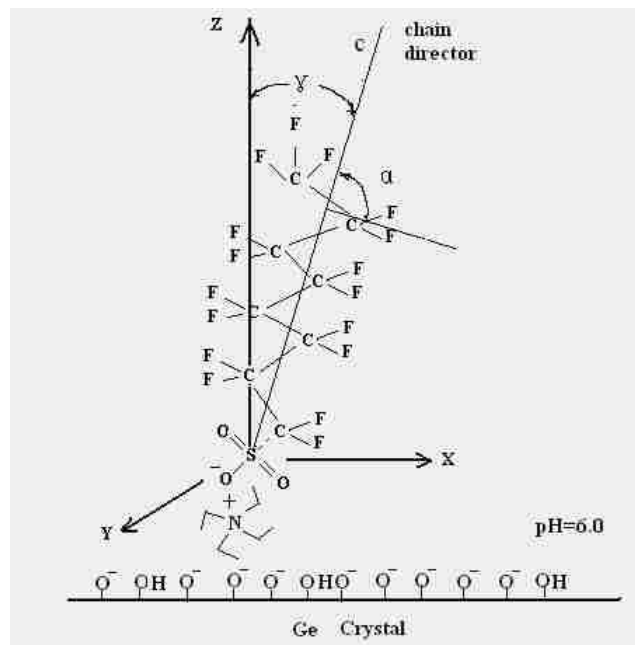
Figure 1.8. Schematic representation of laboratory axes and adsorbed TEA-FOS surfactant on Ge surface.
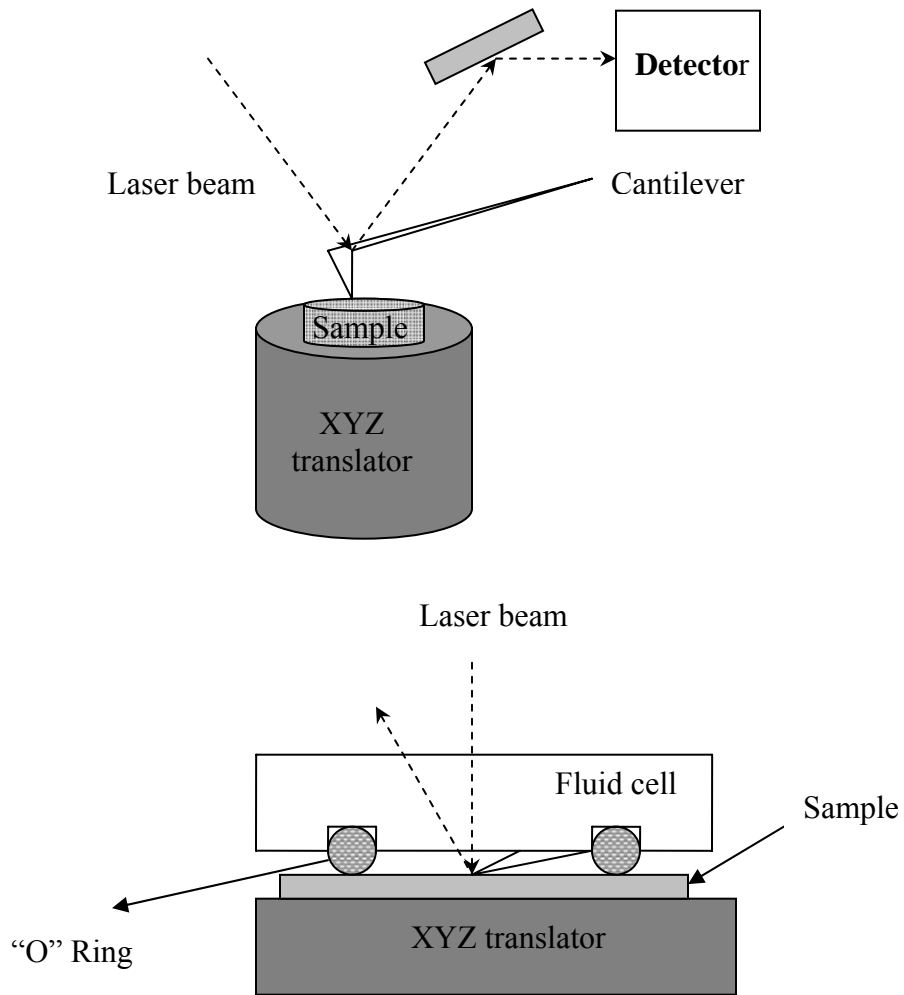
Figure 1.9. (a) Schematic diagram of AFM (Multimode III); (b) Cross section of enclosed cell for liquid sample.

Chapter 2. Three Stage Multilayer Formation Kinetics during Adsorption of an Anionic Fluorinated Surfactant onto Germanium 1. Concentration Effect[*]

2.1. Introduction

Fluorinated surfactants are an important class of amphiphiles. Fluorocarbons are characterized by very strong intramolecular C-F bonds and weak intermolecular interactions. They are not only hydrophobic, but also lipophobic. These properties give rise to the well-known thermal stability, low friction, and non-stick properties of polymers such as poly(tetrafluoroethylene).[1] The torsional potential of fluorocarbons causes them to prefer a stiff helical conformation.[2] This stiffness of fluorocarbons and their weak intermolecular interactions gives them a high capacity for gases (e.g. oxygen)[3] and supercritical fluids (e.g. carbon dioxide).[4] These properties are also found in fluorinated surfactants, which are of interest for applications as diverse as pulmonary oxygen and drug delivery,[3] high-performance nonaqueous cleaning,[5] biological assays,[6,7] surfaces with controlled adhesion and friction,[8] and materials synthesis.[9-12] Either for these applications, or for the recovery of these valuable and useful surfactants, it is important to understand how fluorinated surfactants adsorb and assemble near surfaces.

Fluorinated surfactant bulk self-assembly behavior has been studied, and general trends have emerged. When dissolved in solution, fluorinated surfactants tend to form highly stable and well organized films, bilayers, vesicles, cylinders and tubules.[13] Compared with their hydrogenated counterparts, fluorinated surfactants form micelles with less interfacial curvature at lower concentrations.[14] Generally, the CMC of a fluorinated surfactant is equal to that of the analogous hydrocarbon with a tail that is 1.5 times the length of the fluorocarbon.[15] These trends can be explained by the large volume of the fluorinated chain and high hydrophobicity of the fluorocarbon (increasing the hydrophobic driving force for self-assembly).

The self-assembly of surfactants in solution into a variety of aggregates has been studied in depth for decades. The factors determining the geometric form, size, and stability of these self-assembled structures are relatively well understood.[16,17] At interfaces, however, the self-assembly process is influenced by additional factors such as

surfactant-surface and solvent-surface interactions. There have only been a few investigations of the adsorption of fluorinated surfactants from liquid solution.[18-23] Isotherms were measured with solution depletion measurements by HPLC[18] or ^{19}F NMR,[22] and with in situ ellipsometry measurements[23]. For a number of perfluorocarboxylic acids and perfluorooctanesulfonamide- trimethylammonium iodides (FOSA-TMAI), the adsorption isotherms were found to be consistent with 3- or 4-stage adsorption (depending on the resolution of the technique),[19,22,23] which is typical for adsorption of most ionic surfactants.[24,25] Rojas et al. used force curves to ascertain that the FOSA-TMAI surfactant forms bilayer islands early which grow until the surface is covered.[23] Using AFM, Lamont and Ducker showed that the adsorbed layer of lithium perfluorooctanesulfonate (Li-FOS) on graphite consists of hemicylindrical micelles which become wider but somewhat compressed as the surfactant concentration increases.[21]

As part of these studies, the kinetics of adsorption was sometimes measured, but only to confirm that equilibrium was reached. Generally, investigators found rapid initial adsorption followed by a slow approach to equilibrium.[19,20,23] Equilibrium was sometimes reached quickly, and sometimes slowly; equilibration took as long as ~140 hr in the work of Lai et al.[19] Adsorption of charged surfactants is usually fast (on the time scale of minutes), but at surfactant concentrations above a monolayer concentration, a slow second adsorption step is sometimes observed, which is attributed to adsorption onto a surface with a barrier in conjunction with rearrangement of the adsorbed surfactants.[24] Self-assembled monolayer formation follows similar kinetics,[26] but for some octadecyl surfactants, Schwartz and colleagues observed three-stage adsorption corresponding to fast adsorption, slow continued growth of the layer, and spontaneous acceleration of adsorption prior to saturation.[27,28] The slow intermediate plateau is associated with a barrier created by the fast initial deposition of a low-density surfactant layer from which a high-density solid layer nucleates and grows in the third stage.[29]

In the interest of further understanding of the nature of fluorinated surfactant adsorption, we investigate here the kinetics of adsorption of tetraethylammonium perfluorooctylsulfonate (TEA-FOS), a commercially available fluorinated surfactant. The bulk self-assembly of TEA-FOS has been the subject of numerous investigations,

which have shown that the surfactant has a strong tendency to form threadlike micelles, and that the dynamics of micelle exchange are very slow for this surfactant.[30-33] This behavior contrasts that of Li-FOS, which favors spherical micelles and which undergoes rapid monomer exchange.[31, 32]

Attenuated total reflection Fourier transform infrared spectroscopy (ATR-FTIR) is a good method for the *in situ* study of interfacial phenomena at the solid-liquid interface. The interpretation of the results of this technique is aided by recent research on the nature of evanescent behavior at a multilayer interface.[34,35] ATR-FTIR has been successfully applied to the determination of adsorption kinetics as well as the molecular orientation of hydrocarbon surfactants at the solid/liquid interface.[36-41] However, ATR-FTIR studies of fluorinated molecular layers have been limited to characterization of chemisorbed fluorinated silanes.[20,42] To date, there has not been an ATR-FTIR study of physisorption of a fluorinated surfactant from a liquid phase onto a solid surface.

Here we report measurements of surface excess, adsorption kinetics, and average orientation angle for TEA-FOS adsorption from aqueous solution onto hydroxylated germanium. Germanium is selected as a model metal oxide / hydroxide surface because it is infrared transparent in the fluorocarbon wavenumber range.[42] We will present evidence for three-stage adsorption kinetics during the formation of a multilayer surface structure.

2.2. Experimental section

2.2.1. Materials

Tetraethylammonium perfluorooctylsulfonate (TEA-FOS), $CF_3(CF_2)_7SO_3^-$ $\cdot N^+(C_2H_5)_4$ with purity $\geq$ 98% was purchased from Fluka Chemical Co. and used as received. Solutions were prepared with deionized ultra-filtered water (Fisher Scientific).

2.2.2. Instrumentation

FTIR spectra were obtained with a sealed and desiccated ThermoNicolet Nexus 470 infrared spectrophotometer equipped with a DTGS detector. A specimen for solid-state FTIR was prepared by finely grinding crystalline TEA-FOS, diluting it to 1 wt% with KBr powder, and pressing the mixture into a translucent pellet with a hand press. For liquid samples, transmission FTIR was performed with a demountable liquid cell (Harrick Scientific Corp.) with germanium (Ge) windows. To avoid interference fringes

in the transmission spectra, mismatched Teflon spacers were used to form a liquid wedge. The background spectrum for transmission experiments was the single-beam spectrum of the dry cell.

ATR-FTIR spectra were taken using a horizontal ATR accessory (Pike Technologies) and a liquid nitrogen cooled MCT detector. A 45° trapezoidal Ge internal reflection element (IRE), 80.0 × 8.0 × 4.0 mm, was used. The IRE was housed in a nickel-coated flow-through cell. All the spectra were the result of averaging 128 scans at a resolution of 4 cm^{-1}. Experiments were performed at room temperature (21 +/- 1 °C). Residual bands from atmospheric water and carbon dioxide were eliminated by background subtraction and automatic atmosphere suppression software.

Polarization was achieved by using a wire grid ZnSe polarizer (Spectra-Tech model FT 80) mounted to the ATR accessory just before the IR beam enters. By adjusting the wire grid angle, the polarizer was set perpendicular (S), parallel (P), or at 45 degrees ("unpolarized") to the plane of incidence of the IRE.

Selected quenched films were imaged with a Nanoscope III atomic force microscope (Digital Instruments). Mica was selected as hydrophilic substrate with negative surface charge for these studies. The preparation of quenched surfactant films followed the procedure developed by Woodward et al.[43] Typically, the mica was submerged in 0.1 mM TEA-FOS surfactant solution and removed after immersion for specific times. Upon removal the samples were rinsed in DIUF water for 30 s and blown dry with an ultrahigh purity (UHP) nitrogen stream, then immediately loaded into the AFM. The scanner was calibrated using a standard grid. Silicon nitride(Si_3N_4) tips (RFESP type) were used with a factory-specified spring constant of 3 N/m, length of 220 μm, width of 35 μm, and nominal tip radius of curvature of < 10 nm. Surfactant multilayers were imaged in both topography and deflection mode. No filtering of the images was performed other than flattening along the scan lines to remove background slopes.

2.2.3. Ge surface preparation

Preparation of the IRE for an experiment required first polishing the IRE for 30 min with 0.1 micron diamond paste, then soaking in deionized water for 24 hr to ensure consistent hydroxylation of the surface. After being dried in a stream of ultra pure nitrogen, the IRE was immediately sealed into the flow cell using a PTFE-coated o-ring.

The IRE was cleaned with isopropanol, acetone and deionized water by scrubbing lightly with a cotton-tipped applicator.

2.2.4 Surface excess measurements

Solutions of precisely measured concentration were prepared and introduced into the ATR accessory. For all solutions, the pH was 6.0 ± 0.1. The pH was not 7.0 because the pH of DIUF water that we used was close to 6.0. During adsorption, the electrochemically measured pH of the surfactant solution did not change significantly. The ATR trough was covered with an o-ring sealed metal cover to prevent evaporation. We calculated surface excess using an expression developed by Tompkins[44] (see chapter 1 for a full discussion of the assumptions underlying this model) which is based on the assumption of a step change in absorbance upon going from the adsorbed layer to the bulk solution:

$$\frac{A_t}{N\varepsilon} = Cd_e + (\frac{2d_e}{d_p})(\Gamma_i) \qquad (2.1)$$

where A_t = the total absorbance, N = the number of reflections in the IRE, ε = the extinction coefficient for a given band, C is the bulk concentration, d_e is the effective pathlength per reflection, d_p is the penetration depth, and Γ_i is the surface excess. The total effective pathlength, Nd_e was found in our experiments by calibration of water absorbance intensity using a transmission cell with varying pathlengths. The extinction coefficient was found from calibration using a transmission cell and varying concentrations of surfactant. The penetration depth is given by equation (1.3), where λ = the wavelength of the band being measured, θ is the angle of incidence of the IR beam with the ATR trapezoid, and n_1 and n_2 are the refractive indices of the IRE and the solution, respectively.

2.2.5. Linear dichroism calculation.

The molecular orientation of surfactant TEA-FOS molecules at the Ge/liquid interface can be determined by linear dichroism spectroscopy. The laboratory Cartesian coordinates *(X, Y,* and Z axes) of an adsorbed surfactant molecule are shown in Figure 1.8. In that figure, the Z axis is perpendicular to the IRE surface. S-polarized radiation is orientated with its electric vector in the y- direction, while P- polarization lies in the *XZ*

plane (the plane of incidence), at 45° with respect to each of the two axes. In this description, we assume that a chain axis can be used to represent molecular orientation.

The linear dichroic ratio, LD, is defined in chapter 1 by equation (1.11). At the Ge/solution interface, the electric field amplitude in the three Cartesian directions can be calculated using equations (1.12). These equations are valid for a two-phase system, which is a good approximation when the thickness of the adsorbed film on the IRE is negligible compared to the penetration depth d_p.

In our experiment, the uniaxial model was used to determine the molecular orientation, because there is no external force which causes the absorbed surfactant to orient laterally. With the assumption that $\alpha = 90°$ for both the symmetric and asymmetric CF_2 stretching in equation (1.21), the LD ratio is calculated by using equation (1.19). For those vibration modes with dipole angles at angle $\alpha = 0°$, the LD ratio is calculated by using equation (1.16).

2.3. Results and discussions

2.3.1. In situ adsorption kinetics of TEA-FOS at the Ge/solution interface

An in situ ATR-FTIR technique was developed to investigate the adsorption kinetics of fluorinated surfactant TEA-FOS from aqueous solution. The adsorption process can be followed almost from the first introduction of the surfactant solution. In order to measure surface excess, it is necessary to account for and remove contributions to the adsorbance which come from the isotropic bulk solution, and to know the effective pathlength of the IRE. To determine the extinction coefficient for the surfactant in isotropic aqueous solution, a series of calibration experiments is first described.

2.3.1.1. Calibrating the pathlength of the liquid transmission cell

Liquid transimission cells used in the mid-infrared range typically have very small pathlengths (1000 microns or less), which are required for reasonable absorbance values (~ 1.0 or less) of the strongly absorbing organic compounds typically analyzed. Demountable liquid cells using spacers provide a convenient method to perform analyses of samples. However, for accurate quantitative work, it is frequently necessary to verify the exact pathlength of the cell, even though the nominal spacer thickness may be given by the vendor. Determining the exact pathlength is accomplished by either using interference fringes or developing a calibration curve of absorbance vs. pathlength for a

solvent. We used both methods, the former to calibrate individual spacer thicknesses and the latter to confirm the pathlength with mismatched spacers that are used to eliminate interference fringes for calibrating the surfactant extinction coefficient.

2.3.1.2. Using interference fringes

After nitrogen purge, a backgroud spectrum was collected with the liquid cell removed from the sample compartment. Then take a sample spectrum with the cell in the compartment. The cell was empty (i.e. only air should be in the cell), and a spectrum with an interference fringe pattern was obtained as shown in Figure 2.1. This pattern is generated by partial reflection and self-interference of the IR beam between parallel windows. Two peaks at least 10 waves apart were chosen to determine cell pathlength of interest. The pathlength d, in centimeter, can be calculated by:

$$d = \frac{F}{2 \times n \times W} \tag{2.2}$$

where F is the number of complete oscillations (fringes) being counted, n is the refractive index of the sample between the windows (for air, n=1), and W is the wave number range containing the F fringes.

For the sample spectrum in Figure 2.1., the actual pathlength for a cell with spacers of nominal thickness 0.056 mm can be calculated according to equation (2.2):

$$d = \frac{F}{2 \times n \times W} = \frac{12}{2 \times 1 \times (2745 - 1650)} = 5.5 \times 10^{-3} cm = 0.055 mm$$

This coincides with the spacer thickness given by the vendor (Harrick Scientific). Other spectra of empty cells were collected by using different nominal spacer sizes of 0.025 mm, 0.056 mm, 0.1 mm, 0.15 mm, 0.25 mm, 0.39 mm, respectively. The calibrated results for transmission liquid cells are listed in the Table 2.1.

2.3.1.3. Calibration of absorbance vs. pathlength

For careful quantitative measurements in transmission mode, mismatched spacers are used to form a liquid wedge between non-parallel Ge windows. This eliminates the interference fringes for parallel windows, and the average pathlength obtained of the two spacers from Table 2.1 can be used to approximate the effective pathlength. However, another practical method, developing curve of absorbance vs. pathlength, gives a more accurate estimate. To develop this curve, liquid cells with parallel Ge windows were

filled with deionized water, with matched spacers between 0.016 mm and 0.056 mm in thickness. The integrated intensity of the band at 2135 cm^{-1} was used to calibrate the pathlength. Figure 2.2 shows the resulting linear relationship between absorbance and pathlength, which can be used to determine the effective pathlength by measuring absorbance intensity of the water band for matched or mismatched spacers. Using this calibration, the effective total pathlength (Nd_e) of the germanium IRE was estimated to be 2.97 μ m at 1212 cm^{-1} (see chapter 1 for the wavelength dependence). The calibration was also used to obtain accurate pathlengths with mismatched spacers.

2.3.1.4. Calibrating the absorbance intensiy of TEA-FOS vs. concentration

In order to determine the extinction coefficient for the surfactant TEA-FOS in isotropic aqueous solution, a series of calibration experiments was performed by measuring liquid liquid transmission spectra of surfactant solutions with concentration between 0.5 mM and 5 mM. A plot of the integrated fluorocarbon band region (from 1299.8 cm^{-1} to 1124.3 cm^{-1}) vs. concentration yielded a good linear fit and an extinction coefficient of $\varepsilon = 13.7 \pm 0.4$ mm^{-1}*mM^{-1}.

2.3.2. Surface excess measurements

Both total effective pathlength (Nd_e) of the ATR and extinction coefficient ε have been found from calibration experiments, and the penetration depth d_p in equation (2.1) is calculated as 0.52 μm by using the refractive indices and the angle of incidence of the ATR crystal. With these values, the surface excess can be quantified according to equation (2.1).

Figure 2.3a shows an example of in situ ATR-FTIR data collected during the adsorption of TEA-FOS onto hydroxylated Ge from a 1 mM aqueous solution. The ATR spectra initially show three strong bands at 1242, 1206, and 1152 cm^{-1}. The same set of bands is observed in the transmission spectra used for calibration. The two bands at higher frequencies (1242 cm^{-1} and 1206 cm^{-1}) are attributed to CF_2 asymmetric stretching, and the band at 1152 cm^{-1} to CF_2 symmetric stretching.[45] During adsorption, all of these bands shift to lower frequency. At equilibrium, the three bands appear at 1239 cm^{-1}, 1205 cm^{-1} and 1151 cm^{-1}, respectively. This relative shift, especially in the $(CF_2)_{as}$ band position, from high to low wavenumber as coverage increases indicates

movement of the fluorocarbon tails into a more structured and hydrophobic environment as adsorption proceeds.[40] The $(CF_2)_{as}$ bands also become more intense relative to the other bands during the adsorption process. A similar shift in band positions and $(CF_2)_{as}$ peak intensities was observed in the transmission spectra at concentrations above the CMC due to the transfer of the fluorocarbons from the aqueous environment into the fluorocarbon environment of the micelle core. In spite of these changes, a linear relationship between concentration and the integrated intensity of the fluorocarbon region was still observed in the transmission spectra.

Precise assignments of the individual fluorocarbon IR bands are possible by peak fitting and deconvolution, as shown in Figure 2.3b. Specific bands assignments for the deconvoluted bands in this region (1100 to 1400 cm^{-1}) are summarized in Table 2.2. The set of bands found by deconvolution is consistent with the bands previously assigned in the literature (cited in Table 2.2). The changes observed in these spectra are typical of what we observed for all solutions below, at, and above the CMC of TEA-FOS (1 mM[31]). Figure 2.4 shows examples of the ATR-FTIR spectra of adsorbing TEA-FOS early in the adsorption process (during the second slow adsorption stage discussed below) and near equilibrium. All three concentrations give similar qualitative features in the FTIR spectra. In the following sections we will discuss only the evolution of the intensities of the bands.

2.3.3. Initial adsorption kinetics

Figure 2.5 shows the evolution of surface excess with time up to 800 min for TEA-FOS concentrations ranging from 0.1 mM to 5 mM. The initial kinetics shows similar qualitative features for all compositions: the amount of adsorbed surfactant increases relatively quickly in the first stage (up to ~200 min), but then slows until a constant adsorption rate is reached in the second stage. Such qualitative feature may indicate either diffusion-controlled adsorption or reaction-controlled adsorption, so it is necessary to determine which is more reasonable. If adsorption is completely diffusion-controlled, then we can assume that surfactant molecules are immediately adsorbed upon reaching the germanium surface. This situation is modeled by solving Fick's second law[50] using the following initial and boundary conditions:

$$\frac{\partial C(z,t)}{\partial t} = D\frac{\partial^2 C(z,t)}{\partial z^2} \qquad (2.3)$$

I.C. $C(z, t=0) = C_0$

B.C. $C(z=0, t) = 0$

$$C(z,t) \underset{z \to \infty}{\longrightarrow} finite$$

Where C_0 is the concentration of bulk solution, and the coordinate z is perpendicular to the surface. Solving this gives an expression of the adsorbed amount at the surface as a function of time,

$$\Gamma(t) = 2C_0\sqrt{\frac{Dt}{\pi}} \qquad (2.4)$$

A plot of Γ vs. $\sqrt{t}$ for the 0.1 mM solution can be fit with a line to give an estimate of D = 1.26×10^{-15} m^2/s, which is 5 order of magnitude less than the literature value measured for TEA-FOS monomers by PFG NMR[31] (D = 3.8×10^{-10} m^2/s). Therefore, while it appears qualitatively correct, equation (2.4) can not reasonably describe the kinetics of the adsorption of TEA-FOS onto the Ge surface.

Another potential approach based on diffusion-limited adsorption is a first-order Langmuir adsorption model limited by diffusion through a thin boundary layer near the surface of the substrate.[51,52] Equation (2.5) describes this case.[52]

$$\Gamma(t) = \Gamma_0[1 - \exp(-kt^{1/2})] \qquad (2.5)$$

where k = $\frac{2C_0}{\Gamma_0}\sqrt{\frac{D}{\pi}}$. However, using equation (2.5) to fit our experimental data, the estimated value of D averaged for all five surfactant concentrations is 1.80×10^{-16} m^2/s, which is *six* orders of magnitude less than the literature value for TEA-FOS.[31] In addition to adsorption being much slower than the known diffusion coefficient would suggest, we have found that the initial adsorption rate depends strongly on both pH and ionic strength (results given in the chapter 3). This is difficult to explain by a diffusion controlled process. From the above analysis, we conclude that the adsorption of TEA-FOS from solution onto the Ge surface cannot be simply considered a diffusion-limited process.

Because the adsorption rate is so much slower than the reported diffusion coefficients would predict, we develop a kinetic model based on reaction-limited adsorption process.

In order to formulate a model for what takes place during the initial adsorption stages, we qualitatively study the growth kinetics of quenched surfactant films on mica from 0.1 mM TEA-FOS solution by AFM. The ideal model substrate should be germanium, but the RMS roughness of available Ge wafers is not acceptable for this type of study. Since mica provides a reproducible, flat negatively-charged surface, we use mica as the substrate for these experiments. Figure 2.6 shows representative ex-situ topographic AFM images of adsorbed TEA-FOS on mica. The height image collected after 5 min is displayed in Figure 2.6a, and shows uniform submonolayer patches (brighter regions in the image) and darker holes representing uncovered substrate. The height scale of the bright regions is 1 nm in this figure, which is consistent with the length of TEA-FOS tail. After 25 min of adsorption, we observe admicelles (with a height scale of 2 nm) on the mica surface as shown in Figure 2.6b, which may suggest the formation of bilayers patches or admicellar aggregates. It should be pointed out that these are quenched, dried films, and may not represent that exact structure in solution, but that the in-situ and ex-situ AFM images agree well at late stages of adsorption (to be discussed in chapter 3). After 30 min of adsorption (Figure 2.6c) some tall clusters (white in the image) are observed among the admicelles, suggesting the nucleation of multilayer clusters on the admicelles occurs. With time, the number density and size of the clusters increase. At equilibrium, we observe large patches of clusters with multilayer structure on the mica (Figure 2.6d) but the surface remains heterogeneous in texture.

In the ex-situ AFM study on mica, we can observe sub-monolayer islands in the early stages of adsorption which grow as surface coverage increases. Some of the islands seem to serve as nuclei for multilayer patches which begin to grow before the surface is fully covered by a monolayer. As we will discuss in more detail below, the surface excess during the first two adsorption stages corresponds to less than a monolayer of surfactant. Assuming that the adsorption mechanism is similar on mica and hydroxylated Ge, the following cluster growth reaction scheme can be proposed for the first two stages of adsorption in which patches of uniform surfactant are deposited:

$$A + S \underset{k_1'}{\overset{k_1}{\rightleftharpoons}} \underbrace{A \bullet S}_{C_1}$$

$$A + C_1 \underset{k_2'}{\overset{k_2}{\rightleftharpoons}} C_2 \qquad (2.6)$$

$$A + C_2 \underset{k_3'}{\overset{k_3}{\rightleftharpoons}} C_3$$

$$\vdots$$
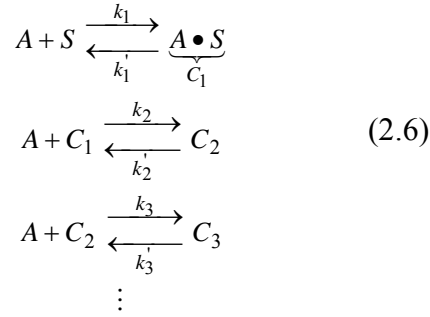
where A represents free surfactant in solution, S is an adsorption site, and C_n refers to a surfactant cluster of size n formed on the Ge surface. This scheme can be simplified by assuming that all of the rate coefficients for addition of a monomer to an existing cluster are the same, so the cluster addition steps can be combined to yield scheme (2.7). In this scheme, we represent an active cluster of any size by C, and a surfactant bound to a cluster by B. When the bulk solution concentration remains constant, the first reaction gives first-order Langmuir-like kinetics, and the second reaction gives rise to an apparent zero-order reaction in the second stage. These kinetics have been observed before for growth of self-assembled monolayers from liquid solution, although no kinetic model was proposed.[53]

$$A + S \underset{k_1'}{\overset{k_1}{\rightleftharpoons}} C$$

$$ \qquad (2.7)$$

$$A + C \underset{k_2'}{\overset{k_2}{\rightleftharpoons}} C + B$$
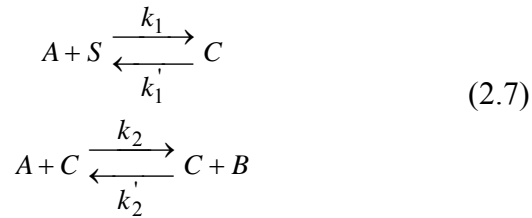
Assuming that these are elementary reactions, and that the ATR response from both types of adsorbed surfactants (C and B) is the same (and therefore $\Gamma = C + B$), the following equation results from the mechanism above:

$$\Gamma = \frac{S_0 k_1^*}{k_{obs}}\left[1 - e^{-k_{obs}t}\right] + \frac{k_2^*}{k_2'}\left\{1 - \exp\left\langle -k_2' \frac{S_0 k_1^*}{k_{obs}}\left[t + \frac{1}{k_{obs}}\left[e^{-k_{obs}t} - 1\right]\right]\right\rangle\right\} \quad (2.8)$$

where the asterisks denote pseudo-first order rate coefficients derived by assuming that the concentration of A in solution is constant, S_0 is the initial concentration of adsorption sites on the Ge surface, and $k_{obs} = k_1^* + k_1'$. This equation was fit to the early kinetic data,

using the Levenberg-Marquardt algorithm, to determine four parameters: $S_0k_1{}^*$, $k_2{}^*$, k_2', and k_{obs}. Figure 2.5 shows that a very good fit could be obtained using this modified Langmuir model for all data in the concentration range from 0.1 to 5 mM. The parameters found are summarized in Table 2.3.

The concentration of surfactant in the bulk solution appears to have a significant effect on the kinetics of the adsorption of TEA-FOS onto the Ge surface. As the bulk surfactant concentration increases from 0.1 mM to 1 mM, the rate coefficients for both adsorption stages increase. However, for concentrations above the CMC (3 mM and 5 mM), the rate coefficients do not change or even decrease as the surfactant concentration increases. This result may be explained based on the ^{19}F NMR studies of surfactant TEA-FOS in bulk solution, which show that the concentration of monomers passes through a maximum at the CMC (1 mM).[31] This correlation suggests that monomers are the main species that participate in adsorption during the initial two stages.

2.3.4. Long-term adsorption kinetics

When we extended our adsorption measurements beyond the times shown in Figure 2.5, we encountered unusual behavior. The surface excess of surfactant adsorbed onto Ge at a pH of 6.0 ± 0.1 over an expanded time scale is shown in Figure 2.7 as a function of TEA-FOS concentration. In addition to the usual two adsorption stages discussed in the previous section, to our surprise we find that the adsorption kinetics exhibits a third stage with a clearly different time scale. This three-stage adsorption is observed well below CMC (0.1 mM solution), at the CMC, and well above the CMC (5 mM). As discussed above, the first stage is characterized by relatively rapid surfactant adsorption within ~ 200 min after introduction of the solution into the cell, and the second stage is characterized by a much slower, constant rate of increase of the surface excess. The duration of the second stage increases as the bulk surfactant concentration decreases, and spans a range from 700 to 1500 min. After this slow stage, there is a sudden *increase* in the rate of adsorption in the third stage. This stage then appears to proceed with Langmuir-like kinetics for a long time (as much as another 4000 min) before the level of adsorption reaches a constant value. This type of three-stage kinetic sequence is highly unusual for surfactants. Most surfactants exhibit only Langmuir adsorption kinetics or the two-stage adsorption that we observed in the first two stages.[24] With our technique,

we also observed one- or two-stage adsorption kinetics for other surfactants adsorbed onto Ge from aqueous solutions, including CTAB, cetylpyridinium bromide, and even other fluorinated surfactants such as (1H,1H,2H,2H)tetrahydroperfluorodecylpyridinium chloride. This study of TEA-FOS on germanium is the first example that we are aware of in which three-stage surfactant adsorption kinetics are observed during multilayer formation. Surfactant adsorption with a suddenly increasing rate in the third stage has only been reported in studies of self-assembled monolayer formation by Schwartz and coworkers.[27,28]

2.3.5. Adsorption isotherm

We have explored extensions of the kinetic model that would allow it to fit the third stage of adsorption. Models with autoaccelerating adsorption (adsorbed molecules creating more adsorption sites for further adsorption) are able to match the sharp increase in adsorption rate in the third stage to some extent. However, it is also possible to explain the third stage through the nucleation and growth of multilayer clusters of surfactants (micelles or disordered aggregates) at the liquid-solid interface. Developing and solving these models requires numerical methods beyond the scope of the present investigation. However, we can gain some insight into the third stage from the final state that is reached.

We first compare the surface excess values to those expected for different adsorbed layer structures. Matsumoto et al.[33] developed a surface tension isotherm for TEA-FOS at the water-air interface, and using the Gibbs equation calculated a limiting area of 0.54 nm^2 per molecule for TEA-FOS near the CMC. This value can be considered as the cross sectional area of the head group for close-packed TEA-FOS molecules in aqueous solution around the CMC. From the TEA-FOS area, we would expect to measure a surface excess of 3.06 μmol /m^2 when the molecules are completely aligned in a close-packed monolayer. The dotted line in Figure 2.7 represents this value. Compared to the measured surface excesses, the first two stages of adsorption lead to the formation of the equivalent of a monolayer or less, while the third stage accomplishes multilayer formation. The value at saturation is more than would be expected for a bilayer, and even more than what would be expected for a 2D hexagonal close-packed layer of spherical micelles (11.0 μmol/m^2). Table 2.4 summarizes the calculated values at saturation for

surface excess and the area occupied per molecule. Assuming an area of 0.54 nm^2 per molecule, the surface excess for all of these concentrations approaches the equivalent of 6 or 7 close-packed monolayers.

Given that we always observe this high level of adsorption, even at a concentration as low as 10% of the CMC, one might be concerned that we are measuring an effect of insolubility of TEA-FOS rather than adsorption. We can rule this out because we found that the Krafft temperature is less than 0 °C, and we have been able to prepare homogeneous solutions containing over 70 wt% TEA-FOS in water at room temperature. Figure 2.4 also shows that the infrared spectrum of crystalline TEA-FOS differs from that of the adsorbed multilayer (especially the band at 1266 cm^{-1}). Still, to gain more understanding of the adsorption process, we measured the adsorption isotherm for TEA-FOS on hydroxylated Ge surface at pH 6 at even lower concentrations using ATR/FTIR, as shown in Figure 2.8. There exist three clearly different regions: (1) a low surface excess region, (2) a hydrophobic interaction region, (3) a plateau region. The adsorption isotherm resembles those of other surfactants except that we cannot clearly resolve all four of the regions often found for charged surfactants.[24,25,54]

Region I in Figure 2.8 exhibits a slow increase of the surface excess with the bulk concentration, which suggests that the surfactant is adsorbing via electrostatic interactions with the Ge substrate. Because the point of zero charge (pzc) of GeO$_2$ < 5,[55] at the conditions of the experiment (pH = 6) the surface of substrate is negatively charged. It is surprising that this anionic surfactant adsorbs at all onto hydroxylated Ge at this pH, but it is not unprecedented. Hankins et al. have summarized several reported cases of anionic hydrocarbon surfactants adsorbing at pH values above the pzc of the adsorbent, and have shown using a model of charged surfactant adsorption on patchy surfaces that counterions mediate the charge interactions in this case.[56] TEA$^+$ ions are weakly dissociated from FOS$^-$ in water at room temperature, so they are likely to stay near the surfactant headgroups at the germanium surface, thus facilitating adsorption.[57] We do not expect any form of aggregation at the interface at this stage, because less than a monolayer of surfactant is present.

Region II in Figure2.8 shows an abrupt increase in surface excess as the bulk concentration increases. This region begins because the most favorable adsorption sites

on the surface have been saturated, and the bulk surfactant concentration is sufficient to lead to hydrophobically driven clustering of monomers. A large amount of surfactant adds over a narrow concentration range because the surfactant already bound to the substrate provides an appropriate environment for formation of adsorbed aggregates.[24,25] This region is very narrow, and suddenly ends in Region III with a plateau. However, unlike most surfactants, many layers have adsorbed at this final stage rather than just a bilayer. There is a very small increase of surface excess as the bulk concentration increases from 0.1 mM to 1 mM compared with the sudden and large increase of adsorption in Region II. Region III begins at a surprisingly low bulk surfactant concentration (10% of the CMC). Other surfactants have been found to reach saturation levels of surface coverage closer to between 50% and 100% of their CMC[24,25,54]. Most hydrocarbon surfactants terminate adsorption after forming a monolayer or a bilayer, however. In the case of TEA-FOS, the extreme hydrophobicity of the tail, and perhaps charge mediation by TEA adsorbed to the head groups, drive the transition directly from submonolayer adsorption to multilayers. In a similar way, hydrophobicity and TEA mediation cause globular micelles of TEA-FOS to string together into threadlike structures in solution.[30]

2.3.6. Linear dichroism measurement

In addition to surface excess measurements, we use linear dichroism to gain insight into the structure of the adsorbed layer formed from TEA-FOS. Because we employ low bulk concentrations of TEA-FOS, we will neglect the absorption of the evanescent wave in the bulk solution in the calculations to be discussed in this section. Figure 2.9 shows examples of the ATR-FTIR spectra obtained using parallel and perpendicular plane polarized infrared beams for 5 mM TEA-FOS solution as a function of time. Differences in intensity can clearly be observed. To quantify the results, we first use equation (1.12) with parameters for our system (n_1 = 4 (Ge), n_2 = 1.33 (water), and θ = 45^0) to get E_x = 1.40, E_y = 1.50, and E_z = 1.59. Using equations (1.18) and (1.19), we predict that LD = 0.5 for a randomly distributed orientation of molecules, LD = 1.14 when the chain axis is normal to the surface, and LD = 0.32 when the chain axis is parallel to the surface. In Figure 2.10, we plot the LD ratio of the CF_2 symmetric stretching bands (wavenumber range 1178.3 ~ 1124.3 cm^{-1}) against time at different bulk TEA-FOS concentrations. In

the third stage of adsorption, a strong correlation is observed between the adsorbed surfactant orientation and the development of surface excess for all solution concentrations.

In Figure 2.10, we also can see that the measured A_s/A_p ratios at 0.1 mM TEA-FOS start out smaller than those for higher concentrations. This difference is probably due to a very dilute surface layer initially present for the 0.1 mM solution. The angle may also be a better reflection of the true surface orientation than the other samples because for this sample, the bulk signal is less than 5% of the total signal, which leads to only small errors in the surface excess via ATR absorbance measurements.[58] The bulk contribution is more important for experiments with higher concentrations. Still, for all samples, this effect is only important at low coverage, and with the increase of surface coverage, the bulk contribution can be neglected. When equilibrium is attained, a plateau in the A_s/A_p ratio with time is observed at a value of around 0.58 for all solution concentrations, corresponding to a plateau in the surface excess.

From the low value of A_s/A_p measured within the first two stages of adsorption, we think that the surfactant is not randomly oriented during the initial adsorption, but instead displays preferred orientation. Using the experimental values for LD and theoretical values of E_x, E_y and E_z, the average tilt angle γ of surfactant can be calculated from equation (1.19). Figure 2.11 shows how the average tilt angle varies with surface excess during adsorption of TEA-FOS at the hydroxylated Ge/solution interface for concentrations below, at and above the CMC. For all solutions, the average tilt angle decreases as the surface excess increases. For the 0.1 mM solution, the angle is large initially, indicating an orientation somewhat parallel to the solid surface. This orientation is consistent with a low density in the adsorbed layer. The parallel orientation may help to create hydrophobic patches on the surface, and thus to facilitate the onset of the third adsorption stage. This parallel orientation is not observed for the other concentrations, either because of the contribution of the bulk solution (noted above) or because there is a genuine difference in the structure of the layer during the first two stages. At equilibrium, the surfactants have preferential orientation somewhat normal to the surface for all bulk concentrations studied here. The calculated average tilt angle of the surfactant is 48° when multilayer adsorption finally approaches equilibrium. This preferred

orientation angle at equilibrium is confirmed by using the measured linear dichroic ratios of different bands oriented parallel or perpendicular to the fluorocarbon axis, as shown in Table 2.5.

Based on the experimental adsorption kinetics and linear dichroism measurements, we propose the adsorption mechanism illustrated in Figure 2.12 to describe the process of TEA-FOS adsorption from aqueous solution onto hydroxylated germanium. Part (a) represents the first stage of adsorption, which leads to the formation of less than a monolayer at the germanium surface. As our modified Langmuir adsorption model above suggests, during the initial adsorption process, monomer surfactant molecules adsorb onto pre-existing charged sites on the Ge surface. The charge between the negative surfactant and the negative surface is mediated by TEA^+. At a TEAFOS concentration less than 0.1 mM, adsorption ends at this stage, while at higher concentrations it continues. At 0.1 mM TEAFOS, the surfactants are aligned somewhat parallel to the surface. A similar orientation has been described for hydrocarbons in the first adsorption stage by Scamehorn et al.,[59] but for TEAFOS, this orientation should be primarily driven by minimizing the area of the fluorocarbon-water interface. Interactions between the fluorocarbon tail and the solid surface may play some role, but fluorocarbons are expected to interact more weakly with a hydrophilic surface than hydrocarbons.

Once the existing charged sites are nearly saturated, adsorption occurs slowly in the second stage (Figure 2.12b). During this stage, there may be continued displacement of water from the surface and slow reorganization of the adsorbed surfactant into clusters. The clustering of surfactants into surface aggregates in a second stage of adsorption is a well-known phenomenon.[24,25,60] The kinetics appears to be zero order during this stage, which suggests that the net concentration of unoccupied adsorption sites remains constant during this stage. The average orientation angle of the fluorocarbon chain decreases during this stage towards 55° for a TEA-FOS concentration of 0.1 mM, and it remains close to 55° for higher concentrations. This average orientation angle is close to the average angle for randomly oriented surfactants (54.7°), and is most likely to be due to the surfactants being organized into either hemimicelles or admicelles with no preferred orientation relative to the surface.[61] Admicelles are more likely to form from TEA-FOS because of the hydrophobicity of the fluorocarbons, and because strong counterion

binding favors admicelles over hemimicelles.[56,62] Because there is no preferred orientation in the admicelles, we depict them as spherical. This interpretation is consistent with the force curves observed by Rojas et al. for a surfactant with the same (C_8F_{17}) perfluorinated tail. At a concentration of $0.3 \times$ cmc, they observed attractive interactions initially (consistent with a patchy monolayer), and repulsive interactions consistent with a patchy admicelle layer after further adsorption ($\sim$ 10 hours).[23]

The second stage ends when the adsorbed surfactant concentration reaches a point where the attraction of surfactant monomers to the surface increases and adsorption accelerates. If we think of the surface as uniform, this would occur when the surface has become hydrophobic enough to become attractive to the tails of the surfactant. However, the model of Harwell and coworkers of a patchy surface with varying charge density and hydrophobicity is more realistic.[56,62] It is likely that the surface is heterogeneous, and that accelerated growth at this stage occurs by nucleation and growth of patches of adsorbed surfactant. This stage differs significantly from the behavior of most hydrocarbon surfactants in that after the second stage, the surface becomes so attractive to TEA-FOS that growth does not stop at bilayers, but continues all the way until multilayers form. During this stage, the surfactants develop an average orientation somewhat normal to the surface, but not completely normal to the surface. This slightly oriented structure would be consistent with the formation of "flattened" admicelles, similar to the structure observed by AFM during the adsorption of Li-FOS onto graphite.[21] The admicelles could be either oblate or elongated ribbon-like structures. Because of high binding coefficient for the organic TEA$^+$ counter-ions on the FOS$^-$ surface,[32,63] the outer layer of admicelles will be covered with the counter-ions of TEA$^+$, and thus may present a positively charged surface for further multilayer formation (Fig. 10c). During the third stage, the adsorbed surfactant molecules pack more closely with time and form flattened admicelles with a preferred average tilt angle slightly below that of randomly oriented surfactant molecules when final adsorption equilibrium is achieved. The precise nature of the onset of this third stage and confirmation of the structure of the multilayer are currently under investigation.

The formation of multilayers demonstrates that the adsorption of TEA-FOS onto hydroxylated germanium at pH 6 is thermodynamically favorable. However, this makes

the slow dynamics of adsorption surprising. As we have shown, the slow adsorption kinetics cannot be explained by diffusion-limited growth. Hence, the only explanation for the slow growth of these multilayers must be that there is a kinetic barrier to the deposition of surfactants and the nucleation and growth of admicelles. At the beginning of the adsorption process, this is likely to be due to the displacement of water from the hydrophilic GeOH surface of the substrate. Later in the process, the stability of the TEA-FOS clusters may present an impediment to their growth. In bulk solution, Bossev et al. showed that TEA-FOS micelles are unusually stable, causing anomalously slow exchange of the surfactant between micelles and monomers in solution.[31] Slow exchange on the surface between surfactant clusters and isolated surfactants may help to explain why the dynamics of adsorption remain slow throughout the adsorption process.

2.4. Conclusions

In the present study, the ATR-FTIR technique was used in situ to investigate the adsorption kinetics, adsorption isotherm and orientation of TEA-FOS deposited from an aqueous solution onto hydroxylated germanium at pH ~6. It was found that the adsorption kinetics shows three stages on clearly different time scales. The first two stages lead to the formation of a monolayer or less of surfactant. Similar to many hydrocarbon surfactants, adsorption during the first stage follows Langmuir kinetics with a finite number of isolated adsorption sites. In the second stage, the surfactant continues to slowly deposit on the surface and the change in the orientation angle suggests clustering of surfactants into admicelles. Admicelle formation is favored by strong counterion binding of TEA^+. The third stage of adsorption is surprising because the rate of adsorption suddenly accelerates at a surface excess below one monolayer, and proceeds until a multilayer structure is formed. The three-stage, fast-slow-fast kinetic trend is observed at all concentrations giving multilayers as the final structure, ranging from 10% of the CMC of the surfactant to at least 5 times the CMC. Below this concentration, only isolated surfactant adsorption occurs, with no hemi- or ad- micelles. The large difference in adsorption levels is unusual, and may be a consequence of the combination of high hydrophobicity of the fluorocarbon and strong counterion binding. The three-stage kinetics are also unusual, and have only previously been observed during

nucleation and growth of dense self-assembled monolayers from less dense intermediate layers.

The evolution of the average molecular orientation of the surfactant was determined from linear dichroism measurements. A correlation was found between the onset of the third stage of adsorption and an increase in the average orientation of the surfactants normal to the surface. Surfactants tend to orient more normally to the surface during adsorption, and achieve a preferred orientation at equilibrium for concentrations above or below CMC. The final average tilt angle was calculated to be 48° for all of the concentrations measured at pH 6. This orientation angle would be most consistent with a flattened admicelle structure, rather than a symmetrical micelle or close-packed layer structure.

Table 2.1. Calibration of pathlength for the liquid transmission cell with different spacers.

Nominal thickness(mm)	Calibration thickness(mm)
0.025	0.033
0.056	0.055
0.1	0.103
0.15	0.132
0.25	0.258
0.39	0.385

Table 2.2. Assignments of IR band in the fluorocarbon region ($1100 - 1400$ cm^{-1}).[a]

Frequency (cm-1)	Mode	Polarization	Reference
1369	ν_{ax} (CF$_2$)	$\parallel$ the fluorocarbon helical axis	49
1328	ν_{ax} (CF$_2$)	$\parallel$ the fluorocarbon helical axis	49
1274	ν (CF$_2$)	$\perp$ the fluorocarbon helical axis	50
1239	ν_{as}(CF$_2$)	$\perp$ the fluorocarbon helical axis	50
1217	δ(CCC), ν (CC)	$\parallel$ the fluorocarbon helical axis	49,51
1205	ν_{as}(CF$_2$)	$\perp$ the fluorocarbon helical axis	49
1181	δ(CCC)	$\parallel$ the fluorocarbon helical axis	52
1152	ν_s(CF$_2$)	$\perp$ the fluorocarbon helical axis	49
1137	ν_s(CF$_2$)	$\perp$ the fluorocarbon helical axis	49
1117	ν (CC), trans planar	$\parallel$ the fluorocarbon helical axis	53

a.ν_s-symmetric stretch; ν_{as}-asymmetric stretch; δ-deformation.

Table 2.3. Parameters for the modified Langmuir model (Eq. 2.8) found by fitting to experimental data.

Bulk Concentration (mM)	$S_0 k_1^*$ (μmol m^{-2} min^{-1})	k_{obs} (min^{-1})	k_2^* (min^{-1})	k_2' (min^{-1})
0.1	0.010	0.021	0.00089	0.00024
0.5	0.018	0.024	0.00102	0.00050
1	0.090	0.066	0.00202	0.00083
3	0.018	0.0135	0.00125	0.00060
5	0.019	0.0163	0.00075	0.00050

Table 2.4. Equilibrium surface coverage and area per molecule for aqueous TEA-FOS adsorption on hydroxylated Ge at pH 6.0 ± 0.1.

Bulk Concentration (mM)	Surface Excess, Γ		Area available per molecule (nm^2)
	(μmol /m^2)	(molecules/nm^2)	
0.1	17.7	10.6	0.094
0.5	18.8	11.3	0.088
1	20.2	12.1	0.082
3	19.5	11.7	0.085
5	20.8	12.5	0.080

Table 2.5. Linear dichroic ratio and average orientation angle at equilibrium for TEA-FOS adsorbed on the Ge surface.

Solution Concentration (mM)	Peak Center (cm^{-1})							
	1204 ($\alpha = 90°$)		1181 ($\alpha = 0°$)		1205 ($\alpha = 90°$)		1152 ($\alpha = 90°$)	
	LD (±0.02)	γ (±1.6)	LD (±0.04)	γ (±2.1)	LD (±0.02)	γ (±1.6)	LD (±0.01)	γ (±0.08)
0.1	0.56	49.5	0.44	51.7	0.55	50.4	0.57	48.7
1	0.58	47.9	0.37	47.9	0.58	47.9	0.59	47.1
3	0.61	45.5	0.34	46.2	0.59	47.1	0.58	47.9
5	0.60	46.3	0.40	49.6	0.60	46.3	0.58	47.1
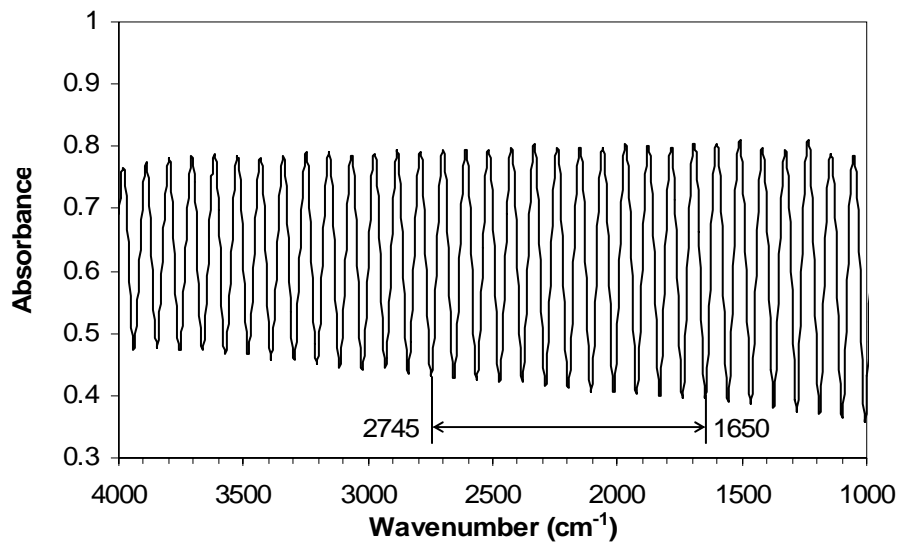
Figure 2.1. Spectrum with interference fringes measured using an empty cell with matched spacers of nominal thickness 0.056mm spacer.
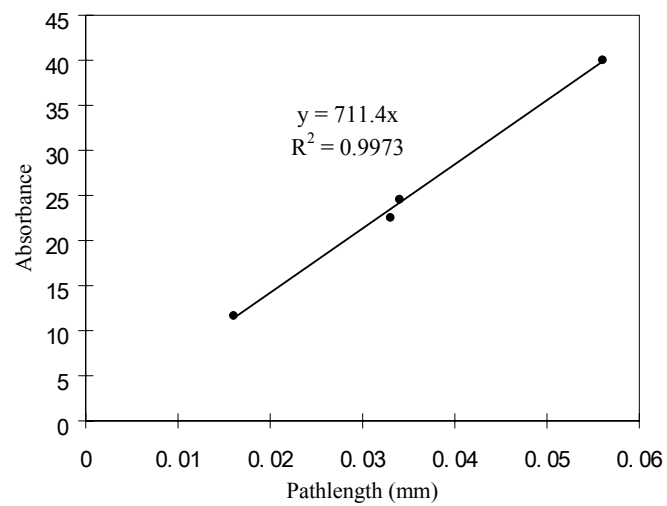
Figure 2.2. Absorbance vs. pathlength for the 2135 cm^{-1} infrared band of water.
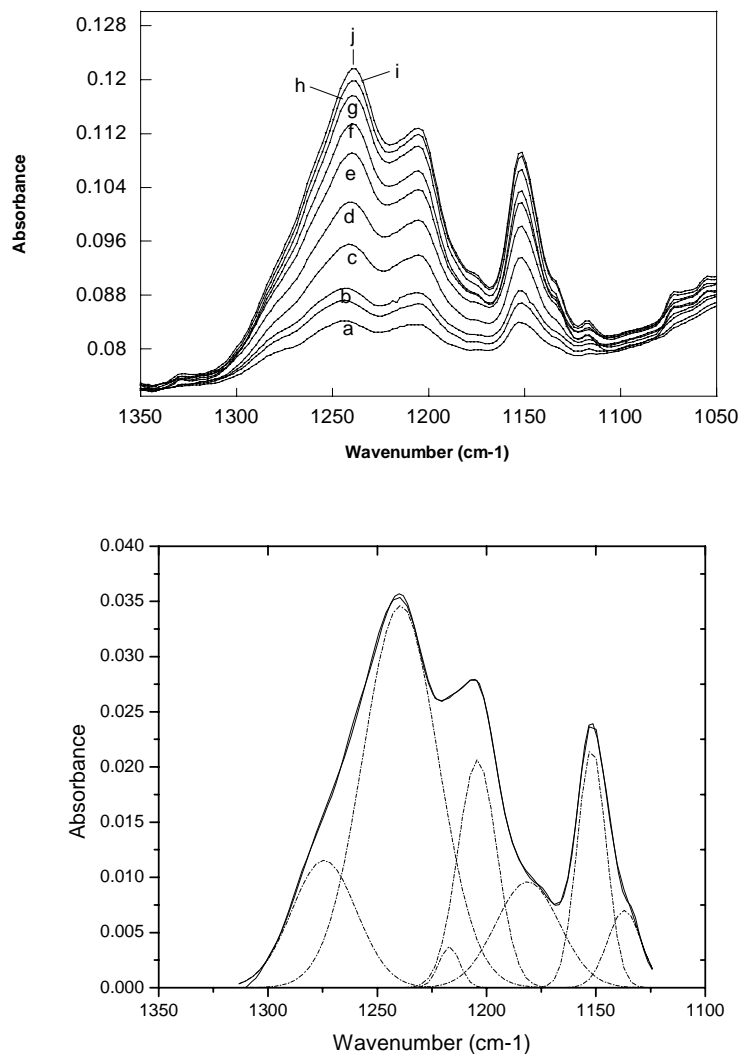
Figure 2.3. (a).Unpolarized ATR-FTIR spectra collected during adsorption of TEA-FOS onto hydroxylated Ge from 1 mM aqueous solution at pH ~ 6 as a function of time after introduction of the solution into the cell: (a) 0.85, (b) 100, (c) 500, (d) 1000, (e) 1500, (f) 2000, (g) 2500, (h) 3000, (i) 3500, (j) 4000 min. (b). Deconvolution and band fitting of the C-F stretching bands (1100 to 1350 cm^{-1}) for 1 mM TEA-FOS adsorption onto Ge surface at equilibrium.
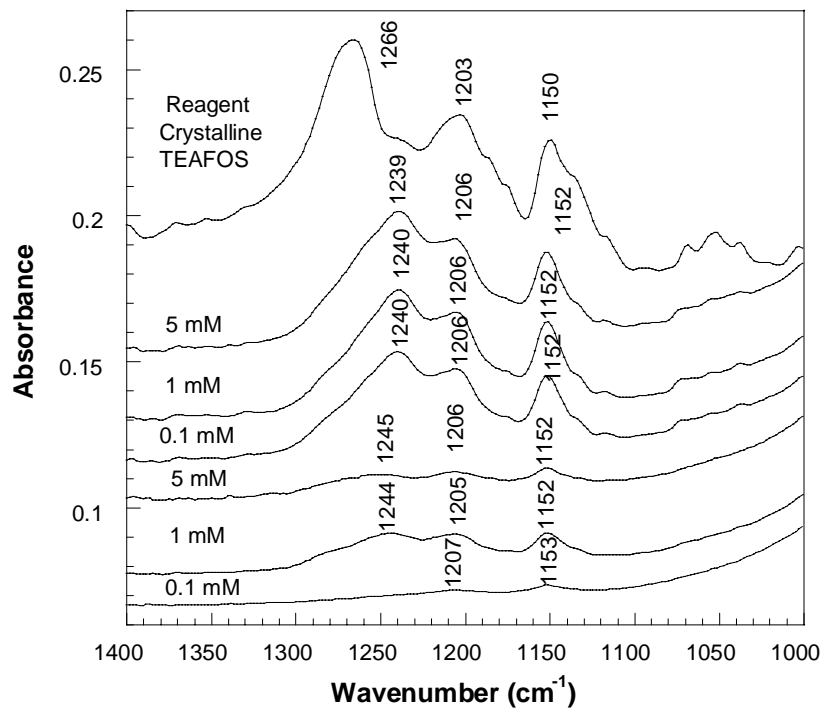
Figure 2.4. Comparison of the ATR FTIR absorbance spectra for different concentrations at the second adsorption stage (lower three spectra) and at equilibrium (middle three spectra), and the transmission spectrum of solid TEA-FOS (top).
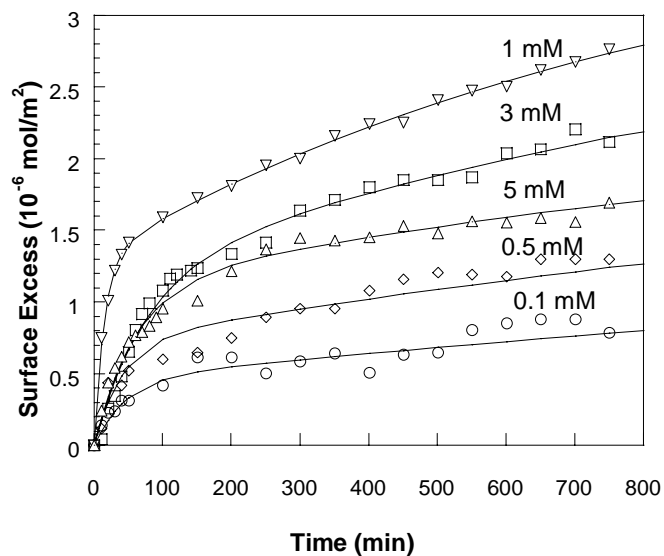
Figure 2.5. Surface excess evolution with time during the adsorption of TEA-FOS from aqueous solution onto hydroxylated germanium during the initial 800 min, as a function of TEA-FOS concentration. Points are data and lines are fits of modified Langmuir adsorption model (Eq. 2.8).
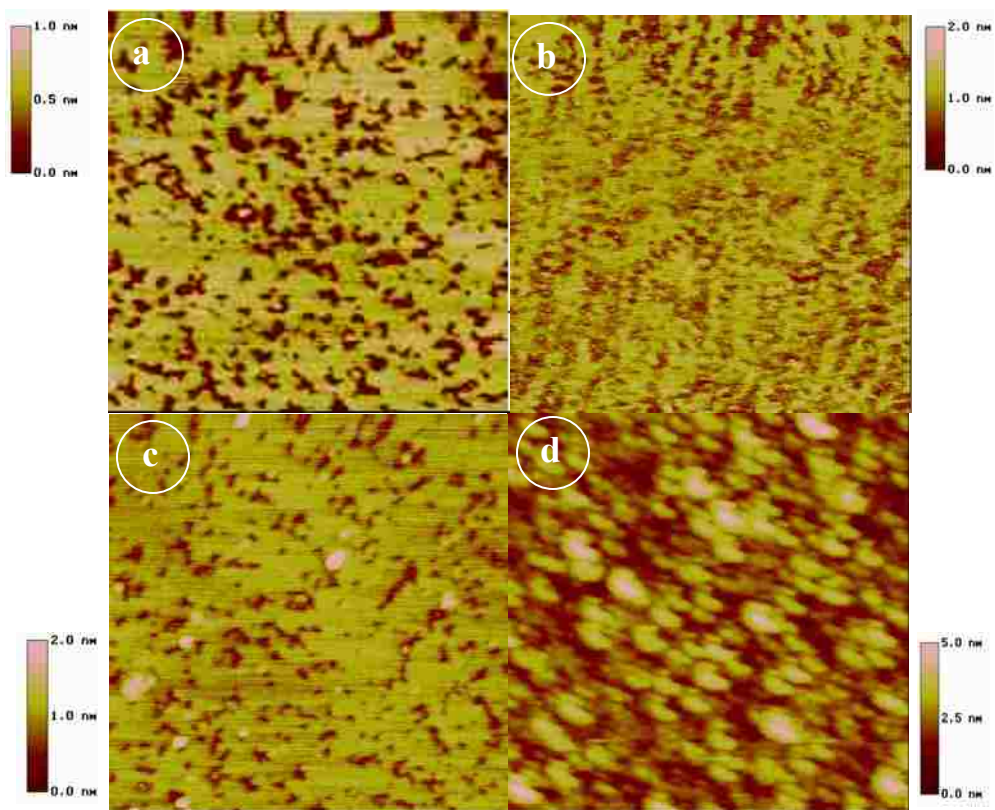
Figure 2.6 Ex-situ AFM images of adsorbed TEA-FOS surfactant on the mica surface as a function of time after soaking the mica in the surfactant solution for (a) 5 min, (b) 25 min, (c) 30 min, and (d) 120 hr. The scan size for all images is 1 μm ×1 μm .
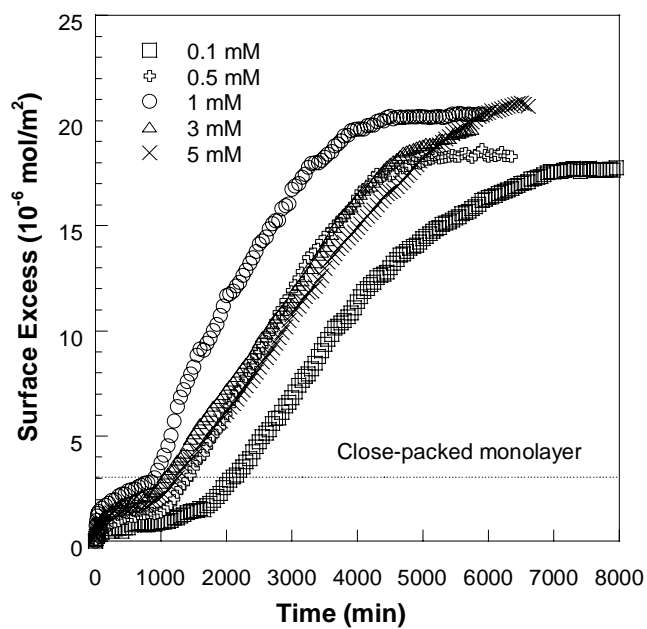
Figure 2.7. Surface excess evolution with time for adsorption of TEA-FOS from aqueous solution onto hydroxylated germanium. The entire time intervals measured for all TEA-FOS concentrations are shown, in comparison to the calculated monolayer surface excess (see text).
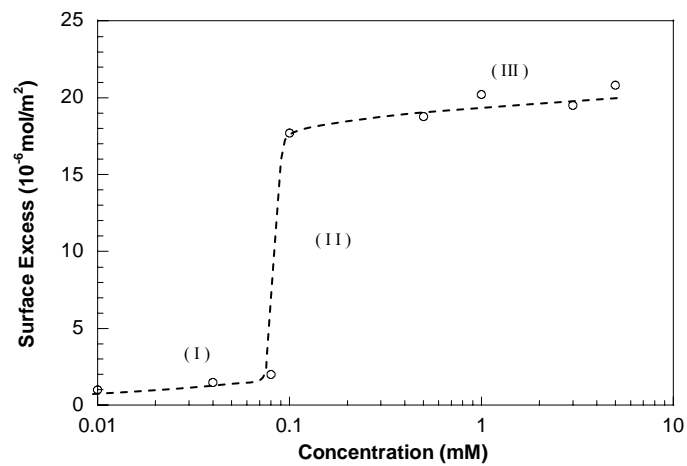
Figure 2.8. Adsorption isotherm of TEA-FOS onto Ge surface at pH = 6.0 ± 0.1 on a linear-log scale
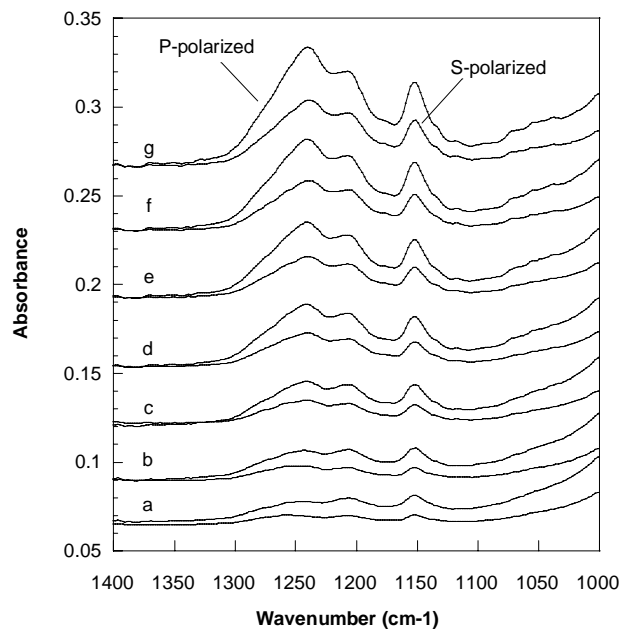
Figure 2.9. Polarized IR-ATR absorbance spectra of 5 mM TEA-FOS solution at different adsorption stages. The lower spectrum is obtained when the beam is S-polarized. The upper spectrum is obtained when the beam is P-polarized. Spectra are shown after (a) 750, (b)1500, (c) 2200, (d) 3000, (e) 3550, (f) 4350, (g) 5750 min
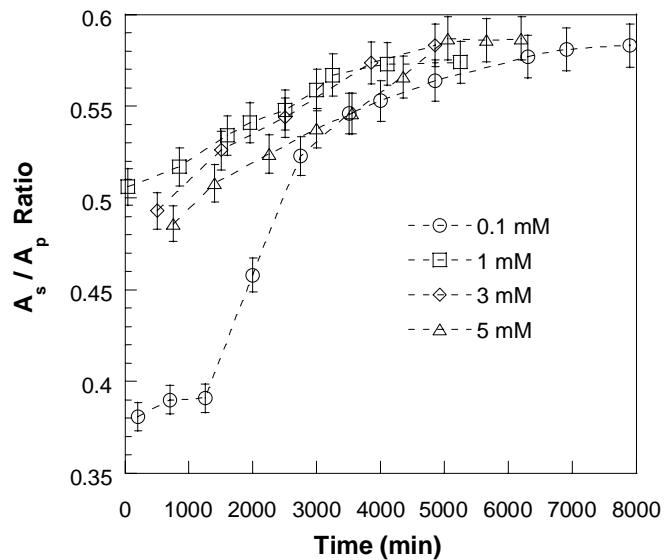
Figure 2.10. The dichroism ratio (A_s/A_p) measured as a function of time during adsorption of TEA-FOS from different solution concentration onto the hydroxylated Ge surface at pH=6.0±0.1.
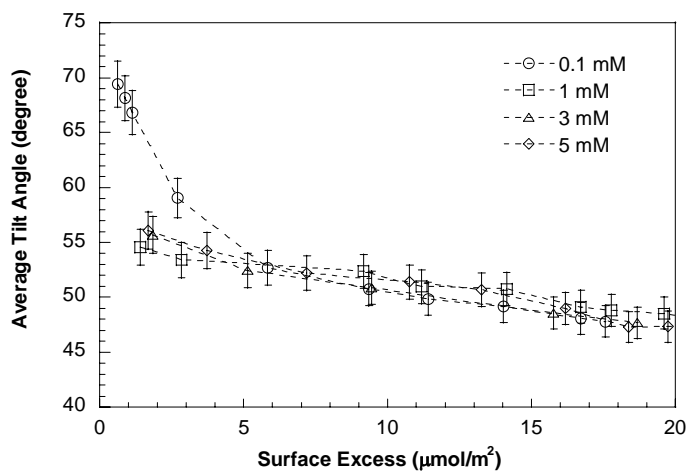
Figure 2.11. Relationship between the average orientation angle and the surface excess during adsorption of TEA-FOS from aqueous solution onto Ge surface.
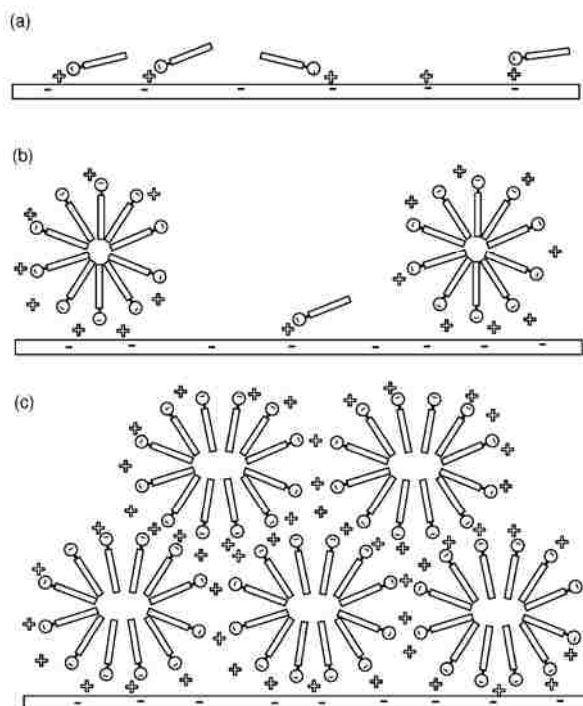
Figure 2.12. Schematic of the stages of adsorption in the formation of TEA-FOS multilayers deposited from aqueous solution onto hydroxylated germanium. (a) Adsorption during the first stage onto charged sites mediated by TEA$^+$ (crosses), (b) admicelle formation during the slow second stage of adsorption, and (c) hydrophobically driven formation of multilayers composed of flattened admicelles following nucleation of hydrophobic patches.

Chapter 3. Three Stage Multilayer Formation Kinetics during Adsorption of an Anionic Fluorinated Surfactant onto Germanium 2. Solution pH and Salt Effects

3.1. Introduction

In chapter 2, the effects of surfactant concentration on the adsorption of the anionic fluorinated surfactant tetraethylammonium perfluorooctylsulfonate (TEA-FOS) onto hydroxylated Ge at pH 6 are investigated by attenuated total reflection Fourier transform infrared spectroscopy (ATR/FTIR). We have presented evidence that the adsorption kinetics occurs in an unusual sequence of three stages for a wide range of concentrations, from well below the CMC of the surfactant (10% of the CMC) to concentrations well above the CMC. The first two stages are concluded to be interfacial reaction-limited adsorption processes, and can be modeled with a modified Langmuir kinetic model. The third adsorption stage is associated with acceleration in the rate of adsorption, which leads to the formation of multilayer clusters of surfactant. Linear dichroism measurements show that adsorbed surfactant molecules initially orient randomly or somewhat parallel to the surface (depending on the bulk concentration), but over time gradually approach surface normal and until surfactants achieve a preferred orientation associated with "flattened" admicelles at equilibrium. Since TEA-FOS is an ionic surfactant, the relative importance of electrostatic interactions in the adsorption process may vary depending on the solution pH, salt amount and type of salt added. Driven by a desire to understand more about the adsorption behavior and structural arrangement of this surfactant under different conditions, we continue to investigate the effects of solution pH and salt concentration on the adsorption kinetics and structural orientation of TEA-FOS onto the Ge surface.

The effects of solution pH and the addition of simple inorganic salts on the adsorption behavior of normal hydrocarbon surfactant at the solid/liquid interface have been widely investigated,[1-12] and general trends have emerged. Changing the solution pH usually varies the surface charge density of the solid by the uptake and release of protons or hydroxyls, thus causing remarkable changes in the initial adsorption rate, equilibrium surface excess and adsorption isotherm, especially for ionic surfactants.[1,2,5,10,11,12] In addition, salts such as NaCl, KCl and $CaCl_2$, are usually added to surfactant solutions to obtain desired interfacial properties in many industrial applications. Thus, salt effects on

kinetics behavior, equilibrium isotherms and structure of adsorbed surfactant layers at the solid/liquid interface have been the subjects of numerous investigations[2-12,14]. Most of them focus on isotherms measured by adsorption of surfactant onto colloidal particles. For example, Atkin et al.[3] investigated the effects of salt on surfactant adsorption isotherms, and concluded that surfactant adsorption takes place at much lower concentrations in the presence of salt, and that the original two-step adsorption isotherms observed in the absence of salt are no longer observed. There have also been studies of salt effects on the structure of adsorbed surfactant layers at the solid/liquid interface, as determined by the adsorption isotherm and other quantitative information obtained from combined measurements such as contact angle and zeta potential. Recently, Ducker and Lamont[15] reported the surface-induced transformations of CTA^+ surfactant aggregates at the mica surface using AFM. They found that more highly curved aggregates are formed with an increase of salt concentration.

The effects of salt on the self-assembly behavior of fluorinated surfactants in bulk solution have been studied[16,17,18,19] and they behave similarly to their hydrogenated analogues.[20,21,22,23] First, the addition of salt reduces the critical micelle concentration (CMC) and the concentration of free surfactant.[24] Second, the addition of salt makes ionic fluorinated surfactant show reduced electrostatic repulsive interactions between the hydrophilic headgroups of surfactants, which increases the aggregation number of micelles or decreases the interfacial area per surfactant molecule.[17] As a result, salt addition promotes the transition of spherical micelles to long cylindrical micelles, which further grow to form threadlike micelles. The threadlike micelles are readily entangled into networks as salt concentration increases.[17] Third, depending on the type of salt used, the addition of salt may make fluorinated surfactant solution become viscous, even viscoelastic.[17,25] However, an excessively high concentration of salt may also transform threadlike micelles back into a homogeneous dispersion of spherical micelles.[18] In contrast to hydrocarbon surfactants, fluorocarbon surfactants demonstrate a higher tendency to form aggregates with less curvature. A very small amount of salt added in the solution is expected to induce the transition of aggregate structure from spherical to rod-like, with accompanied dramatic changes in rheology.

At the solid/liquid interface, however, there have been only a few reports showing the effects of solution pH or salt on the adsorption behavior of fluorinated surfactants. For example, Ducker and Lamont[26] studied the effect of added salt on the ordering of LiFOS at the graphite/solution interface using in situ AFM. They observed that LiFOS adsorbs in a periodic structure, and that the period decreases on addition of salt. Lai et al.[27] investigated the effect of solution pH on adsorption isotherms of perfluorocarboxylic acids and their salts on aluminum oxide, and found that lower pH in solution facilitates the rate of adsorption toward a maximum coverage of a bilayer.

In our study, TEA-FOS exhibits unusual three stage adsorption kinetics because of a complex process driven by ion-pairing and hydrophobic interactions. The interplay among competing weak interactions, such as electrostatics, hydrogen bonding, van der Waals, and steric repulsion, plays an important role in this adsorption process. In this chapter, we will address the effects of solution pH and salt concentration on the adsorption kinetics and structural arrangement of adsorbed TEA-FOS at the Ge/solution interface. TEA-FOS is a thermally and chemically stable surfactant, and micelles can be formed at very high and low pH.[28] In the bulk solution, TEA-FOS has a strong tendency to form anisotropic threadlike micelles even in the absence of any salt. With addition of simple salt, the micellar aggregates grow or become more anisotropic, as determined by electric birefringence measurements of micellar solution of TEA-FOS at a concentration of 4.5 mM.[20] In addition, the dynamics of micelle exchange for TEA-FOS surfactants are usually very slow,[19,29,30,31] which is reflected in the slow adsorption process at pH 6.0 observed in chapter 2.

In the previous chapter, we demonstrated the feasibility of using the ATR-FTIR technique to study the adsorption and molecular orientation of TEA-FOS at the Ge/aqueous solution interface as a function of bulk concentration. The infrared technique has been accepted as an effective in situ technique to measure both adsorption kinetics and the structure of adsorbed surfactants at the solid/liquid interface. This chapter will further take advantage of this technique to investigate the effects of solution pH and salts on the TEA-FOS adsorption onto hydroxylated germanium (Ge). For some cases, in-situ AFM measurements in a liquid environment is used to compare the morphology change of adsorbed surfactant layers at equilibrium due to adding salt.

3.2. Experimental section

3.2.1. Materials

The surfactant, TEA-FOS ($CF_3(CF_2)_7OSO_2^- \cdot N^+(C_2H_5)_4$), with purity $\geq$ 98%, was purchased from Fluka Chemical Co. Surfactant solutions with different concentration were prepared with deionized ultrafiltered (DIUF) water (Fisher Scientific). Solution pH was adjusted using normalized 0.1 N NaOH (Alfa) or 0.1 N HCl (Alfa). NaCl (Merck KGaA), KCl (Mallinkrodt), and $CaCl_2$ (Fisher) were used as received to alter the ionic strength of the surfactant solutions.

3.2.2 Instrumentation

FTIR spectra were obtained with a sealed and desiccated ThermoNicolet Nexus 470 infrared spectrophotometer equipped with a DTGS detector. A specimen for solid state FTIR was prepared by finely grinding crystalline TEA-FOS, diluting it to 1 wt% with KBr power, and pressing the mixture into a translucent pellet with a hand press. For liquid samples, transmission FTIR was performed with a stainless steel demountable liquid cell (Harrick Scientific Corp.) with Ge windows. To avoid interference fringes in the transmission spectra, mismatched Teflon spacers (0.025 mm and 0.006 mm) were used to form a liquid wedge. The background spectrum for transmission experiments was the single-beam spectrum collected using the empty, dry cell.

ATR-FTIR spectra were taken using a horizontal ATR accessory (Pike Technologies) and a liquid-nitrogen-cooled MCT detector. A 45º trapezoidal Ge internal reflection element (IRE), $80.0 \times 10.0 \times 4.0$ mm, was used. The incident beam was reflected roughly 10 times as it traveled the length of the IRE. The IRE was housed in a Teflon-coated flow-through cell. All of the spectra were the result of averaging 128 scans at a resolution of 4 cm^{-1}. Experiments were performed at room temperature (21 ± 1 °C). Residual bands from atmospheric water and carbon dioxide were eliminated by background subtraction and automatic atmosphere suppression software. To study adsorption, solutions of different concentration were introduced into the ATR fluid cell using a peristaltic pump. The Teflon-coated tubes that served as inlet and outlet conduits to the fluid cell were cleaned by copious rinsing with iso-propanol and water followed by drying with dry nitrogen.

Polarization was achieved by using a wire grid ZnSe polarizer (Spectra-Tech model FT 80) mounted to the ATR accessory just before IR beam enters the ATR accessory. By adjusting the wire grid angle, the polarizer was set perpendicular (S), parallel (P), or at 45 degrees ("unpolarized") to the plane of incidence of the IRE.

AFM was performed with a Molecular Imaging Picoscan 5. The substrate used was a mica disc, which was freshly cleaved for each experiment using adhesive tape. Freshly cleaved mica was mounted onto a stainless steel disk, and scanned in an aqueous solution. The surfactant solution was introduced into a fluid cell sealed with an O-ring, and loaded with a holder on the sample stage. The scanner was calibrated with a standard grid. Silicon nitride (Si_3N_4) tips (DNP type) were used with a manufacturer-specified spring constant of 0.12 N/m, length of 196 μm, width of 41 μm, and nominal tip radius of curvature of 10 nm. Surfactant multilayers were imaged in both topography and deflection mode with low feedback gains. No filtering of the images was performed other than flattening along the scan lines to remove background slopes. The images of surfactant aggregates were captured using the soft-contact mode, where the imaging force on the tip is set near to, but below the breakthrough force. All measurements were performed at room temperature. Solutions were equilibrated for 3-4 hr before the start of the experiment to minimize thermal drift.

3.2.3. Ge surface preparation

Preparation of the Ge internal reflection element (IRE) for an experiment required first polishing the IRE for 30 min with 0.1 micron diamond paste, rinsing thoroughly with deionized water, then soaking in DIUF water for 24 hr at room temperature to ensure consistent hydroxylation of the surface. After being dried in a stream of ultra pure nitrogen, the IRE was immediately sealed into the flow cell using a PTFE-coated o-ring. The IRE was cleaned with isopropanol, acetone and deionized water by scrubbing lightly with a cotton-tipped applicator. This method has been shown to generate a reproducible hydroxylated surface (primary GeO_2 and GeOH) while completely removing the residual organic and fluorocarbon contamination from the previous experiments.

3.2.4 Data analysis

The critical micelle concentration (CMC) values of TEA-FOS without and with salt (2 mM) were measured at room temperature by using an Accumet Basic AB30

conductivity meter. The CMC was determined to be the point at which a discontinuous change in slope occurs during successive dilution of a TEA-FOS solution. The CMC of TEA-FOS was determined to be 1.02 mM (without salt added) and 0.83 mM (with 2 mM NaCl added).

The infrared absorption peaks were integrated to determine the surface excess of surfactant. The surface excess was calculated by using equation (2.1) from chapter 2. In our experiment, d_p was calculated to be 0.52 μm at 1212 cm^{-1} and the effective total pathlength (Nd_e) of the IRE was estimated as 2.97 μm at 1212 cm^{-1}. The extinction coefficient ε of the integrated CF$_2$ region (from 1299.8 cm^{-1} to 1124.3 cm^{-1}) was measured to be 13.7 ± 0.4 mm^{-1}*mM^{-1} from calibration experiments.

The uniaxial chain director model was used to determine the molecular orientation, because there is no external force which causes the absorbed surfactant to orient laterally. To quantify the results, we first use equation (1.12) from chapter 1 with parameters for our system (n$_1$ = 4 (Ge), n$_2$ = 1.33 (water), and θ = 45°) to get E$_x$ = 1.40, E$_y$ = 1.50, and E$_z$ = 1.59. Using equations (1.18) and (1.19), we predict that the linear dichroic ratio (LD) = 0.5 for a randomly distributed orientation of molecules, LD = 1.14 when the chain axis is normal to the surface, and LD = 0.32 when the chain axis is parallel to the surface. With the assumption that the angle between the vibrational motion and the chain director (α) = 90° for both the symmetric and asymmetric CF$_2$ stretching in equation (1.21), the LD ratio was calculated by equation (1.19). For those vibration modes with dipole angles at α = 0°, the LD ratio was calculated by using equation (1.16). See chapter 1 for a complete discussion of the orientation calculations.

3.3. Results and discussions

3.3.1. Solution pH effects on adsorption kinetics and equilibrium orientation of TEA-FOS

Figure 3.1 shows in-situ ATR-FTIR spectra collected at equilibrium of TEA-FOS adsorbed from 0.5 mM aqueous solutions onto the hydroxylated Ge surface at pH values of 3.4, 6.0, 8.4 and 10.0. All of the ATR spectra show similar qualitative features, and specific band assignments are discussed in chapter 2. With decreasing solution pH, the relative shift of the (CF$_2$)$_{as}$ band positions (the left two intense peaks) from higher wavenumbers (1244 and 1212 cm^{-1}) to lower wavenumbers (1239 and 1206 cm^{-1}, respectively) indicates that fluorocarbon tails move into a more structured and

hydrophobic environment.[32]   In addition, the CF_2 stretching bands exhibit higher intensities at lower pHs than those at higher pHs, suggesting that the amount of surfactant adsorbed is strongly dependent on the solution pH. The spectrum of solid crystalline TEA-FOS is also shown in Fig. 3.1 to emphasize that the surfactant layers at the Ge/solution interface form due to interfacial adsorption and not due to insolubility of TEA-FOS, even over a wide range of solution pH values.

The calculated surface excess of TEA-FOS adsorbed from 0.5 mM solution onto Ge is shown in Figure 3.2 as a function of solution pH. This Figure shows that three-stage adsorption occurs for all pHs with clearly different time scales, even at pH 10.0 where the surface should be strongly negatively charged. At pH 6.0, where there is no specific acid or base added to the solution, the duration of the whole adsorption process is surprisingly long (at least 5000 min). When the solution pH is changed by adding a small amount acid (HCl) or base (NaOH), the total time to reach equilibrium reduces by almost half (less than 3000 min). The addition of acid or base (HCl or NaOH) also increases the initial adsorption rate slightly, and extends the amount adsorbed in the first two stages, which is probably caused by screening repulsive interactions among headgroups of fluorinated surfactants on the Ge surface. Moreover, the durations in the second and third stage adsorption are determined by the amount of acid or base added in the solution. If we define the duration of the second stage to be the period between the adsorption slowdown in the first stage and the adsorption rate increase at the onset of the third stage, this duration decreases as the amount of acid or base increases, spanning a time scale from 900 to 150 min. This indicates that the presence of electrolytes (acid or base here) influences the reorganization of adsorbed surfactants on the solid. The third stage starts with a sudden increase in the adsorption rate, and then proceeds with Langmuir-like kinetics until the level of adsorption reaches equilibrium.   The duration of the third adsorption stage spans from 2650 to 4000 min depending on solution pH.

We observe that solution pH greatly affects the adsorption process especially at the initial stage, suggesting that the first-stage adsorption is driven by electrostatic interactions.   There are two reasons for this pH effect: first, like other mineral oxide surfaces, the charge density on the Ge surface strongly depends on the solution pH. Second, the ionic strength increases upon addition of HCl, which screens the repulsive

interactions between like-charged headgroups of adsorbed surfactants and allows them to pack more closely on the Ge surface. Since the isoelectric point (IEP) of Ge is at approximately pH 4,[33] a low pH (3.4) gives the surface a low positive charge density due to the uptake of protons from the bulk solution. Thus the anionic FOS$^-$ surfactants directly adsorb onto the solid surface via electrostatic attraction with a fast adsorption rate. With solution pH above the IEP of Ge, the solid surface becomes negatively charged due to release of protons. This negatively charged surface should repel anionic FOS$^-$ monomers but TEA$^+$ binding to the surfactant headgroups mediates the adsorption of FOS$^-$ onto Ge surface even at pH 10. Moreover, the solution ionic strength increases with pH in a logarithmic fashion, which also facilitates the adsorption of TEA-FOS onto negatively charged Ge surfaces due to electrostatic shielding.

In addition to surface excess measurements, we measure the linear dichroic ratio and extract from it the average equilibrium fluorocarbon orientation angle at different pH values, as shown in Table 3.1. For this calculation, we neglect the absorption of the evanescent wave by the bulk solution due to the low bulk concentration employed. From the measured equilibrium surface excess, we find that multilayer clusters are formed for all pH values, assuming that the adsorbed surfactants have a surface excess of 1.84 molecues/nm^2 when they are completely aligned in a close-packed monolayer.[18] The equilibrium surface excess decreases as the solution pH increases, most likely because a higher negative surface charge causes smaller and fewer admicelles to form. At pH 3.4, the adsorbed surfactants self-assemble with an average orientation angle of 40° with respect to surface normal, indicating the admicelles are more bilayers-like (perhaps due to an increased size) than that at pH 6. One the other hand, at pH 10.0, the adsorbed surfactant molecules orient more randomly with an average tilt angle of 52°. This is probably because the clusters are smaller and more curved, to minimize close contacts with the negative Ge surface.

3.3.2. Salt effects on the adsorption kinetics of TEA-FOS under acid or basic condition

In addition to the solution pH effects, we also investigate the effects of salt on the adsorption kinetics of TEA-FOS under acid or basic condition. Adding salt allows us to isolate the ionic strength effects of changing pH from the surface charge effects discussed in section 3.3.1. Figure 3.3 shows an example of in-situ ATR-FTIR spectra collected

during adsorption of TEA-FOS onto Ge from a 0.5 mM aqueous solution with 5 mM NaCl and pH 3.4. The ATR spectrum does not contain distinct peaks 1 min after the solution is introduced to the fluid cell (not shown here). At about 5 min, there are three resolved bands at 1244 cm^{-1}, 1211 cm^{-1}, and 1153 cm^{-1}. During adsorption, all of these bands gradually shift to lower wavenumbers, until reaching 1239 cm^{-1}, 1207 cm^{-1} and 1151 cm^{-1}, respectively, at equilibrium. The evolution of the adsorption spectra suggests that the fluorocarbon environment becomes more ordered and hydrophobic during adsorption. Specific band assignments in this region are discussed in chapter 2.

Under acidic conditions (pH 3.4), the calculated surface excess during the adsorption of 0.5 mM TEA-FOS onto Ge surface is shown in Figure 3.4 as a function of NaCl concentration. Figure 3.4a shows the effect of low concentrations of NaCl (up to 5 mM) on the adsorption kinetics. At pH 3.4, the adsorption kinetics and durations of the first two stages are significantly affected by the amount of NaCl added to the solution. Without added salt, the second stage can be clearly observed, spanning about 200 min. Upon adding a very small amount of NaCl (1 mM), the duration of the second stage reduces so much that it is difficult to identify. With increase of NaCl concentration to 2 mM or 5 mM, a second stage is again visible, but with a surface excess above that of a close-packed monolayer. The adsorption rate in the second stage passes through a maximum at 1-2 mM NaCl. Figure 3.4b shows the effects of a large concentration of NaCl (10-50 mM) on the adsorption kinetics. In contrast to the results in Figure 3.4a, the initial adsorption rate decreases as the NaCl concentration increases, suggesting that too much NaCl in the solution slows down the adsorption of TEA-FOS onto Ge by shielding attractions between the surfactants and the surface. The equilibrium surface excess also decreases with a large excess of added salt, and with 50 mM NaCl, the third stage of adsorption disappears entirely and the final surface excess decreases to a minimum value.

Under basic condition (pH 10.0), the calculated surface excess of TEA-FOS adsorbed from the same 0.5 mM solution onto the Ge surface is shown in Figure 3.5 as a function of time. Figure 3.5a shows the effects of a low concentration of NaCl on the adsorption kinetics. The addition of a small amount of NaCl facilitates the adsorption of TEA-FOS onto a negatively charged Ge surface, and the duration of the second stage decreases as the concentration of NaCl increases. Figure 3.5b shows the effects of large

concentrations of NaCl (up to 50 mM) on the adsorption kinetics. For this series of samples, the initial adsorption rate is a monotonically increasing function of NaCl concentration, but the final surface excess decreases. The differences in adsorption kinetics trends exhibited at acidic or basic pH indicate that the surface aggregation mechanism of TEA-FOS at the Ge surface varies with solution pH, most likely due to the surface charge. At pH 3.4, the surface is weakly positively charged, anionic FOS^- monomers directly adsorb via electrostatic forces. When NaCl is added in the solution, the competitive co-ions are Cl^-, which may adsorb onto the solid surface to block adsorption sites for FOS^-. Low NaCl concentrations ($\leq$ 5 mM) may facilitate the adsorption of FOS^- due to electrostatic shielding of repulsive headgroup-headgroup interactions, while high NaCl concentrations (> 5 mM) may retard the adsorption of FOS^- due to competitive adsorption of Cl^- on the surface. At pH 10, the surface is strongly negatively charged, and the adsorption of FOS^- is mediated by hydrophobic TEA^+ counterions at the Ge surface. In this case, the competitive ions are Na^+. However, bulky TEA^+ ions show a stronger affinity for the Ge surface than Na^+ ions. The addition of NaCl always accelerates the initial adsorption of TEA^+ even at the concentration of 50 mM, indicating that the shielding effect of salt plays a dominant role. Thus, the differences in kinetic trends can be explained based on surface charge and co- / counter-ion effects.

Although salt effects on early-stage adsorption kinetics differ under acid or basic condition, the late-stage effects are similar. Figure 3.6 shows how the final surface excess varies with NaCl concentrations at pH 3.4 or 10. As can be seen, the equilibrium surface excess passes through a maximum as NaCl concentration increases in both cases. At low salt concentration, adding NaCl screens repulsive interactions between neighboring surfactants, thus increasing surface excess. However, the presence of excessive NaCl may weaken the binding affinity of TEA^+ and FOS^- micelles, thus leading to a decrease of adsorbed multilayers of surfactant. The effects of salt on final surface excess are similar to the behavior usually observed for polyelectrolyte or protein multilayer build-up at the solid/liquid interface[34-37]. In both cases, the multilayer buildup is driven by both electrostatic and hydrophobic interactions. Table 3.2 summarizes the measured equilibrium surface excess and the area occupied per molecule.

3.3.3. Salt effects on the adsorption isotherms of TEA-FOS at pH 6

Figure 3.7 shows the adsorption kinetics of TEA-FOS onto hydroxylated Ge from 1 mM aqueous solution as a function of NaCl concentration at pH 6. All samples show three stage adsorption kinetics, but with different time scales. The first stage exhibits rapid surfactant adsorption for all samples, spanning about 200 min after the introduction of the solution into the cell. The presence of NaCl increases the initial adsorption rate slightly and allows the adsorbed surfactants to pack more closely at the solid surface. The second stage exhibits a constant rate of increase of the surface coverage. Surprisingly, a very small amount of salt (2mM NaCl) reduces the duration of the second stage almost by half from 1400 to 800 min. Adsorption during the third stage is also accelerated by adding NaCl, reducing the time to reach equilibrium by roughly 1/4 upon addition of 5 mM NaCl. At pH 6, the addition of salt increases surface coverage in the second stage, but decreases the equilibrium surface excess. This contrasts with the maximum in equilibrium surface coverage with respect to added salt observed at pH 3.4 and pH 10. This discrepancy is likely to originate from differences in the surface charge density. In order to learn more about this unusual salt effects at pH 6, we report adsorption isotherms measured with and without NaCl in Figure 3.8. The NaCl concentration of 2 mM is selected for two reasons: First, we want to avoid a salt-induced micellar structure change in bulk solution due to addition of a large amount of salt. Too much salt can induce the change of aggregate structure for this surfactant[25], with an unknown effect on the adsorption kinetics. Second, the addition of very small amount of salt reduces the possibility of other change of physical properties in the bulk surfactant solution, such as the dissociation degree of TEA-FOS, surface aggregation number, viscosity of solution and CMC. We find that both adsorption isotherms are S-shaped, with three regions on a linear-log scale. The three regions can be classified as a low surface excess region, hydrophobic interaction region and plateau region.

In the first region, there is a slow increase in the surface excess with the bulk concentration, and no three-stage adsorption kinetics is observed. There is only a small difference between the surface excess measured with or without added salt. The surfactants adsorb on the Ge surface by means of only electrostatic interactions. We do not expect any form of surfactant aggregation at the Ge/solution interface in this region

72

because less than a monolayer of surfactant is present. Therefore, the salt does not screen either surfactant-surfactant or surfactant-surface interactions to a significant extent.

The second region starts at a surprisingly low bulk concentrations and suddenly ends with a plateau in the third region. The sudden and large rise in surface coverage in region (II) leads to the formation of admicelles with multilayer structure at equilibrium. However, the final surface excess decreases slightly in the presence of NaCl for all concentrations above 0.1 mM TEA-FOS, indicating that NaCl disrupts continued multilayer buildup at pH 6. This may be caused by the screening of the electrostatic interactions between TEA^+ and FOS^- or conformational changes of adsorbed surfactant aggregates.

3.3.4 Salt effects on the surface morphology at equilibrium

In order to know the salt effects on morphological change of adsorbed multilayers of TEA-FOS, we use in situ AFM to image the equilibrium morphology of adsorbed surfactant layers on the solid surface. A Ge wafer should be the ideal substrate to provide a direct comparison with the FTIR/ATR study. However, Ge wafers with low RMS roughness are not commercially available. We instead choose a negatively charged mica wafer as a model substrate. Figure 3.9a shows both the height and deflection images of adsorbed multilayers deposited from 0.1 mM TEA-FOS solution onto mica in the absence of NaCl at pH 6. The height image shows clusters nucleated by admicelles as brighter protrusions and monolayer/submonolayer regions appear dark. The deflection image shows that clusters of tens of nanometers in size are loosely and randomly formed on the mica surface. From the sectional analysis of their height, the clusters are inferred to have a multilayer structure (approximately > 7 layers). In the presence of 10 mM NaCl, the morphology and orientation of adsorbed clusters both change as shown in Figure 3.9b. The addition of NaCl allows surfactant clusters to pack more closely on the surface, and clusters connect with each other to form string-like features. The adsorbed clusters appear to be oriented relative to each other in the presence of NaCl. From analysis of their height, the adsorbed clusters also are multilayered, but the number of layers is estimated to be less than that observed in the absence of NaCl. This contrast suggests that the addition of salt favors the formation of close-packed clusters on the surface, but not the build-up of multilayers. This result may be used to explain that the addition of NaCl increases the

surface coverage at the second kinetic adsorption stage, while it causes a slight decrease of final surface excess on Ge at pH 6.

A preliminary kinetic study of TEA-FOS surfactant adsorption onto mica has also been conducted by in situ AFM. The results show that the formation of small aggregates of tens of of nanometers in size can be observed approximately 4 hr after introducing the surfactant solution into the fluid cell. With increasing time, the number density of aggregates increases and the aggregates joint together to form large clusters. Unfortunately, we have no clear AFM images to show the morphological evolution of adsorbed layers during the initial stages (before multilayer formation) after introducing the surfactant solution to fluid cell, because TEA-FOS surfactants adsorb onto mica very quickly (ex situ studies indicate that multilayer nucleation occurs after about 30 min) and the AFM detector is not stable due to thermal drift during the initial stages. However, it should be possible to perform an in situ AFM study of the transition from the second stage to the third stage when a low RMS roughness Ge substrate is available. Since it usually takes more than 10 hr for TEA-FOS molecules to form a monolayer on the Ge surface before the start of multilayer build-up (results from chapter 2), the AFM instrument can be stabilized before collecting kinetic data in the second stage.

Force curves for some samples under different conditions have also been measured. We find that the surface force changes from purely attractive in nature to one showing a repulsive force barrier as the surface coverage increases. More detailed analysis of force curves is currently under way.

3.3.5. Salt effects on the molecular orientation

In addition to observing the effects of added NaCl on adsorption kinetics and equilibrium adsorption isotherms, we use linear dichroism to gain more insight into the structure of the adsorbed layers formed from TEA-FOS. Since we employ a low bulk concentration of TEA-FOS, we can neglect the absorption of the evanescent wave in the bulk solution in the calculations to be discussed in this section. Figure 3.10 shows examples of the ATR-FTIR spectra obtained using parallel and perpendicular plane polarized infrared beams for 0.5 mM TEA-FOS solution in the presence of 5 mM NaCl at pH 3.4 as a function of time. Differences in intensity can clearly be observed. From these differences, surfactant tail orientation can be inferred.

Figure 3.11 shows the evolution of measured LD ratio of the CF_2 symmetric stretching bands (wavenumber range 1178.3 - 1124.3 cm^{-1}) with time under some representative conditions. The LD increases with time, and finally achieves a plateau with a preferred orientation for all samples. At pH 3.4 in the absence of added salt, a low LD ratio value of 0.45 is observed 25 min after the solution is introduced into cell, which indicates that the adsorbed surfactants initially orient somewhat parallel to the surface. The LD ratio increases gradually with time and always correlates with the change of surface excess. With the addition of 5 mM NaCl, the LD ratio increases more quickly with time. Even after only 50 min, the surfactants have a preferred angle more normal to the substrate (LD > 0.5). At 500 min, the LD ratio reaches the maximum of 0.72, and remains constant. This indicates that the addition of NaCl helps to promote a structural transition of adsorbed surfactants from spherical admicelles (LD ~ 0.5) to "flattened" admicelles (LD > 0.5). At pH 10, the salt effects play a significant role in promoting the average orientation of adsorbed surfactants on the Ge surface. In the absence of salt, the LD ratio measured at equilibrium is close to the isotropic value of 0.5. However, with the addition of 2 mM NaCl, the LD ratio measured is already above 0.5 at 55 min after adsorption occurs, and increases gradually up to 0.69 at equilibrium. For the samples shown in Figure 3.11, the adsorbed surfactant molecules probably possess an inhomogeneous conformation distribution at equilibrium. However, the final dichroic ratio measured stays between 0.69 and 0.72, which is consistent with "flattened" admicelle multilayer clusters formed on the Ge surface.

Figure 3.12 shows the effects of NaCl concentration on the dichroic ratio and average orientation angle of adsorbed surfactants measured at equilibrium for adsorption from a 0.5 mM TEA-FOS solution at pH 3.4. The linear dichroic ratio of CF_2 symmetric stretching bands is calculated using equation (1.21) from chapter 1. The change in linear dichroic ratio correlates with the change of equilibrium surface excess induced by added NaCl. Initially, the linear dichroic ratio increases with NaCl concentration, and achieves a maximum point at the NaCl concentration of 5 mM, beyond which it decreases gradually. The initial increase of dichroic ratio correlates with an increase in surface excess, and is consistent with closer packing of surfactants in the adsorbed clusters due to a small amount of NaCl. Excessive NaCl causes a loss of both orientational order and of

adsorbed surfactant. In the presence of 50 mM of NaCl, the adsorbed surfactant orientation is close to random ($\sim 54.7^{\circ}$). The conformational change of adsorbed surfactants at high salt concentrations may be caused by screening of electrostatic interactions. The linear dichroic ratios indicate that the average tilt angle first decreases as NaCl concentration is added, and then increases.

Figure 3.13 shows the effects of the valence of added salt on the evolution of LD ratio at pH 6 during adsorption. For comparison, we also plot the dependence of LD ratio on surface excess in the absence of salt. Even on the weakly negative surface at pH 6, the addition of salt greatly increases the LD ratio during adsorption. For monovalent cations (Na^+ and K^+) with the same concentrations (2 mM), no apparent difference in LD ratio can be observed, which is consistent with a charge screening effect. Increasing the salt concentration to 5 mM NaCl causes a slight increase in the LD ratio at a given surface excess, indicating that monovalent salts promote somewhat closer packing of adsorbed surfactants at pH 6. However, to our surprise, the addition of bivalent cation (Ca^{2+}) further increases the LD ratio at a concentration of 2 mM (below the ionic strength of 5 mM NaCl), and even at the same ionic strength as the monovalent salts in Figure 3.13 (results not shown for 1 mM $CaCl_2$ concentration). We conclude that the addition of Ca^{2+} causes the final average orientation of adsorbed TEA-FOS to be tilted more normal to the surface than the addition of monovalent cations. This suggests the type of cations plays a significant role in affecting the structure of the adsorbed surfactants. We observe that, at the initial stage, Ca^{2+} favors a larger LD ratio than that of monovalent cations, which may be associated with increased binding to the Ge surface due to the larger hydrated radius of Ca^{2+} (4.1 Å) compared to either K^+ (3.3 Å) or Na^+ (3.6 Å),[38] as proposed by Sukhishvili et al.[39] for aqueous organic ions adsorbed onto silicon. It is likely that the presence of Ca^{2+} may facilitate closer packing of TEA-FOS by enhancing the electrostatic screening between neighboring FOS$^-$ or even displacing TEA$^+$ to allow adsorbed surfactants to pack more closely.

3.4. Conclusions

In this chapter, we observed the effects of solution pH and salt concentrations on the adsorption kinetics and multilayer assembly of TEA-FOS on the hydroxylated Ge surface using ATR-FTIR. AFM was also used to in situ study the salt effects on the morphology

of adsorbed multilayers at the mica/solution interface (also a weakly negatively charged metal oxide surface near pH 6). In addition to the surface excess and equilibrium isotherms measurements, we analyzed the molecular orientations within the adsorbed multilayers by circular dichroism. Solution pH and salt both are important factors controlling the adsorption kinetics and build-up of multilayers on the Ge surface. At pH 3.4 or pH 10, the equilibrium surface excess passes through the maximum with increasing the NaCl concentrations, while at pH 6, the experiments show a decrease of equilibrium surface excess in the presence of only 2 mM NaCl. The increase in equilibrium surface excess with moderate NaCl concentrations on strongly charged surfaces is accompanied by an increase in orientation of surfactant tails normal to the surface, indicating a closer packing. The loss of adsorbed surfactants with excessive NaCl also leads to a loss of orientation order in the adsorbed multilayer. In a similar fashion, we observed that the kinetics are slightly accelerated in the initial stages of adsorption, that the first two stages proceed to a greater extent, and that multilayer nucleation is accelerated by the addition of a small amount of NaCl. However, in all cases, excessive quantities of NaCl diminish the rate of multilayer buildup, and in extreme cases, no third adsorption stage can be resolved. In situ AFM shows that the addition of NaCl favors the formation close-packed clusters on the mica surface, but that the addition of NaCl is not favorable for the continued build-up of multilayers at pH 6. Moreover, the valence of cations of salt affects the evolution of orientation of adsorbed TEA-FOS from the start of adsorption; a counterion with larger hydrated radius has a stronger screening effect and allows the adsorbed TEA-FOS molecules to tilt more strongly away from the Ge surface.

Table 3.1. Equilibrium surface excess and Linear dichroic ratio (A_s/A_p) of TEA-FOS adsorbed from 0.5 mM solution at pH values of 3.4, 6.0, 8.4 and 10.0.

pH	Γ (molecules/nm^2)	A_s/A_p	γ
3.4	17.3	0.69	39.6
6.0	11.3	0.57	48.7
8.4	10.1	0.55	50.4
10.0	4.6	0.53	52.1

Table 3.2. Equilibrium surface coverage and area per molecule for aqueous 0.5 mM TEA-FOS adsorbed on hydroxylated Ge.

bulk solution pH	NaCl concentration (mM)	surface excess, Γ		area available per molecule (nm^2)
		(μmol /m^2)	(molecules/nm^2)	
pH ~ 3.4	0	28.7	17.3	0.058
	1	31.9	19.2	0.052
	2	35.9	21.6	0.046
	5	42.9	25.8	0.039
	10	25.8	15.5	0.064
	20	23	13.8	0.072
	50	6.47	3.89	0.26
pH ~ 10.0	0	7.58	4.56	0.22
	1	10.2	6.12	0.16
	2	12.2	7.34	0.14
	5	21.0	12.6	0.079
	10	19.6	11.8	0.084
	20	16.1	9.69	0.10
	50	9.83	5.92	0.17
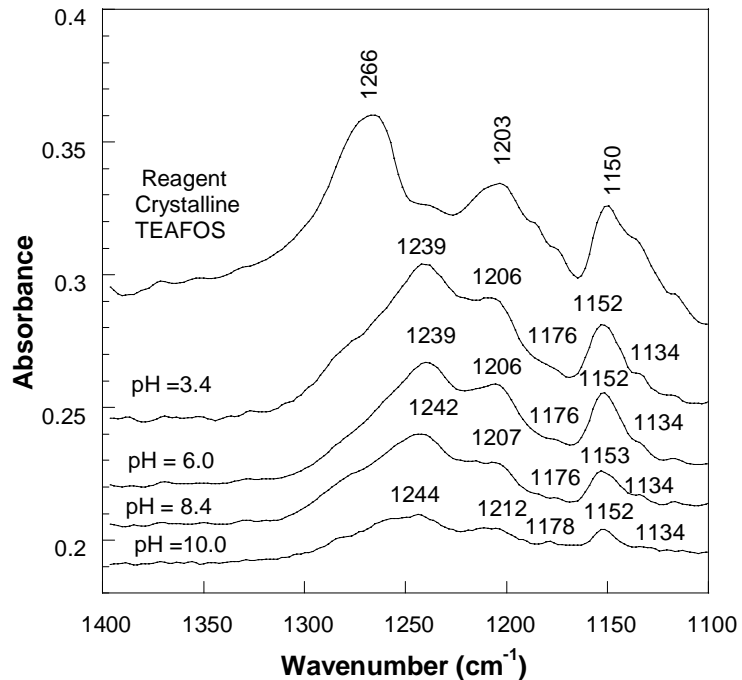
Figure 3.1. Unpolarized ATR-FTIR spectra collected at equilibrium for TEA-FOS adsorbed onto hydroxylated Ge from 0.5 mM aqueous solutions with pH values of 3.4, 6.0, 8.4, 10.0 (the lower four spectra), and the transmission spectrum of solid TEA-FOS (top).
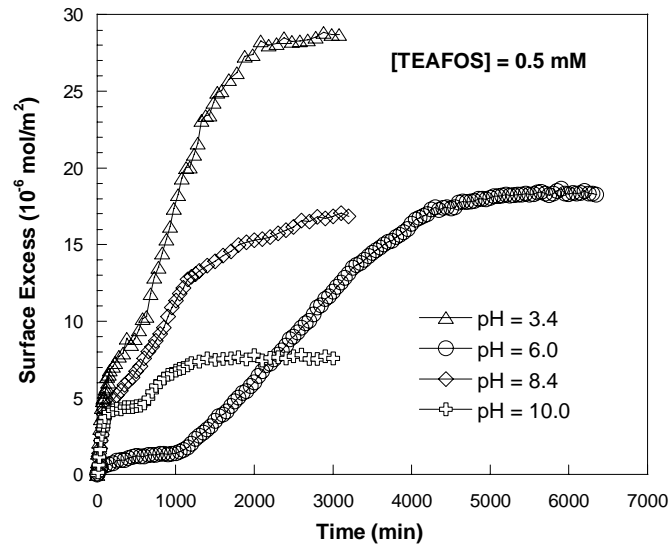
Figure 3.2. Surface excess evolution with time for the adsorption of TEA-FOS from aqueous solution onto hydroxylated Ge at solutions with pH values of 3.4, 6.0, 8.4, 10.0.
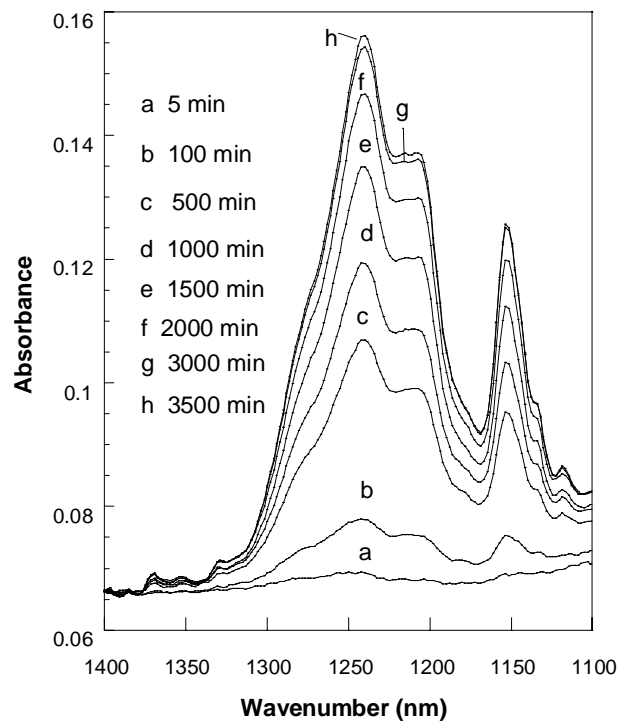
Figure 3.3. Unpolarized ATR-FTIR spectra collected during the adsorption of TEA-FOS onto hydroxylated Ge from 0.5 mM aqueous solution at pH 3.4 as a function of time after the introducing of the solution into the cell. [NaCl] = 5 mM in the solution.

81
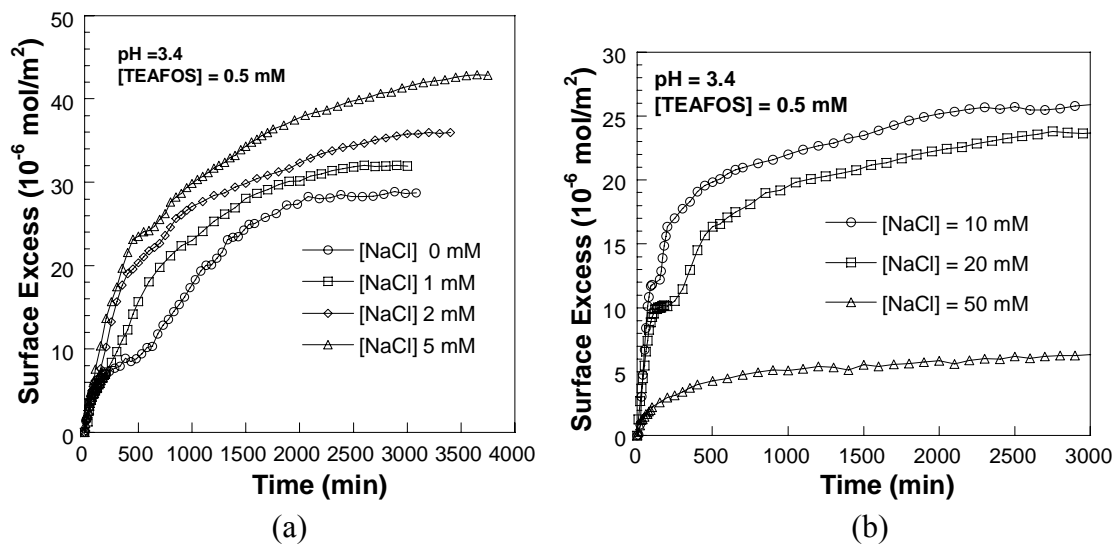
Figure 3.4. Surface excess evolution with time for the adsorption of TEA-FOS from aqueous solution onto hydroxylated Ge at pH 3.4 at different NaCl concentrations. Curves are drawn as guides to the eye.
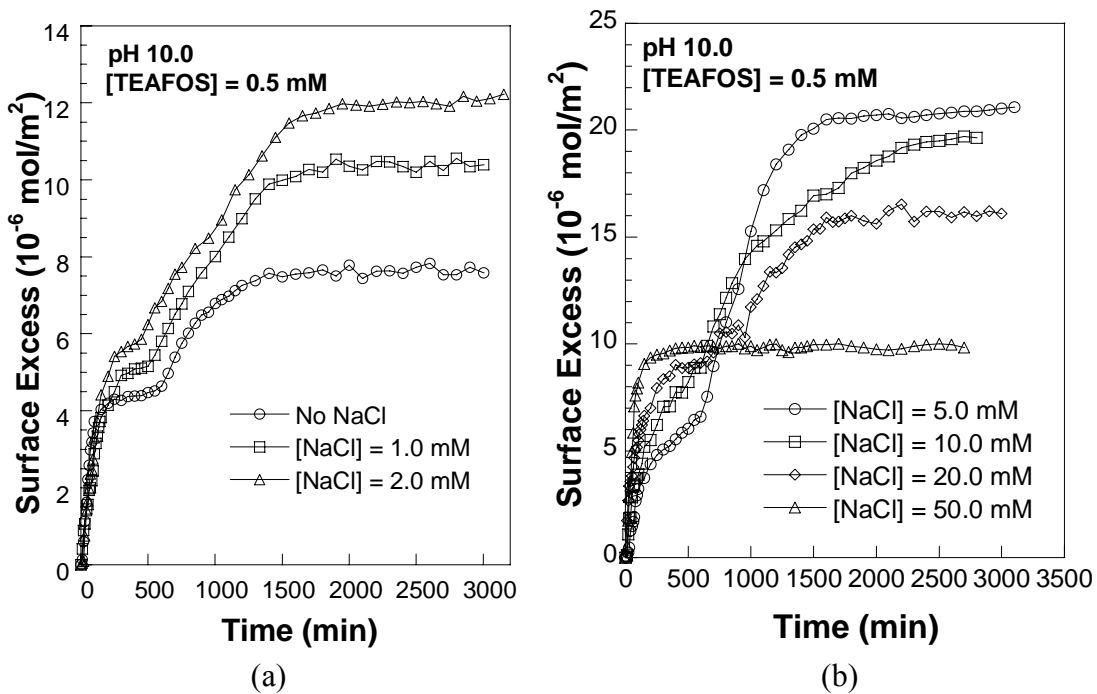
Figure 3.5. Surface excess evolution with time for the adsorption of TEA-FOS from aqueous solution onto hydroxylated Ge at pH 10.0 at different NaCl concentrations.
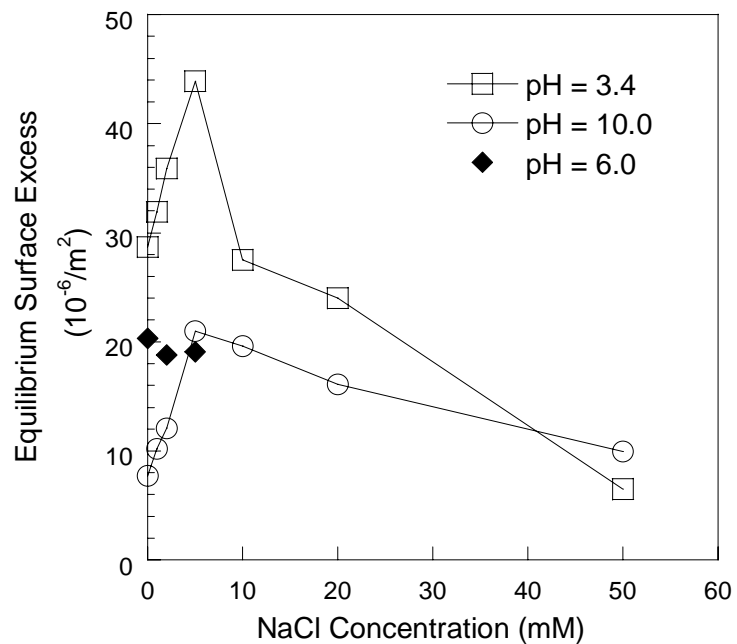
Figure 3.6. Equilibrium surface excess change with salt concentration at three different solution pH values. The solid lines serve as guides to the eye.
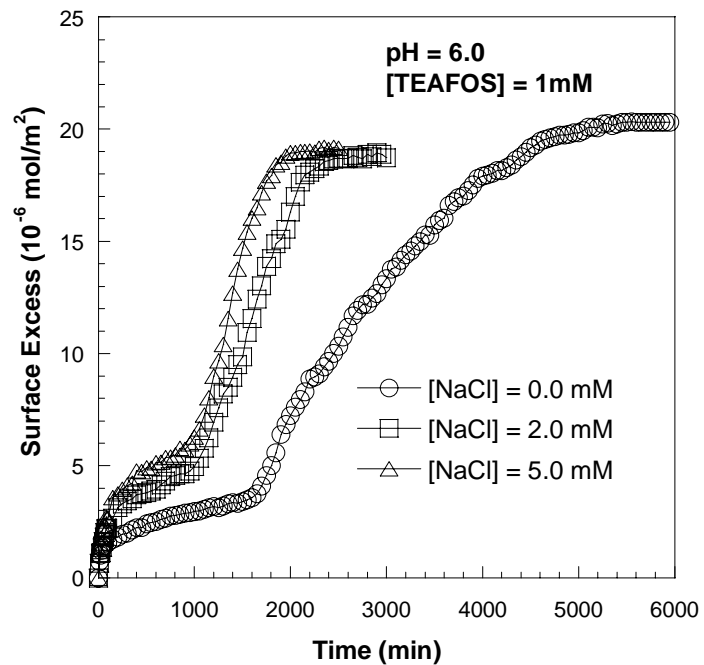
Figure 3.7. Surface excess evolution with time for the adsorption of TEA-FOS from aqueous solution onto hydroxylated Ge at pH 6 at different NaCl concentrations.
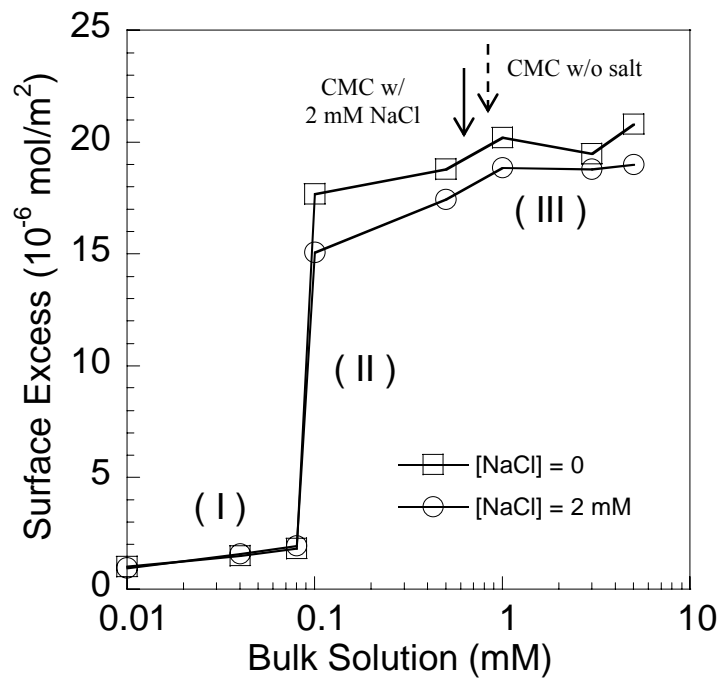
Figure 3.8. Comparison of adsorption isotherms with and without salt. The arrows show the CMC of TEA-FOS in the absence of salt (1.02 mM) and in the presence of 2 mM NaCl (0.83 mM) determined by conductance measurements.
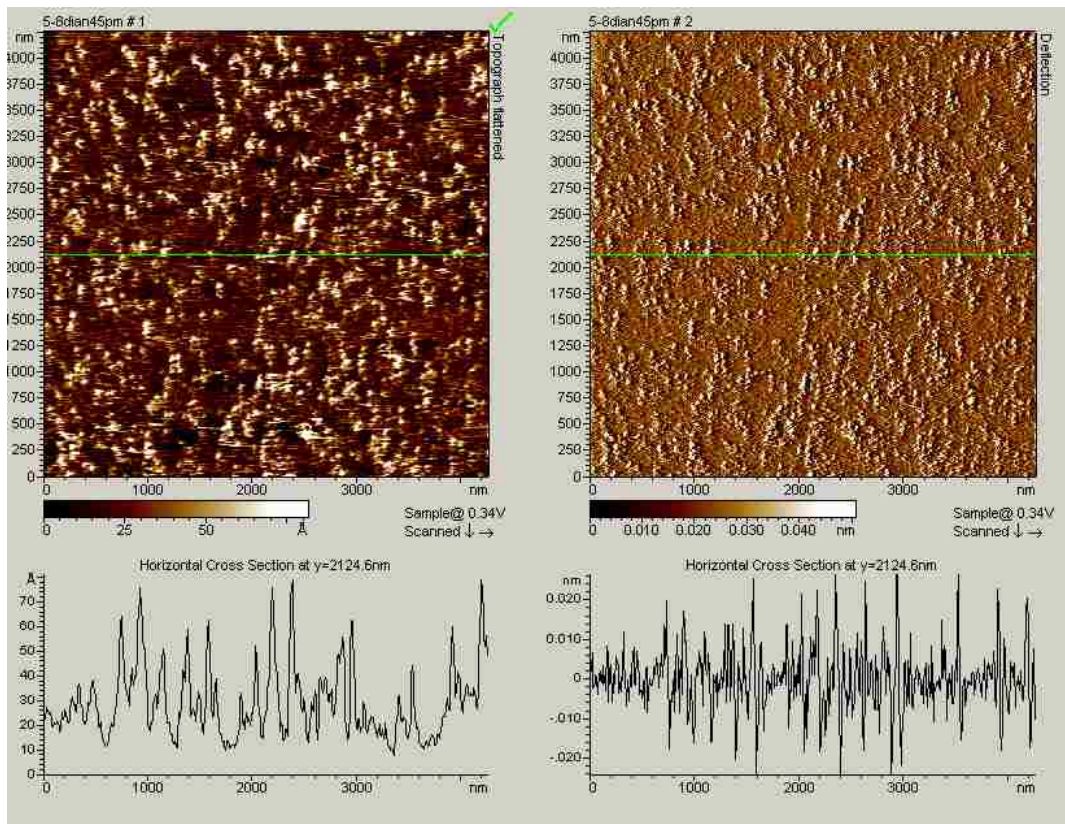
(a)
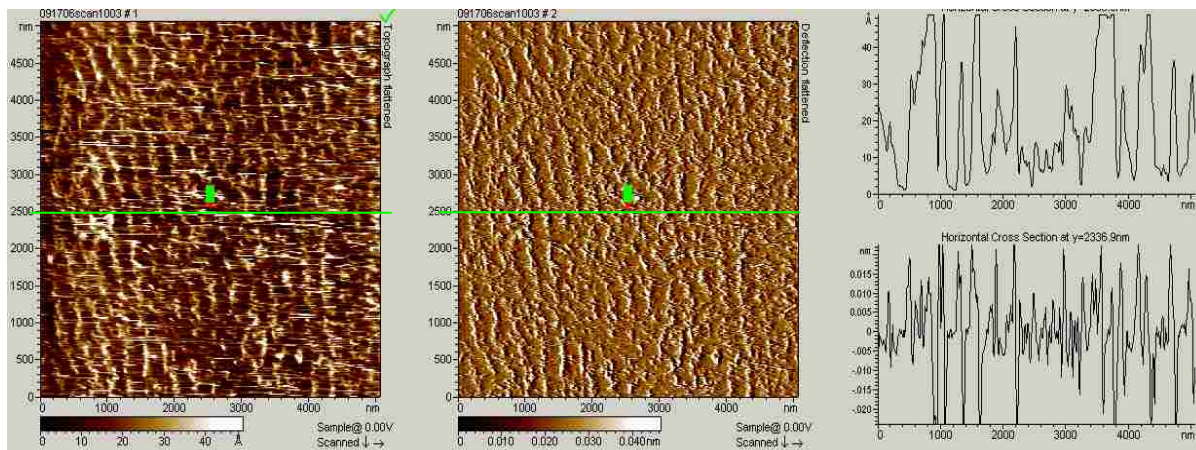
(b)

Figure 3.9. In situ AFM topograph (left) and deflection (right) images at equilibrium (after ~ 7 hr) of adsorbed multilayers on mica in 0.1 mM TEA-FOS solution (a) in the absence of NaCl, and (b) in the presence of 10 mM NaCl.
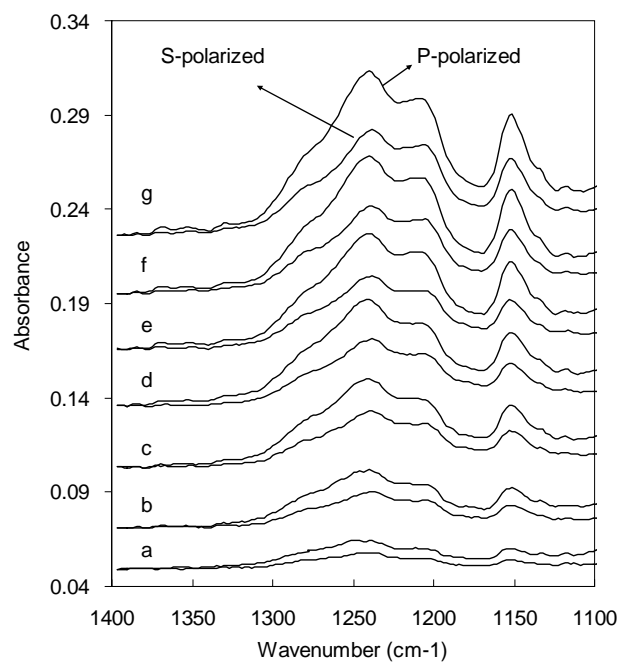
Figure 3.10. Polarized IR-ATR absorbance spectra at different stages of adsorption of a 0.5 mM TEA-FOS solution in the presence of 5 mM NaCl at pH 3.4. The lower spectrum is obtained with the IR beam S-polarized. The upper spectrum is obtained with the IR beam P-polarized. Spectra are shown after (a) 50, (b) 276, (c) 736, (d) 1336, (e) 1582, (f) 2183, (g) 2900 min.
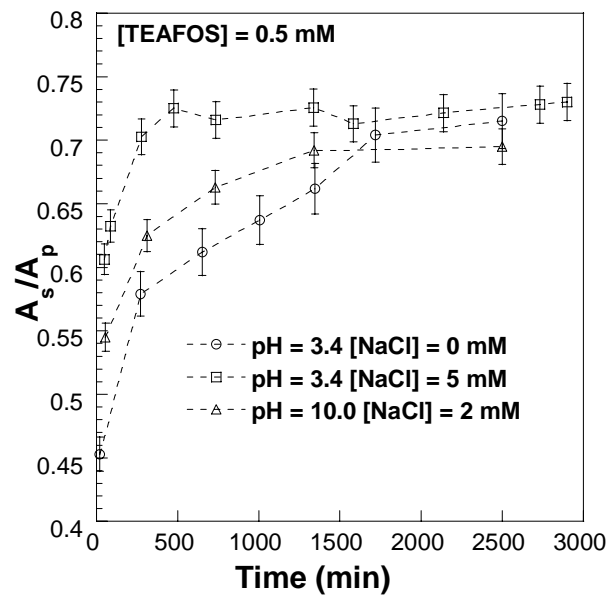
Figure 3.11. The dichroic ratio (A_s/A_p) evolution with time during the adsorption of TEA-FOS of 0.5 mM onto the hydroxylated Ge surface under different conditions.
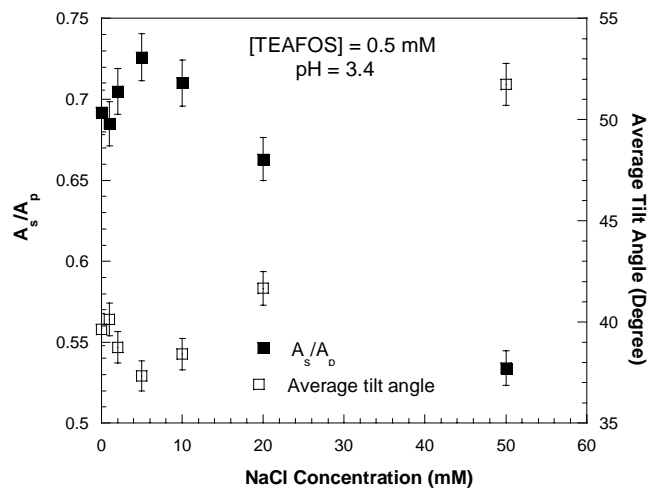
Figure 3.12. The dichroic ratio at equilibrium (filled squares, left axis) and the average tilt angle (open circles, right axis) of the $(CF_2)_s$ stretch vibration at 1251 cm^{-1} of a 0.5 mM TEA-FOS adsorbed onto Ge surface at pH 3.4, plotted against NaCl concentration.
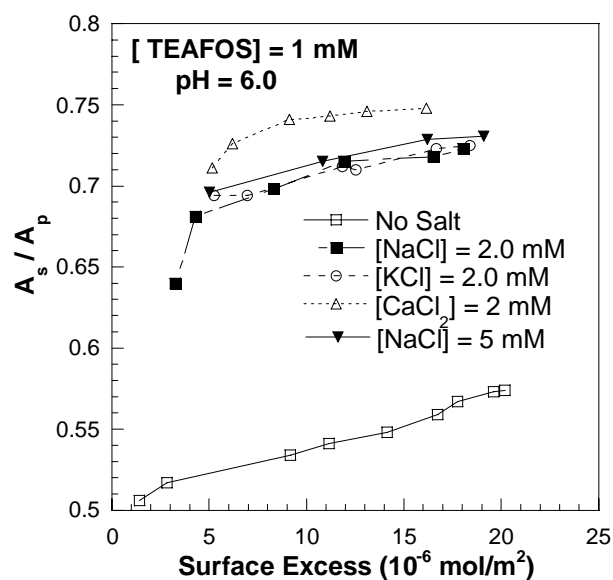
Figure 3.13. Relationship between the dichroic ratio of the $(CF_2)_s$ stretch vibration at 1251 cm^{-1} and the surface excess during the adsorption of a 1 mM TEA-FOS onto Ge surface at pH 6 in the presence of different types of simple salts.

Chapter 4. An Overview of Synthesis of Silica-Based Organic/Inorganic Hybrid Materials Using Dual Templates

4.1. Introduction

The discovery of the M41S family of mesoporous molecular sieves[1] has stimulated great interest in surfactant-directed synthesis of organic/inorganic hybrid silica and other metal oxides. Different type of surfactants, such as ionic or non-ionic, hydrocarbon or fluorocarbon, diblock copolymer or triblock copolymer etc, have been utilized as templates for the purpose of synthesizing mesoporous metal oxides with controlled pore size distributions and a diverse range of pore symmetries, particle sizes, particle morphologies and chemical compositions. Such materials show potential applications in molecular separation, drug delivery, catalysis, biosensors, etc.[2]

In recent years, dual templates, especially mixed surfactant templates, have received growing attention due to the opportunities provided by their unique properties. Binary hydrocarbon surfactant systems usually form mixed micelles with uniform composition in solution, which have been widely used in templating applications for effective phase control and pore size adjustment. Fine-tuning of micelle/mesophase structure is possible with dual surfactants because the packing parameter of a mixture of hydrocarbon/hydrocarbon surfactant molecules can be considered as a simple average of the packing parameters of the constituents. However, incompatible binary mixtures of hydrocarbon and fluorocarbon surfactant molecules in solution can self-organize into two populations of demixed micelles with different size, shape and chemical compositions (one hydrocarbon-rich and one fluorocarbon-rich). Demixed micelles formed at low surfactant concentration (< 10 wt%) are a relative new type of system which has not been explored for surfactant-templated materials synthesis yet. Depending on how they organize, demixed micelles have the potential to give better control over particle morphology, bimodal pore size distribution, and may even lead to novel interconnected phases that are not available in single-surfactant systems.

Since dual templates have advantages over a single template for the synthesis of mesoporous materials, the objective of this chapter is to survey the dual-template synthesis of mesoporous silica materials with a primary focus on dual surfactant systems. In chapters 5 through 9, we will employ different types of dual templates to synthesize

mesoporous silica materials with diverse phase structure, pore size distribution and particle morphologies. The dual templates we will discuss include cationic/sugar-based hydrocarbon surfactants, combined cationic hydrocarbon/fluorocarbon surfactants and cationic hydrocarbon surfactant/latex microspheres.

4.2. Literature review

4.2.1. Surfactant-directed sol-gel process

Surfactant-directed sol-gel chemical synthesis is an effective and simple approach to the assembly of mesoporous metal oxide materials. The surfactants co-assemble with the reacting precursor to form well-defined organic-inorganic hybrid products. Many different hypotheses about the templating mechanism and the interactions that can lead to ordered materials under different conditions have been described.[3-7] Surfactant-directed organic/inorganic co-assembly combined with sol-gel polymerization can be visualized as depicted in Figure 4.1. Surfactant monomers self-organize into micellar aggregates as they normally would in a polar solvent (see chapter 1), but the difference here is that the micelles co-assemble with silicate precursors via weak forces including Coulombic interactions between charges, hydrogen bonding or dipolar interactions to form organic/inorganic hybrid materials with a specific mesophase. While this co-assembly occurs, the sol-gel reactions of the precursors proceed, which can be generalized as hydrolysis of precursor to generate reactive Si-OH groups, alcohol condensation and water condensation (Figure 4.1). The condensation reactions lead to the formation of siloxane bonds, which are the basis for forming stable, solid walls in the resulting material. Upon removal of surfactants by calcination or solvent extraction, mesoporous materials are obtained with different sizes and symmetries, depending on the surfactant and conditions used for forming the material. In the literature, the routes for formation of mesoporous silica are sometimes classified according to the species that interact to drive the assembly of surfactants and inorganic species:

(1). S^+I^-, where S^+ represents a cationic surfactant and I^- represents an anionic silica species. This route was one of the first proposed for the formation of mesoporous silica. It uses the negative charge of silicates present in alkaline solution to drive assembly with dissociated cationic surfactants such as cetyltrimethylammonium chloride (CTAC) into ordered materials such as the M41S series,[1] the UK-series prepared in our group,[8-10] etc.

(2). $S^+X^-I^+$, where X^- represents a counter-anion and I^+ represents a cationic silicate. This route was initially proposed to explain the co-assembly of cationic micelles with the cationic silicate species that are expected to be present in acidic media. The assembly has been proposed to be mediated by counter-anions in acidic media that lead to materials like SBA-n[11].

(3). S^0I^0, where S^0 represents a nonionic surfactant and I^0 represents an uncharged silica species. This route was proposed to explain the co-assembly of non-ionic micelles with silica species near the isoelectronic point of silica (pH ~2), to form materials like HMS HMS,[4] MSU-V,[12] etc. This route also indicates that weak interactions such as hydrogen bonding are capable of driving the co-assembly of neutral surfactant and silicon alkoxides at the organic/inorganic interface. These interactions lead to poorly ordered precipitated particles, but to well-ordered mesophases in evaporation-induced self-assembly and nanocasting (see below).

(4) $S^-M^+I^-$, where M^+ represents a counter-cation to an anionic surfactant S^-. This route represents the co-assembly of anionic micelles and negative silicate precursors mediated by counter-cations in alkaline media, like AMS-x,[13] etc. Since anionic surfactants are mass-produced and relative cheap, this approach has the potential to increase the industrial production of surfactant-templated mesoporous materials. Figure 4.2 shows one representative formation of the mesostructured silica–micelle composite via $S^-M^+I^-$ route. In this work, M^+ represents an ammonium group introduced by co-condensation of tetraethyl orthosilicate (TEOS) and 3-aminopropyltriethoxysilane (APTES), and the charge at the interface depends on the pH of the synthesis solution.

(5) $S^+M^+X^-I^-$: This route represents the co-assembly of cationic micelles and negative silicate precursor in the presence of simple salts such as $NaNO_3$ under mild alkaline conditions. It is a refinement of the S^+I^- interaction model that helps to explain salt and counterion effects. Based on chemical analysis, Echchahed et al.[6] concluded that both cations M^+ and anions X^- can stay at the surfactant/silicate interface, and play a mediating role in the interfacial electrical balance that sometimes leads to a slight charge density mismatch that can change the mesophase of the final silica products.

(6)$N^0M^+X^-I^0$: This route represents the co-assembly of non-ionic micelles and neutral silicate precursor in the presence of simple salts under acid media. Bagshaw et al.[7] investigated the effect of dilute electrolytes on the formation of non-ionic surfactant-templated silica, and found that monovalent cations, like H^+, Li^+, Na^+, K^+, Cs^+ and NH^{4+}, intervene in the surfactant/silicate assembly directing affecting either the shape or the mesostructure, while anions, like F^-, Cl^-, Br^-, I^-, SO_4^{2-}, NO_3^- and OAc^-, interact with the precursor to affect the hydrolysis and condensation rate of precursor, thus influencing the particle size of the final products.

In addition to the classification above based on the interactions at the micelle-materials interface, surfactant templating can be classified as either synergistic sol-gel reaction induced precipitation or nanocasting as illustrated in Figure 4.3. In the former mechanism, co-assembly of surfactant in bulk solution and condensing sol-gel species leads both to mesostructure formation and the formation of the final particles. There has been some controversy in the literature about whether micelles form first and then co-assemble with silicates into particles, or precipitation precedes mesophase ordering. Recent direct evidence of Tan and Rankin suggests that at room temperature, precipitation of micelles and silicates occurs first, but ordering proceeds after particles have already formed.[14] Because the precursors and surfactants partition into a new phase in which they co-assembly, the conditions for forming different pore structures are divorced from the surfactant phase diagram. A kinetic balance is established between the aggregate phase and the bulk solution phase for both surfactants and silicates throughout the whole synthesis process. The latter nanocasting route is similar to the microemulsion gel method in which sol-gel polymerization occurs directly in the surfactant aggregate phase[15]. In this process, an ordered surfactant mesophase is pre-assembled, and an alkoxide precursor is added which hydrolyzes and slowly condense to generate the oxide. However, the alcohol generated by hydrolysis destroys the original order and it is restored by removing the surfactants. Because of this, the process is similar to evaporation-induced self-assembly. In the following chapters, we will utilize both precipitation and nanocasting routes to mesoporous materials for different objectives.

4.2.2. Dual hydrocarbon surfactants as pore template

When mixtures of two kinds of hydrocarbon surfactants are dissolved in an aqueous solution, mixed micelles usually form with the hydrophobic chains of the two surfactants aggregated in the micellar core. Just like ordinary micelles, the size and shape of mixed micelles are governed by hydrophobic forces that drive tail assembly and the charge density of the headgroups at the micelle surface. Both aspects of micelle structure can be finely tuned in mixed micelles by changing the surfactant composition. In such a case, a distribution is expected not only of the aggregation number and size of the mixed micelles, but also of their chemical composition. The distribution of micelle properties has been widely investigated by different techniques, including surface tension[16], NMR[17], conductivity measurements[18] and fluorescence quenching[19]. Mixing surfactants often leads to a synergistic effect that gives the mixed system different (and often improved) properties than either individual surfactant. For example, an anionic-cationic hydrocarbon surfactant pair can effectively act as a double-tailed zwitterionic surfactant to spontaneously form vesicles, which are stable for periods as long as several years and appear to be thermodynamically stable.[20] At the same time, the surfactants interact by physical interactions that can be disrupted by conditions such as ionic strength and temperature, thus providing a means to 'switch' the aggregate structure. In addition, cationic-nonionic hydrocarbon surfactant pairs can be closely associated to form bilayer structures at the hydrophilic silicon surface.[21] Ionic/nonionic surfactant pairs are also widely used in industry to meet the multifunctional demands in consumer applications.

In general, the packing parameter of mixed hydrocarbon surfactant molecules can be considered to be a simple average of two single surfactant packing parameters, which provides an effective and simple way to tune the size or shape of surfactant aggregates by changing the molar composition of the two surfactants. This is an attractive concept for fine pore size and mesostructure control, and dual surfactant templates have begun to receive significant interest for the preparation of mesoporous materials.[22-24] Huo et al.[22] firstly explored the synthesis of mesoporous silica by using mixture of binary Gemini surfactants ($C_{16-12-16}$ and C_{16-3-1} where the first and last numbers indicate the lengths of alkyl chains linked to two ammonium headgroups and the middle number indicates the length of an alkylene chain linking the two headgroups) as templates. The final products

show a transition from Ia3d cubic to P6mm (2D hexagonal) or P6$_3$/mmc (3D hexagonal) as the amount of C$_{16\text{-}3\text{-}1}$ increases relative to C$_{16\text{-}12\text{-}16}$. Ryoo et al.[24] used the mixture of hexadecyltrimethylammonium bromide (C$_{16}$TAB) and tetra(ethylene glycol) dodecyl ether (C$_{12}$(EO)$_4$OH) to prepare mesoporous silica, and observed a mesophase transformation from hexagonal to cubic to lamellar structure depending on the molar ratio of the two surfactants. In addition to the mesophase control, mixed hydrocarbon surfactant templates have been used to adjust pore size and wall thickness,[25] to form stable vesicle-structured materials,[26] to improve the thermal stability of silica materials,[27] and to synthesize temperamental mesophases (such as Ia3d cubic) under mild conditions.[28] In addition, since the repulsive interaction between anionic surfactants and silicate species usually prevents the organization of an ordered mesostructure, anionic surfactants have been combined with other surfactant templates such as triblock polymer system[29] or cationic surfactants[30] for the synthesis of novel ordered mesoporous materials. In chapters 5 and 6, we will investigate nanocasting using mixtures of a new pair of surfactant classes: the cationic surfactant CTAB and the sugar-based surfactant n-octyl-β-D-glucopyranoside (C$_8$G$_1$). The long-term goal will be to introduce functionality and transition metals into the pore walls of the materials using the sugar headgroups of a surfactant such as C$_8$G$_1$. Here, we perform some of the groundwork that will make that possible by investigating the effect of ammonia treatment on the pore structure of the silica materials, and by developing the CTAB/C$_8$G$_1$/water ternary phase diagram and showing that it can be used for predictive mesoporous materials synthesis.

4.2.3. Mixed hydrocarbon/fluorocarbon surfactant systems

Most mixed surfacant studies have focued on surfactants with compatible tails but with differing headgroups selected to tune assembly and micelle properties. In contrast to mixed surfactants of the same tail type, mixed hydrocarbon/fluorocarbon surfactants have unique properties that are both useful and of fundamental interest. A distint difference is the incompatibility between hydrocarbon and fluorocarbon tails in these systems, which cause significant deviation from Raoult's law (ideal mixing) both in solution and at the solid/liquid interface.[31] For surfactants of sufficient length, this can lead to demixing into hydrocarbon-rich aggregates and fluorocarbon-rich aggregates. In addition to chain length, the miscibility of two hydrocarbon and fluorocarbon surfactant molecules is

strongly dependent on the headgroups and the counter-ions. Some mixtures are totally miscible in all proportions, such as lithium perfluorooctanesulfonate (LiFOS)/lithium dodecylsulfate (LiDS), which are miscible both in iostropic micellar solution and in liquid crystal phases.[32] Shinoda et al.[33] systematically studied the mutual solubility of $C_nF_{2n+1}COOH$ (n = 7-12) with $C_mH_{2m+1}COOH$ (m = 7-17) and of $C_nF_{2n+1}CH_2CH_2OH$ (n = 8-10) with $C_mH_{2m+1}OH$ (m = 11-18), and concluded that a carbon chain with at least 8 carbons is necessary to cause the micelle demixing in solutions of these fluorocarbon and hydrocarbon surfactants.

In bulk solution, a significant amount of work has been performed to show that incompatible binary hydrocarbon/fluorocarbon surfactants can segregate into two large populations of segregates with different composition. The co-existence of two kinds of micelles resembles liquid-liquid phase coexistence caused by the lack of dipolar interactions between fluorocarbon and hydrocarbon chains[34]. Mukerjee and Yang[35] first provided evidence of partial miscibility of fluorocarbon and hydrocarbon surfactants based on changes in differential conductance data for different mixtures of sodium dodecylsulfate (SDS) and sodium perfluorooctanoate. Mysels et al.[36] first proposed a theory that could account for the formation of demixed micelle populations. Asakawa et al.[37] successfully applied a group contribution model to mixed micellization to predict the critical micelle concentration (cmc) of mixed hydrocarbon and fluorocarbon surfactants. Based on cmc measurements, Shinodal et al.[33] found that demixing occurs in ammonium perfluorononanoate/SDS mixtures, whereas sodium perfluorooctanoate mixes with SDS in all proportions. A similar demixing phenomenon also occurs in spread monolayers at the air/water interface.[38] Additional evidence for demixing and quantitative information such as aggregation number, micelle composition, aggregate structure and size and micellar pseudophase separation regions has been provided more recently by fluorescence quenching[39], conductivity measurements[35,40], cryo-TEM[41], NMR[42], small angle neutron scattering[43] and surface tension[44].

Because they provide controlled populations of different nanoscale aggregates, mixed hydrocarbon/fluorocarbon surfactants have been used as structure-directing agents (SDA) for mesoporous material synthesis. Mixed hydrocarbon/fluorocarbon surfactants have been employed not only in order to achieve high hydrothermal stability[45], to generate

hierarchical pore structure[46], to control morphology[47], to explore unknown phase behavior[48], and to tailor the porosity, but also in order to facilitate the synthesis of novel biphasic materials with long range ordering. Demixed layers of fluorinated surfactants have been used both as hollow macropore templates[49]and for particle size and morphology control.[50] For example, Han et al.[50] used mixture of hydrocarbon copolymer and the cationic fluorocarbon surfactant $C_3F_7O(CFCF_3CF_2O)_2CFCF_3CONH(CH_2)_3N^+$-$(C_2H_5)_2$-$CH_3I^-$ (FC-4) as template to prepare mesostructured nanoparticles in acidic media. The copolymers were used to control the mesophase structure, and the FC-4 surfactants were shown to primarily influence the particle size and morphology. This is interpreted as indicating that the FC-4 surfactants move to the external particle surface to modify the particle/solution surface energy.

In addition, demixed micellar aggregates have the potential to be selectively swollen with different organic additives to act as templates for the synthesis of materials with controlled bimodal pore size distributions. Furthermore, the principle of selective partitioning into demixed micelles can be applied for controlled deposition of different types of metal oxides into different channels for bi-functional catalyst applications. For example, in many cases, one wishes to prepare an intermediate species using one catalyst, but to use a second catalyst to transform that intermediate into the final product (i.e. to perform reactions in series). If separate catalyst beds are used, the intermediates may decompose prematurely into side products. If the catalysts are mixed in an uncontrolled way, they may interact negatively (for instance by forming an inactive alloy). Being able to form two separate metal oxide particle populations within a single particle would avoid many of these complications. In chapters 7 and 8, we will investigate synergistic sol-gel induced precipitation using mixture of cetyltrimethylammonium chloride (CTAC) and 1H,1H,2H,2H-perfluorodecylpyridinium chloride (HFDePC), to investigate the mixing and demixing behavior of this system. Previous studies have shown that this pair of surfactants form demixed micelles in dilute solution over a range of compositions.[51] Our studies will show the effects of key synthesis parameters (molar composition, synthesis temperature and additives) on the pore structure, particle morphology and pore size distributions of the silica particles.

4.2.4. Other hierarchical dual templates

In addition to mixture of two surfactants, other dual template systems have been explored for controlled porous materials synthesis. Generally, these dual templates are utilized to synthesize porous materials with hierarchical structure, and this is best accomplished by using templates of very different characteristic size. For example, a surfactant or amphiphilic block copolymer is often combined with macropore templates, such as colloidal particles[52], polymer foams[53], bio-cellulose[54], poly(ethylene glycol)[55], emulsions[56], inorganic salts and ice crystals[57], or even bacteria[58] to create hierarchical meso-macroporous materials. The mesopores provide the advantageous confinement effects for adsorption, catalysis, and filtering, while the macropores enable fast diffusion. Stucky et al.[52] reported dual latex/copolymer templating in patterned regions to prepare bimodal meso-macroporous silica with hierarchical ordering over several discrete and tunable length scales. Those bimodal meso-macroporous materials with different length scales have been demonstrated to remarkably improve the activity of mesoporous catalysts due to the enhanced diffusion of reactants and products[59]. In addition, an amphiphilic ionic liquid and polystyrene sphere have been combined in making bimodal micro-macroporous materials.[60] In chapter 9, we will report two-step synthesis of hollow spherical silica particles with inter-connected bimodal mesopore shells by using a dual surfactant/latex system for templating, and demonstrate the accessibility of the hollow cores of the particles to probe molecules of very different size: sulforhodamine B (SRB) dye and green fluorescent protein (GFP). Those hollow particles are designed for controlled drug release, high-capacity absorbents, and for catalysis.

4.3. Characterization methods

In the chapters on dual templating of porous silica, we use different techniques to characterize liquid crystal structure and the pore size and symmetry of porous properties. Pore properties such as pore volume, pore size distribution and pore surface area are measured by nitrogen adsorption. The information about long-range ordering and symmetry of mesopores is obtained from powder XRD at low angles. For different types of ordered structure, XRD patterns show a series of different reflections. For example, the materials with ordered 2 D hexagonal columnar phase (HCP) usually show well-resolved (100), (110) (200) and even (210) reflections at low 2θ values, while lamellar materials

show (100) and (200) reflections. For random mesh phase (also called pillared lamellar phase) structure, one can usually find (001), (002) and low-angle pillar reflections from silica micropillars between layers. The mesophases of micellar liquid crystal of surfactant are identified by using polarized optical microscopy (POM). Anisotropic micellar liquid crystal of surfactant shows polarization contrast phase textures. For example, an angular fan-like pattern is characteristic of the defect structure of a hexagonal mesophase[61], while the Maltese cross texture is typical of lamellar liquid crystals[62]. FTIR and UV-vis provide information about chemical bond vibrations and electronic transitions, respectively, of samples to confirm the presence and absence of surfactants, and to investigate the chemical transformation of some surfactant systems. Electron microscopy (SEM and TEM) provides information about the structure and morphology of samples. For SEM and TEM, careful sample preparations are necessary. The detailed procedures for sample preparation are described in the following chapters. Accessibility tests of dye and protein molecules into the hollow silica core are conducted by a laser scanning confocal fluorescence microscopy.
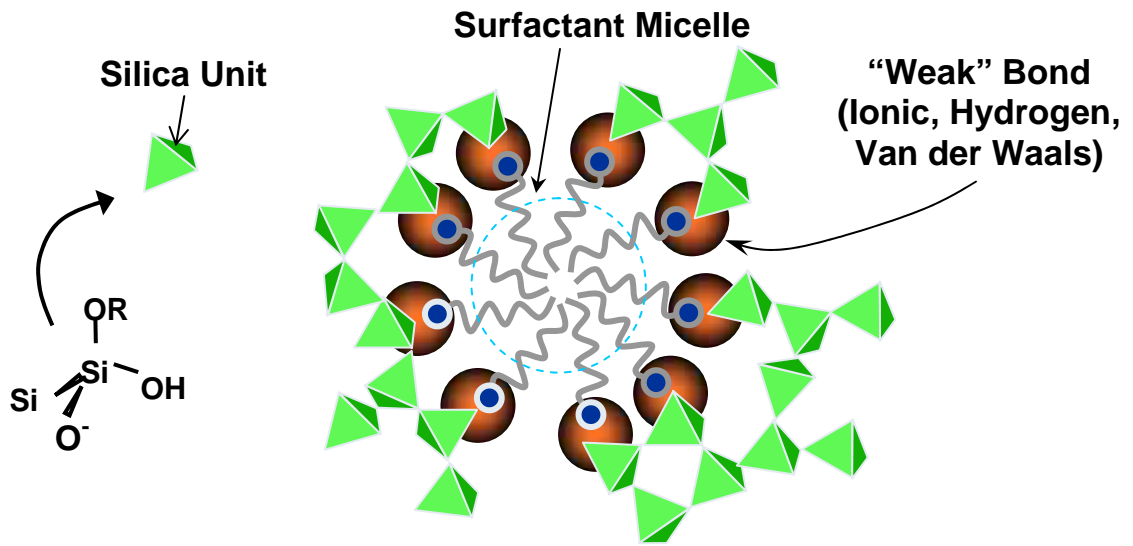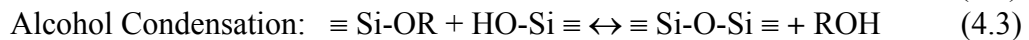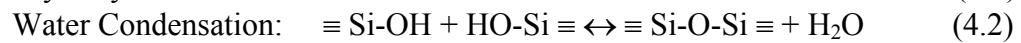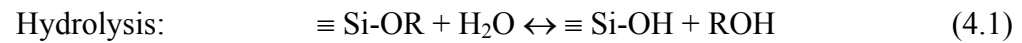
Figure 4.1. Schematic illustration of the surfactant templated sol-gel process.

Sol-gel Reactions

Hydrolysis:	$\equiv$ Si-OR + H$_2$O $\leftrightarrow$ $\equiv$ Si-OH + ROH	(4.1)
Water Condensation:	$\equiv$ Si-OH + HO-Si $\equiv$ $\leftrightarrow$ $\equiv$ Si-O-Si $\equiv$ + H$_2$O	(4.2)
Alcohol Condensation:	$\equiv$ Si-OR + HO-Si $\equiv$ $\leftrightarrow$ $\equiv$ Si-O-Si $\equiv$ + ROH	(4.3)
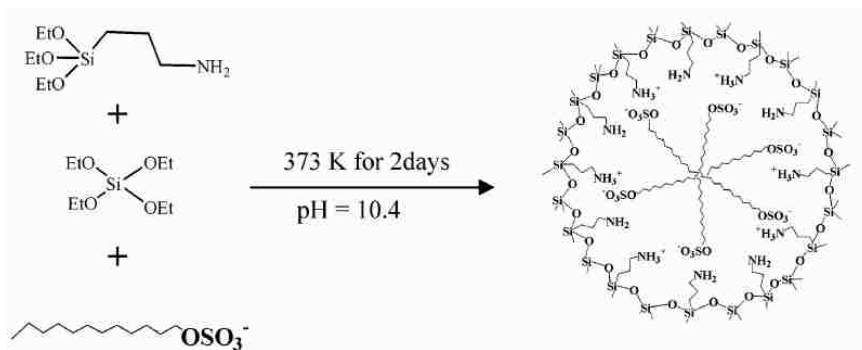
Figure 4.2.[13] Co-assembly of anionic surfactant SDS and silica mediated by positively charged ammonium groups. Reprinted with permission from *Chem. Mater.* **2003**, 15, 4536. Copyright ©2003 American Chemical Society.
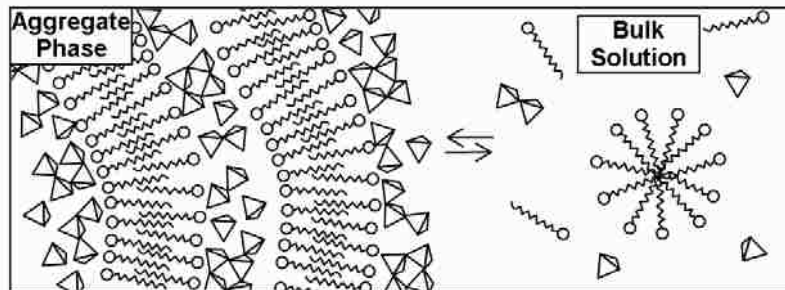
(a)
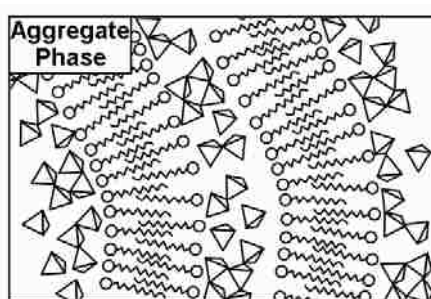
(b)

Figure 4.3. (a) Synergistic sol-gel induced precipitation between silica units (tetrahedral) and surfactants, and (b) nanocasting.

(a)   (b)

(c)   (d)
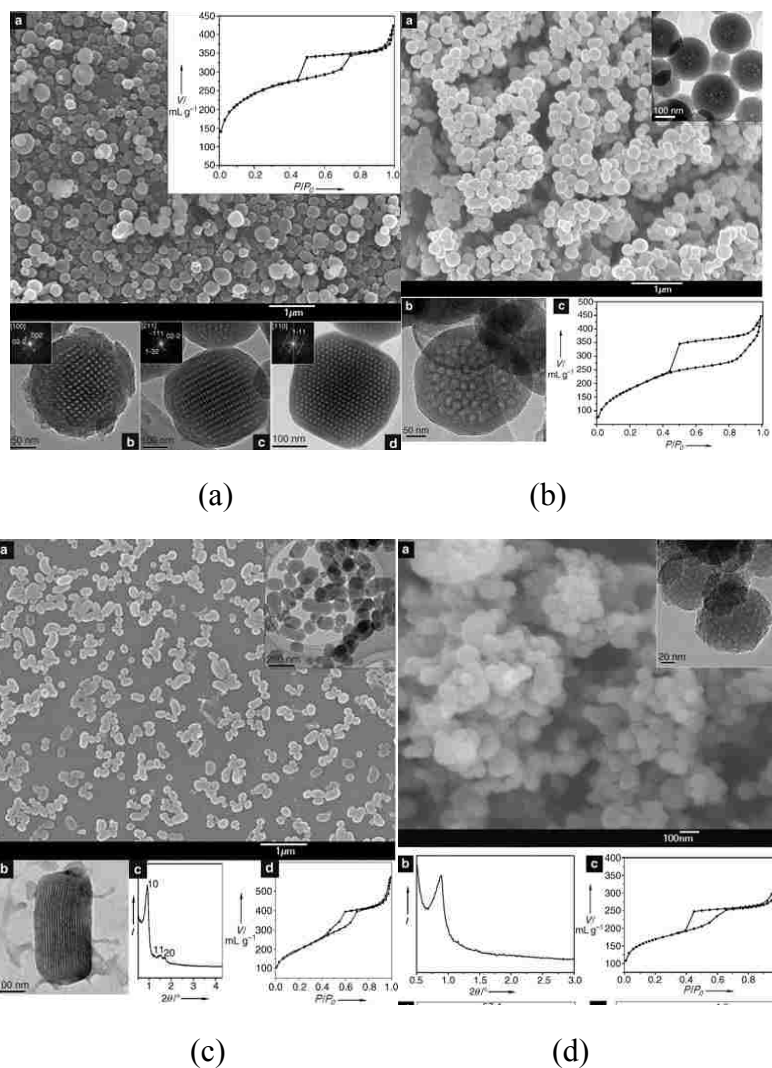
Figure 4.4. [50] Nanoparticles prepared by using mixture of hydrocarbon/fluorocarbon surfactants as templates. (a) Face-centered cubic structure templated by FC+F127+TMB, (b) Mesocelluar foam structure templated by FC+P65+TMB, (c) 2d HCP structure templated by FC+P123, (d) Disordered structure templated by FC+F108. Reprinted with permission from *Angew. Chem. Int. Ed.* **2004**, 44, 288. Copyright © 2004 with permission from WILEY.

Chapter 5. Reactive Pore Expansion during Ammonia Vapor Post-Treatment of Ordered Mesoporous Silica with Mixed Glucopyranoside and Cationic Surfactants[*]

5.1. Introduction

The synthesis of ordered mesoporous metal oxides using surfactant templating was first reported by Beck, Kresge, and coworkers in 1992.[1,2] Since then, ordered mesoporous metal oxides have been the topic of rapid discovery in materials chemistry, catalysis, chemical sensing, and separations.[3-6] Variations in the range of organic supermolecular templates and inorganic ions has led to many advanced materials.[7-9] Here, we report mesopore templating using mixtures of the surfactants illustrated in Figure 5.1: nonionic surfactant n-octyl-β-D-glucopyranoside (C_8G_1) and cationic cetyltrimethylammonium bromide (CTAB). Sugar-based surfactants have many useful properties, but have not been extensively investigated as pore templates. In general, sugar-based surfactants are very hydrophilic because they contain a large number of hydroxyl groups in their headgroup. Sugars are also capable of multiple interactions with silica and transition metals that can lead to templation.[10] They are nontoxic and biodegradable, and can be synthesized from renewable resources.[11,12] They show considerable variety in micelle structure and phase behavior based on the anomeric and chiral form of the surfactant, in addition to the alkyl tail length and the type of carbohydrate head group.[11] In addition, carbohydrate surfactants are models for the types of nonionic molecules that may be useful for molecular imprinting, which transfers specific structural features from nonionic imprinting molecules into the inorganic framework.[13-15]

C_8G_1 is a commercially available surfactant and its phase behavior in water has been well characterized.[16,17] Lavrenčič-Štangar and Hüsing reported the first and only attempt to use C_8G_1 as a pore template in mesoporous silica films prepared via dip-coating.[18] However, they found that C_8G_1 favors lamellar products, which is consistent with the large packing parameter of this surfactant. The binary phase diagram of C_8G_1 in water[16,17] has only two narrow 2D hexagonal columnar phase

(HCP) regions, from 28 to 32 wt% and from 59.5 to 70 wt%. However, the 2D HCP phase has a melting point of only 23°C,[19] which suggests that 2D HCP mesoporous silica cannot be prepared at or above room temperature with C_8G_1 alone. To overcome this problem, a mixture of surfactants may be capable of promoting hexagonal ordering. Cortes et al.[20] investigated the effect of adding 1 wt% C_8G_1 on the phases of CTAB/glycerol/water at 30.0 ± 0.1°C, and found that it expands the 2D HCP phase region significantly. The discovery of an extended 2D HCP region motivates us to further study the CTAB/C_8G_1/water ternary phase diagram (to be reported in chapter 6).

In this chapter, we will show that mixed CTAB/C_8G_1 surfactants can indeed be used as templates to make 2D HCP structured porous metal oxides via nanocasting. Surfactant-templated oxides were first prepared by sol-gel reaction-induced precipitation of silica precursors from dilute (< 30 wt%) surfactant solutions,[21-23] by a mechanism best described as co-assembly.[24,25] However, we use a method similar to the microemulsion-gel method[26] called "nanocasting" in which sol-gel polymerization occurs directly in a lyotropic liquid crystal phase.[27] In this process, a concentrated surfactant solution is prepared, and an alkoxide precursor is added which hydrolyzes and slowly condenses to generate the oxide. The alcohol produced by hydrolysis usually destroys the original order, but by evaporating the alcohol, it is possible to recover a material that mimics the structure of the original liquid crystal.[28-30] The surfactants are present at much greater concentrations than in the reaction-induced precipitation method, and the size, connectivity and ordering of the final nanoscopic pore system can be predicted *a priori* based on the aqueous surfactant phase diagram. Because the liquid crystal structure is lost during hydrolysis and regained during drying, the method resembles the evaporation-induced self-assembly process.[31] Nonionic organic supermolecular templates in acidic media are usually employed in the nanocasting method.[32-35] In these systems, the high surfactant concentration helps to drive co-assembly in the absence of the strong surfactant-silica interactions present in precipitating cationic surfactant systems. Recently, nanocasting has been extended by using mixed immiscible template to generate hierarchical pore systems,[36,37] and mixed short-chain alcohols and block copolymers to control the pore size.[38] Here, we

will for the first time report nanocasing with a mixture of sugar-based and cationic surfactants.

In this chapter, calcination is used to remove the surfactants from all samples (for consistent comparison). However, if mixed surfactants are to be used to impart functionality to the porous oxide, it will be necessary to remove the surfactant by extraction rather than by calcination. Because an acid medium is used for nanocasting, the as-made materials require an extremely long time to condense sufficiently to allow extraction.[39] We hypothesized that exposing the samples to ammonia vapor at 50 °C would be a mild post-synthesis treatment which would stabilize the silica network to allow extraction. Ammonia/water vapor treatment of silica films without surfactant templates has been shown to improve their degree of crosslinking and mechanical strength.[40] Ammonia hydrothermal treatment has been used before to stabilize the structure of acid-catalyzed surfactant-templated samples[41,42] but here we use vapor-phase treatment to limit the extent of pore distortion caused by dissolution of silica and Ostwald ripening.[41] A known side-effect of ammonia treatment with cationic surfactants is pore expansion[41,42] and this effect has been exploited to manipulate the pore size of surfactant-templated silica using various amines added before and after synthesis.[43] Attempting to use a new, mild ammonia vapor treatment leads to much greater pore expansion when C_8G_1 is added than for pure CTAB. The magnitude of the expansion with C_8G_1 can be enough to introduce pore defects, but we will demonstrate strategies to limit its extent. Because pore expansion may or may not be desirable (depending on the application), we will explore the mechanism of expansion using different mixtures of ionic and nonionic surfactants to manipulate the charge density at the silica/surfactant interface. We will show that the Maillard reaction between ammonia and the sugar headgroups plays a surprisingly important role, even under mild treatment conditions.

5.2. Experimental section

5.2.1. Materials and synthesis procedure

Cetyltrimetylammonium bromide, CTAB (99.0%, Sigma), tetramethyl orthosilicate, TMOS (>99.0%, Sigma), n-Octyl-β-D-glucopyranoside, C_8G_1 (≥ 99.0%, Fluka), concentrated aqueous ammonia (28 wt%, Fisher Scientific), deionized ultrafiltered

(DIUF) water (Fisher Scientific), and normalized 0.01 N hydrochloric acid solution (Alfa) were used as received.

The nanocasting procedure was similar to that reported in the literature.[27] In all samples, the ratio of total surfactant to water was 50 wt%. Typically, 1 g CTAB and X g C_8G_1 were dissolved in (1+X) g of aqueous hydrochloric acid (pH = 2) with stirring, and the mixture was heated at 50 °C for at least 30 min to reach a liquid crystal-like state. Then TMOS was added to these mixtures. The amount of TMOS used was always less than 0.25 mole equivalents with respect to the water. In this way, the water content in the mixture was slightly higher than that required for the complete hydrolysis of the TMOS. Hydrolysis with stirring proceeded for 20 min, and then the transparent mixture was exposed to a gentle vacuum to remove the methanol. The resulting viscous solution was transferred into a Petri dish to form a film and aged at 50 °C in a temperature-controlled digital dry bath for 48 hr. The surfactant templates were removed by calcination in air at 550 °C for 6 hr.

Post-synthesis treatment of some as-made samples was accomplished by first spreading the as-made sample on a watch glass, which was then placed into a Petri dish. A measured amount of concentrated aqueous ammonia (28 wt%) was added to the dish around the watch glass without touching the sample, and the dish was covered with parafilm and stored at 50 °C overnight. While the long-term goal of doing this is to allow the surfactant to be extracted, we still calcined the ammonia-treated samples, for direct comparison with the samples that were not treated with ammonia. The quantities of all materials used are reported in Table 5.1.

5.2.2. Characterization methods

The long-range order of the samples was characterized with a Siemens 5000 X-ray diffractometer using 0.154098 nm Cu-K$_\alpha$ radition, a graphite monochromator, and a scan rate of 1 °/min. Nitrogen adsorption-desorption isotherms were obtained at -196 °C using a Micromeritics Tristar 3000 automated adsorption instrument. Typically the samples were degassed at 120 °C for 4 hr prior to analysis. For transmission electron microscopy (TEM), samples were ground and loaded onto lacey carbon grids for analysis using a JEOL 2010F instrument at a voltage of 200 kV. Fourier transform infrared (FTIR) spectra were obtained with a dessicated and sealed ThermoNicolet

Nexus 470 infrared spectrometer with a DTGS detector. Samples were finely ground and diluted to 1 wt% with KBr powder before being pressed into translucent pellets with a hand press. UV-visible (UV-vis) spectroscopy was performed with a HP8453 UV-visible spectrophotometer using disposable UV-transparent plastic cuvettes from Fisher Scientific. For UV-vis analysis, the organic reaction products and surfactants were extracted with dry ethanol, and the extracts were diluted 2-fold before testing. The phase behavior of ternary $CTAB/C_8G_1$/water mixtures was investigated using a Zeiss Axioskop microscope with crossed polarizing filters, and the images were recorded using a Nikon Coolpix 995 digital camera. Microscope samples were first prepared by weighing the required amounts of surfactants and water into PVC vials which were sealed and homogenized in an ultrasonic bath before being transferred into silicone spacers and sandwiched between a glass slide and cover slip. To ensure that no evaporation occurred, each side of the coverslip was sealed with vacuum grease. The samples were aged in a temperature-controlled dry bath for 24 hr to reach equilibrium before analysis. The temperature of the sample in the microscope was maintained with a heated stage during analysis.

5.3. Results and discussion

Before attempting to make materials via the nanocasting procedure, we first analyzed the phase behavior of a number of ternary $CTAB/C_8G_1$/water samples using polarized optical microscopy (POM). As an example, Figure 5.2 shows the POM image of a mixture consisting of 50 wt% DIUF water, 40 wt% CTAB, and 10 wt% C_8G_1 at 50 °C after equilibration for 24 hr. Figure 5.2 shows a fanlike texture, which is a typical 2D HCP pattern. The phase behavior study using POM suggests that it may be feasible to prepare materials with 2D HCP structure using the $CTAB/C_8G_1$ compositions investigated here (summarized in Table 5.1).

5.3.1. Nanocasting using $CTAB/C_8G_1$ without NH_3 vapor post-treatment

The nitrogen adsorption isotherms for a series of calcined samples with varying C_8G_1 content are shown in Figure 5.3. In this series, the C_8G_1 content increases from MST-1C through MST-6C. All samples have typical reversible type IV isotherms.[44] A sharp inflection between relative pressure $p/p_0 = 0.1$ and 0.2 corresponds to capillary condensation in uniform mesopores. The sharpness of this step reflects the uniformity

of the mesopores. The inflection point occurs around 0.135 for all samples except MST-6C, whose isotherm shows an inflection at $p/p_0 = 0.116$. The pore size distributions of all samples were calculated from adsorption data using the BJH method with a modified Kelvin equation and the Harkins-Jura equation for film thickness (also known here as KJS pore size distributions).[45,46] The pore size distributions of samples MST-1C through MST-5C are centered around 2.68 nm with a full-width at half-maximum (FWHM) of 1.2 nm. Sample MST-6C also has a narrow pore size distribution, but a smaller pore size of 2.58 nm.

The XRD patterns for this series of calcined samples are shown in Figure 5.4. All of the samples synthesized with different concentrations of C_8G_1 show one intense (100) reflection and weaker (110) and (200) reflections, indicating that the prepared materials contain well-ordered 2D hexagonal close packed (HCP) pores. However, the peak intensity decreases and the higher order (110) and (200) diffractions become less resolved gradually, showing that the mesopore ordering decreases with the increase of C_8G_1 content. This is consistent with C_8G_1 having a higher packing parameter than CTAB, which causes it to favor the formation of a lamellar phase at this temperature.[16] TEM micrographs (Figure 5.5 shows examples for MST1C and MST3C) confirm that the mixed-surfactant-templated silica materials contain well-ordered, 2D HCP pores.

To learn more about the pore structure, we calculate other structure parameters based on the nitrogen adsorption measurements of the calcined materials. Using the methods of Sayari et al.,[47] we obtain the mesopore diameter w_d, primary mesopore volume V_p, total surface area S_t, and external surface area S_{ex} by making and analyzing α_s plots. The standard reduced nitrogen adsorption isotherm data (α_s) for the reference material, LiChrospher Si-1000 silica, are taken from Jaroniec et al.[48] All of the results, with the d_{100} spacings obtained from XRD, are listed in Table 5.2. Some interesting trends emerge in this set of data. The w_d values vary little, and agree with the estimates of pore diameter calculated from the KJS pore size distributions (W_{KJS}), which is consistent with the pores being cylindrical.[46] All of the d_{100} values are smaller than those of MCM-41 synthesized by reaction-induced precipitation under basic conditions.[47] The values decrease from 3.04 to 2.74 nm as the C_8G_1

content increases. The wall thickness decreases monotonically from 0.84 to 0.58 nm as the C_8G_1 content increases. Also, the primary pore volume increases from 0.56 to 0.66 cm^3/g between samples MST-1C and MST-5C. According to Polarz et al.,[49] nanocasting should result in a 1:1 imprint of the organic template. Therefore, we interpret the changes in pore texture between sample MST-1C and MST-5C as being caused by an increase in the number of micelles in the synthesis solution as C_8G_1 is added. The size of the micelles (which determines the pore size) remains constant with even up to 0.3 g C_8G_1 per gram of CTAB. This suggests that C_8G_1 is readily substituted for CTAB in the micelles. The increase in the total surfactant amount increases the micelle number density. This increase explains both the increase in specific pore volume and the decrease in wall thickness as C_8G_1 is added.

5.3.2. Nanocasting using CTAB/C_8G_1 with NH_3 vapor post-treatment

In this section, we compare samples prepared under the same experimental conditions as samples MST-1C through MST-6C, but with the NH_3 vapor post-treatment described in the Experimental section. Figure 5.6 shows the nitrogen adsorption isotherms and pore size distributions for this series (MST-1NC through MST-6NC). Ammonia treatment causes significant changes in both isotherms and pore size distribution. All isotherms are still of type IV, but type H2 triangular hysteresis loops with steep desorption branches begins to appear when the amount of C_8G_1 used exceeds 10% of the amount of CTAB (see sample MST-3NC). The area traced out by the hysteresis loop increases as the C_8G_1 concentration increases. The H2 hysteresis loop is associated with a nonuniform pore diameter, or with branching between pores. Therefore, as more C_8G_1 is used during the synthesis, we find evidence that ammonia treatment causes more distortion of the pores. The pore size distributions also show that the pore diameter and the breadth of the pore size distribution increase with more C_8G_1 in the synthesis solution. The peak pore size (W_{KJS}) increases monotonically, from 3.06 to 4.18 nm, as the C_8G_1 content increases (see Table 5.2). All of these pore sizes are greater than those found in the samples that were not treated with ammonia, but apparently more C_8G_1 allows more distortion to be caused by ammonia treatment.

The XRD patterns for this series of samples are shown in Figure 5.7. The long-

range order is improved after NH_3 vapor treatment, even for those samples with the greatest C_8G_1 contents. The pore texture parameters and d_{100} spacings for this series of samples are given in Table 5.2. As the C_8G_1 content of the materials increases, both the pore size (W_{KJS}) and the primary mesoporous volume (V_p) increase. The pore diameters calculated based on the surface area and pore volume (w_d) and W_{KJS} begin to disagree when the amount of C_8G_1 exceeds 10% of the CTAB amount, which indicates that the pore structure gradually departs from perfect 2D HCP cylinders. The loss of perfect pore uniformity is correlated with the gradual increase in the size of the H2 hysteresis loop in the adsorption isotherms. There are a few possible reasons for the H2 hysteresis loops.[44] One possibility is the partial collapse of pores during ammonia vapor treatment, which would shrink some of the pores into the micropore range. However, we can rule this out because of the absence of any detectable micropore filling at low p/p_0. Another possible reason for the H_2 hysteresis loop is increased pore connectivity.[46] We doubt this interpretation because even the sample with the highest amount of C_8G_1 in this series (MST-6NC) still shows a strong d_{100} peak in the XRD patterns, and long cylindrical pores in the TEM image (Figure 5.5). Therefore, we interpret the H_2 hysteresis loops as coming from variations in pore diameter along the length of the pores. This is a variation of the ink bottle pore shape interpretation, and is consistent with the TEM images (for example, MST-6NC in Figure 5.5).[44,50] This interpretation is consistent with more extensive expansion of the micelles during ammonia treatment of the samples with more C_8G_1. This expansion creates large, axially non-uniform pores.

To learn more about the chemical changes induced by ammonia treatment, we analyzed samples by FTIR. This was in part motivated by the observation that samples containing more than 0.1 g C_8G_1 : 1 g CTAB developed a brown color during NH_3 treatment (discussed more below) which was lost upon calcination. Figure 5.8 shows the infrared spectra for one representative sample (with a surfactant mixture containing 0.2 g C_8G_1 : 1 g CTAB). Bands at 2919 cm^{-1} and 2850 cm^{-1} are attributed to CH_2 asymmetric and symmetrical stretching, respectively, of the mixed surfactants.[51] Bands around 1486 cm^{-1} are attributed to surfactant deformation modes.[52] After calcination, these peaks disappear, showing that surfactants are

removed completely.   The band at 963 cm^{-1} has previously been attributed to the asymmetric CH$_3$-N$^+$ stretch of the surfactant.[53]   The band at 951 cm^{-1} is attributed to Si-OH stretching,[54] and the 963 cm^{-1} band may also be associated with Si-OH. In addition, all three samples exhibit a broad, asymmetric Si-O-Si stretching band at 1020-1090 cm^{-1}.[53] The sharp Si-O-Si stretching peak maxium is shifted and intensified to higher wavenumber, from 1067 to 1069 cm^{-1}, which suggests enhanced sol-gel condensation after ammonia treatment. The appearance of a new siloxane LO$_3$ stretching band[54] at 1233 cm^{-1} after ammonia treatment shows that the condensation of remaining silanol groups in the silicate phase becomes more complete.[53] Also with ammonia treatment, the broad OH stretching band near ~3300 cm^{-1} shifts to ~3500 cm^{-1}, suggesting weaker hydrogen bonding among the hydroxyls.[54,55] This is consistent with increased condensation among the silanols due to ammonia exposure. Aside from the increase in condensation of the siloxane network, no other chemical change can be clearly deduced from the FTIR spectra of the ammonia-treated samples.

Based on the analysis of the ammonia-treated samples in Figs. 5.5-5.8, we determine that ammonia strengthens the silica network by increasing the degree of siloxane condensation, but that with larger amounts of the glucoside surfactant, more pore expansion and greater disorder is introduced. The development of pore shape distortion is correlated with the presence of hysteresis loops. We hypothesize that pore expansion is enhanced by the reaction of NH$_3$ with C$_8$G$_1$ in materials with soft, thin walls. To test this hypothesis, we next examine the effects of the amounts of NH$_3$ and TMOS on the expansion of the pores.

5.3.3. Effect of the amount of ammonia vapor

One representative mixed surfactant composition (0.2 g C$_8$G$_1$: 1 g CTAB) was chosen to investigate of the effect of the amount of NH$_3$ vapor used. Three new samples (MST-7NC through MST-9NC) were synthesized for this purpose. Figure 5.9 shows the nitrogen sorption isotherms and pore size distributions for the series of samples treated using different amount of NH$_3$ vapor (for specific experimental conditions see Table 5.1). Adsorption isotherms clearly show that the occurrence and development of a H2 hysteresis loop are closely related with the amount of NH$_3$ used during post-synthesis treatment. With the smallest amount of ammonia employed in

this series (MST-7NC), no hysteresis loop is found. However, with more ammonia used to treat the as-made materials, the hysteresis loops grow until, at a certain size, the amount of ammonia shows little influence on the size of the hysteresis loop. Paralleling the hysteresis loop development, the pore size distribution shifts towards larger pores and a broader distribution.

These results suggest that both the expansion of the pore size and the gradual condensation of silanol groups proceed at the same time during ammonia post-treatment. Because condensation is slow under acidic conditions, the as-made silica materials have flexible walls which would easily collapse during surfactant extraction. During the post-synthesis treatment described here, NH_3 can interact with the micelles present in the surfactant-rich nanochannels to expand the pores (see below for more discussion of the mechanism). At the same time, ammonia and water adsorb at the silica/surfactant surface, thus increasing the effective pH value and enhancing the condensation rate to solidify the network. The competition between expansion and rigidification induced by ammonia leads to increased expansion until a plateau pore size is reached which is controlled by the silica condensation rate (3.69 nm for the series of sample under study). The XRD patterns for this series of samples (not shown) all show HCP ordering, so the amount of ammonia has little effect on the long-range order of the materials. Table 5.2 shows the other pore texture parameters and the XRD-derived d_{100} spacing.

5.3.4. Effect of the amount of silica precursor

The precursor amount in the system is critical to the formation of an ordered material, especially at a high concentration of surfactants.[56] In the nanocasting procedure, the template assembles with silicates in a concentrated phase in a way that mimics the formation of aqueous liquid crystals. Changing the amount of precursor should be analogous to changing the volume of water used in a liquid crystal. Thus, nanocasting provides a controllable way to study the effect of precursor content on the wall thickness and its effect on the stability of the resulting material.

One representative mixed surfactant composition (0.1 g C_8G_1 : 1 g CTAB) was chosen for the investigation of the effect of precursor content during ammonia treatment. Three new samples were prepared in this series, MST-10NC through MST-

12NC. Figure 5.10 shows the nitrogen adsorption and desorption isotherms and pore size distributions for this series after ammonia treatment and calcination. A smaller amount of precursor leads to a larger hysteresis loop in the samples. The isotherm of the sample prepared with the least amount of precursor (MST-10NC) has a hysteresis loop spanning a large range of relative pressure, which indicates extensive swelling and deformation of the pores caused by pore expansion during ammonia treatment. With the largest amount of precursor (MST-12NC), no indication of a hysteresis loop is found after ammonia treatment. All these results show that the strength of the pore walls can be adjusted by precursor content if correct proportions of precursor, surfactant and water are used. Presumably, less distortion can be associated with thicker (stronger) pore walls. Like the other samples prepared with ammonia treatment, the presence of a hysteresis loop is associated with larger pores and a broader pore size distribution. The x-ray diffraction patterns for this series of samples are shown in Figure 5.11. The sample with the least precursor (MST-10NC) loses its long-range order after ammonia treatment, which is consistent with its adsorption isotherm. For the other two samples, some long-range order is preserved, but not a perfect 2D HCP pattern because the pore shape has been distorted by ammonia treatment. Other structural parameters are listed in Table 5.2.

5.3.5. Mechanism of pore expansion with glucoside surfactant

It has previously been demonstrated that hydrothermal (>100 °C) post-synthesis treatment with ammonia can improve the order and stability of mesoporous materials made with cationic surfactants under acidic conditions.[41] This can be explained by the replacement of weak $S^+X^-I^+$ electrostatic interactions and hydrogen bonding with stronger S^+I^- interactions at the silica-surfactant interface.[41,57] At the same time, hydrothermal ammonia treatment leads to expansion of the pores in the materials for reasons that are not fully understood. The main explanation cited in the literature is increased hydration of silica.[58] Swelling of the micelle cores by ammonia (uncharged NH_3) may play a role similar to the intentional amine swelling reported by Sayari et al.[43] Decomposition of the pore template has also been cited as a cause for extensive swelling for cetylpyridinium chloride templating.[42] However, none of these effects explains why we see a difference in expansion depending on the quantity of C_8G_1

used.

In the present case, we are for the first time exploring the vapor-phase ammonia treatment at a mild temperature of 50 °C of acid-catalyzed materials prepared with mixed surfactant templates. As described above, when CTAB is used as the sole template, post-synthesis ammonia vapor treatment improves the hexagonal order of the meso-structure and slightly increase the pore diameter (around 0.4 nm). There is no indication of the development of a hysteresis loop in the ammonia-treated CTAB sample. However, when sugar-based surfactant C_8G_1 is introduced to the template system, a large increase of pore diameter (up to 1.6 nm), broadening of the pore size distribution, development of a hysteresis loop, and (sometimes) loss of long-range order are observed. The degree of these variations depends strongly on the amounts of C_8G_1, ammonia, and precursor employed. To elucidate the mechanism causing the change of porosity during ammonia vapor treatment, we conducted experiments to test two hypotheses: (1) that because C_8G_1 is non-ionic, the degree of stabilization of the silica-surfactant interface is reduced, allowing the micelles to swell more as CTAB is replaced in the system; and (2) that a reaction analogous to the Maillard reaction occurs, as suggested by the brown color formation after ammonia vapor treatment of the surfactant/silicate composites prepared with more than 0.1 g C_8G_1 per g CTAB.

To test the first hypothesis, we investigated the influence of ammonia vapor treatment on a series of as-made 2D HCP structured materials made with various surfactants, as shown in Table 5.3. Those samples were prepared by nanocasting under the same experimental conditions as the CTAB/C_8G_1 samples in Table 5.1. From Table 5.3, at least three conclusions can be reasonably drawn. First, if a single template is used, whether cationic (CTAB) or non-ionic (Brij56), the pore size expansion is almost the same, only around 0.4 nm. However, when a cationic surfactant (CTAB) and a non-ionic surfactant (Brij56, Brij52, or C_8G_1) are mixed together as templates, the pore size expands more as the amount of nonionic surfactant increases, which indicates that our first hypothesis is correct. Second, when combined with a non-ionic surfactant (C_8G_1) as template, a cationic surfactant (C_nTAB series, n= 10, 12, 16) with a longer tail permits a greater degree of pore

117

expansion. In addition, the type of headgroup on the cationic surfactant influences the degree of pore expansion; a trimethylammonium headgroup (as in $C_{16}TAB$) permits greater expansion than a pyridinium headgroup (as in HPBr). All of these results indicate that the change of physical interactions occurring both inside the core of the micelles and at interfaces between micelles and silicate during ammonia vapor treatment influence the degree of pore expansion. Our experiments do not allow us to directly determine whether NH_3 vapor causes pore expansion by swelling of the cores of the micelles or by expansion near the headgroups. Pure NH_3 is sparingly soluble in n-hexadecane (3 wt% at 30 °C),[59] so although ammonia is usually considered hydrophilic, either expansion mechanism is possible.   Third, when C_8G_1 is combined with a cationic surfactant (C_nTAB or HPBr), significantly greater pore size expansion is observed than for other cationic-nonionic surfactant mixtures (~ 1.6 nm), accompanied with a color change from white to brown and the appearance of a hysteresis loop in the adsorption isotherm. As discussed above, the degree of pore expansion and the size of the hysteresis loop increase with increasing C_8G_1 content. Obviously, all of these changes can not be simply explained by the first hypothesis.

   To test the second hypothesis that a Maillard-like reaction occurs during ammonia vapor treatment of the C_8G_1-containing samples, we analyzed by UV-vis and FTIR spectra of products extracted with ethanol from the as-synthesized samples. Figure 5.12 show the UV-vis absorbance spectra of representative samples extracted from materials prepared with 0.2 g C_8G_1 : 1 g CTAB (MST-5NC) before and after ammonia treatment. A significant increase in absorbance develops in the wavelength range 300-400 nm due to treatment with ammonia vapor. Only a chemical change could be responsible for the change in the absorbance spectrum. The peak occurs in the range associated with aromatic compounds produced by reactions between carbohydrates and amines known collectively as the Maillard reaction.[60] IR spectroscopy also shows evidence of new bands in the "fingerprint" region of the spectrum of the material extracted from the ammonia-treated sample, suggesting that some reaction happened during ammonia vapor treatment. Unfortunately, the infrared bands could not be clearly assigned to one reaction product, but may be associated with a variety of organic groups.

The Maillard reaction was first described as a reaction between reducing sugars and amino acids,[61] but now has been extended to include many other carbohydrate and amine groups. The mechanism of the reaction is quite complex, and involves a series of reactions that yield a multicomponent mixture of organic compounds. The precise mechanism and distribution of reaction products remains an open topic of research in carbohydrate chemistry. However, it is well documented that there are usually volatile heterocyclic compounds formed during the reaction process, such as pyrazines, pyrroles, pyridines, oxazoles and oxalines.[62] Some of these uncharged, low molecular weight organic species would be expected to expand the micelles, leading to the extensive changes in pore structure that we have observed. This mechanism is similar to the mechanism proposed by Yuan et al. for pore expansion of cetylpyridinium chloride-templated materials.[42,47,63] Since the glucopyranoside heagroups of C_8G_1 should be able to react with ammonia to form many types of volatile compounds such as pyrazines, imidazole, furfuryl alcohol etc.,[64] we propose that the Maillard reaction between the sugar-based surfactant C_8G_1 and ammonia vapor at the silica surface causes enhanced pore expansion and the development of hysteresis loops in the nitrogen adsorption isotherms of the samples. This is consistent with all observations in this paper, including an increase in expansion with more C_8G_1, an increase in expansion with more ammonia, and a decrease in pore expansion when a greater amount of precursor is used to make stronger pore walls. Surprisingly, the reaction seems to be facilitated by intimate contact between silica and C_8G_1. Pure C_8G_1 or physical mixtures of MCM-41 with C_8G_1 and CTAB do not develop a brown color upon ammonia vapor treatment at 50 °C. Enhanced adsorption of ammonia at the silanol surface or chemical bonding between silica and the sugar[65] may help to explain the enhancement of the Maillard reaction in silica containing a carbohydrate template.

5.4. Conclusions

A series of siliceous materials with 2D hexagonal close packed mesopores were synthesized using mixed cationic CTAB and nonionic sugar-based surfactant C_8G_1 as templates via the nanocasting method. The effects of ammonia vapor treatment of the as-made samples at a mild temperature (50 °C) was observed. Ammonia vapor

treatment led to retention or improvement of the long-range order among the pores as assessed by x-ray diffraction. It was found not only that the pore diameters were enlarged after ammonia treatment, but that the degree of pore size expansion could be controlled by adjusting the amount of C_8G_1 in the mixed surfactant system. A larger amount of C_8G_1 led to greater pore expansion, but too much expansion led to a loss of pore uniformity. The degree of expansion of the pores could be reduced by using less ammonia vapor or a larger amount of silica precursor. Based on a series of investigations with other nonionic surfactants (Brij56 and Brij52), we conclude that pore expansion is associated not only with a change in the physical interactions between silica and the surfactants, but also with the occurrence of the Maillard reaction between the sugar-based surfactant C_8G_1 and ammonia vapor at the surface of silica. Nonpolar, low-molecular weight byproducts of this reaction would be expected to swell the micelles, leading to the observed expansion of pore size, and in extreme cases, degradation of pore uniformity. Controlled use of the pore expansion of carbohydrate / cationic surfactant mixtures may be useful for tuning mesoporous metal oxides for size exclusion applications. However, if the goal is to preserve the structure templated by carbohydrate-based surfactants, one must be surprisingly cautious to avoid the Maillard reaction even under mild conditions. It is possible that silica catalyzes this sugar transformation reaction.

Table 5.1. Experimental conditions for the synthesis of mixed-surfactant-templated (MST) silica materials. All samples were prepared with 1 g of CTAB and cured at 50 °C.

Sample name	Amount of C_8G_1 (g)	Amount of H_2O (pH=2) (g)	Amount of TMOS (g)	Amount of ammonia (ml)
MST-1C	0	1	1.5	-
MST-2C	0.01	1.01	1.5	-
MST-3C	0.1	1.1	1.6	-
MST-4C	0.15	1.15	1.65	-
MST-5C	0.2	1.2	1.7	-
MST-6C	0.3	1.3	1.8	-
MST-1NC	0	1	1.5	1
MST-2NC	0.01	1.01	1.5	1
MST-3NC	0.1	1.1	1.6	1
MST-4NC	0.15	1.15	1.65	1
MST-5NC	0.2	1.2	1.7	1
MST-6NC	0.3	1.3	1.8	1
MST-7NC	0.2	1.2	1.7	0.5
MST-8NC	0.2	1.2	1.7	2
MST-9NC	0.2	1.2	1.7	2.5
MST-10NC	0.1	1.1	0.80	1.5
MST-11NC	0.1	1.1	1.6	1.5
MST-12NC	0.1	1.1	3.2	1.5

Table 5.2. Structural parameters of the mixed-surfactant-templated silica materials.[a]

Sample Name	d_{100} (nm)	W_{KJS} (nm)	w_d[b] (nm)	V_p[b] (cm^3/gm)	S_t[b] (m^2/gm)	S_{ex}[b] (m^2/gm)	S_{BET} (m^2/gm)	Wall thickness t (nm)
MST-1C	3.04	2.67	2.76	0.57	860	12.5	1390	0.84
MST-2C	2.96	2.67	2.66	0.56	827	12.9	1370	0.75
MST-3C	2.92	2.68	2.66	0.59	860	8.6	1130	0.70
MST-4C	2.90	2.68	2.64	0.59	867	10.8	1170	0.67
MST-5C	2.87	2.68	2.68	0.66	945	3.6	1220	0.63
MST-6C	2.74	2.58	2.47	0.56	866	5.4	1060	0.58
MST-1NC	3.29	3.06	3.14	0.74	864	10.9	1000	0.74
MST-2NC	3.22	3.18	3.08	0.75	809	11.0	914	0.54
MST-3NC	3.25	3.33	3.12	0.76	802	11.9	939	-
MST-4NC	3.34	3.54	3.29	0.87	823	18.1	930	-
MST-5NC	3.27	3.83	3.27	0.97	839	20.3	902	-
MST-6NC	3.34	4.18	3.34	0.96	706	16.7	723	-
MST-7NC	3.15	3.12	3.0	0.74	861	16.9	1060	0.52
MST-8NC	3.34	3.69	3.27	0.85	748	20.4	895	-
MST-9NC	3.37	3.69	3.31	0.87	769	18.6	838	-
MST-10NC	-	3.84	-	0.62	683	119.2	724	-
MST-11NC	3.34	3.7	3.26	0.83	768	18.0	832	-
MST-12NC	3.27	3.39	3.03	0.64	710	10.9	793	-

[a] d_{100} = (100) spacing determined by XRD, W_{KJS} = pore diameter at peak of KJS pore size distribution, w_d = pore diameter calculated from $w_d = 1.213d_{100}(\rho V_p/(1+\rho V_p))^{1/2}$, V_p = primary mesopore volume, S_t = total specific surface area, S_{ex} = external specific surface area, S_{BET} = BET surface area,[66] and $t = (2/\sqrt{3})d_{100}-W_{KJS}$.
[b] Calculated using α_s comparative nitrogen adsorption plots.[47]

Table 5.3. Comparison of characteristics of mesoporous silica prepared
with different surfactants.

Surfactant system (masses used)	Calcined samples				Ammonia vapor treated [a] + calcined samples				
	W_{KJS} (nm)	S_{BET} (m^2/g)	V_p (cm^3/g)	Hysteresis loop?	W_{KJS} (nm)	S_{BET} (m^2/g)	V_p (cm^3/g)	Hysteresis loop?	Color change
C$_{16}$TAB (1)	2.67	1387.1	0.57	no	3.06	1000.9	0.74	no	white →white
Brij56 (1)	3.26	660.7	0.52	no	3.67	647.0	0.60	no	white →white
C$_{16}$TAB/Brij56 [b] (1:0.1)	2.68	891.5	0.47	no	3.04	782.0	0.52	no	white →white
C$_{16}$TAB/Brij56 [b] (1:0.2)	2.68	869.3	0.45	no	3.41	802.5	0.62	no	white →white
C$_{16}$TAB/Brij56 [b] (1:0.3)	2.68	780.0	0.41	no	3.68	837.4	0.78	no	white →white
C$_{16}$TAB/Brij52 [b] (1:0.3)	2.83	770.4	0.48	no	3.53	654.6	0.64	no	white →white
C$_{16}$TAB/C$_8$G$_1$ (1:0.3)	2.58	1059.9	0.56	no	4.18	723.4	0.96	yes	white →brown
C$_{12}$TAB/C$_8$G$_1$ (1:0.3)	2.18	768.1	0.42	no	3.53	714.5	0.78	yes	white →brown
C$_{10}$TAB/C$_8$G$_1$ [c] (1:0.3)	< 2.00	621.7	0.35	no	2.82	839.3	0.63	yes	white →brown
HPBr/C$_8$G$_1$ [d] (1:0.3)	2.68	881.3	0.45	no	3.53	794.0	0.77	yes	white →brown

[a] All samples here were treated with 1 ml of concentrated ammonia as described in the experimental section.
[b] Brij52 and Brij56 = C$_{16}$H$_{33}$O(C$_2$H$_4$O)$_n$H where n ~ 2 and 10, respectively.
[c] For only this sample, no 2D HCP order was detected by XRD before or after ammonia treatment. All other samples had 2D HCP order.
[d] HPBr = Hexadecylpyridinium Bromide.

Cetyltrimethylammonium Bromide (CTAB)
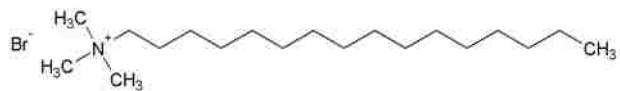
Octyl-β-D-Gluocopyranoside (C₈G₁)
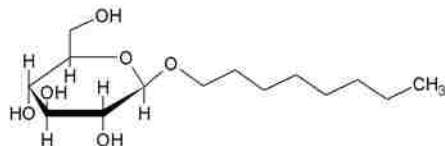
Figure 5.1. Molecular structures of surfactants used for materials synthesis.

Figure 5.2. Polarization contrast optical micrograph of a mixture of 50 wt% water, 40 wt% CTAB and 10 wt% C_8G_1 at 50 °C (200x magnification).
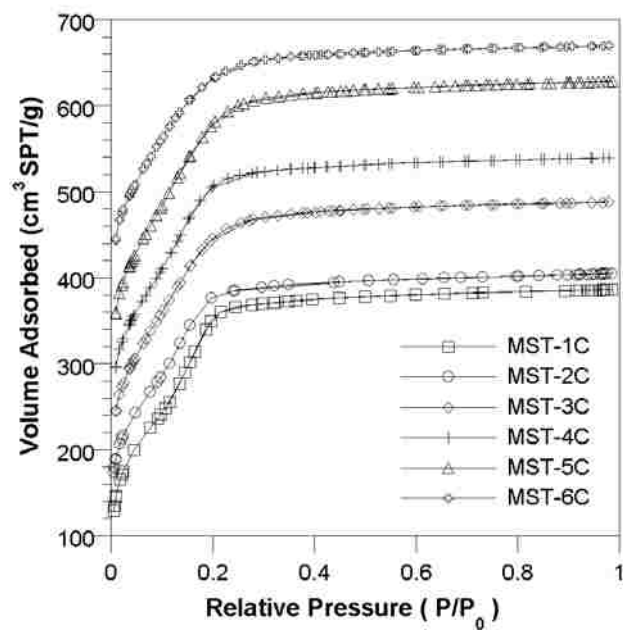
Figure 5.3. Nitrogen adsorption isotherms of calcined MST-#C samples.
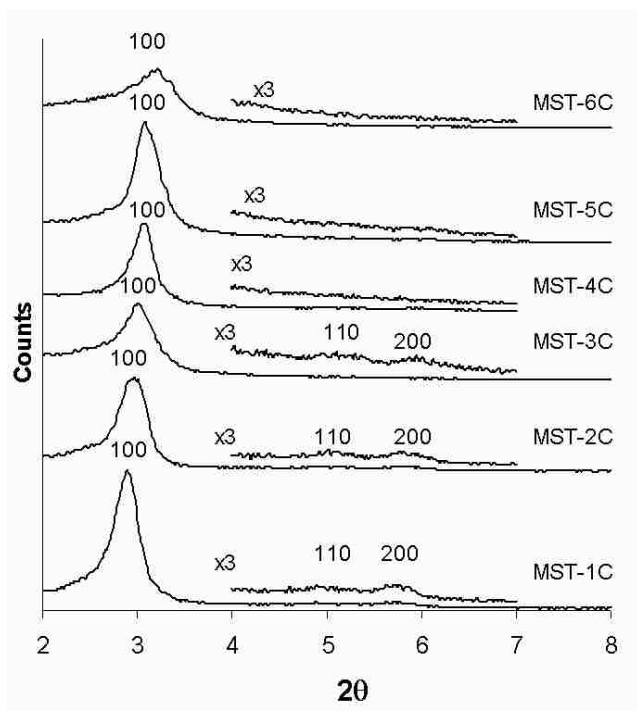
Figure 5.4. X-ray diffraction (XRD) patterns for calcined MST-#C samples.

127
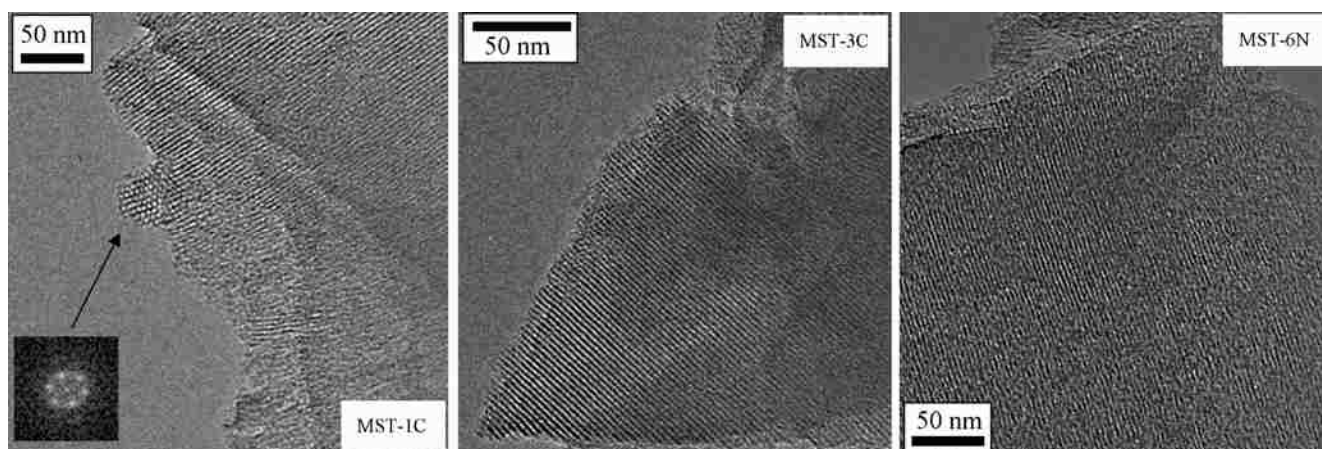
Figure 5.5. Representative transmission electron micrographs of MST series samples after calcination. The inset is a Fourier transform of the indicated region.
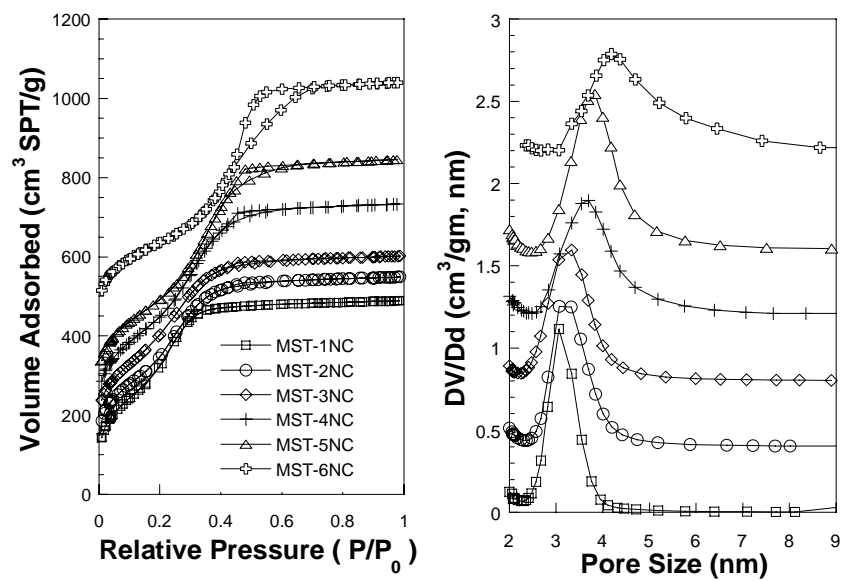
Figure 5.6. (L) Nitrogen adsorption isotherms and (R) KJS pore size distributions of calcined MST-#NC samples after ammonia treatment.
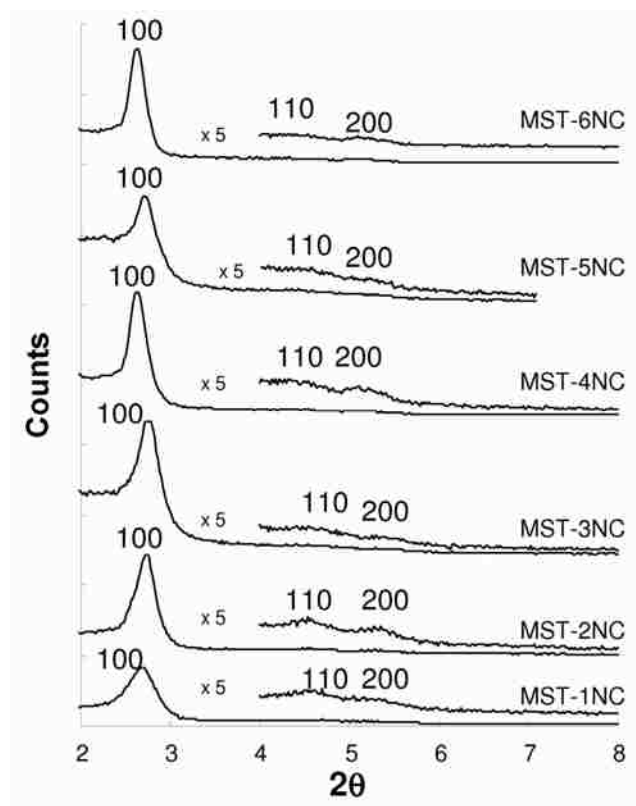
Figure 5.7. XRD patterns for series MST-#NC samples after ammonia treatment and calcination.
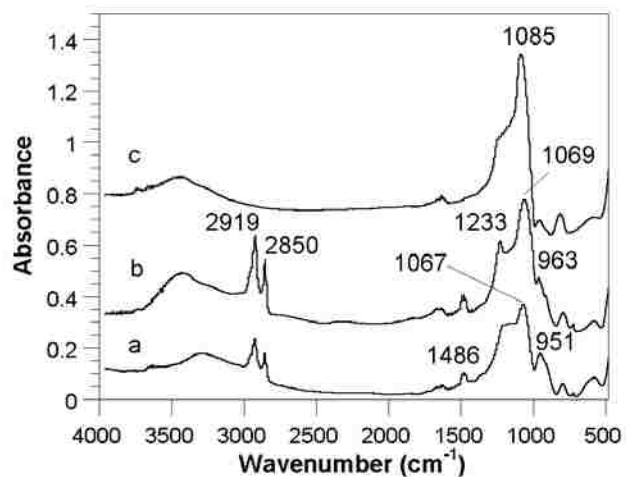
Figure 5.8. FTIR spectra for one representative mixed surfactant composition (1 g CTAB : 0.2 g C_8G_1) (a) as-made material before ammonia treatment, (b) as-made material after ammonia treatment, and (c) mesoporous silica material after calcination.
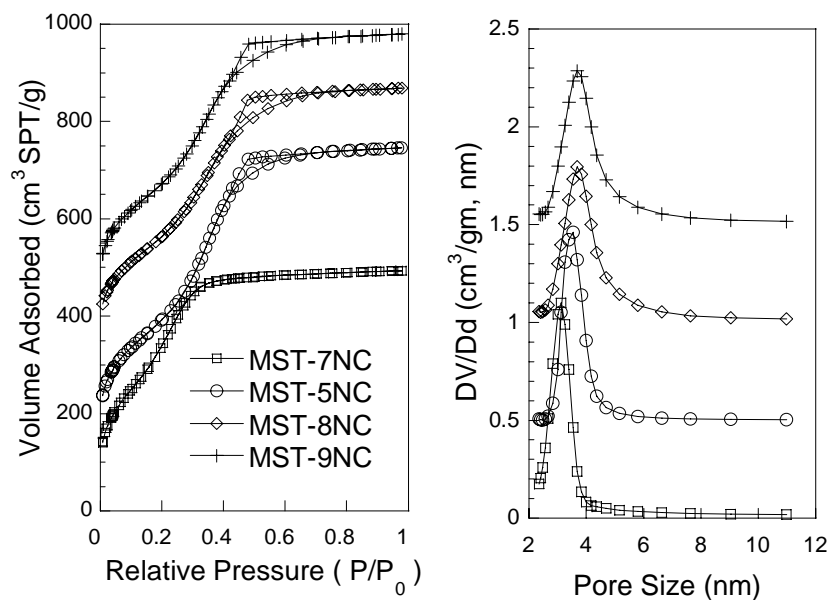
Figure 5.9. (L) Nitrogen adsorption isotherms and (R) KJS pore size distributions for samples treated with different amounts of ammonia (increasing from bottom to top) after calcination.
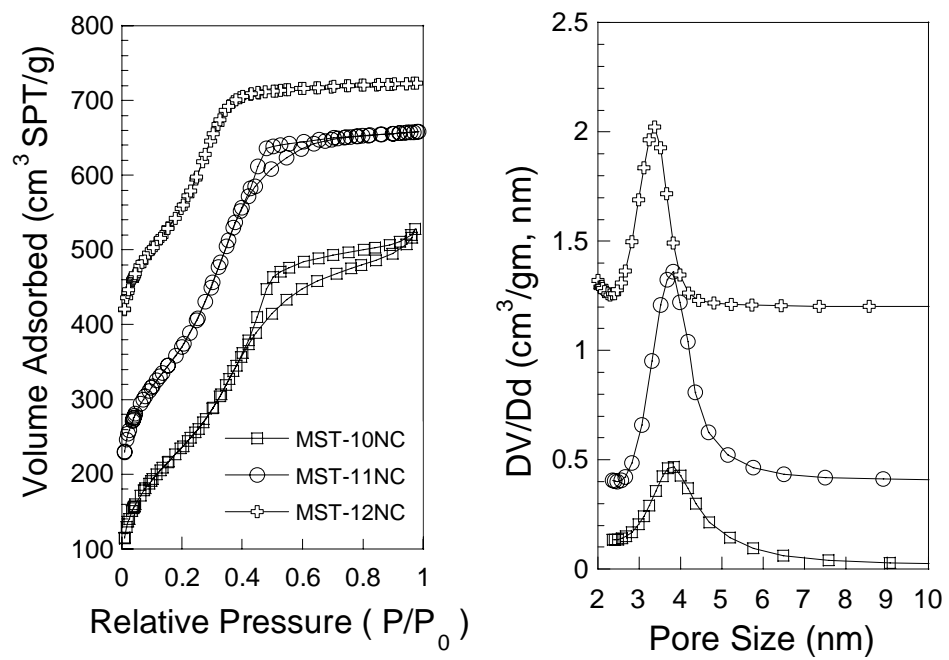
Figure 5.10. (L) Nitrogen adsorption isotherms and (R) KJS pore size distributions for samples synthesized with different amount of precursor (increasing from bottom to top).
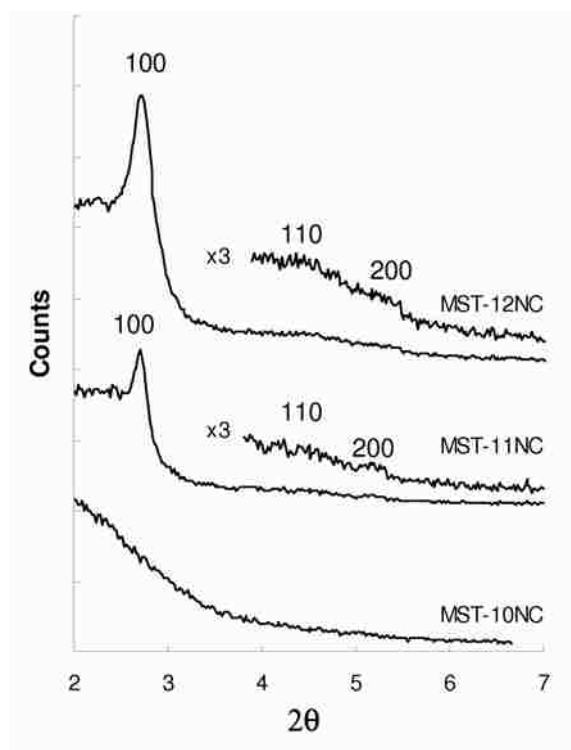
Figure 5.11. XRD patterns for samples synthesized with different amounts of precursor (increasing from bottom to top).
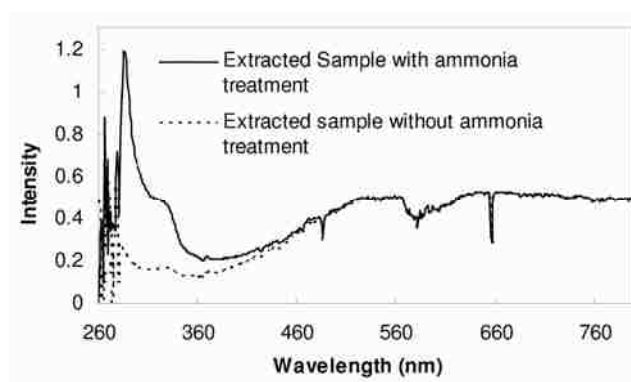
Figure 5.12. The UV-visible absorbance spectra of ethanol solutions extracted from uncalcined materials prepared with 0.2 g C_8G_1 : 1 g CTAB and with or without ammonia treatment.

Chapter 6. Use of the Ternary Phase Diagram of a Mixed Cationic/Glucopyranoside Surfactant System to Predict Mesostructured Silica Synthesis

6.1. Introduction

Since surfactant-templated ordered mesoporous ceramics were first synthesized by Beck, Kresge, and coworkers in 1992,[1,2] organic-inorganic co-assembly combined with sol-gel polymerization has rapidly led to a series of discoveries in materials chemistry, catalysis, chemical sensing, and separations.[3-10] The synthetic pathways to these materials can be classified as either synergistic precipitation or nanocasting. Most mesoporous materials, including the M41S series[1,2], SBA-15 [11,12] and the samples prepared with fluorinated cationic surfactants in our group,[13-15] were prepared by the synergistic precipitation of silica precursors from dilute (< 30 wt%) surfactant solutions. Their mechanism of formation can best be described as co-assembly of surfactants and ceramic precursor into ordered particles.[16,17] Because the ceramic precursors and surfactants partition into a new phase in which they co-assemble, the conditions for formation of different pore structures are divorced from the surfactant phase diagram. In addition, the co-assembled material often undergoes phase transitions as the condensation and charge density of the silica evolve, making the structure of the product difficult to predict.[18]

Nanocasting, first developed by Attard et al.[19], more closely resembles liquid crystal templating. In this process, an ordered surfactant mesophase is pre-assembled, and a metal alkoxide precursor is added and hydrolyzed to generate the ceramic. The alcohol produced by hydrolysis destroys the original order, but by evaporation of the alcohol, it is possible to recover a material that mimics the structure of the original liquid crystal[20-22]. Because the surfactants are present at much greater concentrations than in the precipitation method, the structure of the final nanoscopic pore system can be designed *a priori* based on the corresponding surfactant phase diagram. Because the liquid crystalline structure is actually formed during drying, the method also resembles the evaporation-induced self-assembly process of films and aerosol particles.[23]

Recently, mixed surfactants have begun to be explored for templating mesoporous materials because of their advantages over single surfactants. Mixed surfactant templates has been used in particulate samples to fine-tune pore sizes and wall thickness.[24-27] to

adjust the preferred interfacial curvature of aggregates to produce novel nanoscopically ordered composite materials,[28] to stabilize the mesostructure during thermal treatments,[29] and to synthesize some temperamental intermediate phase structures, such as the Ia3d cubic phase.[29-34] A few examples of nanocasting with mixed surfactants have been reported including hierarchical pores generated with immiscible surfactants[35,36] and pore tuning by adding short-chain alcohols to block polymers.[37]

Here, we will investigate nanocasting using mixtures of the cationic surfactant cetyltrimethylammonium bromide (CTAB) and n-octyl-β-D-glucoside (C_8G_1), whose structures are illustrated in Figure 6.1. Alkyl polygluocosides (C_mG_n, where m is the number of carbon atoms in the akyl chain and n is the number of glucose units in the hydrophilic head group) have not been extensively investigated as pore templates. In general, these surfactants are very hydrophilic because they contain a large number of hydroxyl groups in their headgroup, and should be capable of hydrogen bonding with silica for templating.[38] They are nontoxic and biodegradable, and can be synthesized from renewable resources.[39,40] They show considerable variety in micelle structure and phase behavior based on the anomeric and chiral form of the surfactant, in addition to head group type and alkyl tail length.[39] In addition, there is growing interest in using molecular imprinting methods to prepare porous materials with structure recognition, which transfers specific information from nonionic imprinting molecules into the inorganic framework.[41-43] Polyglucoside surfactants can be considered models of surfactants with complex polar headgroups.

C_8G_1 is a commercially available surfactant and its phase behavior in water has been well characterized.[44,45] Lavrenčič-Štangar and Hüsing reported the first and only attempt to use C_8G_1 as a pore template in mesoporous silica films prepared via dip-coating.[46] However, they found that C_8G_1 favors lamellar products, which is consistent with its large packing parameter. The binary phase diagram of C_8G_1 in water[44,45] has only two narrow hexagonal phase regions, from 28 to 32 wt% and from 59.5 to 70 wt%. However, the hexagonal phase has a melting point of only 23 °C.[47] The binary phase diagram thus predicts that it may be difficult or impossible to prepare hexagonal mesoporous silica at or above room temperature via nanocasting with C_8G_1 alone. However, a mixture of surfactants may be capable of promoting hexagonal ordering. Cortes and Valiente[48]

investigated the effect of a minimal amount of C_8G_1 on the phases of CTAB/glycerol/water at 30.0 ± 0.1 °C, and found that the incorporation of 1 wt% C_8G_1 with CTAB extends the hexagonal phase region significantly. Phase behavior of other CTAB/C_8G_1 mixtures has not been reported. In addition, because C_8G_1 favors cubic and lamellar phases, mixtures with CTAB may extend the composition range available for cubic mesoporous silica synthesis. The binary phase diagram of both C_8G_1/water and CTAB/water have narrow concentration ranges over which the bicontinuous Ia3d cubic phase forms at 50 °C: from 72 wt% to 76 wt %[44,45] and from 77 wt% to 80 wt%, respectively. Such narrow binary concentration ranges of Ia3d cubic phase make it difficult to make mesoporous material by direct liquid crystal templating. Mixing the two surfactants has the potential to have a synergistic effect that would expand the range giving the Ia3d cubic phase in the ternary system with water. If so, we hypothesize that nanocasting will allow bulk Ia3d cubic mesoporous materials synthesis at a mild temperature. The possibility of finding an extended hexagonal phase region with significant amounts of C_8G_1 and the possible existence of Ia3d cubic phase at mild temperature motivate us to investigate the CTAB/C_8G_1 system.

In this chapter, we will present a study of the ternary phase behavior of mixed CTAB/C_8G_1 surfactants in water at 50 °C, and then show that the phase diagram of the ternary system CTAB/C_8G_1/H_2O can indeed be used as a guide to prepare ordered mesoporous materials with different phase structures by nanocasting.

6.2. Experimental section

6.2.1. Materials.

Cetyltrimetylammonium bromide, CTAB (99.0%, Sigma), tetramethyl orthosilicate, TMOS (>99.0%, Sigma), n-Octyl-β-D-glucopyranoside, C_8G_1 (≥99.0%, Fluka), and normalized 0.01 N hydrochloric acid solution (Alfa) were used as received.

6.2.2. Phase diagram determination.

The phase behavior of ternary CTAB/C_8G_1/water mixtures was investigated using an Axioskop microscope with crossed polarizing filters, and images were recorded using a Nikon Coolpix 995 digital camera. Microscope samples were first prepared by weighing the required amounts of surfactants and water into PVC vials which were sealed and homogenized in an ultrasonic bath, then left for equilibration at 50 ± 0.2 °C for at least

one day (and typically one or two weeks depending on the concentration of surfactant) before being transferred into silicone spacers and sandwiched between a glass slide and cover slip. To ensure that no evaporation occurred, each side of the coverslip was sealed with high vacuum grease. The samples were aged in a temperature-controlled dry bath for 24 hr to reach equilibrium before analysis. The temperature of the sample was maintained with a heated stage during analysis.

6.2.3. Mesoporous materials synthesis.

Typically, one point representing a certain composition of mixed surfactants CTAB/C_8G_1 with solvent water was first chosen from the measured ternary phase diagram. The precursor amount required to form the same phase was determined from the following relationship suggested by Alberius, et al. [50],

$$V_{inorg} = V_{H_2O} = \frac{m_{SiO_2}}{\rho_{SiO_2}} + \frac{m_{H_2O}}{\rho_{H_2O}} \quad (6.1)$$

where V_{inorg} is the estimated volume of the nonvolatile inorganic components required in the mixture and V_{H_2O} is the volume of water determined from the weight composition on the ternary CTAB/C_8G_1/Water diagram. m_{H_2O} is the amount of water released during condensation of $Si(OH)_4$ and m_{SiO_2} is the amount of silica formed finally. ρ_{H_2O} and ρ_{SiO_2} are the densities of water (1 g/cm^3) and silica (2.2 g/cm^3), respectively. After the required amounts of CTAB and C_8G_1 was dissolved in 0.01 M aqueous hydrochloric acid at room temperature under vigorous stirring, the mixture was heated at 50 °C for at least 30 min to reach a liquid crystal-like state. Then the required amount of TMOS was added to these mixtures. Hydrolysis with stirring proceeded for 20 min, and then the isotropic and transparent mixture was exposed to a gentle vacuum to remove the methanol. The resulting viscous solution was transferred into a Petri dish to form a film and aged at 50 ± 0.2 °C in a temperature-controlled digital dry bath for at least 48 hr. The surfactant templates were removed by calcination in air at 550 °C for 6 hr. For some samples, in order to clearly identify the phase structure, hydrothermal treatment was used to improve the order of mesoscopical structure by immersing the as-made samples in 1 M NH$_4$OH and heating for 6 hr at 100 °C.

6. 2. 4. Mesoporous materials characterization.

Characterization of the long-range order of the samples was undertaken with a Siemens 5000 X-ray diffractometer using 0.154098 nm Cu-K$_\alpha$ radiation and a graphite monochromator. Nitrogen adsorption-desorption isotherms were obtained at -196 °C using a Micromeritics Tristar 3000 automated adsorption instrument. Typically the samples were degassed at 120 °C for 4 hr prior to analysis. For transmission electron microscopy (TEM), samples were ground and loaded on lacey carbon grids for analysis using a JEOL 2010F instrument at a voltage of 200 kV. FTIR spectra were obtained with a dessicated and sealed ThermoNicolet Nexus 470 infrared spectrometer with a DTGS detector and a nitrogen-purged sample compartment. Samples were finely ground and diluted to 1 wt% with KBr powder before being pressed into translucent pellets with a hand press.

6.3. Results and discussion

6.3.1. Ternary CTAB/C$_8$G$_1$/water phase diagram

Figure 6.2 presents the ternary phase diagram of water/CTAB/C$_8$G$_1$ at 50.0 ± 0.2 °C. We observe regions of isotropic micellar L$_1$ phase, liquid crystalline hexagonal (H$_1$), bicontinuous cubic (Q$_1$) and lamellar (L$_\alpha$) phases, and solid surfactant (S) phase. No biphasic or three phase regions could be identified. The polarization contrast phase textures of three representative samples are shown in Figure 6.3. Figure 6.3a displays an angular fan-like optical pattern, which is characteristic of the defect structure of a hexagonal mesophase.[51] The Maltese cross texture shown in Figure 6.3b is typical of lamellar liquid crystals.[52] Other surfactant solutions in the lamellar region had smooth sand-like or marble-like textures that are also consistent with lamellar phases. Figure 6.3c shows an example of a polarized optical micrograph for hydrated solid surfactant crystals.

Along the binary CTAB/water axis of Figure 6.2, the hexagonal phase first appears at 25 wt% surfactant, in agreement with the precise binary phase diagram reported by Klotz et al.[49] Along the binary C$_8$G$_1$/water axis, the first liquid crystal, an Ia3d cubic phase starts at 72 wt% of surfactant C$_8$G$_1$ and ends at 78 wt%, and the lamellar phase follows until a weight concentration of 90 wt% C$_8$G$_1$. For the binary C$_8$G$_1$/water system, no hexagonal phase is observed. In the ternary phase diagram, the hexagonal phase with the largest amount of C$_8$G$_1$ is formed with 70 wt% of C$_8$G$_1$ with only 3 wt% CTAB. With a

further increase of CTAB content, we find a large region of hexagonal phase. When using polarization contrast optical microscopy to scan the phase behavior of the ternary system, fully dark images were observed within a long narrow stripe spanning from the CTAB/H_2O axis to the C_8G_1/H2O axis of the ternary phase diagram. Considering that this region lies intermediate between the hexagonal region and the birefringent lamellar region, we assign it as a cubic intermediate phase. Though the range of total surfactant concentration range yielding a cubic phase is relatively narrow, the width of the cubic phase region is maximized near 25 wt% C_8G_1 (near sample l) compared to both binary surfactant/water systems, which may be useful in preparing cubic mesoporous materials by nanocasting. The lamellar phase and solid surfactant regions also span across the entire ternary diagram. However, because neither L_α nor solid surfactant phases can be used to prepare stable mesoporous materials, the boundary between these two phases was measured only approximately, and is represented with a dashed line.

In addition to reporting the phase diagram of the ternary cationic surfactant/sugar surfactant/water system shown in Figure 6.2, our aim is to also test the use of this phase diagram to predict the structure of mesoporous silica. We hypothesize that replacing the water at a point corresponding to a composition on the phase diagram with an equivalent volume of silica (see above for calculation method) will yield the same type of structure from acid-catalyzed polycondensation of tetramethoxysilane in a concentrated surfactant solution. We prepared dozens of samples, and always found that the as-synthesized sample corresponded to the expected phase of the ternary surfactant/water system. In other words, if we draw a ternary pseudo-phase diagram for the structure of as-synthesized materials, with wt% of the two surfactants and the water equivalent to the silica as axes, we are not able to distinguish it from the ternary phase diagram in Figure 6.2. Detailed results for just 18 of these samples will be discussed below. However, a red-dashed line is drawn on Figure 6.2 to represent a concentration stability limit obtained from the entire set of material synthesis experiments. On the right side of the limiting line (equivalent to > 70 wt% surfactant), the structure of the as-synthesized materials can not be preserved after either solvent extraction or calcination at 550 °C. To the left of the line, the structure was preserved. This demarcation is found because for samples corresponding to compositions with > 72wt% surfactant, the silica network is too

fragile to withstand either the stress of removing the surfactant and drying the sample, or the decomposition of surfactant and sintering that occur at high temperature. New methods will need to be developed to preserve the structure of such gossamer sol-gel networks. Nevertheless, this study of the ternary phase behavior of CTAB/C_8G_1 suggests that the ternary phase diagram of miscible nonionic/cationic systems may be used to predictively synthesize mesostructured silica/surfactant composites with hexagonal, cubic or lamellar structure via the nanocasting technique.

6.3.2. Synthesis of mesoporous silicate materials

In order to fully demonstrate the feasibility of using the phase diagram in Figure 6.2 for predictive materials synthesis, we prepared two series of samples along different straight lines, each corresponding to keeping the weight concentration of one component constant in the ternary phase diagram (open symbols in Figure 6.2). In addition, several other representative materials which correspond to the ternary composition points located close to phase borders (filled symbols in Figure 6.2) were also prepared as illustrations of how well the mesophase of the silica/surfactant composite is predicted. We first discuss the series of samples lying along a line on the left of the phase diagram.

Samples **a** to **g** have a fixed total concentration of surfactant but differing C_8G_1 content, corresponding to the leftmost line of samples in Figure 6.2. Like all of the samples discussed here, they were synthesized by first preparing an acid-containing liquid crystal, adding TMOS, removing the methanol of hydrolysis, and curing the sample at 50 °C. In this series, the C_8G_1 content increases from sample **a** through sample **g.** Infrared spectroscopy, as shown in Figure 6.4 confirms that mixed surfactants are incorporated into the as-synthesized silica samples, and that calcination at 550 °C removes both surfactants completely. The FTIR spectra of solid crystalline samples of both CTAB and C_8G_1 show several bands in the regions from 3100 cm^{-1} to 2800 cm^{-1} and from 1500 cm^{-1} to 700 cm^{-1}. The former bands are associated with CH_2 vibrations (left shaded region), including CH_2 asymmetric stretching at 2919 cm^{-1} and CH_2 symmetric stretching at 2849 cm^{-1}.[53] The latter bands are associated with other alkyl group vibrations. For the CTAB crystalline surfactant, the most prominent band is close to 1486 cm^{-1} (right shaded region), and is assigned to surfactant deformation modes.[54] After calcination (e.g. Figure 6.4f), all of these bands are absent from the FTIR spectra. The

band at 1063 cm^{-1} is attributed to asymmetric Si-O-Si stretching in a weakly condensed network,[54] and shifts to 1085 cm^{-1} after calcination (Figure 6.4f). In addition to this shift, an apparent shift of the position of this peak from 1063 cm^{-1} to 1077 cm^{-1} in as-made materials is observed as more C_8G_1 is introduced (Figures 6.4c-e). This is most likely due to an overlap of the band from C_8G_1 at 1084 cm^{-1} with the Si-O-Si stretching at 1063 cm^{-1} as more C_8G_1 is introduced. The appearance of peaks at 1370 cm^{-1} (marked with stars) in Figure 6.4e also indicates the incorporation of more C_8G_1 into the as-made silica materials.

The nitrogen adsorption isotherms and pore size distributions for calcined samples **a-g** are shown in Figure 6.5. We can see that all samples have typical reversible type IV isotherms.[55] A sharp inflection between relative pressure p/p$_0$ = 0.1 and 0.2 corresponds to capillary condensation in uniform mesopores. The sharpness of this step reflects the uniformity of the mesopores. The pore size distributions were calculated from adsorption data using the BJH method with a modified Kelvin equation and the Harkins-Jura film thickness equation.[56,57] The pore size distributions of samples **a** through **c** are centered around 2.67 nm, while the samples **d** through **g** are centered around 2.58 nm. The decrease in pore diameter is consistent with the smaller length of the hydrocarbon tail in C_8G_1 compared to CTAB.

The X-ray diffraction patterns for this series of calcined samples are shown in Figure 6.6. All of the samples synthesized with low C_8G_1 content show one intense (100) peak and two weak (110) and (200) peaks, indicating that the prepared materials contain well-ordered 2D HCP patterns. The hexagonal ordering of the samples in this series is confirmed by TEM, as illustrated with samples **a** and **d** in Figure 6.7. However, the peak intensity decreases and the higher order (110) and (200) diffractions become less resolved, suggesting worse mesopore ordering as the C_8G_1 content increases. This phenomenon can be explained by the high packing parameter of C_8G_1, which prevents this surfactant from forming hexagonal phases in binary mixtures with water at this temperature.[44] When the concentration of C_8G_1 increases up to the equivalent of 30 wt% (for sample **g**), the structural order deteriorates. Only one broad (100) peak in the XRD pattern suggests a less ordered hexagonal structure, which may result from a defective hexagonal liquid crystal or threadlike micelle solution. The deterioration in structure

corresponds to the close proximity of the composition of sample **g** to the phase boundary between hexagonal and micellar solution phase. If we further increase the C_8G_1 content along the left-hand line on the phase diagram, only disordered mesoporous silica can be obtained (not shown).

To learn more about the pore structure, we calculated other structure parameters based on the nitrogen adsorption measurements of the calcined materials. By comparing the nitrogen adsorbed on our sample to a macroporous reference material according to the α_s plot method proposed by Sayari et al,[58] we obtain the mesopore diameter w_d, primary mesopore volume V_p, total surface area S_t, and external surface area S_{ex}. The standard reduced nitrogen adsorption isotherm data (α_s) for the reference material, Lichrospher Si-1000 silica, are taken from Jaroniec et al.[59] One representative N_2 adsorption isotherm α_s plot of calcined sample **c** is shown in Figure 6-S-1, and shows that the sample is free of micropores. All other results, together with the d_{100} spacing obtained from XRD, are listed in Table 6.1. Some interesting trends emerge in this set of data. The w_d values vary little, and agree well with the pore diameters estimated from the peak in the pore size distribution (W_{KJS}), which is consistent with the pores being cylindrical.[57] It is worth noting that all the d_{100} values of the silica prepared by nanocasting in acid medium, even for the as-synthesized materials, are smaller than those of MCM-41 synthesized by precipitation under basic conditions,[58] which may be explained by incomplete condensation of the silica walls and large amounts of terminal hydroxyl groups due to the acid-catalyzed sol-gel process. The d_{100} spacing of the hexagonal phase decreases from 3.02 to 2.64 nm as the C_8G_1 content increases. The wall thickness of mesoporous silica materials decreases from 0.84 to 0.47 nm as the C_8G_1 content increases, which indicates the importance of interactions between the silica and the head group on the development of the walls of these materials. The series of materials prepared along the line on the left side of the phase diagram clearly show that the phase diagram developed using POM technique is reliable and can be reasonably used as guidance for predictive material synthesis, although the perfection in the long-range order decreases upon moving towards more C_8G_1 or towards the H_1 phase boundary.

In the lefthand series of materials, the compositions were kept equivalent to a constant level of water at 50 wt%, so the effects of gradually replacing CTAB with C_8G_1

within the hexagonal region of the phase diagram could be examined. A second series of samples was prepared, progressing along the right hand side of the phase diagram (from sample **h** to **n** in Figure 6.2) with compositions corresponding to a fixed CTAB composition of 50 wt%. In this series, the amount of precursor corresponding to the amount of water in the ternary diagram (related by equation 6.1) decreases as the C_8G_1 content increases. In order to completely dissolve the increased amount of total surfactant and to maintain a homogeneous solution before removing methanol, the molar ratio of water to precursor in the synthesis solution had to be increased to 6 for the sample series from **h** through **l,** and to 8 for samples **m** and **n**. The phase diagram suggests that there should be a transition from hexagonal to cubic to lamellar phase materials across this series of samples.

Figure 6.8 shows the nitrogen adsorption isotherms and pore size distributions for the series of sample from **h** through **k.** All samples have typical reversible type IV isotherms, similar to those of samples **a-g**. For samples of **h** and **i**, a sharp inflection corresponding to capillary condensation in uniform mesopores is obvious. With an increase of the C_8G_1 surfactant content in samples **j** and **k**, the inflection becomes less prominent as the capillary condensation is spread out over a larger range of relative pressures, showing that the pore size distribution becomes broader. The pore size distributions calculated from the adsorption branch using the modified BJH method[56,57] show that the pore size decreases significantly with increasing C_8G_1 content in this series. The wall thickness also decreases substantially with an increase of C_8G_1 for samples from **h** through **j** (Table 6.1) which can be explained by the smaller amount of precursor used with increasing C_8G_1 in this series. Figure 6.9 shows the XRD patterns of the as-synthesized and calcined samples from **h** through **k.** For samples **h, i** and **j,** One intense (100) reflection and weak (110) and (200) reflections can be observed, indicating that the prepared materials contain well-ordered 2D hexagonal columnar phase (HCP). Unexpectedly, calcination has little effect on improving the order of the mesostructure, but produces a higher degree of shrinkage (increase in the angle at which the (100) peak appears) with increase of C_8G_1. Two representative TEM micrographs for calcined sample **i** and **j** are shown in Figure 6.10, which confirms that the synthesized materials contain well-ordered, 2D HCP pores. For sample **k,** we can see some differences in the XRD pattern, specifically that

the reflections can not be simply indexed according to 2D HCP structure, but can be reasonably indexed with Ia3d cubic structure. However, the characteristic (220) reflection usually observed for the Ia3d cubic structure is not clear. Considering that the corresponding phase point is located close to the phase boundary between hexagonal and cubic phases, the material obtained at this point could be either transitional or a mixture of hexagonal and cubic domains. For sample **k**, no evidence for mixed phase coexistence could be found by TEM (in spite of extensive searching), and instead only views consistent with the side-view of cylindrical pores could be found. This may be due to a large amount of shrinkage during calcination.

Figure 6.11 presents the calculated d_{100} values of the righthand series of mesoporous silica materials with 2D HCP structure (and for comparison, sample **k** is included although it has mixed phases). Similar to the left-line series of samples, the d_{100} spacing for both as-made and calcined samples decreases with increasing C_8G_1 content, which may be explained by both a reduction in micelle diameter and a decrease of wall thickness with increase of C_8G_1 content. In addition, we find that the C_8G_1 amount has a large effect on the difference in d_{100} spacing between as-made and calcined samples. Considering that the structural order becomes worse after calcination, we conclude that more C_8G_1 content allows more shrinkage to occur. The adverse shrinkage caused by calcination may result from the incomplete condensation of the silica wall in the presence of sugar-based surfactant C_8G_1. Because the C_8G_1 surfactant is very easily hydrated, the reversible condensation reaction may be inhibited by adsorbed water. Incomplete condensation makes the as-made material more vulnerable to shrinkage and pore deformation during calcination. Because the total amount of silica is also reduced along the righthand series of samples, the walls are also thinner, and thus more susceptible to shrinkage. The large degree of shrinkage makes it difficult to preserve the structural order after calcination even when the equivalent weight composition of sugar-based surfactant C_8G_1 is only above 20 wt% (i.e., the equivalent water composition is just below 30 wt%) in the ternary CTAB/C_8G_1/water phase diagram. The black dashed line in Figure 6.2 shows the minimal equivalent weight percentage of water required to prepare stable samples; to the right of this line, the structure can not be preserved after either calcination or solvent extraction.

Bicontinuous cubic phases are usually found as intermediate phases that form over a narrow composition range, which makes it difficult to prepare ordered cubic meso-structured silica thick films. At a high concentration of mixed surfactant, the amount of precursor is very important for the formation of different types of ordered materials. In order to improve the structural order of as-synthesized acid-catalyzed material, we found it necessary to perform ammonia hydrothermal post-treatments on some samples with high concentrations of mixed surfactant templates, including samples **l, m, n, p and r**. Selecting the correct combination of treatment time, ammonia solution concentration and temperature for the treatment is essential. For example, if the time is too long, the structure degrades due to Maillard reactions between ammonia and sugar-based surfactant.[60] If the ammonia concentration is too high, the silica may reorganize and the pores may merge together.

By using the nanocasting method, Ia3d cubic silica / surfactant composite monoliths can be successfully synthesized with mixed surfactants CTAB and C_8G_1 as templates at a mild temperature of 50 °C (compared to the temperatures > 100 °C usually used for hydrothermal synthesis). The XRD powder pattern of sample **l** is depicted in Figure 6.12, which shows some distinguishable Bragg peaks verifying a typical Ia3d cubic phase with unit cell dimension of ~ 87.2 Å (as-synthesized) and ~ 91.6 Å (after ammonia hydrothermal treatment). The increase in unit cell dimension is in good agreement with results reported in the literature.[61] Compared with as-made mesoporous silica material, the long-range order decreases slightly, which can be explained by the Maillard reaction between the C_8G_1 headgroup and ammonia. Previous experiments in our group show that the Maillard reaction causes more pore swelling and pore shape distortion than is caused by physical swelling, which makes the materials lose structure order and pore size uniformity.[60] The TEM images of the as-synthesized sample **l** is shown in Figure 6.13, and is consistent with well-ordered cubic mesostructure. Because the structure can not be preserved after either calcination or extraction, this sample could not be characterized by N_2 adsorption. From TEM images, we can approximately estimate the width of the micelles in as-synthesized sample **l** to be around 2.8 nm.

With further decrease of the precursor content along the right-hand series, the expected lamellar meso-structured material can be synthesized, as shown in Figure 6.14.

The lamellar structure is improved and the d spacing is increased by ammonia hydrothermal post-treatment. For sample **m,** the d_{100} spacing of the as-synthesized thick film is 32.2 Å, and increases to 34.2 Å after ammonia treatment. For the sample **n**, the d spacing increases from 33.7 Å to 34.8 Å. After either calcination or extraction, the lamellar mesostructures collapse. Taken together, the righthand series of materials shows that the ternary phase diagram that we measured can be used for predictive material synthesis of hexagonal, cubic, and lamellar materials by nanocasting.

In the present investigation, a few more representative samples were synthesized based on the ternary phase diagram and fully characterized. We chose four points from the phase diagram close to the H_1-Q_1-L_α boundaries, to emphasize how well phase structure can be predicted from the phase diagram in a mixed surfactant system. All of the XRD results are shown in Figure 6.15. Sample **o** is synthesize by using C_8G_1 surfactant as the sole template, and has the expected XRD powder pattern typical of a lamellar phase. We observed that the material condensed very slowly and the structure improved with time, which may attributed to extensive hydration of sugar based surfactant C_8G_1. The XRD pattern in Figure 6.15 was collected two months after preparing the sample. The phase point corresponding to sample **p** is located in the upper part of the ternary phase diagram, and corresponds to an isotropic phase (by POM) in the ternary surfactant/water system. We could not distinguish whether the phase was isotropic micellar or a cubic phase based on the POM measurements. However, the material corresponding to this phase point clearly has a cubic mesostructure. The as-synthesized sample **p** produces an XRD pattern with two obvious Bragg peaks that can be indexed to (211) and (200) reflections, respectively. The (200) reflection suggests a typical Ia3d cubic phase, though evidence for good long range order is not prominent. The phase point **q** is located near the center of the phase diagram, and represents a hexagonal phase containing a large fraction of C_8G_1. The material synthesized based on this phase point shows a strong (100) peak, and weak (110) and (200) peaks even after ammonia hydrothermal post-synthesis. We found it difficult to isolate a sample with a high degree of long-range HCP ordering even with ammonia post-synthesis treatment, but this may be because C_8G_1 itself causes a higher defect density to be found in the hexagonal phase itself. Sample **r** is a typical hexagonal phase structure with three well-

defined peaks that can be indexed as (100), (110) and (200). These reflections verify the presence of a 2D HCP pattern.

6.4. Conclusions

The ternary phase diagram of CTAB, C_8G_1 and water at 50 °C has been developed by using polarized optical microscope (POM). While the binary C_8G_1 / water system displays no hexagonal phase at this temperature, the ternary phase diagram has a very large region where mixed C_8G_1 and CTAB form hexagonal phases in water. Narrow cubic, lamellar and solid surfactant phases form at compositions spanning the phase diagram from binary C_8G_1 / water to binary CTAB / water.

Mesostructured silica/surfactant composite materials with all of the mesophase structures found in the phase diagram, including 2D hexagonal, Ia3d cubic and lamellar structure, were successfully prepared by using mixed surfactant CTAB/C_8G_1 as structure-directing agents through an acid-catalyzed nanocasting procedure. The calcined samples have high BET surface area, large pore volumes and uniform pore sizes as long as the composition corresponds to the equivalent of at least 30 wt% water. Because less water in the ternary phase diagram translates into less silica (thinner walls) in the materials, materials corresponding to points with <30 wt% water are not stable towards removal of the surfactant templates. In spite of this limitation, the experimental results show that the ternary phase diagram can be used to predict the synthesis of ordered thick mesoporous silica films, and the phase domains over which different types of mesostructured materials are prepared correspond well with those of the ternary phase diagram. The material with a desired phase is made by using enough precursor to produce a volume of silica equivalent to the volume of water at a point on the surfactant / water phase diagram.

Table 6.1. Structure parameters of the mixed-surfactant-templated mesoporous silica materials[a]

Sample name	d_{100} (nm)	w_d (nm)	W_{KJS} (nm)	V_p^b (cm^3/g)	S_t^b (m^2/g)	S_{ex}^b (m^2/g)	S_{BET}^a (m^2/g)	Wall thickness t (nm)
a	3.02	2.66	2.67	0.51	775.5	5.03	995.4	0.84
b	2.89	2.54	2.67	0.51	773.9	4.98	979.0	0.67
c	2.87	2.54	2.68	0.51	782.1	4.88	990.2	0.63
d	2.81	2.47	2.58	0.50	786.4	4.66	967.2	0.66
e	2.68	2.32	2.57	0.47	759.8	4.93	913.9	0.52
f	2.64	2.28	2.58	0.46	752.8	4.88	904.2	0.47
g	-	-	2.58	0.41	694.7	4.48	813.7	-
h	2.90	2.58	2.70	0.47	725.8	6.11	1096.8	0.66
i	2.85	2.61	2.69	0.57	873.2	7.07	996.7	0.63
j	2.66	2.28	2.46	0.45	814.3	5.58	860.3	0.61
k	2.37	1.92	2.12	0.36	761.6	4.44	666.4	0.62

[a] d_{100} = (100) spacing determined by XRD, W_{KJS} = pore diameter at peak of KJS pore size distribution, w_d = pore diameter calculated from $w_d = 1.213d_{100}(\rho V_p/(1+\rho V_p))^{1/2}$, V_p = primary mesopore volume, S_t = total specific surface area, S_{ex} = external specific surface area, S_{BET} = BET surface area,[62] and t = $(2/\sqrt{3})d_{100}$-W_{KJS}.
[b] Calculated using α_s comparative nitrogen adsorption plots.[58]

CTAB

Octyl-β-D-Gluocopyranoside
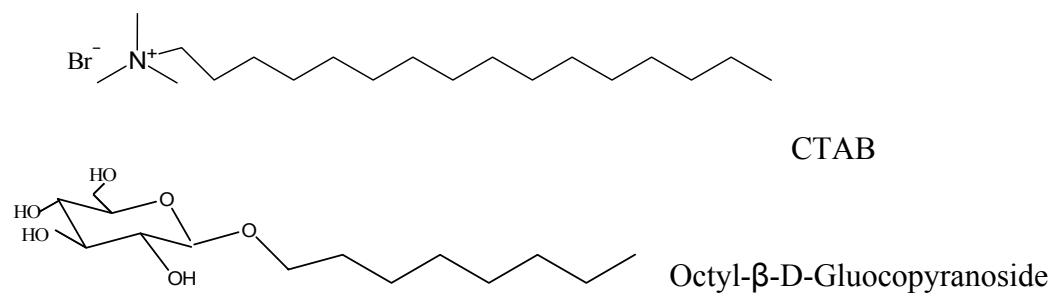
Figure 6.1. Molecular structures of surfactants used for materials synthesis.
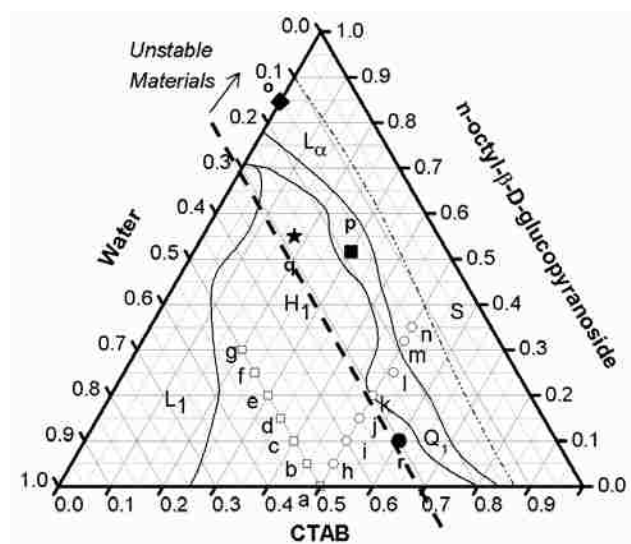
Figure 6.2. Phase diagram for the ternary CTAB/C_8G_1/water system at $50.0 \pm 0.2℃$. Phase notation: L_1 – micellar solution, H_1 – hexagonal phase, Q_1– bicontinuous cubic phase, L_α – lamellar phase and S – solid phase.
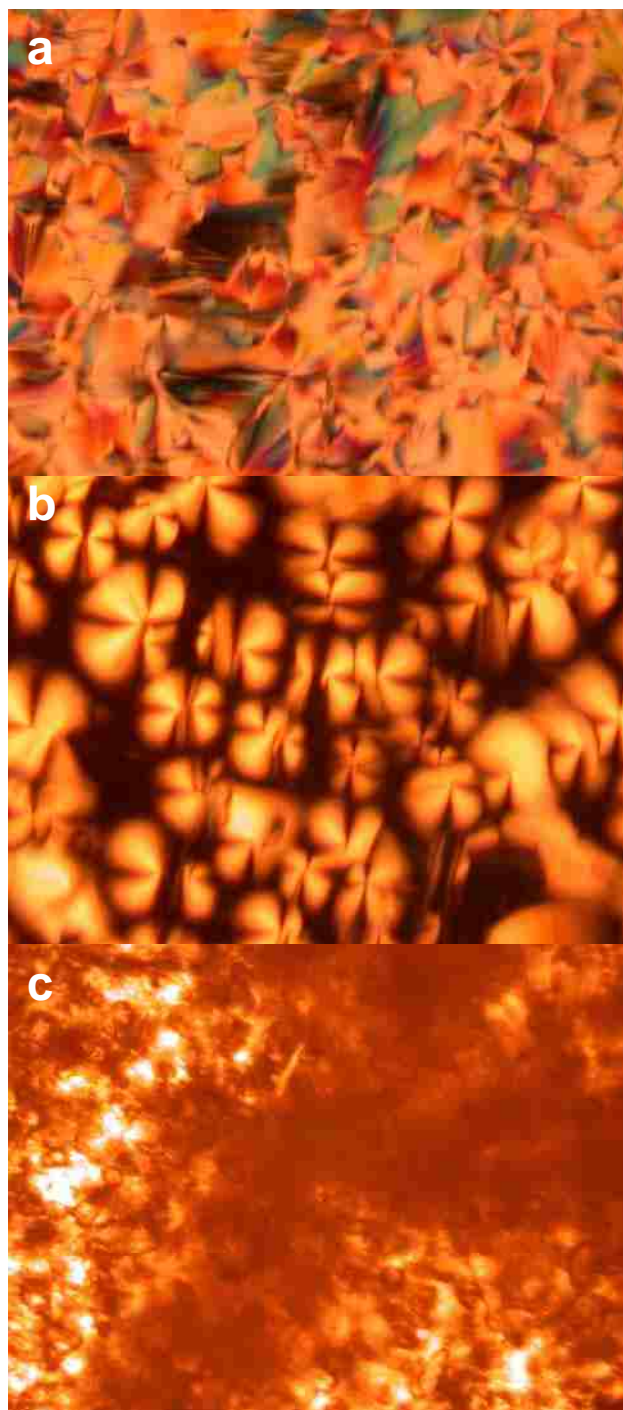
Figure 6.3. Representative cross-polarized optical micrographs for different phases: (a) the fan-shaped texture of the hexagonal liquid crystal with 27 wt% CTAB, 15 wt % C_8G_1, and 58 wt%, H_2O; (b) the typical defect patterns for lamellar liquid crystal with 75 wt% CTAB, 10 wt % C_8G_1 and 15 wt%, H_2O; and (c) the solid surfactant crystal phase with 79 wt% CTAB, 11 wt% C_8G_1 and 10 wt% H_2O. All these textures were viewed at 200x magnification.
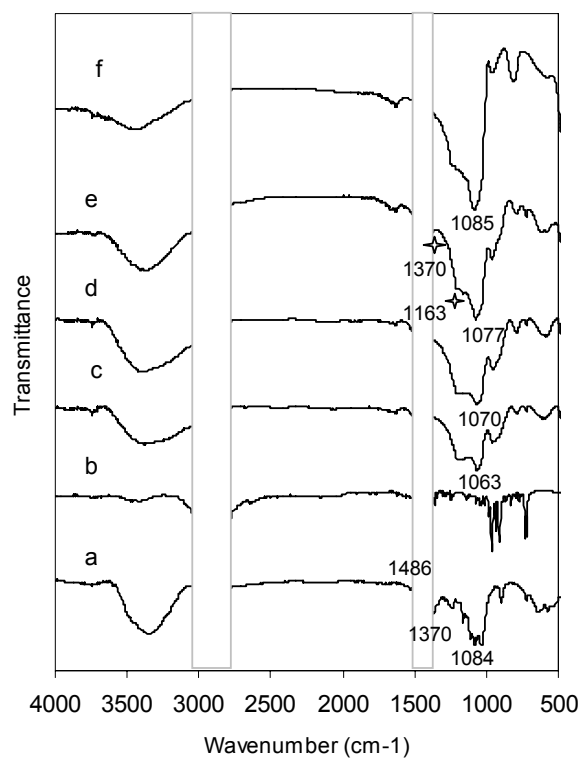
Figure 6.4. FTIR spectra of KBr pellets pressed with 1 wt% of (a) the crystalline surfactant C_8G_1, (b) the crystalline surfactant CTAB, (c) sample **a** as synthesized, (d) sample **d** as synthesized, (e) sample **g** as synthesized, (f) sample **g** after calcination.
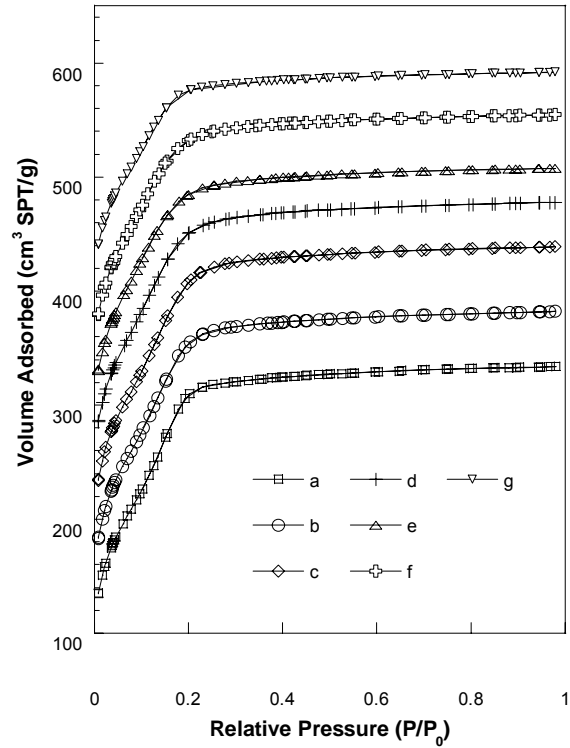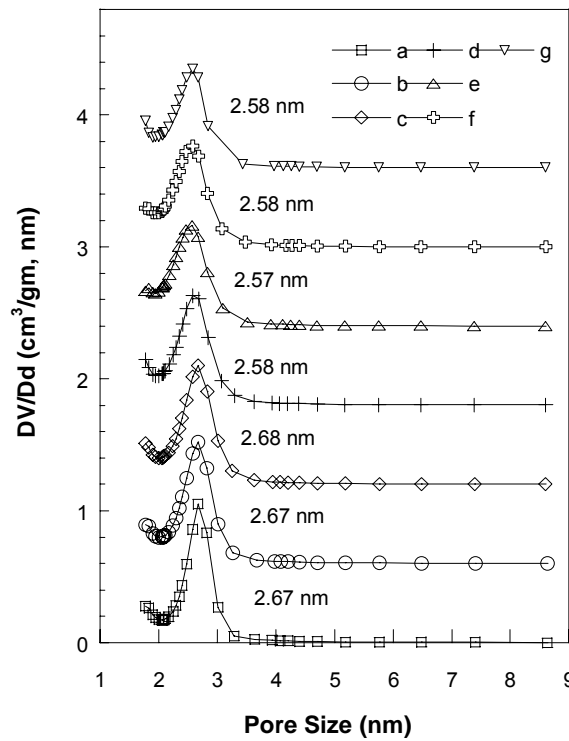
Figure 6.5. (a).Adsorption isotherm for the calcined **a-g** samples and (b) the pore size distribution of the calcined **a-g** samples calculated by the KJS method.
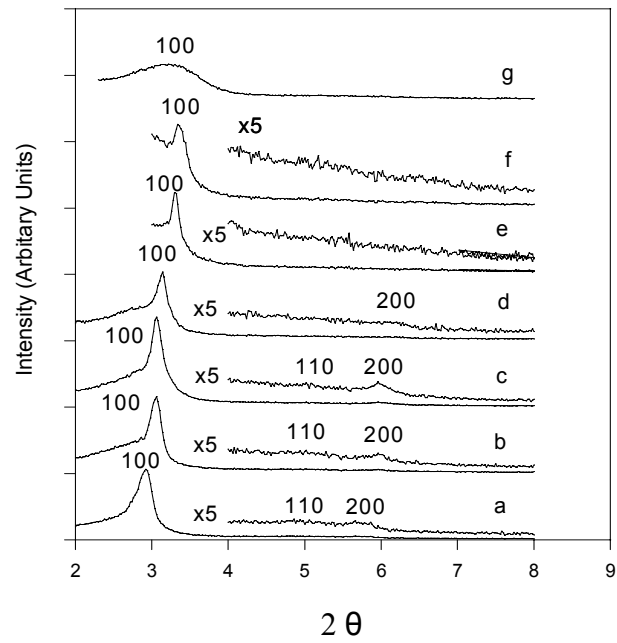
Figure 6.6. XRD results for calcined **a-g** samples.
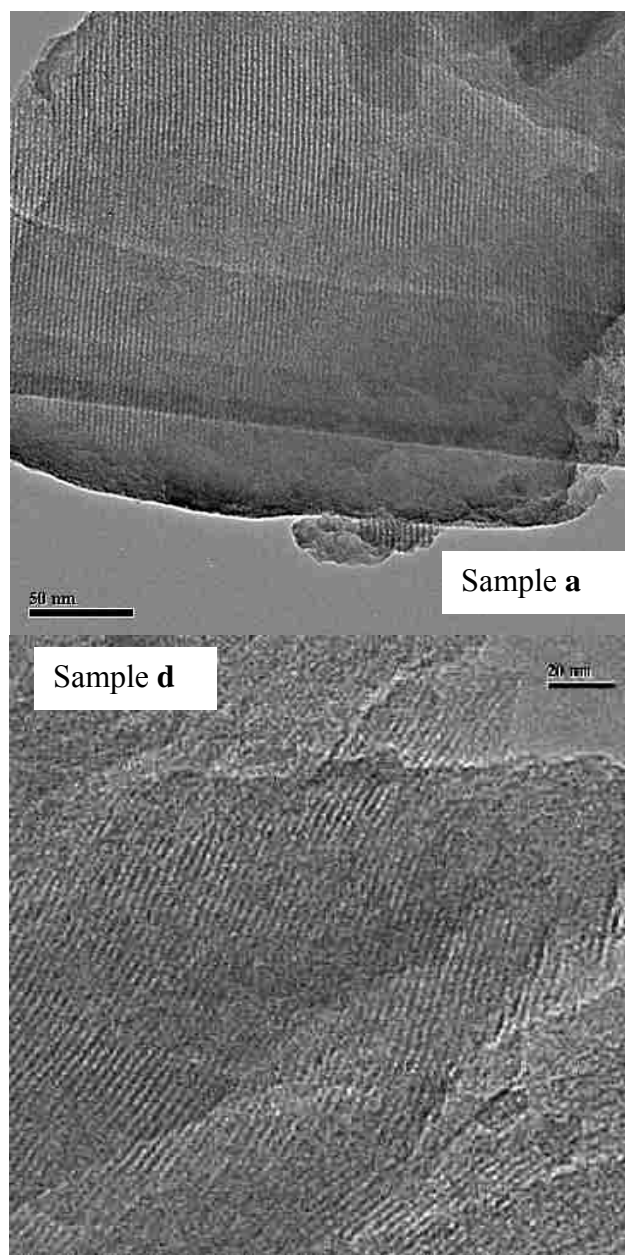
Figure 6.7. Representative transmission electron micrograph of samples **a** and **d**.
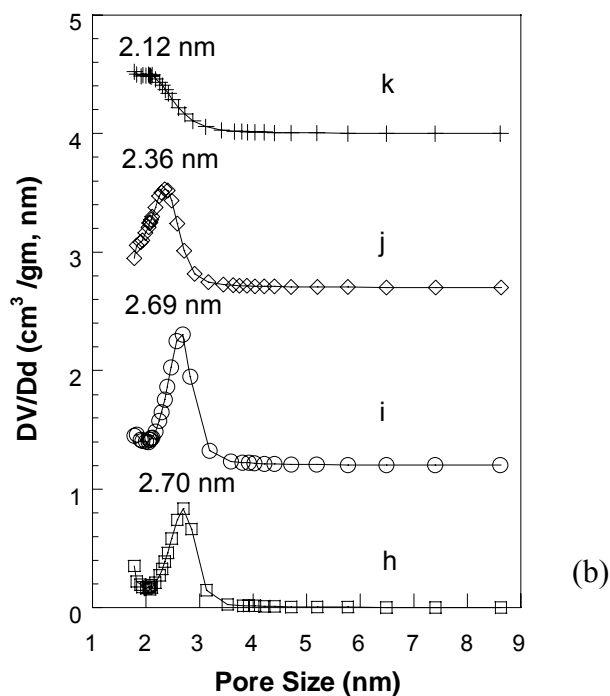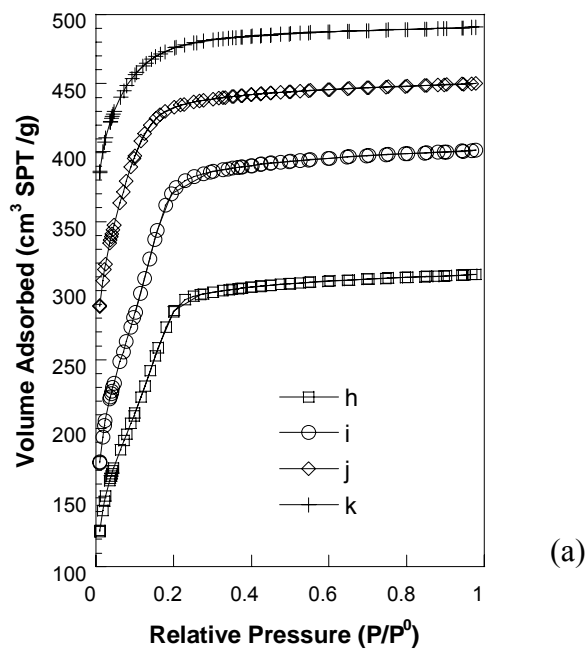
Figure 6.8. (a).Adsorption isotherm for the calcined **h-k** samples. (b). The pore size distribution of the calcined **h-k** samples calculated by the KJS method.
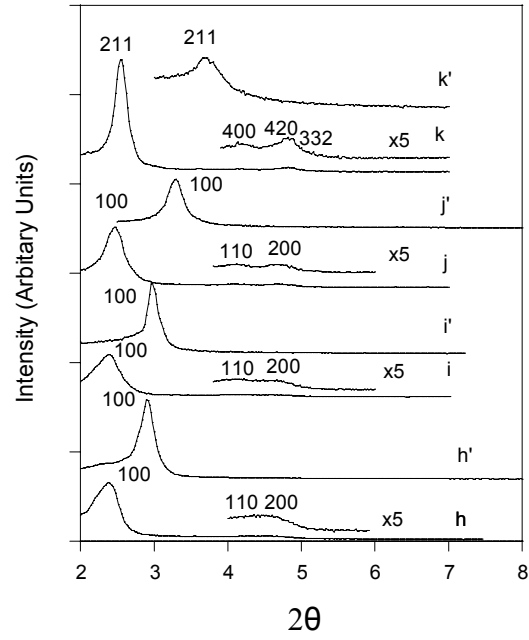
Figure 6.9. XRD results for as-made **h**, **i, j, k** samples and calcined **h', i', j' and k'** samples.
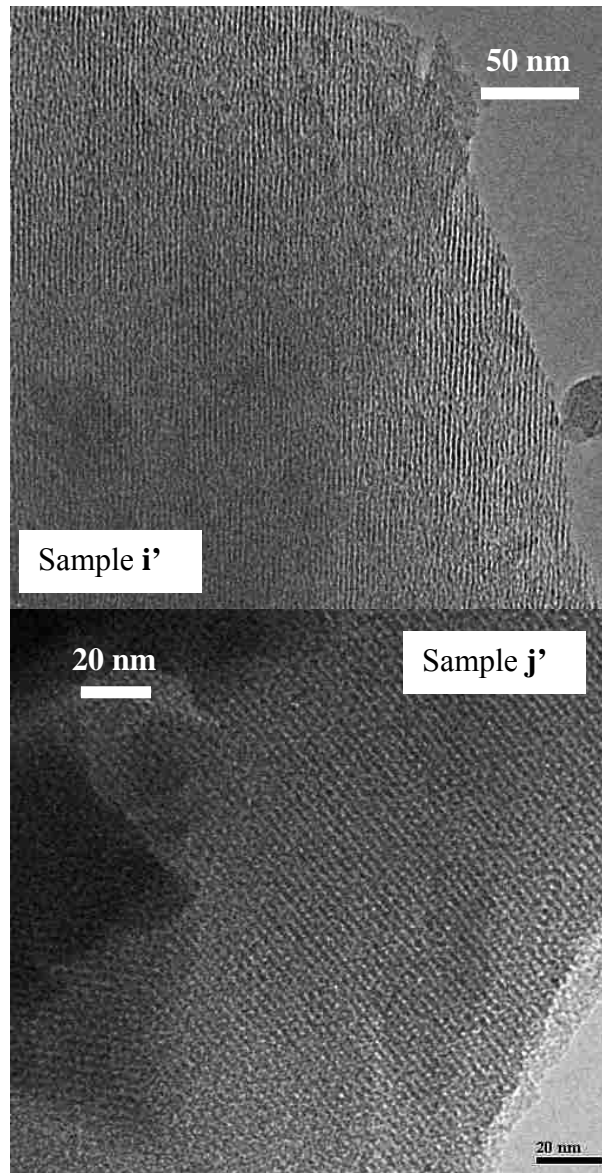
Figure 6.10. Representative transmission electron micrograph of samples **i'** and **j'.**
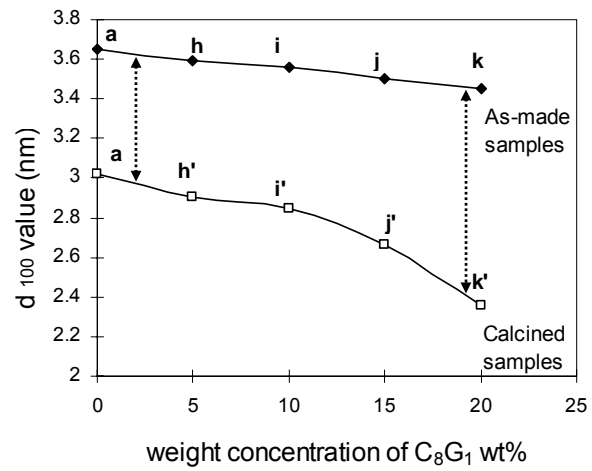
Figure 6.11. The calculated d_{100} value changes with weight concentration of C_8G_1 surfactant.
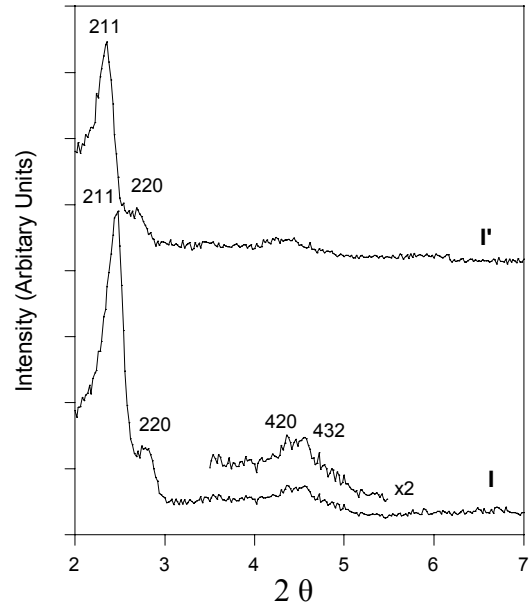
Figure 6.12. XRD results for as-made **l** sample and ammonia hydrothermal post-synthesis calcined **l**'.
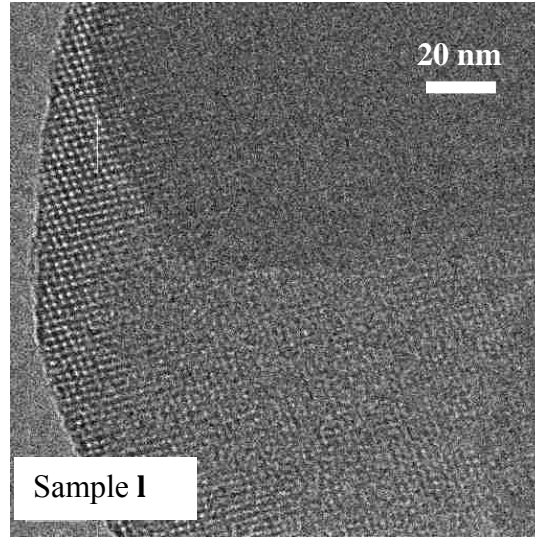
Figure 6.13. Representative transmission electron micrograph of sample **l.**
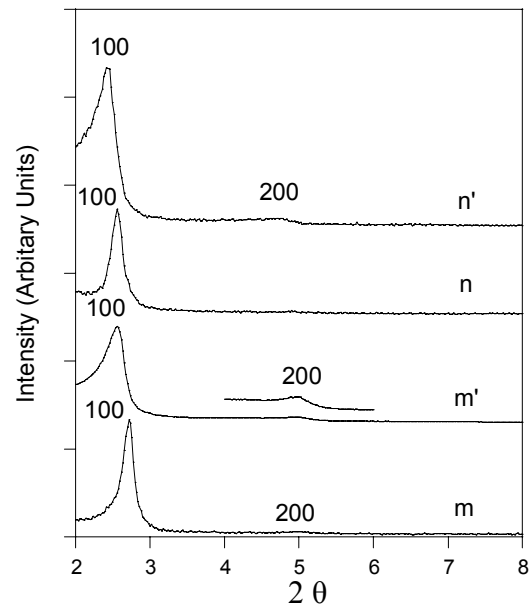
Figure 6.14. XRD results for as-made **m** and **n** samples and ammonia hydrothermal treated samples **m**'and **n**'.
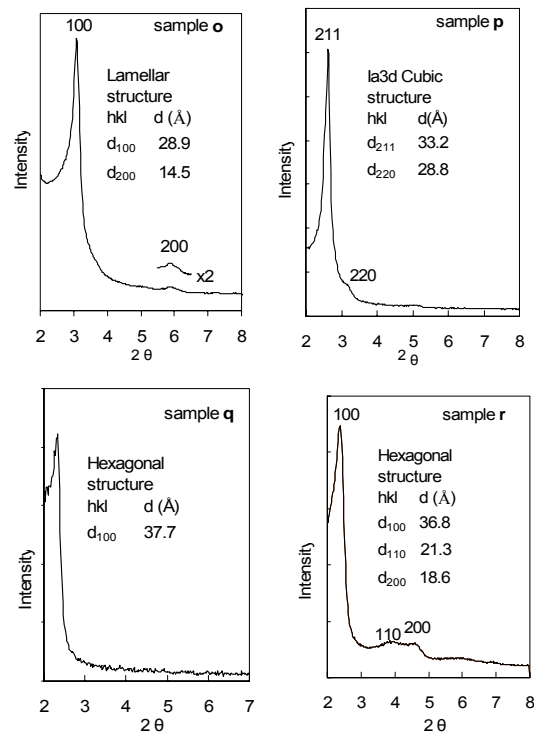
Figure 6.15. XRD for some representative samples of as-synthesized sample **o**, as-synthesized sample **p**, as-synthesized sample **q**, and ammonia hydrothermal treated sample **r**.
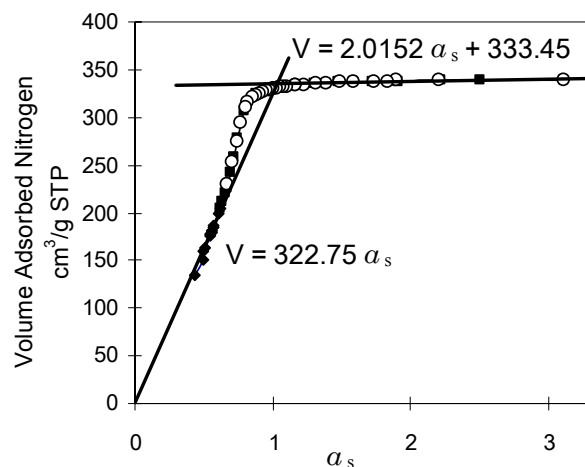
Figure 6-S-1. Representative N_2 adsorption (○) and desortpion (■) isotherm data plotted in the form of an α_s -plot for calcined sample **c**.

Chapter 7. Mixing and Demixing in Combined Hydrocarbon and Fluorocarbon Cationic Surfactant Templating of Mesoporous Silica

7.1. Introduction

Hydrocarbon and fluorocarbon surfactants both are important classes of amphiphiles, and have been widely studied. However, fluorocarbon surfactants have properties that are very different from hydrocarbon surfactants.[1,2] In contrast to the relative soft straight hydrocarbon chain, fluorocarbons prefer a stiff helical conformation because of their torsional potential.[3] Due to the large volume and electronegativity of fluorine compared to hydrogen, fluorocarbon surfactants are characterized by very strong intramolecular C-F bonds and weak intermolecular interactions. These properties give rise to the well-known chemical and thermal stability, low friction, and non-stick properties of polymers such as poly(tetrafluoroethylene).[4] Moreover, fluorocarbon surfactants allow co-solubilization of different solvents with strongly opposed affinities, such as water and perfluoroalkanes.[5,6]

Mixing together colloidal templates creates tremendous opportunities to tune the size, shape, symmetry, and functionality of mesoporous materials. For instance, hierarchically organized porous metal oxides prepared from latex/surfactant mixtures have been developed for adsorption[7], separation[8] and catalysis.[9] Mixing together miscible hydrocarbon surfactant templates for mesoporous ceramics has also been used to tune pore sizes and wall thicknesses,[10] to functionalize the pore surface,[11] and to stabilize otherwise metastable structures.[12,13] Mixture of fluorocarbon and hydrocarbon surfactants have not been utilized as often, but have significant potential for novel templating. Because they are not only severely hydrophobic but also lipophobic, fluorocarbon surfactants do not mix well with hydrocarbon surfactants. Hydrocarbon and fluorocarbon surfactants exhibit non-ideal mixing behavior, which often leads to micelle demixing. The triphasic nature of demixed surfactants in a polar matrix may lead to rich phase behavior analogous to triblock copolymers,[14] or to completely demixed mesophases.[15] In addition, the stiffness of bulky fluorocarbon tails causes fluorocarbon surfactants to prefer aggregates of low curvature (rods and discs) and novel "intermediate" phases which can lead to as-yet unexplored phase behavior.[16] There have been several recent reports of mixed fluorocarbon and block polymer surfactant templating to produce silica with high hydrothermal stability[17] and

generation of hierarchical pore systems.[18,19] Demixed layers of fluorinated surfactants have been used both as hollow macropore templates[20] and for particle morphology control.[21] However, the formation of particles using a combination of cationic surfactants that are both capable of co-assembling with silica into ordered phases has not yet been reported.

In this chapter, we discuss cases in which micelle mixing or demixing occurs in precipitated silica templated with mixed hydrocarbon and fluorocarbon surfactants. We also explore the effects of synthesis parameters, such as molar composition of mixed surfactant, ammonia concentration, salt amount, ethanol concentration and synthesis temperature, on micelle mixing in mesoporous materials prepared using mixed cetyltrimethylammonium chloride (CTAC) and 1H, 1H, 2H, 2H-perfluorodecylpyridinium chloride (HFDePC) surfactants as templates. Both surfactants have similar values of critical micelle concentration (CMC) and the same counter-ion. This pair has been studied extensively in dilute solution, and shown to demix into CTAC-rich micelles and HFDePC-rich micelles in a wide range of compositions.[22] The mesostructured silica formed using this pair of surfactants not only represents a novel approach to the synthesis of hierarchical mesostructure materials, but also demonstrates evidence of micelle demixing in a concentrated solution of silica and surfactant. There have many reports of micelle demixing in dilute hydrocarbon / fluorocarbon surfactant mixtures, but also of mixing in concentrated liquid crystal phases.[23] Blin et al. recently reported a phase diagram with demixed hexagonal liquid crystals in a mixed hydrocarbon / fluorocarbon nonionic surfactant system, but still found that the surfactants mixed during mesorpoous materials synthesis.[15] Here, conditions are found for micelle demixing in hydrocarbon/fluorocarbon surfactant templated silica.

7.2. Experimental section

7.2.1. Materials

The hydrocarbon surfactant CTAC (98%+) and tetraethylorthosilicate, TEOS (98%) were purchased from Sigma. The fluorocarbon surfactant HFDePC was synthesized by alkylation of pyridine with 1H, 1H, 2H, 2H-perfluorodecyl iodide followed by ion exchange, as described previously, and supplied by Dr. Hans Lehmler of the University of Iowa for use in this study.[24] The molecular structures of CTAC and HFDePC are shown in Figure 7.1. Concentrated aqueous ammonia (29 wt% NH_4OH, Merck),

deionized ultra-filtered (DIUF) water, anhydrous ethanol (Aaper Alcohol and Chemical) and NaCl (Merck KGaA) were used for material synthesis. Concentrated aqueous HCl (ACS grade, Fisher Scientific) and anhydrous ethanol were used for surfactant extraction.

7.2.2 Silica materials synthesis

The synthesis of mesoporous silica materials was carried out in dilute solution of CTAC, HFDePC and silica precursor under mild basic conditions. We prepared five series of samples to investigate the effects of key synthetic parameters: the molar composition of the mixed surfactant system, the amount of ammonia, the addition of NaCl, the ethanol concentration and the synthesis temperature. For all the samples discussed in this chapter, the total molar concentration of mixed surfactant was kept constant. The initial molar composition of reactants for the synthesis of silica materials can be generalized as follows: TEOS : H_2O : HFDePC : CTAC : NH_3 : NaCl : C_2H_5OH = 1 : 148 : 0.12x : 0.12(1-x): y : s : z. The specific initial molar ratios of reactants will be described in the following sections. A typical synthesis procedure is as follows: the calculated amounts of CTAC and HFDePC were mixed with DIUF water and concentrated ammonium hydroxide. If needed, the appropriate amount of NaCl or C_2H_5OH was also added at this time. The mixture was vigorously stirred for at least 30 min to completely dissolve and equilibrate the surfactants. The calculated amount of TEOS was then slowly added and the solution was aged for 24 hr at room temperature with gentle stirring (~100 rpm). To allow direct comparison, the size of reactor vessel, the stir bar, stirring speed, mixing time and the TEOS addition speed were kept the same for all of the macroscopically well-mixed samples. The precipitate was isolated by filtration, dried in air, and the mixed surfactants were removed by washing twice with an acidic mixture of 6 % concentrated HCl and 94 % ethanol. The washing time for each step was 24 hr.

7.2.3. Characterization

X-ray diffraction (XRD) patterns were obtained with a Siemens 5000 diffractometer using Cu K_α radiation (λ = 1.54098 Å) and a graphite monochromator. Scanning electron microscopy (SEM) studies were performed on either a Hitachi S-900 or a Hitachi S-3200 microscope. Solid samples were loaded on the PELCO carbon tabs, and then coated with gold under vacuum conditions for SEM imaging. Transmission electron microscope

(TEM) images were collected with a JEOL 2010F electron microscope operating at 200 kV. Solid samples were dispersed in an iso-propanol solution by sonication and then deposited on lacey carbon grids for TEM observation. Nitrogen sorption measurements were performed on a Micromeritics Tristar 3000 system. All samples were degassed at 120 °C for 4 hr under flowing nitrogen prior to measurements. For different types of pore geometries, the pore size distributions (PSD) were calculated using different variants of the Kelvin equation, but always from the adsorption branch of the isotherms. FTIR spectra were obtained with a dessicated and sealed ThermoNicolet Nexus 470 infrared spectrometer with a DTGS detector and a nitrogen-purged sample compartment. Samples were finely ground and diluted to 1 wt% with KBr powder before being pressed into translucent pellets with a hand press.

7.3. Results and discussion

7.3.1. Effect of molar composition of CTAC and HFDePC

A series of samples with different molar ratios of HFDePC to CTAC were synthesized with initial reactant molar ratios of 1 TEOS : 0.12x HFDePC : 0.12(1-x) CTAC : 10 NH_3 : 148 H_2O with x = 0, 1/3, 1/2, 2/3 or 1. The products will be called samples A-1 through A-5 corresponding to the order from x = 0 to x = 1. For comparison with the other series of samples, A-3 is denoted as the base sample.

Infrared spectroscopy, as shown in Figure 7.2, confirms that mixed hydrocarbon and fluorocarbon surfactants are both incorporated into the as-made silica samples, and that both can be extracted finally by acidic alcohol washing. The FTIR transmission spectra of the surfactant reagents, CTAC and HFDePC, show several bands in two regions from 3100 cm^{-1} to 2700 cm^{-1} and from 1500 cm^{-1} to 400 cm^{-1}. For CTAC, The bands at 2920 cm^{-1} and 2850 cm^{-1} are attributed to CH_2 asymmetric and symmetric stretching, respectively.[25] Bands around 1486 cm^{-1} are attributed to CTAC surfactant deformation modes.[26] For HFDePC, the former bands in the range from 3100 cm^{-1} to 2700 cm^{-1} are associated with both C-H stretching in the headgroup of the pyridinium ring and CH_2 stretching in the spacers between pyridinium and the fluorocarbon tail. The latter bands from 1500 cm^{-1} to 1100 cm^{-1} are primarily attributed to C-F vibrations including CF_2 asymmetric stretching at 1246 cm^{-1} and symmetric stretching at 1204 and 1151 cm^{-1}).[27] The intense band at ~ 1490 cm^{-1} is associated with pyridinium. The strongest bands from

CTAC and HFDePC can be clearly resolved in the as-synthesized sample, although they shift slightly compared to the pure compounds (to 2926/2855 cm^{-1} and 1150 cm^{-1}, respectively). After washing twice using acidic alcohol solvent, all the surfactant bands are absent from the FTIR spectra. The band at 959 cm^{-1} is attributed to Si-OH stretching.[28] The sharp band at 1070 cm^{-1} is attributed to asymmetric Si-O-Si stretching[29] and shifts to 1085 cm^{-1} after extraction, which suggests enhanced sol-gel condensation after extraction.

Representative TEM images of this series of samples are compared in Figure 7.3. Sample A-1, prepared with only CTAC, shows ordered domains of perfect 2D hexagonal columnar phase (HCP) cylindrical pores. Both stripe and spot patterns are observed, corresponding to two different views, edge-on and end-on, respectively. This sample shows predominantly rough round particle morphology in the TEM images. Sample A-2, prepared with almost equal weight of HFDePC and CTAC, also shows large domains of ordered cylindrical pores similar to sample A-1. However, some hollow cells with sizes on the order of tens of nanometers are formed in this sample, and the hollow cells appear to be captured within larger particles to form a bimodal pore structure. Similar hollow cells were reported previously when just dilute HFDePC was used as a template under similar conditions. Based on TEM studies[30,31], the formation mechanism of hollow cells was proposed to be coalescence of individual vesicle-like hollow silica particles. If only CTAC surfactant is employed as a template, there are no vesicle-like hollow cells formed under similar conditions.[32] The formation of co-existing domains of 2D HCP phase and vesicle-like hollow cells suggests that CTAC and HFDePC do not mix when they are combined together with equal weight fraction. The demixed structure of sample A-2 suggests that there exist two populations of cationic micelles composed of CTA$^+$-rich and HFDePy$^+$-rich surfactant in bulk solution, as reported by Almgren et al.[22] After precursor is added, CTA$^+$-rich and HFDePy$^+$-rich micelles co-assemble with silicate species separately and precipitate to form particles with bimodal pores. In this sample, most particles are found by TEM to be round with hollow cells incorporated. There are also some elongated particles identified in low magnification TEM of this sample as shown in Figure 7.3. Further increase of the molar fraction of HFDePC in sample A-3 leads to primarily elongated particles containing a large number density of hollow cells. Multiple

distinct hollow cells captured within individual particles are highly curved and self-assembled along their axes. The increase of number density of hollow cells corresponds with the increased molar fraction of HFDePC, consistent with the idea that hollow cells form by merging together of vesicle-like silica particles templated by HFDePy$^+$-rich surfactants. In this sample, CTA$^+$-rich templated silica particles exhibit less-ordered mesopore structure than that of sample A-2, and some regions with deformed 2D HCP and even wormhole-like mesopores are found as shown in Figure 7.3. This observation suggests that CTA$^+$-rich templated mesopores follow the tendency of cetyltrimethylammonium salt to go from lamellar to hexagonal to wormhole-like phases as the surfactant concentration decreases.[33,34] Increasing the molar fraction of HFDePC to 2/3 in sample A-4 leads to particles possessing disordered mesopores. No hollow cells are found in this sample by TEM, and all particles have irregular shape. Interestingly, although the sample is disordered, there is no evidence of demixed domains in this sample even after extensive searching. The TEM results suggest that hydrocarbon CTA$^+$ surfactant molecules have some degree of solubility with HFDePy$^+$-rich micelles. This result is similar to the report by Asakawa, et al.[22], who theoretically predicted a solubility of about 17 mol % CTAC in HFDePC micelles when the total concentration was above the second CMC, 2.6 mM. In addition, the structure of final materials seems to be governed by HFDePy$^+$ micelles in this sample because the disordered channel arrangement follows the phase transition sequence of HFDePC templated mesostructures from vesicular to disordered particles as the HFDePC concentration increases.[31] Sample A-5, prepared with HFDePC alone, shows elongated particles with random mesh phase structure. The uniform mesopores orient perpendicular to the particle axis. The structure of sample A-5 is consistent with the detailed characterization reported by Tan et al.[24]

Some representative SEM images of the A-x series samples are shown in Figure 7.4. The particle size dramatically decreases from micrometer to nanometer scale as the molar fraction of HFDePC increases, which can be explained by the fact that HFDePC has higher surface activity than that of CTAC. At 25 °C, the surface tensions of HFDePC and CTAC above their CMC are 26.1 and 42.3 mN/m, respectively.[22] As a consequence, the addition of fluorocarbon surfactant in template favors the formation of small silica particles. In addition, sample A-1 consists of predominantly rough spherical particles,

while sample A-3 contains a mix of spherical and elongated particles. With a further increase of HFDePC in sample A-5, only small elongated particles with uniform size are found.

The XRD patterns for this series of extracted samples are shown in Figure 7.5. Samples A-1 and A-2 show three well-resolved intense peaks that are indexed to (100), (110) and (200) diffractions of 2D HCP silica, and one weak peak indexed to (210) diffraction. These diffraction peaks indicate that A-1 and A-2 both contain long-range ordered 2D HCP structure. For these two samples, synthesized with low molar fraction of HFDePC surfactant, the XRD patterns of final materials are governed by CTA^+-rich/silica aggregates. With increasing the molar fraction of HFDePC in the template to sample A-3, the material displays low angle XRD patterns with one strong peak and one broad signal of relatively low intensity, which can be attributed to the (100) and overlapping (110) and (200) reflections of a 2D HCP pattern, respectively. The XRD pattern in sample A-3 indicates the order of the original hexagonal phase structure degrades, which can be understood with the aid of TEM images showing the formation of deformed 2D HCP and wormhole-like mesopores. Sample A-4 exhibits no reflections, consistent with the disordered structure observed by TEM (see above). Further increasing the molar fraction of HFDePC causes a gradual transition from a disordered structure to a random mesh phase. At x = 5/6, we can see only one intense reflection in XRD (not shown). At x = 0.95, we can see two reflections in XRD (not shown) similar to sample A-5. The XRD patterns of sample A-5 show one intense peak of (001) diffraction and one weak (002) diffraction peak from the mesh phase. We expect there to be one pillar peak for the random mesh phase below 2θ of 1.6, which can not be observed because of instrumental limitations. The results of XRD and TEM both confirm that this sample has a random mesh phase similar to the previous result reported by our group.[24] XRD indicates that the pore structure of the final materials undergoes a transition from hexagonal to disordered 2D HCP to disorder to random mesh phase as the molar fraction of HFDePC increases.

Nitrogen sorption isotherm plots and pore size distributions of this series of samples are shown in Figure 7.5. All samples have typical reversible type IV isotherms as defined by IUPAC[35], indicating uniform mesopores for all samples in this series. As the molar

fraction of HFDePC increases, a small H3 type hysteresis loop appears in sample A-2, and enlarges to maximum size in sample A-3, then reduces in sample A-4 and A-5. The size of the hysteresis loop correlates with the number density of hollow cells observed by TEM. The upturn at high relative pressure also becomes stronger as the molar fraction of HFDePC increases, indicating that the textural porosity between clusters of particle is enhanced. The increase of textural porosity reflects the formation of smaller and more elongated particles. In addition, the inflection points corresponding to capillary condensation in mesopores shift to lower relative pressure as the molar fraction of HFDePC increases. For sample A-4, the pore size distribution was calculated using the traditional BJH method.[36] For sample of A-1, A-2, A-3 and A-5, the pore size distributions were calculated using BJH method with modified Kelvin equation and the Harkins-Jura equation for film thickness (also known here as KJS pore size distributions).[37] The first three samples have 2D HCP mesophase, so their pore size distributions were calculated assuming cylindrical pore geometry. Because sample A-5 has random mesh phase structure, the pore size distribution was calculated assuming slit pores. The results are shown in Figure 7.5b. For the first three samples, one peak in the PSDs around 3.7 nm is present, suggesting that the mesopore size is governed by CTAC micelles when the molar fraction of HFDePC is less than or equal to 1/2. For sample A-4 and A-5, the pore size dramatically decreases suggesting that the pore size is governed by HFDePy$^+$ micelles. In addition, the peaks in the PSDs for this series of samples become broader as more fluorinated surfactant is introduced. To learn more about the structure, we calculated other structure parameters based on the nitrogen adsorption measurements of extracted materials. Using the method developed by Sayari et al.[38] we obtain the primary mesopore volume V_p, total surface area S_t and external surface area S_{ex} by making and analyzing α_s plots. The standard reduced nitrogen adsorption isotherm data (α_s) for the reference material, LiChrospher Si-1000 silica, are taken from Jaroniec et al.[39] All of the results are listed in Table 7.1. The mesopore volume and S_{BET} in sample A-4 are minimized (for this series of samples) due to its disordered pore structure.

From this series of samples, we find that different phases or mixture of phases can be obtained when the molar ratio of mixed surfactants are varied. The external surface area and the adsorption in textural pores at high relative pressure depend on the particle

size. An unusual transition sequence of pore structure from hexagonal to wormhole-like to disordered to random mesh phase is observed as the molar fraction of HFDePC increases. For pores templated by CTA^+-rich aggregates, the transition of mesopore structure is from ordered hexagonal to wormhole-like to disordered structure as the CTA^+ concentration decreases, which exactly follows the phase behavior of mesoporous materials templated with only CTA^+ salts. For pores templated by $HFDePy^+$-rich aggregates, an unusual sequence from close-packed cylinders to vesicular to disordered pores to mesh-phase is observed, which differs the usual transitions seen during HFDePC surfactant templating[31]. The difference is that a disordered structure forms before a random mesh phase with increasing mole fraction of HFDePC in the mixed template system, which may be caused by repulsive hydrocarbon-fluorocarbon interactions.

7.3.2. Ammonia concentration effect

A series of samples was synthesized to investigate the effect of ammonia concentration. The reactants had the initial molar ratios 1 TEOS : 0.06 HFDePC : 0.06 CTAC : y NH_3 : 148 H_2O with y = 5, 10 and 15 for samples B-1, B-2 and B-3, respectively. Sample B-2 is the base sample in this series.

Powder XRD patterns of this series of samples after extraction are shown in Figure 7.7. The pattern of sample B-1, synthesized at the lowest ammonia concentration, shows two strong diffractions and one weak diffraction. Together with nitrogen adsorption isotherm and TEM results (see below), this pattern is interpreted as co-existing domains of deformed 2D HCP and wormhole-like phase. The three diffractions in this sample can be indexed from left to right as (100), (**001**) and (110). The (100) and (110) diffractions come from deformed 2D HCP phase templated by CTA^+-rich surfactant, while the (**001**) diffraction comes from a wormhole phase templated by $HFDePy^+$-rich surfactant. With more ammonia in the synthesis solution (sample B-2), the XRD pattern shows one strong diffraction of (100) and one broad peak including (110) and (210) diffractions of the HCP phase. Further increase of ammonia (sample B-3) yields a product with at least six distinct reflections, indicating a novel two- or three dimensional pore structure. An initial hypothesis was that three-dimensional $Pm\overline{3}n$ cubic structure might have formed in this sample, given that the mixed CTAC/HFDePC surfactant system can produce samples with $Pm\overline{3}n$ cubic structure in concentrated acid-catalyzed solutions (unpublished results).

However, careful XRD indexing, N_2 adsorption isotherm and STEM analysis together rule out this possibility and suggest that the structure consists of co-existing but highly ordered phases. Four peaks are indexed as (100), (110), (200) and (210) reflections from a 2D HCP phase with a unit cell parameter of a = 4.4 nm. The first reflection to the left of (100) is interpreted as a characteristic diffraction from silica micropillars between layers[22] in a random mesh phase, and the shoulder to the right of (100) is indexed as the (**001**) reflection from mesh phase layers with a layer spacing of 3.3 nm. However, the (**002**) diffraction supposed from mesh phase can not be clearly resolved because it overlaps with the (210) reflection. Because no more reflections could be found to indicate a periodic 3-dimensional arrangement of silica micropillars into an ordered mesh phase, we assign the (**001**) and low-angle pillar reflections to a random mesh phase. The set of reflections for sample B-3 could not be indexed to any other single known mesophase.

Nitrogen sorption isotherms for this series of extracted samples are shown in Figure 7.8a. All samples have type IV with upturns at high relative pressure. In contrast to sample B-1 and B-3, sample B-2 shows a hysteresis loop, indicating the formation of non-uniformly mesoporous materials. For sample B-3, two distinct capillary condensation steps can be observed under relative pressure (P/P_o) ranging from 0.12 to 0.25 and 0.32 to 0.4, which indicates a bimodal pore size distribution. The pore size distributions (PSDs) of this series of samples were calculated by the KJS method. For sample B-1 and B-2, cylindrical pore geometry was assumed in the PSD calculation. For sample B-3, because XRD indicates the co-existence of two different types of pore geometries, i.e. slit pores and cylindrical pores, we calculated the PSDs for both shapes. All the results are shown in Figure 7.8b. As we can see, sample B-1 and B-2 show unimodal distribution of mesopores but sample B-3 clearly shows bimodal mesopore size distribution. In addition, the peaks become sharper as ammonia concentration increases. PSD of sample B-3 confirms a bimodal pore size distribution. The part of the PSD that we believe accurately represents the dominant pore shape for that region is solid, and the rest of each PSD is dashed. The 2D HCP mesophase with cylindrical pore geometry has a peak in the PSD of around 3.7 nm, which is consistent with the pore size of 3.8 nm in sample A-1 and the 2D HCP unit cell size. The random mesh phase with slit pore geometry has a peak in the PSD of 2.4 nm, which is consistent with sample A-5, prepared

with only HFDePC surfactant. The other pore texture parameters for this series of extracted samples are shown in Table 7.1.

Representative TEM images of this series of sample are shown in Figure 7.9. Sample B-1 shows coexisting rough spherical and elongated particles by TEM, indicating the micelle demixing in the precipitated particles. Based on the analysis above, the spherical particles are formed by CTA^+/silica aggregates, while the elongated particles are formed by $HFDePy^+$/silica aggregates. In the spherical particles, cylindrical pores can be found with short range order, indicating weak 2D HCP ordering. For the elongated particles, wormhole-like mesopores are formed as shown in Figure 7.9. The d-spacings measured from TEM are consistent with XRD. Sample B-2 is the base sample, which has improved 2D HCP ordering of the CTA^+ aggregates and vesicular elongated particles. High magnification TEM images of sample B-3 confirm the presence of co-existing ordered domains. Figure 7.9 shows a brightfield TEM image of this sample, suggesting that particles are composed of distinct domains with different pore orientations, some of which appear to be oriented parallel to the domain boundary while others are perpendicular to the domain boundary. The measured d_{100} and d_{001} spacings from the TEM images are consistent with XRD, showing that the order mesopores are really biphasic. Based on the XRD spacings and bimodal PSD, we conclude that they are templated by CTA^+-rich and $HFDePy^+$-rich micelles separately. The co-existing distinct domains of mesostructure can be more easily observed in the dark field STEM images shown in Figure 7.10. The entire particle consists of many ordered domains, and the insets show examples of 2D HCP cylindrical pores (both edge-on and end-on views) and mesh phase pores. Pillars between the silica layers are apparent in the mesh phase image. Figure 7.11 shows the SEM images of the extracted samples B-1 and B-3. Sample B-1 consists of both spherical and elongated particles, which is consistent with TEM. Sample B-3 shows that the materials are composed of rough particle with a heterogeneous size and shape distribution.

From this series of sample, we conclude that the ammonia amount is an important parameter to affect the mixture of phases in the final products. The formation of biphasic domains was observed for all samples in this series. The biphasic domains change from deformed 2D HCP/wormhole to 2D HCP/vesicle to well-ordered 2D HCP/mesh as the

ammonia concentration increases. The phase changes caused by increasing solution pH are in agreement with previous reports on the pH effect on templating with a single cationic surfactant. Echchahed et al.[40] proposed that counterion displacement plays an important role for cationic surfactant templating based on the chemical analysis. They found that increasing pH causes an increase of the amount of anions (like Cl⁻ here) left in the solid, which induces a phase change. Here, ordered biphasic 2D HCP/mesh domains with well-defined bimodal mesoporosity are promoted by using a large amount of ammonia. More ammonia induces faster hydrolysis and precipitation of TEOS, which apparently allows the rapid formation of small, separate demixed domains that are better preserved than they are when hydrolysis and precipitation are more gradual. The mechanism of biphasic transition driven by increase of ammonia concentration requires detailed investigation, but competitive precipitation between $HFDePy^+$/silica and CTA^+/silica aggregates probably plays a dominant role. At low ammonia concentration, the precipitation rate of $HFDePy^+$-rich/silica and CTA^+-rich/silica aggregates is different due to low availability of hydrolyzed TEOS, and the aggregates of $HFDePy^+$-rich/silica may precipitate first. At medium ammonia concentration, $HFDePy^+$-rich/silica aggregates may still precipitate first but higher charge density between $HFDePy^+$-rich and silica causes the formation of vesicles. At high ammonia concentration, separate precipitation of $HFDePy^+$/silica and CTA^+/silica at similar rates would explain the formation of biphasic mesh/2D HCP particles.

7.3.3. The effect of adding salt

A series of samples was prepared to investigate the effects of adding salt on the mixed surfactant system. The reactants have the initial molar ratios 1TEOS : 0.06 HFDePC : 0.06 CTAC : $10NH_3$: $148H_2O$: s NaCl with s = 0, 0.28, 2.8 and 5.6. Sample C-1 through C-4 correspond to the order from s = 0 to s = 5.6, and sample C-1 is the base sample in this series.

Powder XRD patterns for this series of extracted samples are shown in Figure 7.12. The base sample C-1 shows one strong reflection (100) at low angle and a broad peak at higher angle from overlapping (110) and (200). Sample C-2, prepared with a small amount of NaCl, shows a XRD pattern similar to that of KIT-1[41], which possesses shorter-range order than the 2D HCP mesophase. The intensity and resolution of higher order peaks are

lower than sample C-1, indicating diminished hexagonal ordering. A transition towards wormhole-like pores occurs as salt is added, which is consistent with previous reports on the effects of adding NaCl to chloride-based cationic surfactant solutions.[42,43] Large enough concentrations of salts can transform cylindrical micelles into a homogeneous dispersion of spherical micelles.[44] In addition, the (100) peak shifts to a lower angle, suggesting the average pore-pore distance increases. Increasing the NaCl amount further in sample C-3 causes a further shift of the reflection to lower angle. Sample C-4, prepared with the highest salt concentration (2 M) is completely disordered, consistent with previous reports that high NaCl concentrations disrupt micelle ordering[45].

Figure 7.13 shows the nitrogen sorption isotherms and pore size distributions of this series of extracted samples. For direct comparison, the pore size distributions of all samples were calculated by the KJS method assuming cylindrical pore geometry. Sample C-2 shows two distinct capillary condensation steps at relative pressure (P/P_o) ranges of 0.12 to 0.25 and 0.3 to 0.4, indicating that bimodal mesoporous materials are formed in the presence of a small amount of NaCl. The pore size distribution of this sample is weakly bimodal with two peaks at 3.3 nm and 3.8 nm. Compared to sample C-1, the hysteresis loop disappears and the upturn at high relative pressure reduces, showing that salt reduces both the number of vesicle cavities and the textual porosity between clusters of particle. The isotherm for sample C-3 more clearly shows two capillary condensation steps, and a bimodal pore size distribution with well-defined peaks at 3.3 nm and 3.8 nm. To our knowledge, this is the first reported example of well-defined bimodal mesoporous silica with such a small pore size difference (only 0.5 nm). Sample C-4, prepared with a large amount of NaCl, shows only one capillary condensation step and a single PSD peak. The α_s plot of this sample shows the largest micropore volume of any sample reported here. The other structure parameters of this series of samples are shown in Table 7.1. This series shows that salt can induce the transition of the mesoporous matrix from unimodal to bimodal then back to unimodal. The pore sizes in the mesopore distribution remain almost constant with increasing NaCl. In addition, the BET surface area and total mesopore volume all reach maxima in sample C-3. The bimodal PSD suggests templating with two large populations of separate CTAC-rich and HFDePC-rich micelles that co-assemble with negative-charged silica to form an intimately mixed single phase. When

the salt amount is excessive in sample C-4, effective micelle templating cannot occur and the resulting materials exhibit low surface area and considerable reduction in mesophase structure.

Representative TEM images of samples C-2 through C-4 are compared in Figure 7.14. Sample C-2 consists predominantly of ~ 100 nm spherical particles. Unlike base sample C-1, there are no elongated particles with hollow cells observed in this sample. In the high magnification TEM image of this sample, we can see that both the pore size and shape are not uniform, indicating those mesopores may be templated by different size or shape of micelles. Together with the XRD and pore size distribution data, we conclude that a bimodal mixture of wormhole-like mesopores is produced in C-2 instead of the original 2D hexagonal order in sample C-1. The loss of vesicular HFDePy$^+$-templated chambers is accompanied with the addition of smaller 3.3 nm pores in the PSD, which presumably are formed by HFDePy$^+$-rich micelles. In TEM, separate ordered domains can not be found, so the bimodal mesopores templated by either CTA$^+$-rich or HFDePy$^+$-rich micelles coexist within one large particle. Some non-uniform domains mainly containing large mesopores or small mesopores can be observed. The short wormhole-like channels in this sample are connected with each other to form 3D network, while the channels of 2D HCP mesophase are one-dimensional. In addition to ~100 nm particles, we observe either spherical or stripe-like layers of small silica pieces surrounding the large spherical particles. With the further increase of salt in sample C-3, the TEM image shows predominantly spherical particles with larger size than in sample C-2. The small silica particles surrounding the large particles found in sample C-2 are absent in C-3, which makes the particles smoother. Sample C-4 shows mainly disordered wormhole-like pores. The formation of a unimodal distribution of wormhole-like mesopores may indicate enhanced mixing of CTAC and HFDePC surfactants in the presence of a sufficient amount of salt. This result is consistent with the effect of salt on mixing of hydrocarbon and fluorocarbon surfactants in solution determined by fluorescence quenching.[46]

Figure 7.15 shows effect of salt on the morphology of this series of extracted samples. Unlike sample C-1, the SEM image of sample C-2 consists of only rough spherical particles with sizes near 100 nm, coated with smaller secondary spherical

particles with sizes less than 30 nm. Sample C-3 consists of smooth spherical particles. Sample C-4 consists of large irregular-shaped microparticles along with a small amount of sheet-like silica particles, all of which are flocculated into even larger aggregates. The difference in morphology should be due to screening of electrostatic interactions between surfactants and silicates. This decreases the difference in the rate of precipitation of CTA^+-rich and $HFDePy^+$-rich micelles with silica, leading to more homogeneous and uniform particles. The appropriate amount of salt results in predominantly globular inorganic-organic hybrid aggregates with sizes of 100 nm.

From this series of samples, we conclude that adding salt significantly affects the structure of both particles and pores by influencing the co-assembly behavior of demixed micelles with silicate species in the solution. The formation mechanism of bimodal mesoporous materials in the presence of an appropriate amount of NaCl requires detailed investigation, but this structure probably forms by precipitation of intimately mixed $HFDePy^+$/silica and CTA^+/silica aggregates. On the one hand, the addition of a large amount of NaCl may greatly widen the molar concentration range for demixing into $HFDePy^+$-rich and CTA^+-rich micelles as reported by Asakawa, et al.[47], who found that the addition of LiCl causes almost perfect demixing for the lithium perfluorooctanonate (LiPFN)/lithium dodecyl sulfate (LiDS) system, with micelles divided into one population with 5 mol% fluorinated surfactant and another with 99 mol%. On the other hand, adding NaCl introduces an equivalent increase in Cl^- at cationic micellar interfaces[48], which would introduce strong electrostatic shielding of charge interactions between cationic surfactant micelles and negative silica and thus slow down precipitation. As a result, this allows the composition of demixed micelles composed of CTA^+-rich and $HFDePy^+$-rich in solution to be better balanced so that separate micelles can simultaneously co-assemble with silica and precipitate together leading to the formation of materials with intimately mixed bimodal pores.

7.3.4. The effect of ethanol addition

A series of samples was prepared with different amounts of ethanol added to the synthesis solution to give molar ratios of 1 TEOS : 0.06 HFDePC : 0.06 CTAC : 10 NH_3 : 148 H_2O : z with z = 0, 10, 20, 30. Samples D-1 through D-4 correspond to the order from z = 0 to z = 30, and D-1 is the base sample.

Figure 7.16 shows representative TEM images of samples D-2 and D-4. Sample D-2 contains co-existing spherical and elongated silica particles, which by analogy to the base sample can be inferred to be templated by $HFDePy^+$-rich and CTA^+-rich micelles, respectively. Both spherical and elongated particles show wormhole-like pore structure. With a further increase of the ethanol amount, the elongated particles disappear, and all particles show predominantly spherical shape.

The morphology change of samples in this series is confirmed by SEM as shown in Figure 7.17. Without ethanol, the particles primarily show elongated shape with many hollow cells inside the particles evident by TEM as shown in Figure 7.3. When a small amount of ethanol is added, the products contain co-existing elongated and spherical particles with a wide particle size distribution. When ethanol is further increased to sample D-4, all particles show uniformly spherical shape with different size. The sizes of the particles are in the range of 0.1-1 μm.

The nitrogen sorption isotherms of this series of samples are shown in Figure 7.18a. All samples in this series exhibit type IV isotherms. For samples D-1 and D-2, the capillary condensation takes place at a relative pressure P/P_0 between 0.2 and 0.4. With a further increase in the amount of ethanol in samples D-3 and D-4, capillary condensation happens at a lower relative pressure P/P_o between 0.15 and 0.3. When ethanol is added, the H3 hysteresis loop of the base sample disappears indicating that ethanol does not favor the formation of vesicle-like particles templated by $HFDePy^+$-rich micelles. The textural porosity decreases as ethanol is added due to the formation of uniform, smooth particles. Figure 7.18b compares the pore size distributions of this series of samples. With increasing ethanol, the average pore size decreases. This change suggests that the ethanol acts as cosolvent to reduce the micelle (pore) size by decreasing the aggregation number[49]. The other structural parameters are given in Table 7.1. The BET surface area and mesopore volume increase as ethanol is added and the external area decreases as longer, more uniform particles are produced. This change indicates that by acting as cosolvent, ethanol plays a key role in determining mixing of hydrodrocarbon and fluorocarbon surfactant micelles in material synthesis applications.

Figure 7.19 presents the XRD patterns for the series of samples with increasing amount of ethanol. Sample D-1 has a disordered hexagonal mesophase with wormhole-

like or deformed hexagonal pores. With z = 10 in sample D-2, a distinct reflection appears close to the original (100) peak. The appearance of a new reflection at this position looks similar to the Ia3d cubic phase transformation induced by adding ethanol to CTAB-templated silica prepared at room temperature.[50] However, careful XRD indexing, the appearance of the N_2 adsorption isotherm and TEM analysis together rule out this possibility and suggest that the structure primarily consists of two co-existing microphase-separated domains due to micellar demixing of CTAC and HFDePC. Further increase of ethanol to 20 mol in samples D-3 and D-4 leads to a loss of order and only one broad peak, indicating a wormhole-like structure.

The observations for this series of samples are consistent with ethanol acting as a co-solvent in the mixed CTAC/HFDePC system. In demixed surfactant templating system, ethanol can still influence mesophase structure by separately altering surfactant packing parameters within segregated surfactant micelles, which is in agreement with previous reports in single surfactant templated system[51,52]. We found that a small amount of ethanol promotes co-aggregation of demixed hydrocarbon and fluorocarbon micelles, initially leading to bimodal particle shapes and bimodal pore size distribution. With increase of ethanol, the miscibility of hydrocarbon surfactant with fluorocarbon surfactant is enhanced leading to unimodal pore structure and particle morphology.

7.3.5. The effect of synthesis temperature

A series of samples were prepared at different temperature with molar ratios of 1 TEOS : 0.06 HFDePC : 0.06 CTAC : 10 NH_3 : 148 H_2O. Synthesis temperatures of 21 °C (room temperature), 40 °C, 60 °C and 80 °C were used to prepare E-1 through E-4, respectively. E-1 is the base sample.

The nitrogen sorption isotherms and calculated pore size distributions are shown in Figure 7.20. All samples have type IV isotherms with hysteresis loops. Except for the base sample, the other three samples clearly show two well-defined adsorption steps, indicating the formation of bimodal mesopores in the final products. The first step takes place at an intermediate relative pressure of 0.35-0.45 due to capillary condensation inside of intra-particle mesopores. The second step takes place at high relative pressure of 0.8-1, and corresponds to filling of the large meso- or macro-pores among the primary particles.[53] The curves in the second step show hysteresis, indicating a broad pore size

183

distribution. The calculated pore size distributions confirm the co-existence of small uniform mesopores and a broad distribution of large mesopores in samples E-2 through E-4. Sample E-1 only shows a narrow distribution of small mesopores centered at 3.7 nm. The primary mesopore size increase from 3.7 nm to 4.4 nm as the synthesis temperature increases, suggesting that increasing temperature facilitates the mixing of hydrocarbon and fluorocarbon surfactants in the solution. This is in agreement with the previous report by Almgren et al.[22] who found that increasing temperature facilitate the formation of mixed micelles in solution for this pair of surfactants.

The nature of the bimodal pore structure is revealed by TEM imaging. A representative TEM image of sample E-2 is shown in Figure 7.21. The sample shows an unusual sponge-like architecture: a 3D interconnected small mesopore network is formed inside intimately mixed small particles, the porosity between which gives rise to the disordered large pores in the image. Because of the focusing condition, these pores appear dark in Figure 7.21.

Figure 7.22 shows representative SEM images of extracted samples E-2 and E-3. We can see that samples are composed of many 10-20 nm uniform nanoparticles. These nanoparticles fuse together and generate large pores, which is consistent with TEM. The XRD patterns of samples E-2 through E-4 all show only one strong reflection at low angle, indicating the formation of less-ordered pore channels than in sample E-1.

From this series of samples, we can see that synthesis temperature affects particle size and aggregation in CTAC/HFDePC templated particles. In contrast to the synthesis at room temperature, the particle size dramatically decreases and miscibility of two surfactants seems to be enhanced when synthesis temperature increases to just 40 °C. The demixed vesicular particles of the base sample are not formed at elevated temperature. Interestingly, upon further increasing the temperature up to 80 °C, there is no other dramatic change in the structural features of the products like pore size, particle size, etc.

7.4. Conclusions

Mesoporous materials with diverse phase and pore structure have been synthesized using mixtures of CTAC and HFDePC as templates. The structure of the final material is influenced by many factors, such as molar ratio of CTAC to HFDePC, the ammonia concentration, addition of NaCl, ethanol concentration, and synthesis temperature.

Evidence for demixing can be observed under many conditions in these silica samples. The phase structure of the final material changes from 2D HCP to wormhole-like to disordered to random mesh phase as the molar fraction of HFDePC increases in the mixture. At low fraction of HFDePC, the phase structure is governed by the hydrocarbon surfactant CTAC. With increase of the fraction of HFDePC to above 50%, the phase structure is governed by the fluorocarbon surfactant. At equal molar fraction of CTAC and HFDePC, biphasic matererials were prepared with different ammonia concentrations. With the increase of ammonia concentration, a transition of the biphasic structure can be observed from disordered 2D HCP/wormhole-like to 2D HCP/vesicular to well-ordered 2D HCP/mesh. The largest amount of ammonia studied causes the formation of ordered biphasic 2D HCP/mesh materials with well-defined bimodal mesoporosity. Addition of an appropriate amount of NaCl or ethanol can promote the formation of wormhole-like mesoporous materials with bimodal mesoporosity, presumably due to incorporation of demixed CTA^+-rich and $HFDePy^+$-rich micelles into single particles. Increasing the synthesis temperature causes the formation of small mesoporous silica particles, which fuse together to form secondary large pores.

The present work shows the use of a sol-gel approach not only to verify mixing or demixing in concentrated mixture of surfactants in precipitated silica, but also the ability to control the demixed micelle architectures in combined hydrocarbon/fluorocarbon surfactant templating of mesoporous material. In addition, a facile methodology for the synthesis of porous materials with well-defined biphasic mesostructure and bimodal mesoporosity is demonstrated by using mixed hydrocarbon/fluorocarbon surfactant templates that are known to demix in dilute solution. In the future, more work needs to be pursued to gain deeper insight into the fundamental factors that underlie the formation of novel biphasic and hierarchical structures presented here, as well as morphology control of the precipitated particles. The triphasic mixture of co-existing mesostructured domains in the as-synthesized materials also provides an opportunity to selectively tune either pore size, and to utilize the separate hydrocarbon and fluorocarbon domains for controlled deposition of two different transitional metal oxides into different regions of intimately mixed mesopore channels. For these applications, we will report our findings in the next chapter.

Table 7. 1. Structure parameters of the mixed-surfactant-templated mesoporous silica materials[a]

Sample name	S_{BET} (m^2/gm)	$V_{P/Po=0.95}$ (cm^3/gm)	V_p[b] (cm^3/gm)	V_m (cm^3/gm)	S_t[b] (m^2/gm)	W_{KJS} (nm)	S_{ex}[b] (m^2/gm)
A-1	947.0	0.76	0.68	0.033	796.5	3.8	55.0
A-2	963.0	0.86	0.69	0.021	817.3	3.7	117.9
A-3	856.8	0.76	0.52	~0	699.1	3.7	158.5
A-4	712.8	0.74	0.36	~0	571.2	2.4	250.2
A-5	895.2	0.73	0.39	0.0038	680.8	2.4	248.3
B-1	901.8	0.63	0.61	0.022	818.4	3.6	152.6
B-3	906.6	0.75	0.56	0.012	885.48	2.4, 3.8	158.2
C-2	912.8	0.62	0.53	0.0098	729.3	3.3, 3.8	65.6
C-3	934.2	0.70	0.63	0.025	788.8	3.3, 3.8	44.1
C-4	550.6	0.29	0.27	0.14	214.7	3.7	12.1
D-2	1089.3	0.89	0.65	0.0075	864.8	3.0, 3.5	159.5
D-3	1143.2	0.61	0.62	~0	843.5	3.0	59.8
D-4	1174.3	0.67	0.60	~0	813.5	3.0	36.4
E-2	756.5	1.13	1.22	0.010	633.8	4.0	-
E-3	747.0	1.37	1.33	0.0053	630.3	4.4	-
E-4	854.8	1.34	0.94	0.011	725.1	4.4	-

a. S_{BET} = BET surface area,[54] the adsorbed volume $V_{p/po=0.95}$, W_{KJS} = pore diameter at peak of KJS pore size distribution, V_p = total mesopore volume, the micropore volume V_m = I×0.001547 (cm^3) where I represents the Y-intercept in the V plot, S_t = total specific surface area, S_{ex} = external specific surface area.

b. Calculated using α_s comparative nitrogen adsorption plots.[38]
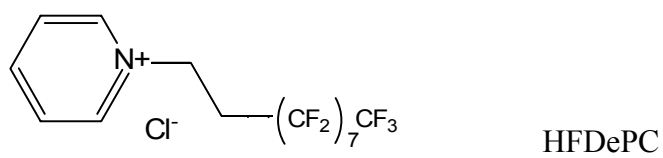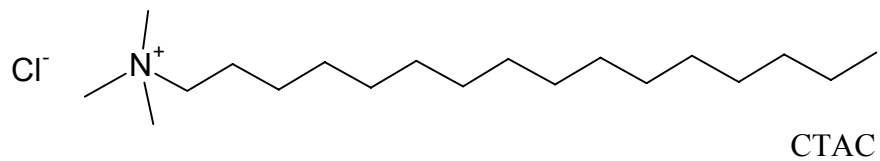
CTAC

HFDePC

Figure 7.1. Molecular structures of surfactants used for materials synthesis.
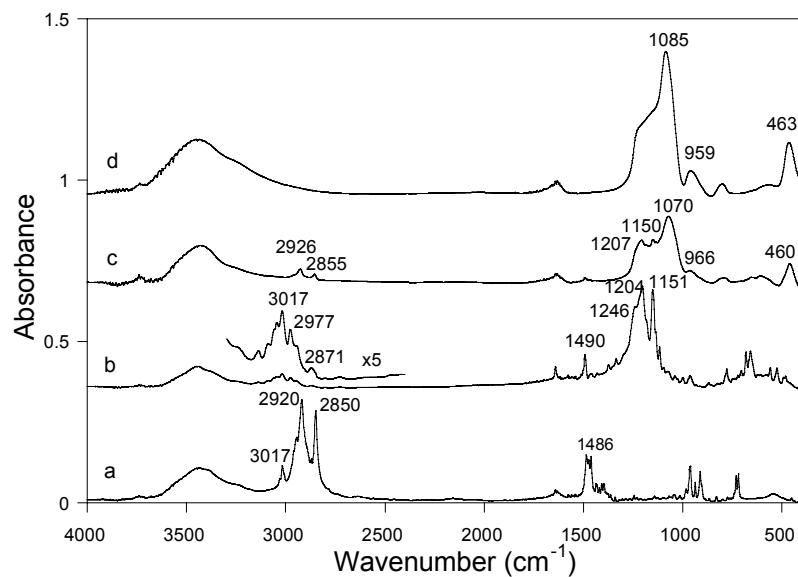
Figure 7.2. FTIR spectra of KBr pellets pressed with 1 wt% of (a) the reagent CTAC, (b) the purified reagent HFDePC, (c) sample A-3 as synthesized, and (d) sample A-3 after extraction.
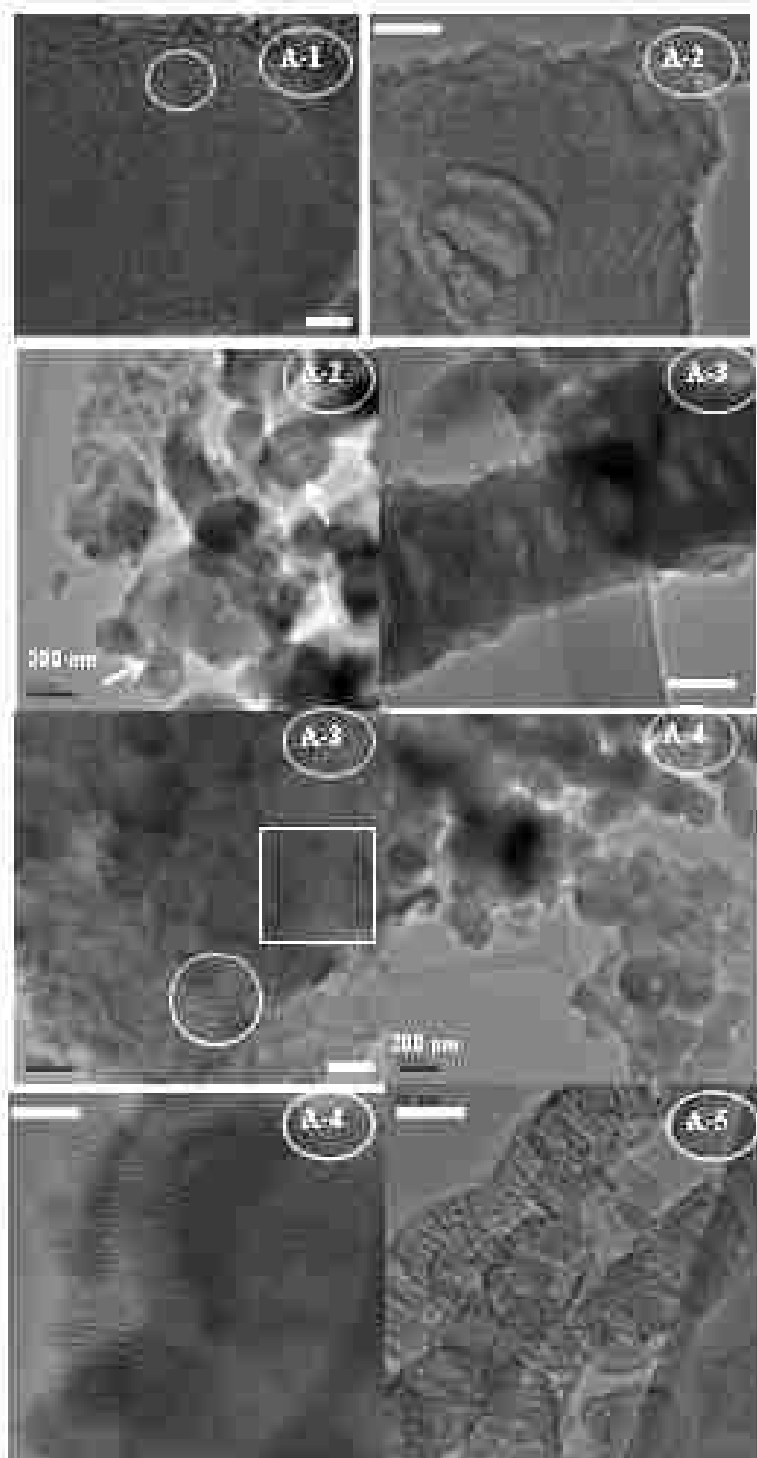
Figure 7.3. Representative TEM images for a series of extracted samples A-1 through A-5. The white scale bar in sample A-1 is 20 nm wide, and all other white scale bars of sample A-2 through A-4 are 100 nm wide. The white circle in sample A-1 indicates hexagonal pores, and the white arrows in sample A-2 indicates elongated particles. The white circle in sample A-3 shows cylindrical pores and the white square shows deformed hexagonal mesopores.
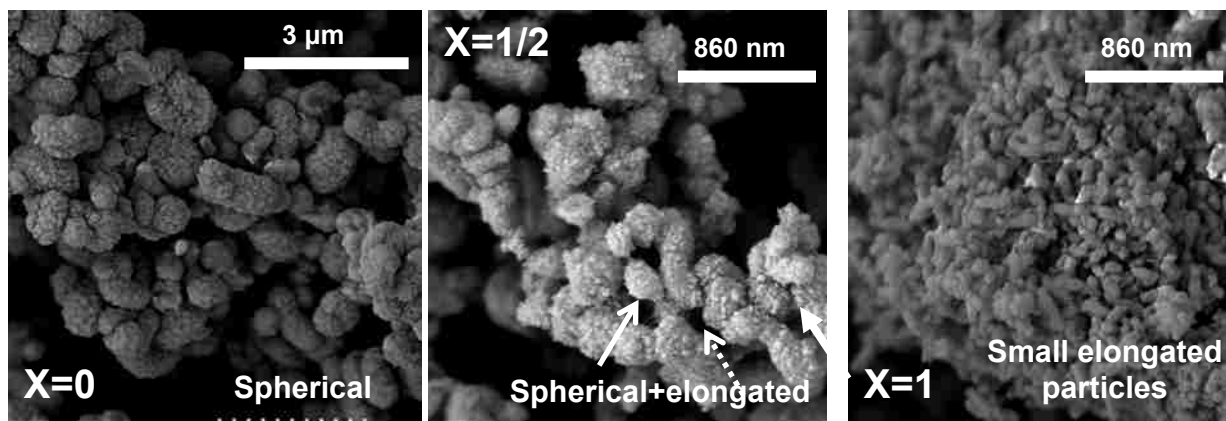
Figure 7.4. Representative SEM images for extracted samples A-1, A-3 and A-5 (from left to right).
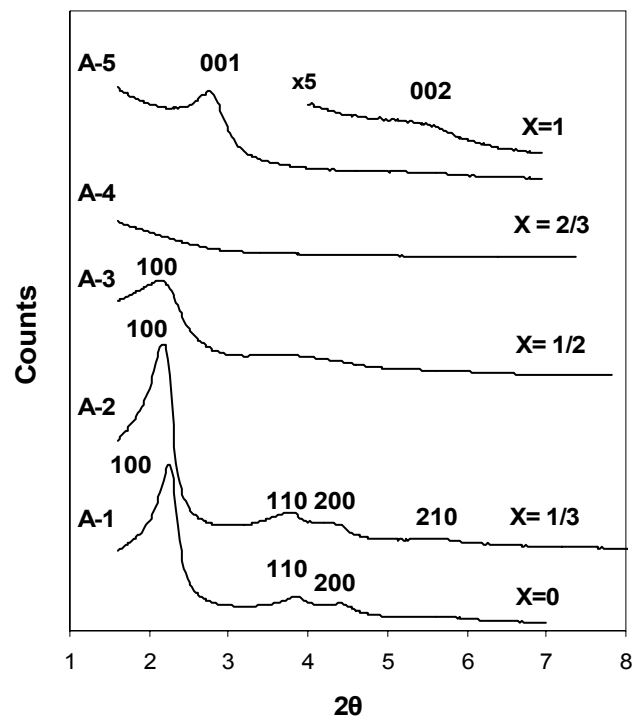
Figure 7.5. XRD results for a series of extracted samples A-1 through A-5.
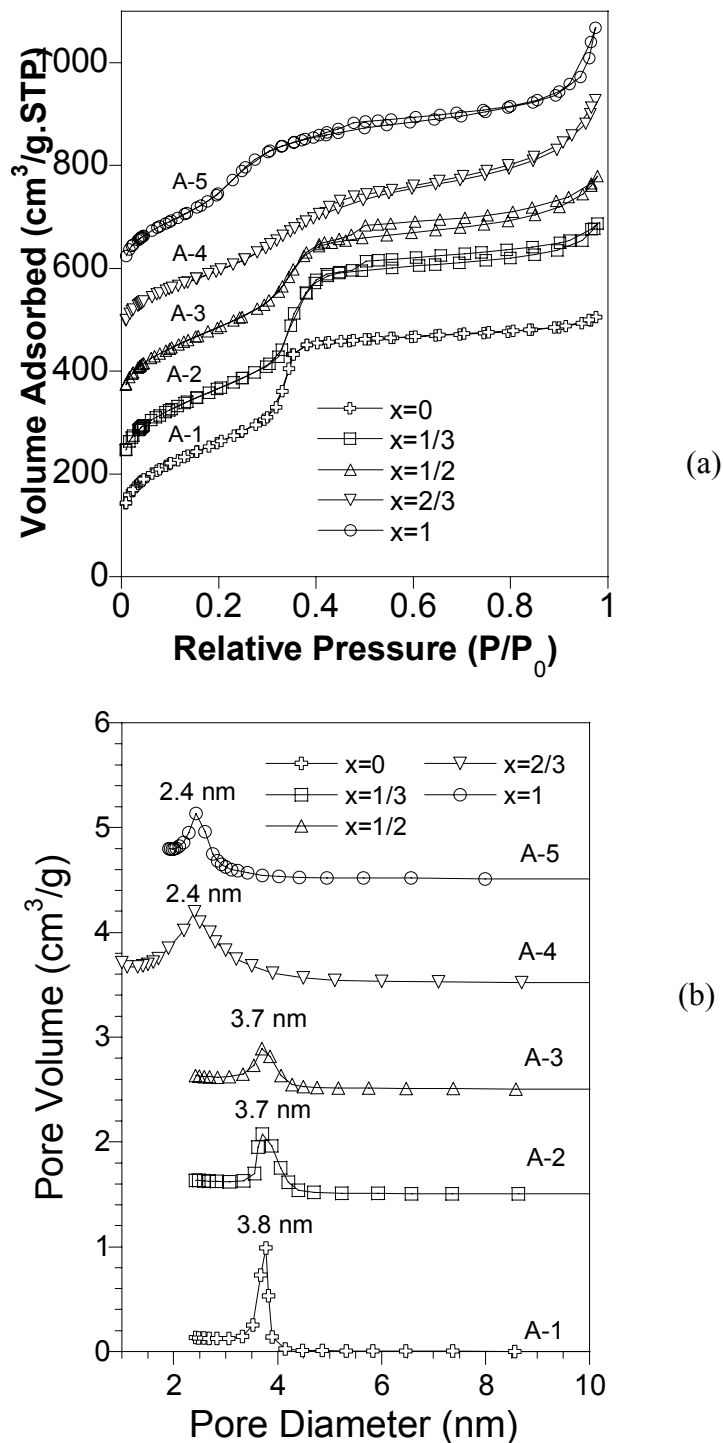
Figure 7.6. (a) Nitrogen adsorption isotherm plots of a series of samples A-1, A-2 (upshifted 100 cm^3/g), A-3 (upshifted 150 cm^3/g), A-4(upshifted 400 cm^3/g) and A-5 (upshifted 500 cm^3/g) made with different molar ratios of mixed surfactants. (b) Pore size distributions of this series of extracted samples calculated using modified KJS method assuming cylindrical pore geometry (sample A-1 through A-3), modified KJS method assuming slit-like pore (sample A-5), or the BJH method (sample A-4).
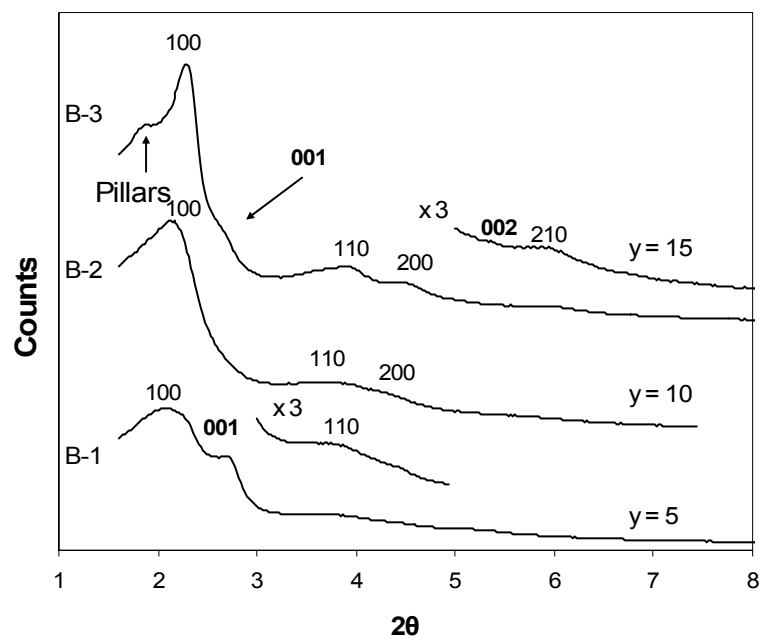
Figure 7.7. XRD results for a series of extracted samples B-1 through B-3.
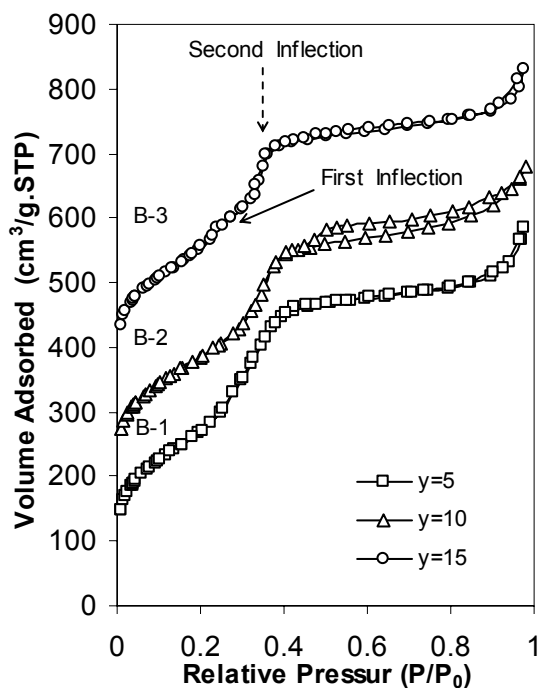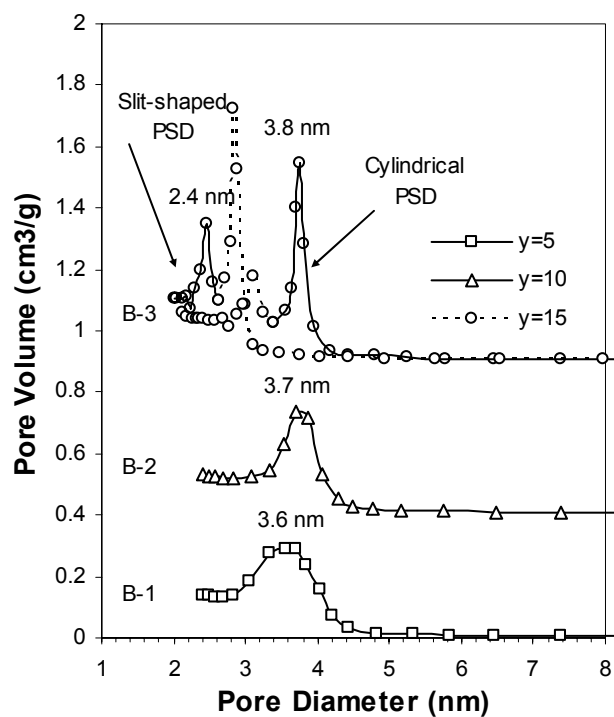
Figure 7.8. (a) Nitrogen adsorption isotherm plots of samples B-1, B-2 (upshifted 150 cm^3/g), B-3 (upshifted 300 cm^3/g) made with different ammonia concentration. (b)Pore size distributions of this series of sample B-1 through B-3 calculated using the KJS method.
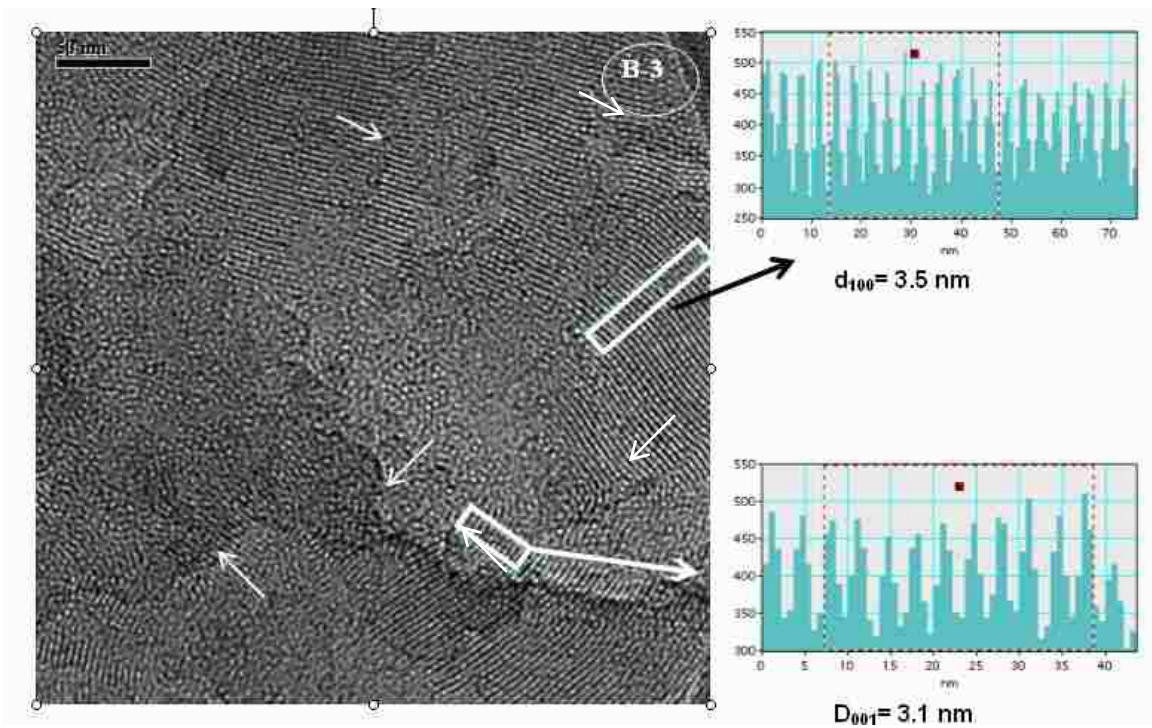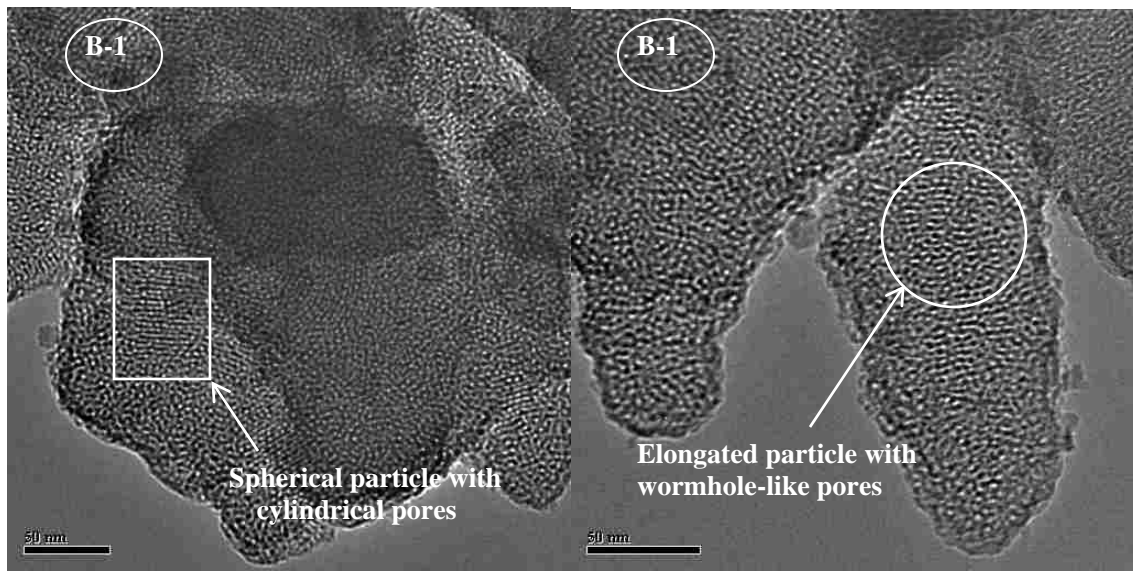
Figure 7.9.Representative TEM images of samples B-1 (top) and sample B-3 (bottom). The white arrows in sample B-3 indicate some of the boundaries between different domains. The two white squares in sample B-3 represent the regions used to measure d spacings for (100) and (**001**) diffractions, respectively, using the inset density plots.
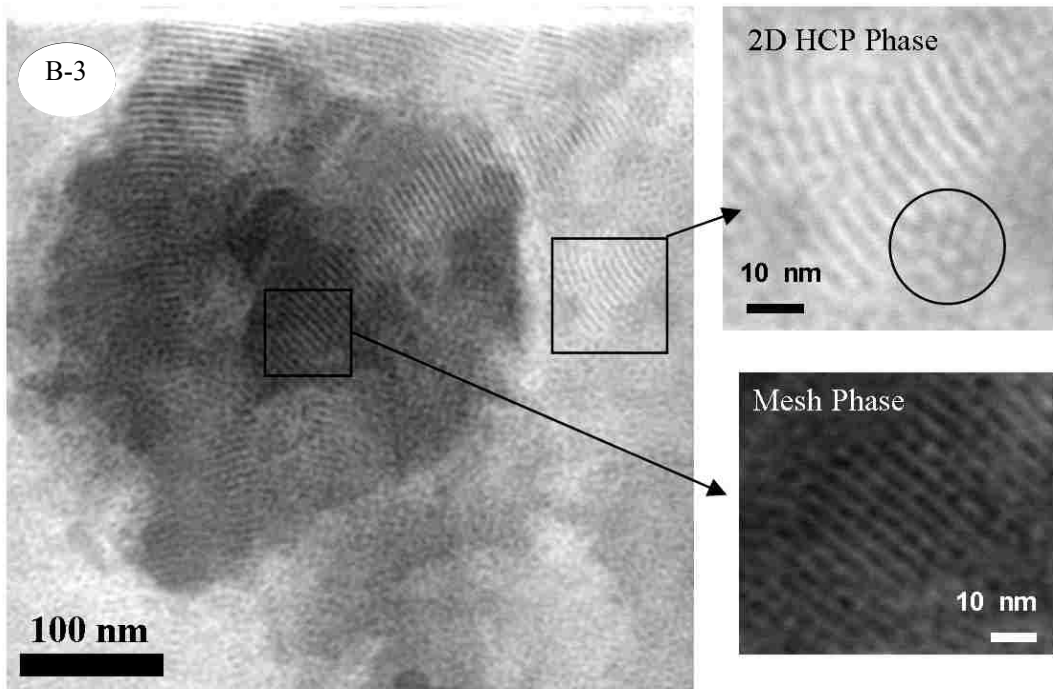
Figure 7. 10. Representative STEM image of sample B-3. The two squares in this sample represent co-existing ordered 2D HCP phase region (top right) and mesh phase region (bottom right).
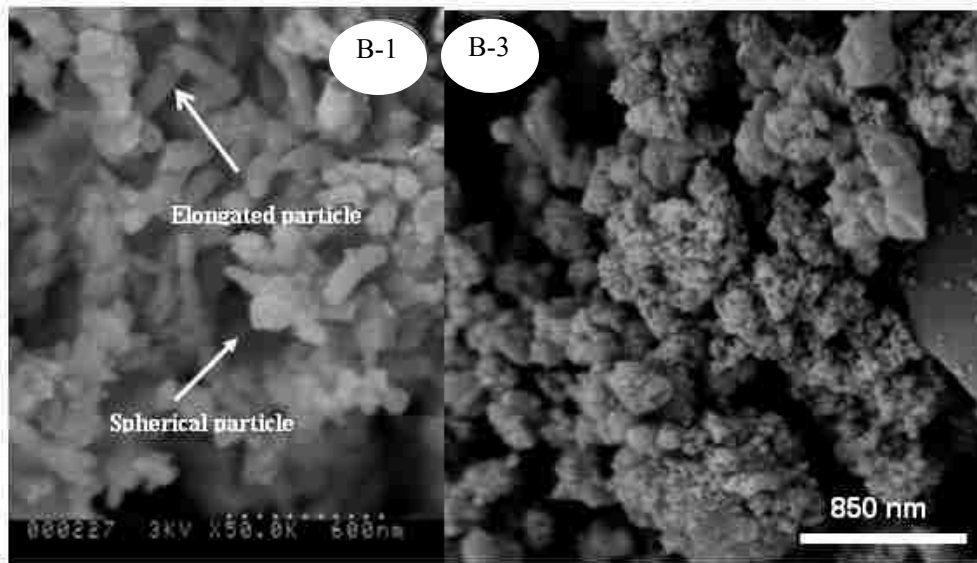
Figure 7.11. Representative SEM image of samples B-1 and B-3.
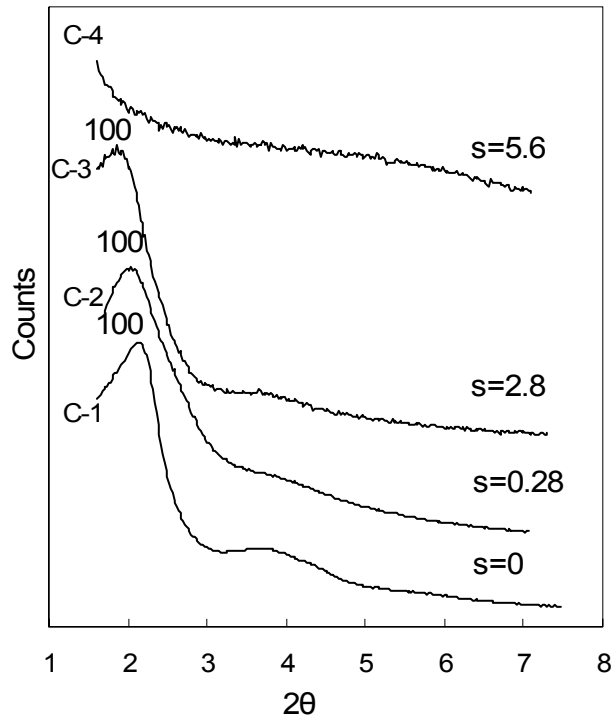
Figure 7.12. XRD results for a series of extracted samples C-1 through C-4 made with different amounts of NaCl.
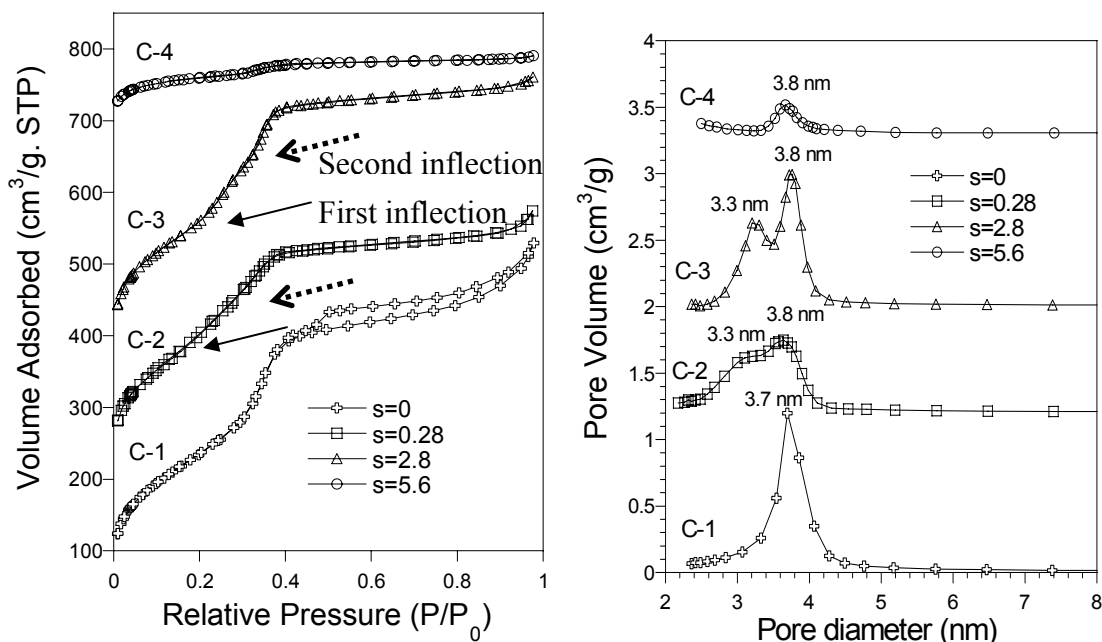
Figure 7.13. (a) Nitrogen adsorption isotherms of samples C-1, C-2 (upshifted 150 cm^3/g), C-3 (upshifted 300 cm^3/g) and C-4 (upshifted 600 cm^3/g) made with different amount of NaCl. (b) Pore size distribution of samples C-1 through C-4 calculated using the KJS method assuming cylindrical pore geometry.
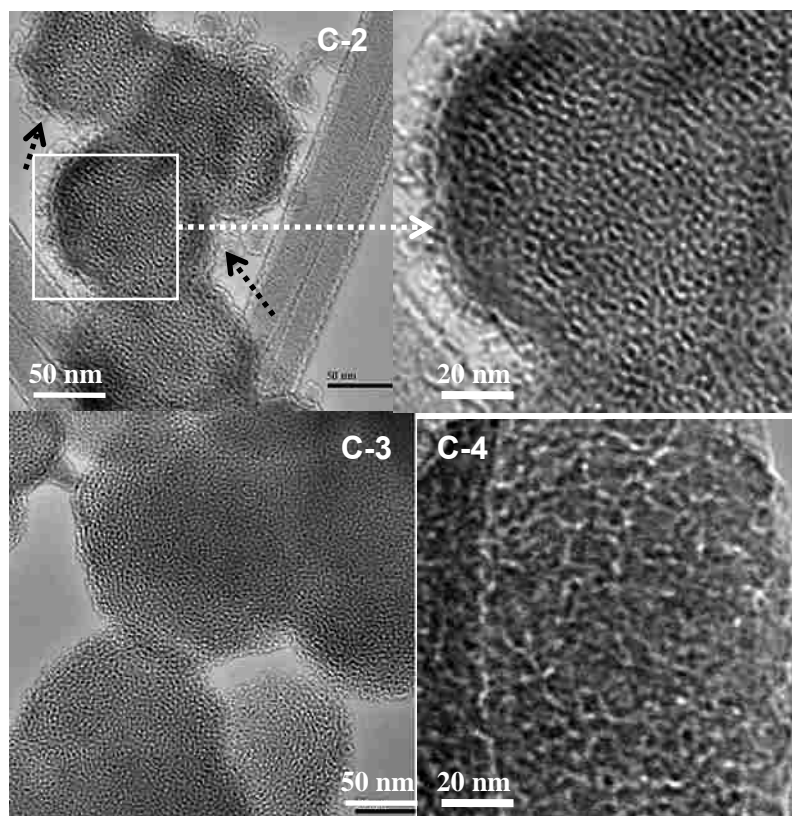
F**igure 7.14**. Representative TEM images of sample C-2 through C-4. The black arrows in sample C-2 refer to small silica particles surrounding the large particles.
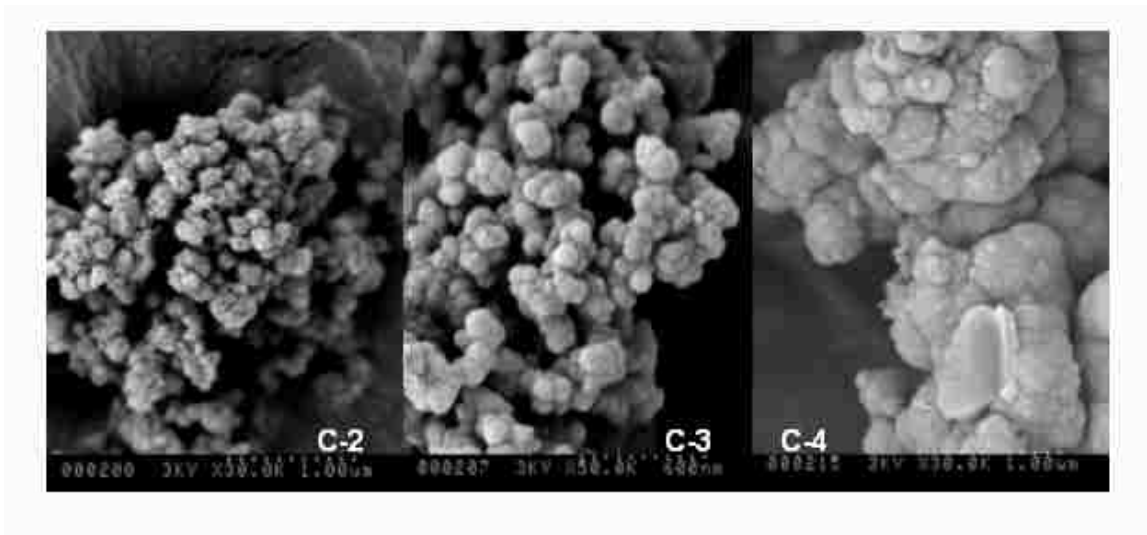
Figure 7.15. Representative SEM images of samples C-2 through C-4.
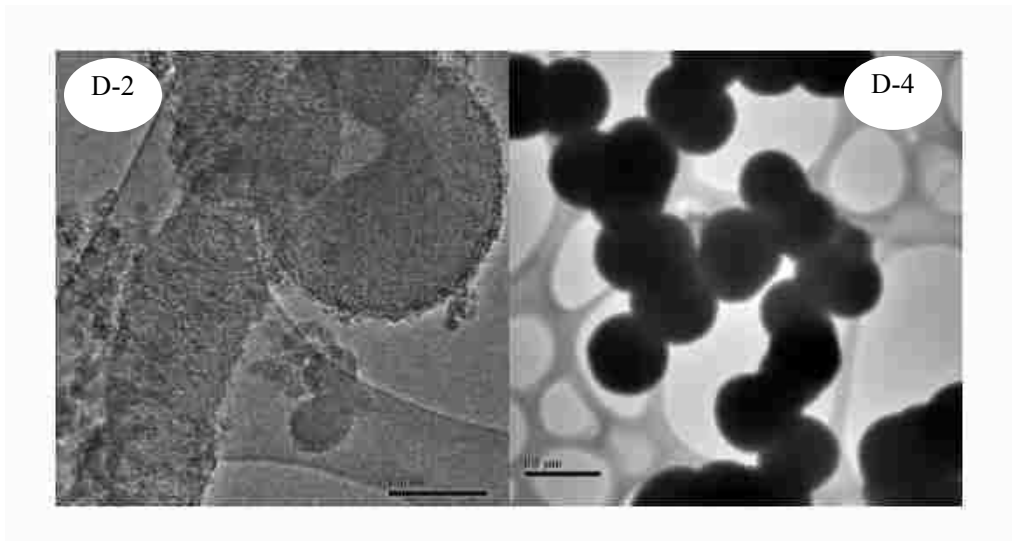
Figure 7.16. Representative TEM images of samples D-2 and D-4.
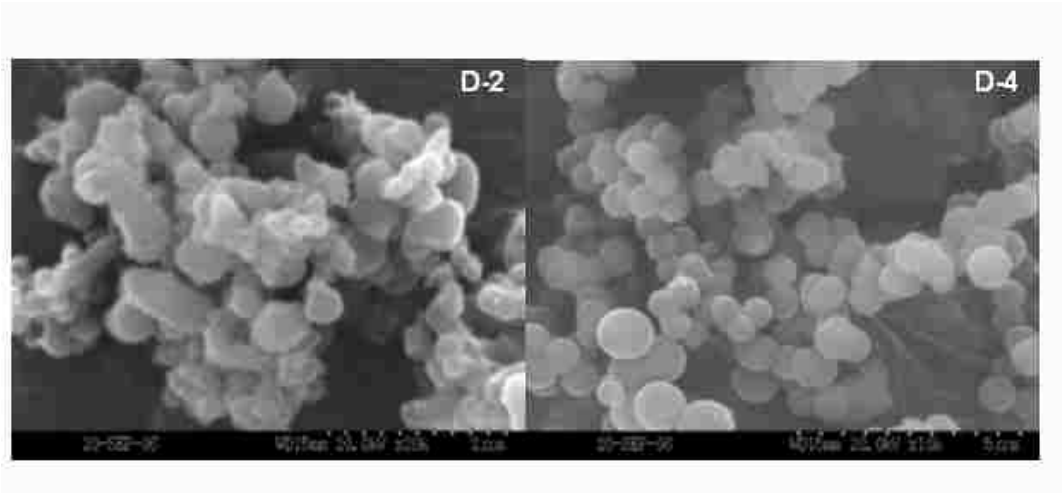
Figure 7.17. Representative SEM images of samples D-2 and D-4.
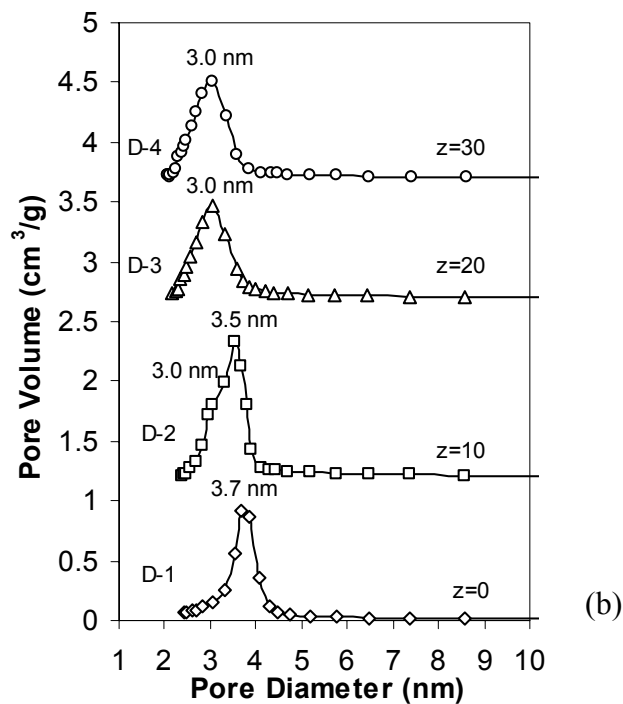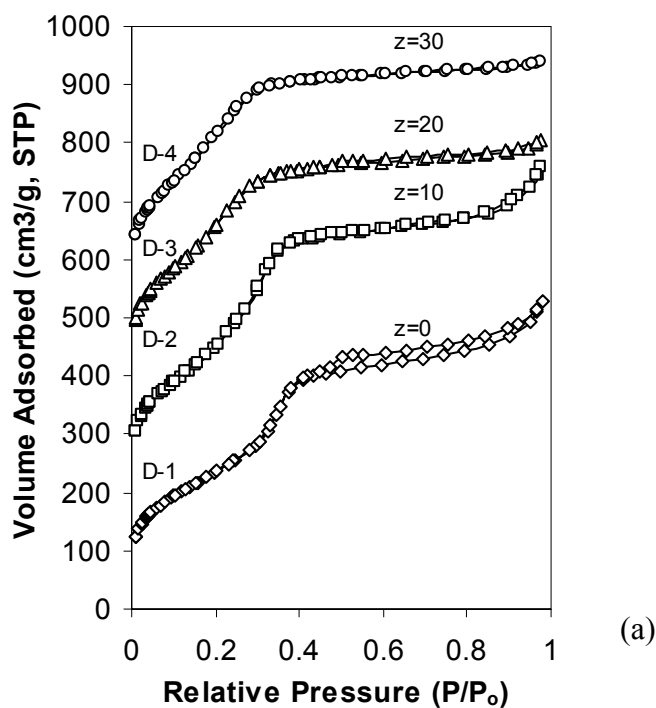
Figure 7.18. (a) Nitrogen adsorption isotherms of samples D-1, D-2 (upshifted 150 cm^3/g), D-3 (upshifted 350 cm^3/g) and D-4 (upshifted 500 cm^3/g) made with different amounts of ethanol. (b) Pore size distribution of this series of sample D-1 through D-4 calculated using the KJS method assuming cylindrical pore geometry.
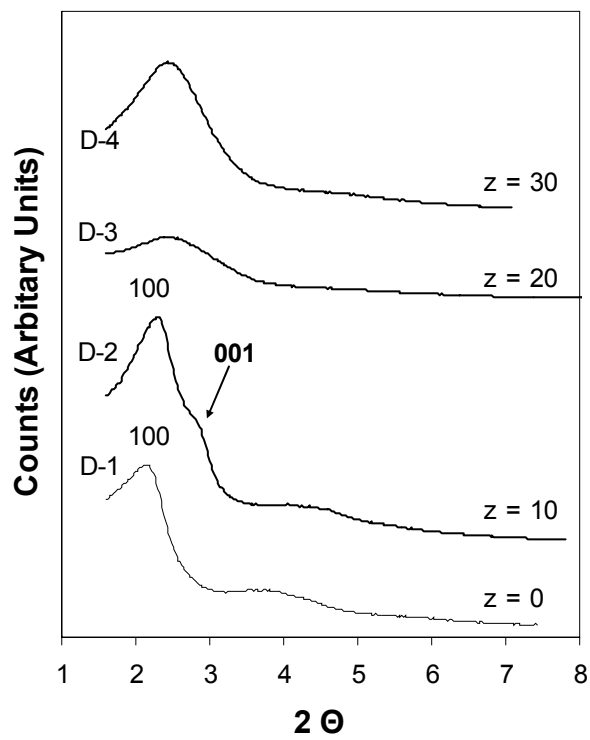
Figure7. 19. XRD patterns of this series of extracted samples D-1 through D-4.
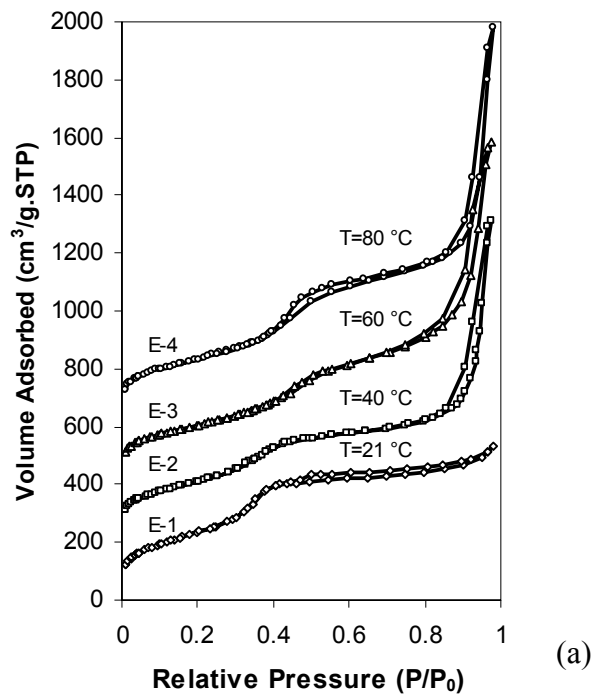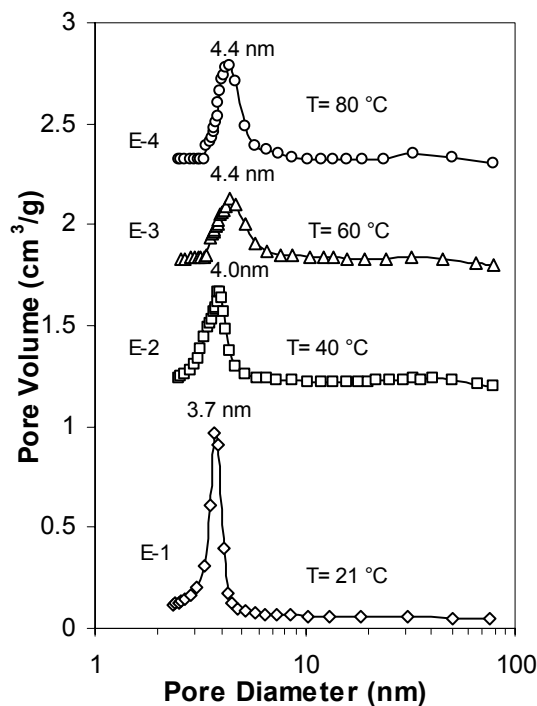
Figure 7.20. (a) Nitrogen adsorption isotherms of samples E-1, E-2 (upshifted 200 cm^3/g), E-3 (upshifted 400 cm^3/g) and E-4 (upshifted 600 cm^3/g) made at different temperatures. (b) Pore size distribution of this series of sample E-1 through E-4 calculated using the KJS method assuming cylindrical pore geometry.

206
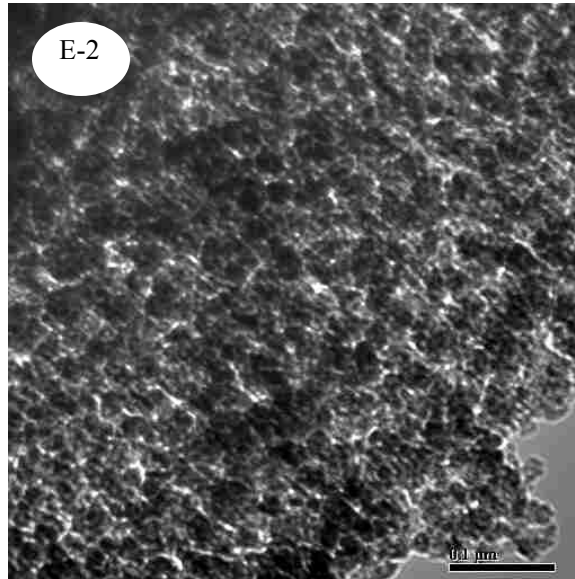
Figure 7.21. Representative TEM images of sample E-2.
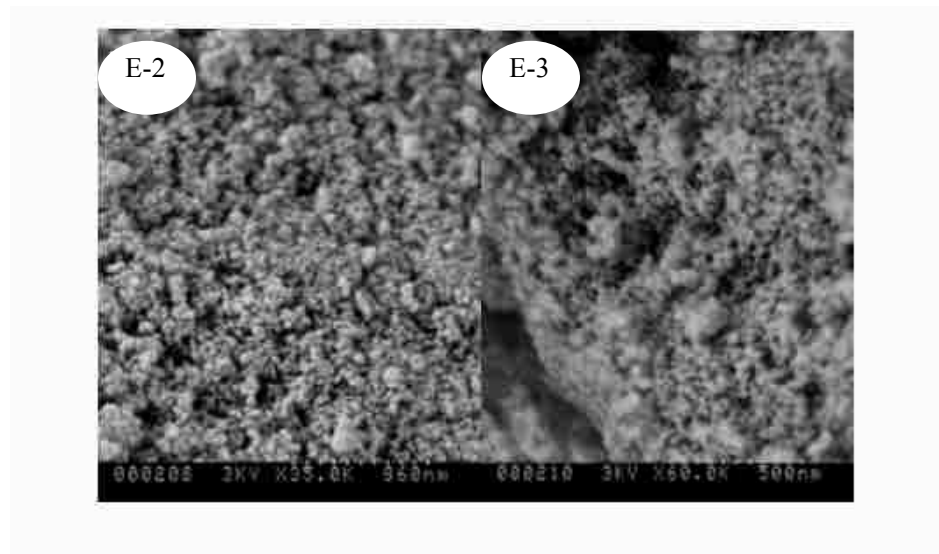
Figure 7.22 Representative SEM images of samples E-2 and E-3.

Chapter 8. Tailored Hierarchical Bimodal Mesoporous Silica Particles Prepared Using Mixed Hydro/Fluorocarbon Cationic Surfactants

8.1. Introduction

In chapter 7, we investigated how some synthesis parameters, including the molar ratio of mixed cetyltrimethylammonium chloride (CTAC) and 1H, 1H, 2H, 2H-perfluorodecylpyridinium chloride (HFDePC), the ammonia concentration, addition of NaCl, ethanol concentration and synthesis temperature, affect the translation of micelle (de)mixing in bulk solution into micelle-templated silica materials. We have demonstrated that demixed micellar aggregates formed in the presence of an appropriate amount of NaCl can be directly templated by the hydrolysis of tetraethoxysilane (TEOS) in aqueous ammonia to produce silica particles in which the micelles remain demixed, leading to bimodal mesoporosity. The particles formed have two populations of well-defined mesopores, which may find potential applications in size exclusion chromatography, biochemical sensors, surfactant-enhanced ultrafiltration[1], controlled drug delivery, and multifunctional catalysis. This finding motivates us to complete an in-depth investigation of how to tune the bimodal pore size distribution by adjusting the parameters that lead to their formation.

We have shown in chapter 7 that the addition of NaCl to CTAC / HFDePC templated silica solutions causes changes in the structure of the final mesopores templated by CTA^+-rich and $HFDePy^+$-rich, respectively. For example, the CTA^+-rich micelle templated pores transform from 2D HCP to wormhole-like, while the $HFDePy^+$-rich micelle templated pores transform from vesicular to wormhole-like. Apparently, the templating mechanism in the interfacial region of the silicate-surfactant mesophase in the presence of added salts can not be simply explained using the well-accepted $\{S^+, I^-\}$ pathway[2], where S^+ refers to a cationic surfactant and I^- represents an anionic silica species. A more refined picture of the surfactant/silica interface is needed that accounts for the influence of ions besides the surfactants and silicates on the pore structure and size distributions. Salt effects have been studied previously, and we address two issues before describing our work:

(1) What general advantages do simple salts provide in the synthesis of micelle templated silica?

Previous work has demonstrated advantages of adding simple salts during the synthesis of surfactant-templated mesoporous materials. First, addition of a small amount of salt has been used to modify the non-ionic surfactant templating process and to produce a bimodal pore system.[3] Second, simple salts can also be used to improve hydrothermal stability of mesoporous silica either during synthesis[4-7] or during postsynthesis treatment[8]. Third, the use of "salting-out" ions can dramatically widen the synthesis domain and broaden the range of surfactants that can be used to produce highly ordered 3D mesostructures.[9] Fourth, simple salts have been used to tune the particle size, pore shape and wall thickness.[8-11] Lin et al.[8] proposed that the effects of the anion of sodium salts (NaX) added during post-synthesis hydrothermal treatment on the pore size and wall thickness of MCM-41 could be explained by an equilibrium between surfactants inside the MCM-41 channels and in solution. For example, anions X^- that bind strongly with cationic surfactant S^+ in solution shifts the equilibrium of S^+/I^- binding to reduce the aggregation number, and thus the pore size. They concluded that the effects of anions X^- follows the binding strength of the Hofmeister series for cationic surfactant micelles, $NO_3^- > Br^- > Cl^- > SO_4^{2-} \sim F^-$. Newalkar et al.[10] demonstrated that the pore size and microporosity within the pore walls of ordered SBA-15 materials can be tuned by means of salt addition under microwave-hydrothermal conditions. Since a non-ionic surfactant is used to produce SBA-15, the mechanism for pore size adjustment by salts is different than for MCM-41. They proposed that hydration of the added salt (NaCl) enhances self-association of the PEO-PPO block copolymers into a nonpolar environment, which reduce the penetration of the PEO blocks into the walls of the SBA-15 framework, leading to decreased microporosity. Last but not least, simple salts are also important in controlling phase structure and morphology. Yu, et al.[7] found that mesophase transformations occur depending strongly on the type and concentration of added salt. When NaCl is added, the pore structure changes from 2D hexagonal columnar phase (HCP) to disordered 2D HCP to ordered 2D HCP to disordered 2D HCP to completely disordered as the addition of NaCl increases. They proposed three effects of adding salt to explain this sequence of transformations to and from ordered phases. They are (1) an increase of silica condensation, (2) screening of anions and (3) perturbation of the double layer potential. The increase of silica condensation decreases the surfactant packing

parameter, inducing the change from 2D HCP to disordered 2D HCP with a small amount of added NaCl. With further increase of NaCl, the screening effect of anions becomes dominant, which increases the surfactant packing parameter, allowing the system to change back to ordered 2D HCP pores. A further increase of NaCl decreases the order of the materials due to the perturbation of the double layer potential. When NH_4Cl is added, the pore structure changes from 2D HCP directly to completely disordered.

To summarize, salts have been widely studied as additives for the synthesis of mesoporous materials, but the roles of salt may be different depending on the type of surfactants (especially nonionic vs. ionic) and synthesis conditions. Still, most general trends can be rationalized based on what is known about salt effects on surface forces and surfactant aggregation.

(2) Are ions besides S^+ and I^- be retained at the interface during synthesis?

In surfactant templated materials synthesis, electrolytes are almost always present - if nothing else, the counterions to the surfactant (often a halide) and to the silanols (hydronium ions). As was just discussed, salts have been proposed to influence many aspects of surfactant templating through their influence on micellization, sol-gel chemistry, and screening of electrostatic interactions. Some studies have also been conducted to determine whether electrolyte ions can compete with S^+ and I^- at the micelle interface, which would cause them to be incorporated into the mesoporous products during synthesis. The initial description the cationic surfactant templating mechanism assumed that the surfactant counter-anions are completely replaced by condensing silicate polymers.[12,13] Recently, Badiei et al.[14,15] used chemical analysis to show that anions (such as F^-, Cl^-, Br^-, NO_3^-, and SO_4^{2-}) can be partly retained in the channels of micelle templated silica prepared in basic media, and concluded that the well-accepted $\{S^+\ I^-\}$ pathway would be better referred as to $\{S^+\ mX^-\ (1-m)I^-\}$ to reflect the competition for binding to S^+. Lin et al.[16] found that the anions in sodium salts affect the condensation rates of the silicate precursors, and they concluded the strength in counter-ion binding of X^- to cationic micelles follows the order: $ClO_3^- > NO_3^- > Br^- > SO_4^{2-}, SO_3^{2-} > Cl^- > F^-$, which agrees with the Hofmeister series. Since strongly adsorbing X^- blocks the adsorption of silicate ions onto micelles and delays the formation of the silica-surfactant mesophase. Thus, weakly binding F^- produces the fastest precipitation. In addition, F^-

anions play a specific role as catalyst for sol-gel reactions,[17] leading to its use for forming nanoporous silica film with ultra-low dielectric constant (κ)[18], and for generating thermally and hydrothermally stable mesoporous silica[19,20]. In these case, F- anions are incorporated into the silica framework by the formation a hypervalent silicon species, which usually requires careful optimization of the molar ratio of F- to surfactant to form well-ordered materials.[21] Specific anions have been studied, like SO_4^{2-}, and found to show good improvements in the long-range order of MCM-41 materials.[22] Effects of various anions on the formation of mesoporous molecular sieves have been reviewed by Leontidis et al.[23] and Pastore et al.[24]

In contrast to anions, cations generally produce weaker "Hofmeister" effects. Corma et al.[25] found that the cations of added salts, such as tetramethylammonium (TMA+), tetraethylammonium (TEA+) and Na+, can also be incorporated in the mesoporous products during the synthesis, although Na+ is included into the final solid in a lower molar fraction than the others. The cations are found to replace some cationic surfactant species at the micelle interface, and therefore increase the pore size. At a fixed temperature, a higher content of cations retained in the products is correlated with a larger pore size. Na+ seems to show a weaker swelling effect than TMA+ or TEA+. Das et al.[4] found by 29Si MAS NMR that the presence of cations such as Na+ and TEA+ seems to facilitate increased condensation of the silanol groups during the formation of the mesostructure. However, the roles of specific cations are still not entirely clear. Recently, Echchahed, et al.[26] investigated ion effects on the phase transition of cationic micelle templated silica from lamellar to cubic to hexagonal, and proposed that water also needs to be included as a species at the micelle interface $\{(1-p)S^+, pC^+, mH_2O, nX^-, (1-n)I^-\}$. The added salt plays a mediating role in the electrical balance at the interface that sometimes leads to a slight charge density mismatch that can change the mesophase of the final silica products.

Since it is clear from the literature reviewed above that salt ions influence the assembly of surfactants and silicates, and are retained at the micelle interface during synergistic precipitation, in this chapter, we will investigate how salt ions (both cations and anions) affect the pore structure, particle morphology, and especially the pore size distributions of final products prepared using mixed hydrocarbon/fluorocarbon

surfactants as templates. In bulk solution, the addition of salt not only changes the phase behavior and aggregate properties of mixed hydrocarbon and fluorocarbon surfactant solutions, but also affects their mixing, as reported by Asakawa et al.[27,28]. Based on fluorescence-quenching measurements[27], they found that the addition of sufficient salt (LiCl) tends to increase the micellar size to form large mixed micelles with intramicellar phase separation for both lithium perfluorononanoate (LiPFN) / lithium dodecyl sulfate (LiDS) and lithium perfluorooctylsulfonate (LiFOS) / LiDS mixtures. The hydrophobic chain of the surfactant give access to the neighboring hydrocarbon chain due to the presence of sufficient counterions, and the hydrocarbon and fluorocarbon surfactant each form islands in the large mixed micelle due to mutual immiscibility of the chains. Based on conductivity measurements[28], Asakawa et al. compared the effects of diethylammonium (DEA$^+$) and Li$^+$ counterions on the immiscibility of fluorocarbon and hydrocarbon surfactants in mixed micelles, and found that DEA$^+$ binds more strongly to fluorocarbon micelles than Li$^+$ due to hydrogen bond and/or hydrophobic interactions. A smaller amount of DEA$^+$ relative to Li$^+$ increases both the growth of fluorocarbon-rich micelles and the miscibility of fluorocarbon and hydrocarbon surfactants.

In addition to salt addition, organic additives (oils) have been used in mesoporous materials synthesis solutions to change the properties of the final product.[29-40, 42-47] Hydrocarbon oils strongly affect surfactant aggregation in aqueous solution[29,38,44], thus affecting the mesoporous structure. When oil is added in the synthesis sols, there are two kinds of effects on self-assembled micelles. One is a "penetration effect", in which oil molecules penetrate into the surfactant palisade layers and increase the effective headgroup area. The other is a "swelling effect", in which oil molecules form a core inside the micelles and swell the volume of micelles. Both effects may coexist, depending on how oils partition.[29] In mesoporous material synthesis, the goal of adding organic additives is usually to swell micelle templates in the initial solutions. 1, 3, 5-trimethylbenzene (TMB)[30-33], triisopropylbenzene (TIPBz)[34], amines[35], polypropylene glycol (PPG)[36] and alkane[31, 37-39] have been used as swelling agents for mesoporous silica. TMB is usually used for the expansion of mesopores templated by hydrocarbon surfactants or copolymers. For example, Zhao et al.[30] used TMB to enlarge the pore size of SBA-15 from 10 nm to 30 nm. Ottaviani, et al.[32] utilized TMB to swell the

cetyltrimethylammonium bromide (CTAB) micelles, and found ^{1}H NMR and EPR evidence that TMB is partly localized around the headgroups of CTAB. Blin et al.[39] explored using a pair of organic additives to tailor the pore size of mesoporous silica. They concluded that jointly incorporating decane and TMB in the synthesis solution allows larger expansion of the pore size than each oil on its own. For polyoxyethylene dodecyl ether ($C_{12}EO_n$)-water system[40], Kunieda et al. has proposed a mechanism to interpret the change of phase behavior of liquid crystal upon addition of different organic additives.

In addition to hydrocarbon amphiphiles, fluorocarbon surfactants have also been used as templates in the synthesis of mesoporous materials due to their high thermal stability.[41] Since fluorinated surfactants allow co-solubilization of water and perfluorocarbons,[42-44] some perfluorocarbons have been incorporated in fluorinated surfactants as organic additives.[29,45,46] Blin et al.[45] found that the liquid crystal phase of $CF_3(CF_2)_7C_2H_4$-$(OC_2H_4)_9OH$ plus water can incorporate up to 14 wt% of perfluorodecalin (PFD) at 20 °C, whereas only 1 % of a hydrocarbon oil can be incorporated into the hydrophobic core of the micelles (L_1). They investigated the effect of fluorocarbon addition on the pore size and structure of mesoporous materials prepared with non-ionic fluorinated surfactants.[46] They showed that perfluoroheptane and PFD both can be incorporated into the HCP phase to swell the micelles, while perfluorooctane only penetrates between the hydrophobic chains of the mesophase without swelling the micelles, so neither the structure nor the pore sizes are modified. In some cases, hydrogenated oil has been used as an effective agent for improving the hexagonal ordering during synthesis of mesoporous silica materials with semi-fluorinated surfactants as template.[47]

In this chapter, we first show the effects of salt type (both cation and anion effects) on the phase and pore size distributions of silica materials templated with combined CTAC and HFDePC surfactants, and demonstrate that the sizes of pores templated by CTAC-rich or HFDePC-rich micelles can be independently tailored by adding organic additives that selectively partition into one type of micelle. Finally, we investigate the effect of the alkyl chain length of the fluorinated surfactant on the occurrence of demixed micelle templating and on the structure of the material.

8.2. Experimental section

8.2.1. Materials

Cetyltrimethylammonium chloride, CTAC (98%+) and tetraethylorthosilicate, TEOS (98%), were purchased from Sigma. 1H, 1H, 2H, 2H-perfluorooctylpyridinium chloride (HFOPC), HFDePC and 10-perfluorooctyldecylpyridinium bromide (PFODPB) were synthesized as described previously by researchers in the group of Hans Lehmler at the University of Iowa.[48] The molecular structures of these surfactants are shown in Figure 8.1. Concentrated aqueous ammonia (29 wt% NH_4OH, Merck), deionized ultra-filtered (DIUF) water (Fisher Scientific), NaCl (Merck KGaA), NaF (MCB), KCl and $NaNO_3$ (Mallinckrodt), CsCl (Aldrich), NH_4Cl (EMD) and TEACl (Fluka) were used as received for material synthesis. Hydrogenated solvent TMB and fluorinated solvent PFD (95 wt%) were purchased from Aldrich. Concentrated aqueous HCl (ACS grade, Fisher Scientific) and anhydrous ethanol (Aaper Alcohol and Chemical) were used for surfactant extraction.

8.2.2 Silica materials synthesis

The synthesis of mesoporous silica materials was carried out in dilute solution of CTAC, HFDePC (or HFOPC or PFODPB) and silica precursor under mild basic conditions. We prepared five series of samples to investigate the effects of the types of salt added, the types of organic additives, and the alkyl chain length of the fluorocarbon surfactants. For all the samples in this chapter, the molar ratio of hydrocarbon surfactant to fluorocarbon surfactant was equal to one, and the total molar concentration of mixed surfactant was kept constant. The initial molar composition of reactants used for the synthesis of silica materials are: TEOS : H_2O : HFDePC (or HFOPC or HFOdPB) : CTAC : NH_3 : MCl (or NaX) : TMB(or PFD) = 1 : 148 : 0.06 : 0.06 : 10 : 2.8 : x TMB (or PFD) where $x = 0$ for all solutions unless specified otherwise. In a typical synthesis procedure, the calculated amounts of CTAC and fluorinated surfactant were mixed with DIUF water, concentrated aqueous ammonia and the salt. The mixture was vigorously stirred at room temperature for at least 30 min to completely dissolve the surfactants. If used, organic additives were then added and stirred for another 2 hr to attain equilibrium. The required amount of TEOS was slowly added and the solution was aged for 24 hr at room temperature with gentle stirring (~100 rpm). After the TEOS was added, we

observed that the initially transparent solutions became turbid at different times, depending on sol composition. To allow direct comparison, the size of reactor vessel, the stir bar, the stirring speed, and the TEOS addition rate were kept the same for all of the samples. The precipitate was isolated by filtration, dried in air, and the surfactants were removed by washing twice with an acidic mixture of 6 % concentrated HCl and 94 % ethanol. The washing time for each step was 24 hr.

8.2.3. Characterization

X-ray diffraction patterns were obtained with a Siemens 5000 diffractometer using Cu K_α radiation (λ = 1.54098 Å). Scanning electron microscope (SEM) images were obtained with a Hitachi S-900 microscope. Solid samples were loaded onto PELCO carbon tabs, then coated with gold under vacuum prior to SEM imaging. Transmission electron microscope (TEM) images were collected with a JEOL 2010F electron microscope operating at 200 kV. Solid samples were dispersed in isopropanol by sonication and then deposited onto lacey carbon grids for TEM observation. Nitrogen sorption measurements of extracted examples were performed with a Micromeritics Tristar 3000 automated gas sorption analyzer. All samples were degassed at 120 °C for 4 hr under flowing nitrogen prior to measurements. The pore size distributions (PSDs) were calculated using modified BJH method of Kruk, Jaroniec and Sayari (the KJS method) from the adsorption branch of the isotherms.[34] For some samples with bimodal pore size distributions, volumes of each size of pore was determined by extrapolation from regions of α_s plots corresponding to filling of each pore population.

8.3. Results and discussion

8.3.1. Effect of the type of salt

A series of samples labeled a-1 through a-5 shows the effect of salt cations (M^+) on templating with the mixed surfactant system. The salts are chlorides of Na^+, K^+, Cs^+, NH_4^+ and TEA^+, respectively. Sample a-1 (prepared with NaCl) is the base sample in this series.

Figure 8.2 shows the nitrogen sorption isotherms and calculated PSDs of this series of samples. Pore texture parameters extracted from the isotherms such as the BET surface area (S_{BET}), total surface area (S_t), external surface area (S_{ex}), primary mesopore volume

216

(V_p), and total pore volume at $p/p_o=0.95$ (V) for all samples are compiled in Table 8.1. The determination of these quantities was done using the methods described in chapter 7.

All samples have type IV isotherms, which are characteristic of materials with uniform mesopores. Samples a-3 and a-5, like most mesoporous materials, possess inflection corresponding to capillary condensation, but samples a-1, a-2 and a-4 show two inflections, corresponding to capillary condensation in two populations of well-defined pores with different sizes. Since both the concentration of Cl^- and ionic strength are constant for this series of samples, the differences in the shape of the isotherms result from the type of cations used. Sample a-5 shows a slight upturn at high relative pressure, indicating textural porosity between clusters of particles in the products formed in the presence of TEACl. The PSDs confirm the change of pore diameters by the position of the inflections in the isotherms. Samples a-1, a-2 and a-4 show bimodal PSDs, while a-3 and a-5 show unimodal PSDs. The bimodal distributions are associated with separate $HFDePy^+$ templated pores and CTA^+ templated pores. The sharpness of peaks corresponding to two pore sizes is greatest for NH_4Cl (sample a-4). From these three samples, we observe a simultaneous increase of both pore sizes when the cation is changed from Na^+ to K^+ to NH_4^+, which shows, as suggested by Echchahed et al[26], that added cations can be incorporated at the micelle-material interface. Similar to anions, cations in salts are also expected to be involved in the perturbation of the double layer potential around micelles.[2] With Cs^+ and TEA^+, bimodal mesoporous materials are not be obtained under the same synthesis conditions, and the pore sizes are intermediate between the two pore sizes in the bimodal materials. The formation of unimodal pores, instead of bimodal pores, suggests that the miscibility of $HFDePy^+$ and TMA^+ can be enhanced by specific chloride salts. In other words, the composition of micelles that are segregated in the absence of salt can be changed by adding simple salts [27].

Presumably, the cations are incorporated at the micelle/silica interface, but the question is how to explain the effect of cation type. All cations used here are of the same charge, so size is the next most likely property that can explain the observed effects. The size of ions not only defines the excluded volume interaction in solution and at interfaces, but also determines the strength of the electric field around an ion and its polarizability[22]. In aqueous solution, the hydrated radius of the cations used here follows the following

order: K^+ (3.3 Å) ~ NH_4^+ ~ Cs^+ (3.3 Å) < Na^+ (3.6 Å) < TMA^+ (3.7 Å) < TEA^+.[49] Obviously, the size of hydrated cations is not a good explanation for the cation effect on pore structure; for instance, K^+ and Cs^+ have the same hydrated radius but produce different PSDs in the final products. The order of the strength of the Hofmeister effect for these cations is: $TMA^+ > NH_4^+ > Cs^+ > K^+ > Na^+$, which also does not correlate with the trends in Fig. 8.2 since, for instance, K^+ and NH_4^+ produce bimodal PSD, but Cs^+ unexpectedly produces a unimodal PSD. However, we find that the PSD trend does follow the order of molar aqueous ionic volume for this series of cations, Na^+ (-6.7 cm^3/mol) < K^+(+3.5 cm^3/mol) < NH_4^+(+12.4 cm^3/mol) < Cs^+ (+15.8 cm^3/mol) < TMA^+(+84.1 cm^3/mol).[50] This can be explained by cations with large ionic volume (Cs^+ and TEA^+) more effectively expelling cationic surfactants from interfaces than smaller Na^+, K^+ and NH_4^+ cations, which may reduce interactions between the surfactants and allow CTA^+ and $HFDePy^+$ to mix. The textural properties such as S_{BET}, S_{ex}, S_t and V_p also depend on the kind of salt added. Both V_p and S_{BET} are greatly reduced for sample a-3, suggesting that addition of cations with large molar ionic volume is not favorable for cationic surfactant templating.

Powder x-ray diffraction (XRD) patterns for this series of samples are shown in Figure 8.3. Except for sample a-3, all other samples show only one intense peak, indicating that a poorly ordered wormhole-like structure is formed. The peak position represents an average pore-pore distance. As discussed in chapter 7, the addition of salts results in the formation of wormhole-like materials, similar to the way that salt causes micelles to coalesce and form less-ordered aggregates in some surfactant solutions.[51,52] Sample a-3 exhibits very weak reflections, consistent with the strongly disruptive effect of Cs^+.

Representative TEM images of this series of samples are compared in Figure 8.4. Basically, all samples show wormhole-like mesopores. No long-range order is found from the micrographs or the electron diffraction pattern for this series of samples. Consistent with the PSD and XRD results, sample a-3 appears to have less short-range order in the uniformity of the pores.

Figure 8.5 shows the effect of the type of cations on the morphology and particle size of this series of samples after extraction. The SEM images show that all samples

consist of small particles, which flocculate together to form large solid aggregates. The morphologies of samples a-1 and a-2 are both smooth spherical particles with uniform particle size distributions. However, the particles synthesized with KCl are about three times larger than those prepared with NaCl. Sample a-3 consists of small rough particles. Sample a-4 consists of a bimodal distribution of spherical particles. The large particles are 300-500 nm in diameter, while small particles are ~100 nm. Particles with similar size appear to flocculate together. From TEM, both small and large particles have similar wormhole-like pore structures but different pore sizes, indicating that small and large particles are templated by different type of micelles. The particle size distribution observed by SEM suggests that NH_4Cl favors microphase separation of CTA^+-rich/silica and $HFDePy^+$-rich/silica aggregates. The segregated micelles of CTA^+ and $HFDePy^+$ in the solution co-assemble with silicate species separately and finally form co-existing but bimodal sizes of silica particles. Sample a-5 consists of irregular, rough 200-300 nm particles. The difference of particle size may reflect differences in nucleation and precipitation rates for different salts. For this series of samples, sample a-4 shows the earliest onset of turbidity in this series samples.

We also examine the effect of anions (X^-) of sodium salts on the PSD. Because both CTA^+-rich and $HFDePy^+$-rich micelles are positively charged, their properties are expected to be strongly affected by type of anion. Samples b-1 through b-3 were prepared using NaX as the salt, where X is F^-, Cl^- or NO_3^-, respectively. For this series of samples, the onset of turbidity was fastest for sample b-1, slower for sample b-2, and slowest for sample b-3.

The nitrogen sorption isotherms and calculated PSDs are shown in Figure 8.6. All samples have type IV isotherms, but different extents of hysteresis. Sample b-1 and b-3 have type H2 hysteresis loops with triangular shape, while sample b-2 displays no hysteresis. In contrast to sample b-1, samples b-2 and b-3 show two well-defined capillary condensation steps. The calculated PSDs of samples b-2 and b-3 confirm bimodal PSDs. The two pore sizes of sample b-3 are 4.6 nm and 6.5 nm, which are far larger than those of b-2. Sample b-1 has a broad, diffuse pore size distribution. This suggests that NO_3^- has stronger binding strength for cationic micelles than Cl^- and F^-. The addition of NO_3^- screens the electrostatic repulsion between hydrophilic groups in

micelles more than Cl$^-$ and F$^-$, thereby allowing both types of micelles to expand significantly.[28] In contrast to partially hydrated Cl$^-$ and NO$_3^-$ ions, F$^-$ anions are fully hydrated and do not shield electrostatic interactions effectively.[23] F$^-$ also catalyzes rapid precipitation of silica, which may contribute to the disordered, broad pore size distribution. The other pore parameters are listed in Table 8.1. Consistent with its uniform PSD, the mesopore volume V$_p$ and surface area S$_{BET}$ of sample b-2 are the highest of this series of samples.

Figure 8.7 shows the effect of anion type on the morphology and particle size of this series of extracted samples. The SEM images of all samples show that they are predominantly smooth spherical particles. There are two apparent differences for this series of samples. One is their particle sizes, which increase in the order b-1 $\leq$ b-2 < b-3. This suggests that weaker binding strength of anions to cationic micelles increase the precipitation rate (most importantly, the nucleation rate of particles), leading to smaller particle sizes. The other difference is the distribution of particle shapes. Other than spherical silica particles, sample b-1 has some foam-like particles and sample b-3 has some sheet-like particles. There are no other shapes of particles observed in sample b-2, even after extensive searching.

From these two series of samples, we conclude that the type of salt significantly affects the morphology, particle size and PSDs of CTAC/HFDePC templated silica. With the addition of salts having small cation volumes and weakly associated anions including NaCl, KCl and NH$_4$Cl, the materials prepared show bimodal mesoporosity, and both pore sizes can be adjusted by changing the cation. Cations with large hydrated ion volume (Cs$^+$ and TEA$^+$) are found to promote the mixing of CTAC and HFDePC, thus producing silica materials with unimodal PSD. In addition, we find that the effect of anions X$^-$ on the PSD follows the binding strength of Hofmeister series for cationic surfactant micelles even in the mixed cationic CTAC/HFDePC system.

8.3.2. Effects of organic additives

In dilute solution, solutions containing CTAC and HFDePC micelles have been shown to demix into CTA$^+$-rich micelles and HFDePy$^+$-rich micelles over a wide range of compositions.[53] With addition of appropriate type and amount of NaCl, KCl or NH$_4$Cl, we have shown that bimodal mesopores form during templating that are consistent with

preserving separate populations of CTA$^+$-rich and HFDePy$^+$-rich micelles from the solution phase. In contrast to the hydrogenated core of CTA$^+$ micelles, the fluorinated core of HFDePy$^+$ is not only hydrophobic but also lipophobic. The different solvent affinities in the cores of the two kinds of micelles provide opportunities to independently tailor the bimodal PSD by controlled swelling of micelles. Scheme 8.1 shows the hypothesized selective swelling of CTA$^+$-rich and HFDePy$^+$-rich micelles by different solvents. TMB, a hydrogenated oil, is expected to preferentially dissolve in the hydrocarbon core of CTAC micelles and to swell them. As a fluorophilic oil, PFD is expected to preferentially swell HFDePC micelles. Assuming that this preferential swelling occurs in the silica/surfactant particles that precipitate from solution, tuning of the bimodal PSD will result.

To test this hypothesis, a series of samples containing TMB additives is first discussed. The composition of the sols is detailed in the experimental section, and we set x = TMB/TEOS equal to 0, 0.054, 0.228, 0.30, 0.44 and 0.61 for samples c-1 through c-6 (where c-1 is the base sample).

Figure 8.8 shows nitrogen sorption isotherms and calculated PSDs for this series of extracted samples. All samples have type IV isotherms, and samples c-2 through c-6 have type H2 hysteresis loops at relative pressure of 0.35-0.7. Two capillary condensation steps can be clearly identified, indicating that all samples are bimodal mesoporous materials. Sample c-2, prepared with small amount of TMB, shows a shift of the second inflection to higher relative pressure (approaching $p/p_0 = 0.4$) and a small hysteresis loop. This suggests that TMB molecules swell CTA$^+$-rich micelles, which leads to non-uniform pores or branching, and hence to type H2 hysteresis.[54] With more TMB, the second adsorption step gradually shifts to higher relative pressure of 0.65. The hysteresis loop grows in area and is associated with the second adsorption step, which is consistent with increased swelling of CTA$^+$-templated pores. With the increase of TMB, the relative pressure corresponding to the first adsorption step increases only a little, indicating that TMB has slight solubility inside the fluorocarbon cores. The calculated PSDs confirm the bimodal PSDs of all samples. Figure 8.9 compares both pore sizes from the bimodal distribution and the corresponding pore volumes for this series of samples. This figure clearly shows that as TMB is added, the CTA$^+$-rich micelle templated pore diameter

increases from 3.8 up to 6.5 nm, while the HFDePy$^+$-templated pore diameter increases only slightly. Correspondingly, the CTA$^+$-rich templated pore volume gradually increases until a plateau, while the HFDePy$^+$-rich templated pore volume keeps almost constant as TMB increases. The plateau in the degree of swelling suggests that the largest amount of TMB that can be incorporated into the core of CTAC-rich micelles is about 0.44 TMB per TEOS. Other structure parameters of this series of samples are shown in Table 8.1. The total mesopore volume, V_p, increases from 0.63 to a maximum of 1.04 as the amount of TMB increases, but as Fig. 8.9 shows, this is entirely due to swelling of the CTA$^+$-rich micelles. The BET surface area S_{BET}, V_p and S_t all reach maxima in sample c-5. An excessive amount of TMB (beyond 0.44 TMB/TEOS) decreases the pore volume and total surface area of the final products because the porous network becomes unstable.

Figure 8.10 shows XRD patterns of this series of samples c-1 through c-5 as a function of the amount of TMB. All samples have broad peaks showing poor long-range order. For samples c-1 and c-2, the broad peak includes two reflections, which correspond to the average pore-pore distance of CTA$^+$-templated pores and HFDePy$^+$-templated pores, respectively. With addition of TMB, the reflection of CTA$^+$-templated pore shifts to lower 2θ due to the swelling effect, and eventually the reflection moves outside of the range that we can detect, whereas the reflection of HFDePy$^+$-templated pores shifts only slightly to lower 2θ as shown in sample c-3 through c-5.

As shown in Figure 8.4, the base sample (c-1) has wormhole-like pores. Due to the small difference (only 0.5 nm) in pore size between CTA$^+$-templated mesopores and HFDePy$^+$-templated mesopores in sample c-1, it is difficult to determine how the bimodal pores are distributed within the particles by TEM. Fortunately, adding TMB increases pore size difference, so we can observe the location of the pore domains by electron microscopy. Figure 8.11 presents a representative TEM image of sample c-5, illustrating that pores of different sizes (~4 nm and ~6 nm) are randomly distributed and both lack long-range order. Both sets of mesopores are present in a 'homogeneous' mixture throughout the entire sample. For the single particle in Figure 8.11a, we collected a scanning transmission electron micrograph (STEM) (Figure 8.11b) with a high resolution probe with a diameter of 2 nm. The depth of field for this sample is

between 50-100 nm. The STEM image shows 3D interconnected worm-hole like pores with non-uniform pore size, all within a single particle, suggesting that the CTA^+-rich templated pores are intimately mixed with $HFDePy^+$-rich templated pores.

Representative SEM images of samples c-1, c-3 and c-5 are shown in Figure 8.12. All samples are composed of smooth round particles that are flocculated into large aggregates. However, the particle shape and size change as more TMB is added. The morphology changes from uniform spherical particles to irregular particles with more TMB. The size of particles increases from ~ 100 nm in sample c-1 to micron-scaled aggregates in sample c-5 as the molar fraction of TMB increases, which can be explained by a reduction in the rate of precipitation as TMB is added – perhaps because TEOS associates with excess TMB. For this series of samples, we observe that the onset of turbidity starts later and the amount of final precipitates decreases as more TMB is added.

In addition to adding TMB, we investigate the selective swelling of fluorophilic domains with PFD. Samples d-1 through d-6 have the molar composition discussed in the experimental section, with x = PFD/TEOS = 0, 0.02, 0.36, 0.56, 0.86 and 1.08, respectively (d-1 is the base sample). Figure 8.13 shows nitrogen sorption isotherms and PSDs for this series of extracted samples. All samples have type IV isotherms. Sample d-1, d-4, d-5 and d-6 clearly show two adsorption steps, while samples d-2 and d-3 appear to have only one adsorption step. Two dashed lines on the isotherm plots indicate the shift of capillary condensation steps corresponding to CTA^+-templated mesopores and $HFDePy^+$-templated mesopores, respectively. Without added PFD, the pore size templated by $HFDePy^+$ is below the pore size templated by CTA^+. However, as PFD is added, this inflection shifts to larger relative pressure, and eventually an inflection at a relative pressure larger than the step for CTA^+-templated pores appears. The capillary condensation step corresponding to CTA^+-templated mesopores only has a very small shift to higher relative pressure as PFD is added. This suggests that the added PFD preferentially swells the fluorinated $HFDePy^+$-rich micelles and that these swollen micelles preserved in the templated materials. It is difficult to be sure that swelling of the $HFDePy^+$-templated pores is responsible for the overlap of pore sizes in samples d-2 and d-3 (rather than surfactant mixing) but a separate experiment showed that PFD does not swell the pores of CTAC-templated materials significantly (results not shown here). Along with the crossover of the two dashed lines

223

due to the preferential swelling of fluorinated micelles by PFD, type H2 hysteresis loops start to appear in sample d-2, and gradually increase in area as the PFD amount increases, suggesting that the swelling of HFDePy$^+$-rich micelles by PFD distorts the final pore channels. The calculated PSDs confirm our analysis of the isotherms. Figure 8.14 compares the sizes and volumes of each population of pores in this series. Adding PFD increases the diameter of HFDePy$^+$-rich micelle templated pores from ~ 3.3 to 5.8 nm, whereas the CTA$^+$-templated pore diameter only increases slightly, from 3.7 nm to 3.9 nm. Correspondingly, the HFDePy$^+$-rich templated pore volume gradually increases until a maximum is reached, while the CTA$^+$-rich templated pore volume keeps almost constant as PFD increases. From this series of samples, we found that only 0.02 mol of PFD (per mole TEOS) can be incorporated into CTA$^+$-rich micelles, in contrast to 0.86 mol of PFD incorporated into HFDePy$^+$-rich micelles. In addition, the peak of the PSD in sample d-3 is sharper than in sample d-2, indicating that the pore size of HFDePy$^+$-templated mesopores most closely matches that of CTA$^+$-rich templated mesopores when 0.36 mol of PFD is used. The other pore properties are summarized in Table 8.1. The main observation is that the total mesopore volume increases from 0.6 cm^3/g to 0.74 cm^3/g as more PFD is used in the synthesis, mainly due to HFDePy$^+$-rich micelle swelling.

XRD patterns for members of this series after extraction are shown in Figure 8.15. All samples show poorly ordered wormhole-like structure. In contrast to sample d-1, the addition of a small amount of PFD improves the ordering, as indicated by more intense primary and secondary reflections in samples d-2 and d-3. The strong peaks at the lowest angle represent the average pore-pore distance, and gradually shift to lower 2θ as more PFD is used. Presumably the strong peak in each sample includes two reflections, from mesopores templated by CTA$^+$-rich and HFDePy$^+$-rich micelles. The position of the two reflections is too close to be resolved for samples d-1 through d-3, however. Continued swelling of HFDePy$^+$-rich micelles eventually shifts the reflection from pores templated by HFDePy$^+$-rich micelles to an angle low enough to resolve, as shown in sample d-4. The lower-angle peak of sample d-4 gives a spacing of 5.3 nm between HFDePy$^+$-micelle templated pores, and the higher peak indicates 4.6 nm between CTA$^+$-micelle templated pores. These results are consistent with the calculated PSDs.

The pore structure and morphology of particles were examined by TEM and SEM. Generally, the particle size increases as more PFD is used, and the pore structure of this series of samples show poorly ordered wormhole-like pores. Representative TEM and SEM images of sample d-4 are shown in Figure 8.16.

From the two series of samples prepared by swelling segregated hydrocarbon-rich and fluorocarbon-rich micelles by corresponding lipophilic and fluorophilic oils, we have successfully demonstrated that the bimodal PSDs of silica materials can be finely tailored by selecting different organic additives. In addition, the amount of added oil affects the onset of turbidity, the final pore volume, particle size and particle morphology. This finding can be extended to incorporate different metal oxides within different mesoporous channels by solubilizing appropriate lipophilic and fluorophilic metal complexes within the different channels. A preliminary study shows that the hydrogenated metal complex $Cr(acac)_3$ can be preferentially deposited within CTA^+-rich micelle templated channels. Attempts with hexafluoro-acac complexes led to less selective metal oxide deposition, most likely because they are not fluorophilic enough.

8.3.3. Effect of alkyl chain length

As a final exploration of methods to tune the pore size distribution in demixed hydrocarbon/fluorocarbon surfactant templated materials, a series of samples was prepared with variable fluorocarbon chain length in the presence of CTAC and NaCl, with compositions indicated in the experimental section. Surfactants HFDOPC, HFDePC, and HFODPB were used to prepare samples e-1, e-2, and e-3, respectively (e-2 is the base sample).

Figure 8.17 shows the nitrogen sorption isotherms and PSDs for this series of extracted samples. All isotherms are of type IV, with sample e-3 showing a type H2 hysteresis loop at a relative pressure of 0.4-0.5. Compared with sample e-1 and e-3, only e-2 sample shows two step capillary condensations. The calculated PSDs confirm that samples e-1 and e-3 each have narrow unimodal PSDs while the base sample (e-2) has a bimodal PSD. The unimodal PSDs suggest that fluorocarbon and hydrocarbon surfactants mix in samples e-1 and e-3. HFDOPC has a fluorocarbon segment with only six carbons, compared to the eight fluorocarbon segments in HFDePC. This small change in structure reduces the lipophobicity of HFDOPC enough that demixing is not

225

observed. This result is in agreement with the miscibility study of fluorocarbon and hydrocarbon surfactants by Shinoda et al., who concluded that a fluorocarbon chain with at least 8 carbons is necessary to cause micelle demixing in combinations of hydrocarbon and fluorocarbon surfactants.[55] The pore size of the final products is 3.8 nm, similar to that of materials templated with CTAC alone, suggesting that the longer tails of CTAC govern the pore size and structure. For sample e-3, although HFODPB has a fluorocarbon tail with 8 carbons, a large decamethylene spacer separates the pyridinium head group and the fluorocarbon tail. It is reasonable that mixed micelles of CTAC and HFODPB can be formed due to attractive interactions between CTA^+ hydrocarbon tails and hydrocarbon spacers of PFODPB. The pore size of 4.5 nm of final products suggests that the CTAC surfactants penetrate inside of the palisade of HFODPB micelles driven by van der Waals interactions between of the spacers of PFODPB and CTA^+ tails. Although HFDePC also has two methylene groups, they are too short to provide an effective interaction with long hydrocarbon chains.[56] Asakawa et al[53,57] even suggested that for small globular micelles, one or two methylene groups in HFDePC may be outside the micelle core. Based on the increase in pore size for sample e-3, it seems that HFODPB governs the pore size and structure. Other pore parameters in this series are given in Table 8.1.

The XRD patterns of this series of samples are shown in Figure 8.18. All samples have wormhole-like pores due to the amount of NaCl in the synthesis solutions. Compared with sample e-2, the structure of e-1 and e-3 improved due to enhanced mixing of surfactant micelle.

Representative TEM images of samples e-1 and e-3 are shown in Figure 8.19, which confirm the wormhole-like structure of these samples. Consistent with the PSD measurements, the TEM of e-3 shows larger pores than e-1 and they appear to be organized into more of a network. The morphology of all samples in this series consists of flocculates of small, uniform spherical particles. SEM images of samples e-1 and e-3 are shown in Figure 8.20. The particle sizes follow the order e-2 < e-3 < e-1.

From this series of sample, we can conclude that the fluorocarbon surfactant with large hydrocarbon spacers (at least > 2 carbon) or short fluorocarbon tail (< 8 carbon) allows fluorinated surfactants to mix with CTAC, leading to a unimodal PSD in the final

materials when they are combined as templates. In the mixed micelles formed in samples e-1 and e-3, the pore size appears to be determined by the length of the longer surfactant tail.

8.4. Conclusions

Effects of different type of salts (MCl and NaX), organic additives (TMB and PFD) and alkyl chain length of fluorocarbon surfactant (hydrocarbon spacer and fluorocarbon tail) on the pore size distributions (PSDs), ordering, particle sizes and particle morphologies of mesoporous silica templated with combined fluorinated and hydrocarbon surfactants have been investigated.

We found that particle morphology and PSDs are sensitive to the type of salt used. When MCl was added to the initial solution composed of hydrocarbon and fluorocarbon mixtures, the ionic volume of M^+ influences the PSDs of the products. A large cationic volume of M^+ (for example in Cs^+ or TEA^+) promotes mixing of fluorocarbon and hydrocarbon micelles, which is not favorable for the formation of bimodal mesopores. When NaX was added, the binding strength of X^- to cationic micelles is crucial for the particle sizes and PSDs. Weak binding of X^- to cationic micelles allows fast precipitation, leading to smaller particles. Weak binding also allows demixing to occur, leading to a bimodal PSD, which is consistent with the Hofmeister effect.

In addition to adding salts, we have confirmed that the two populations of micelles can be independently swollen by adding a lipophilic oil (TMB) to swell the hydrogenated cores of CTA^+ micelles or a fluorophilic oil (PFD) to swell the fluorinated cores of $HFDePy^+$ micelles. The pretreated micelles serve as templates during the hydrolysis of TEOS in aqueous ammonia to form silica particles with controlled bimodal mesoporosity. Increasing the amount of either oil delays the onset of turbidity, increases the particle size, and decreases the yield of particles. This effect suggests that excess oil may mix with unhydrolyzed TEOS and shield it from the solution, thus delaying its hydrolysis and precipitation.

Finally, we found that the structure of the partially fluorinated tail in the surfactant must be well designed to allow demixing to be observed when it is combined with CTAC. We found that a fluorocarbon surfactant with a long hydrocarbon spacer (at least >2 carbon) is able to mix with CTAC, which is consistent with a favorable interaction

among long alkylene chains. Short fluorocarbon tails (< 8 carbons) also allow mixing with CTAC surfactant, thus causing the formation of unimodal PSD of final silica materials. When mixed micelles are formed, the pore size of the product seems to be governed by the surfactants with longer tails.

Table 8.1. Pore structure parameters of all mixed-surfactant-templated mesoporous silica materials after extraction.[a]

Name	S_{BET} (m²/gm)	V_p[b] (cm³/gm)	$V_{@p/po=0.95}$ (cm³/gm)	V_m (cm³/gm)	W_{KJS} (nm)	S_t[b] (m²/gm)	S_{ex}[b] (m²/gm)
a-1	934.2	0.63	0.70	0.025	3.3, 3.8	788.8	44.1
a-2	792.4	0.61	0.64	0.0015	3.4, 3.9	670.8	19.4
a-3	451.7	0.30	0.34	0.023	3.5	392.3	30.5
a-4	868.4	0.67	0.70	0.025	3.6, 3.9	742.9	20.7
a-5	888.8	0.42	0.65	0.0029	3.6	730.7	164.6
b-1	487.9	0.46	0.54	0.0065	3.6, 4.0	398.8	53.9
b-3	667.1	0.55	0.60	0.074	4.6, 6.5	429.9	31.8
c-2	871.9	0.65	0.71	0.019	3.3, 4.2	731.1	42.0
c-3	890.5	0.75	0.79	0.014	3.4, 4.7	744.7	24.7
c-4	900.2	0.86	0.91	0.022	3.7, 5.2	770.3	35.6
c-5	938.7	1.04	1.11	0.031	3.7, 6.5	809.6	46.5
c-6	882.4	0.87	1.00	0.020	3.2, 6.5	761.6	92.5
d-2	859.7	0.66	0.71	0.011	3.9	713.2	33.4
d-3	857.2	0.69	0.74	0.024	3.9	732.3	35.2
d-4	854.1	0.70	0.78	0.0061	3.9, 5.2	714.5	36.0
d-5	852.1	0.74	0.80	0.011	3.9, 5.8	716.1	39.1
d-6	863.2	0.75	0.79	0.0067	3.9,5.6	718.0	28.2
e-1	954.8	0.67	0.71	0.045	3.8	828.0	23.7
e-3	765.2	0.62	0.74	0.033	4.5	683.5	89.1

a. S_{BET} = BET surface area,[58] the adsorbed volume $V_{p/po=0.95}$, W_{KJS} = pore diameter at peak of KJS pore size distribution, V_p = total mesopore volume, the micropore volume $V_m = I \times 0.001547$ (cm³) where I represents the Y-intercept in the V-α_s plot, S_t = total specific surface area, S_{ex} = external specific surface area.

b. Calculated using α_s comparative nitrogen adsorption plots.[59]

CTAC

HFDePC

HFDOPC

PFODPB
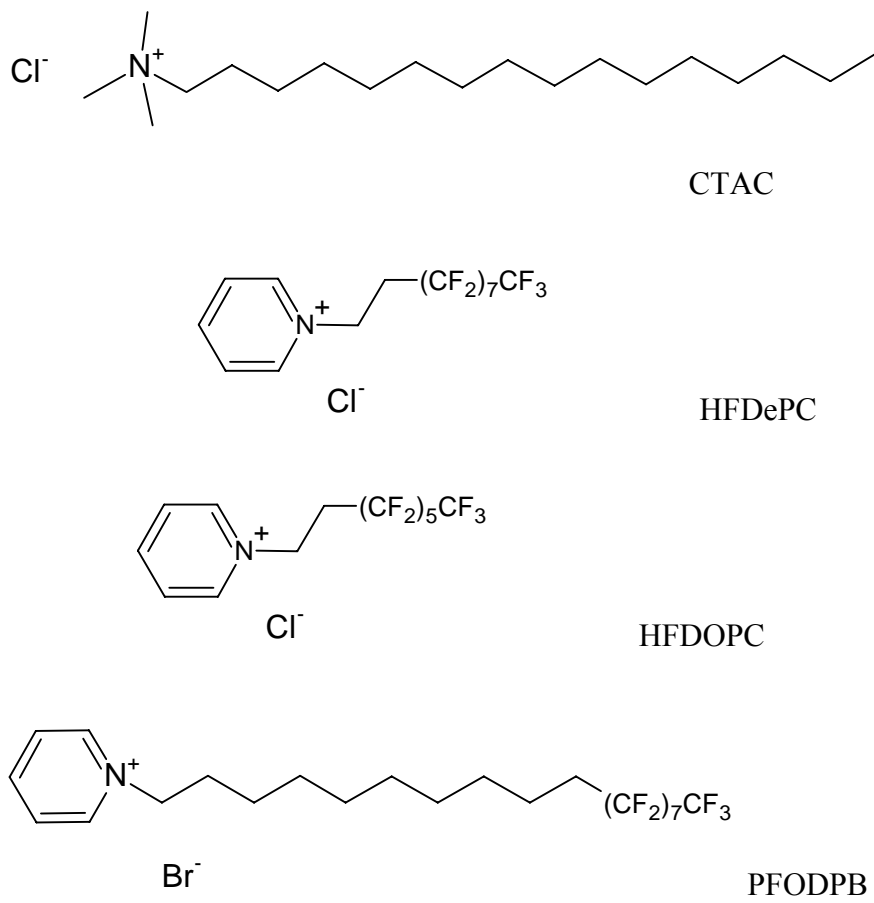
Figure 8.1. Molecular structures of surfactants used for materials synthesis.
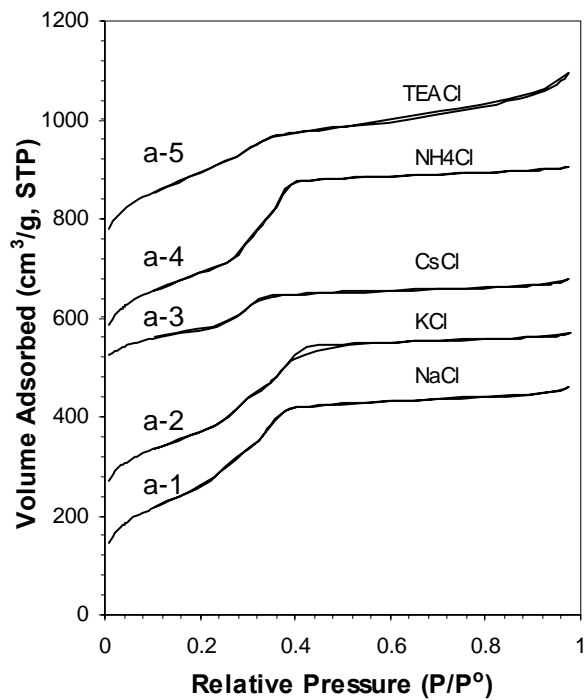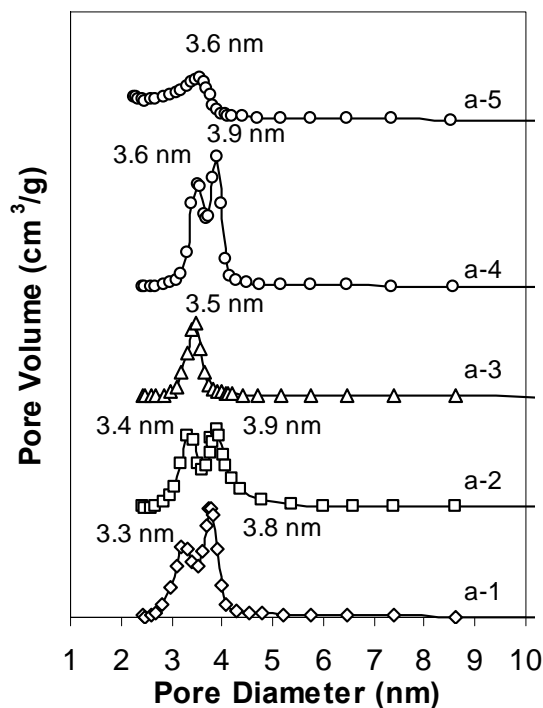
Figure 8.2. (a) Nitrogen adsorption isotherm plots of a series of samples a-1, a-2 (upshifted 150 cm^3/g), a-3 (upshifted 450 cm^3/g), a-4 (upshifted 450 cm^3/g) and a-5 (upshifted 650 cm^3/g) made with different type of chloride salts. (b) Pore size distributions of this series of samples after extraction, calculated using the KJS method assuming a cylindrical pore geometry.
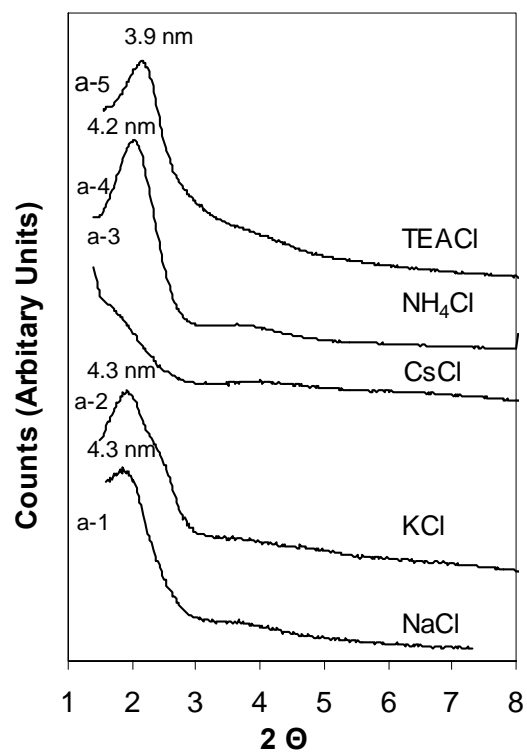
Figure 8.3. XRD results for samples a-1 through a-5.
(The numbers represent calculated d spacings)
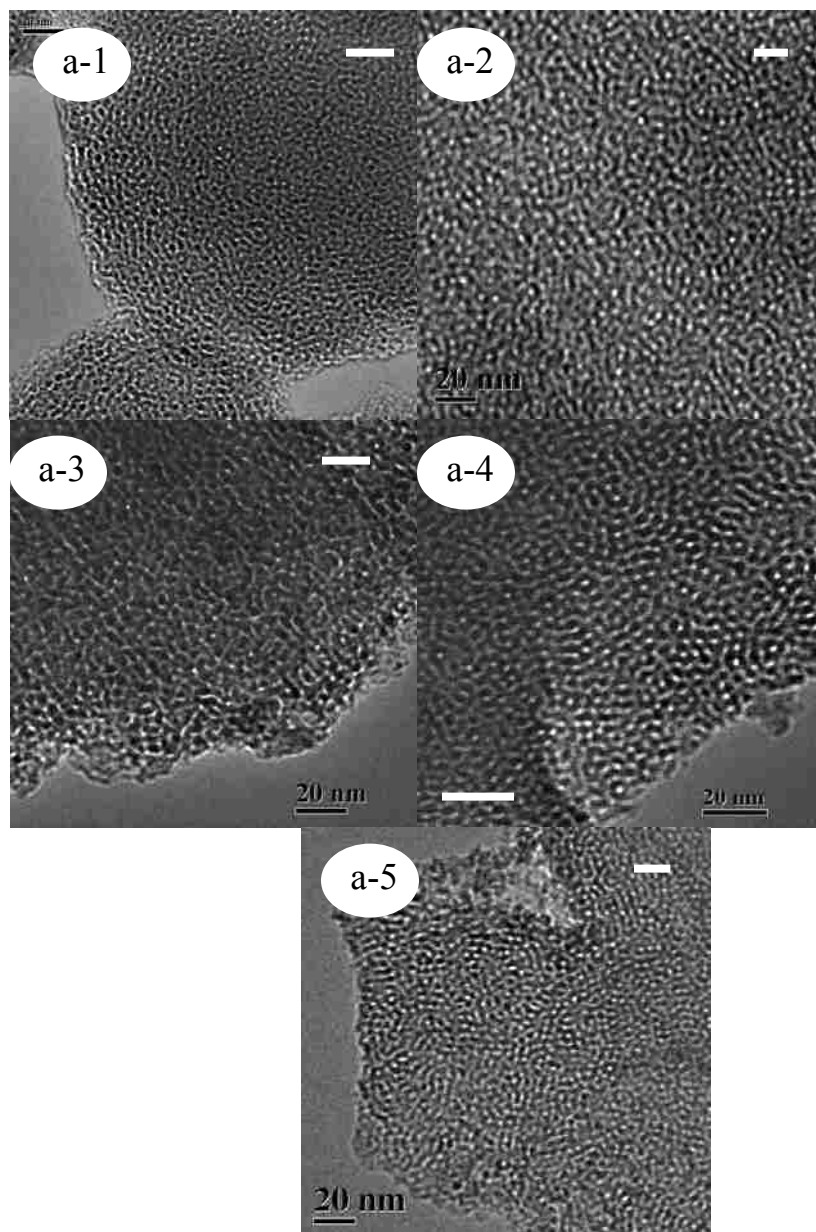
Figure 8.4. Representative TEM images for samples a-1 through a-5.
All scale bars represent 20 nm.
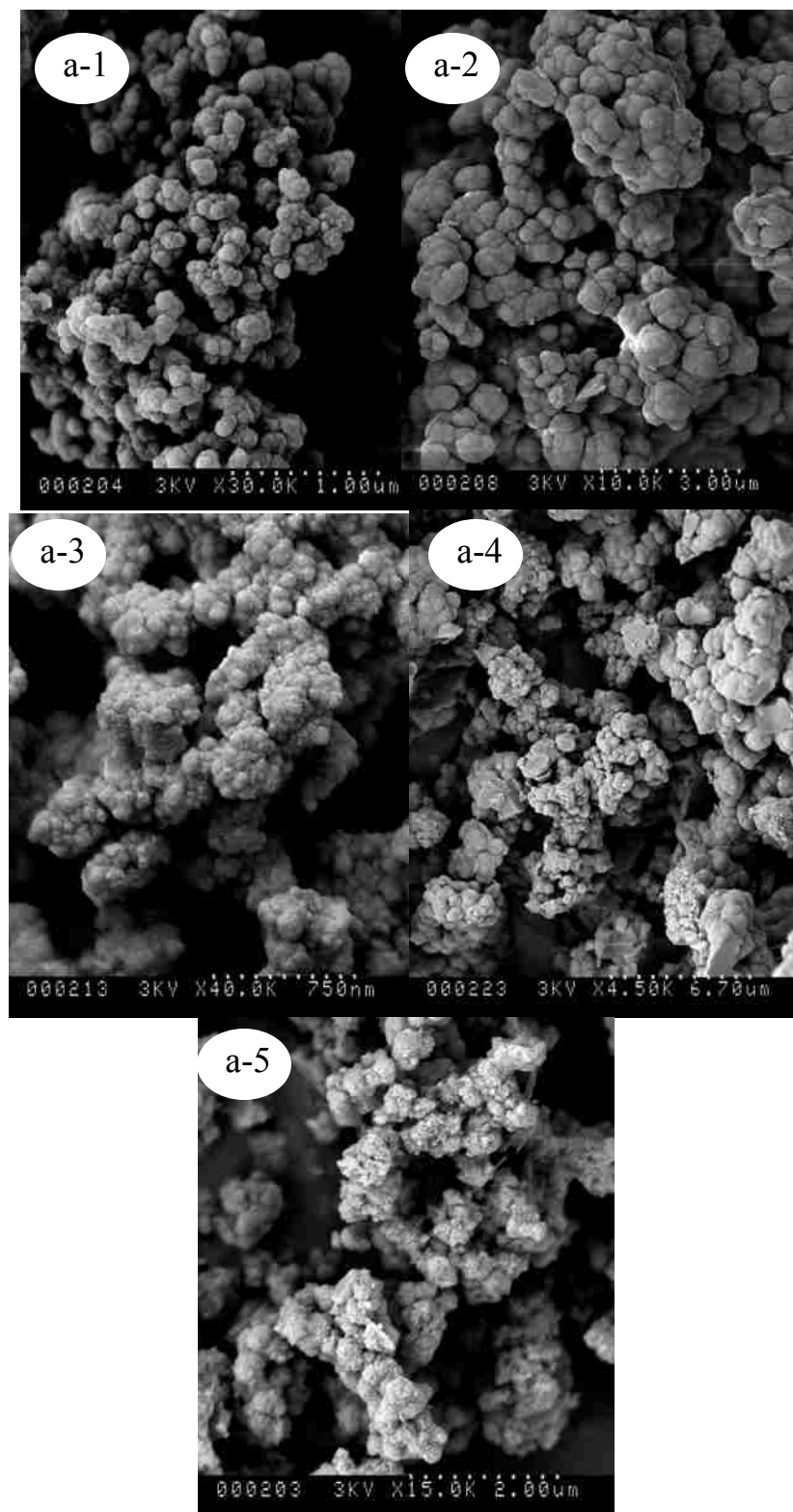
Figure 8.5. Representative SEM images for extracted samples a-1 through a-5.
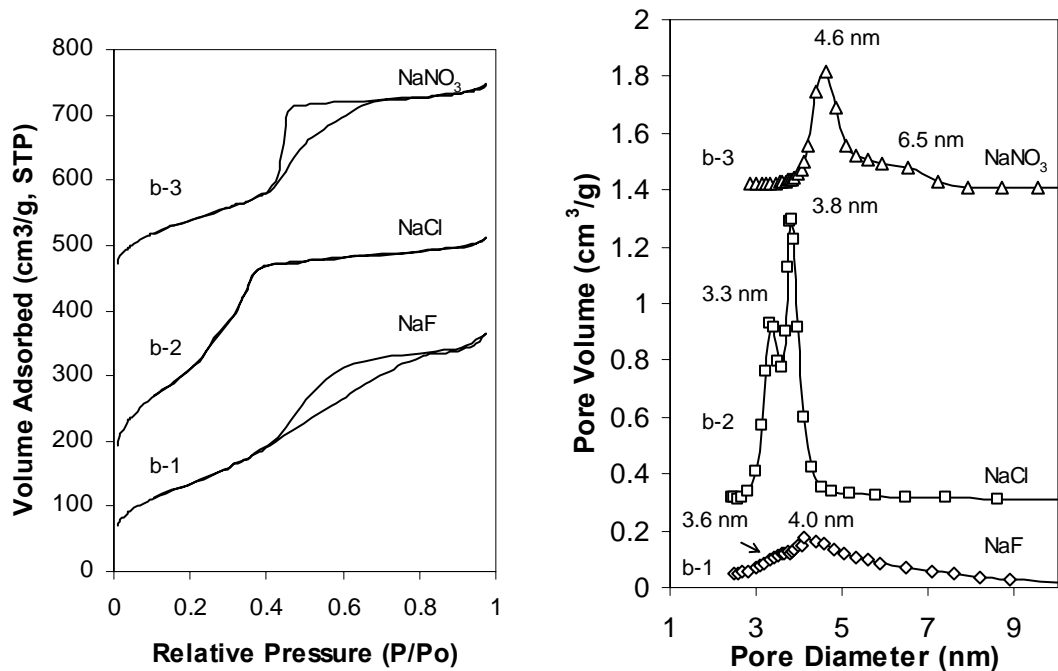
Figure 8.6. (a) Nitrogen adsorption isotherm plots of a series of samples b-1, b-2 (upshifted 50 cm^3/g), b-3 (upshifted 350 cm^3/g) made with sodium salts with different anions. (b) Pore size distributions of this series of sample after extraction, calculated using the KJS method assuming cylindrical pore geometry.

b-1

750 nm

Foam-like particles

000214 3KV X40.0K 750nm

b-3

2 μm

Sheet-like particles

000208 3KV X15.0K 2.00um
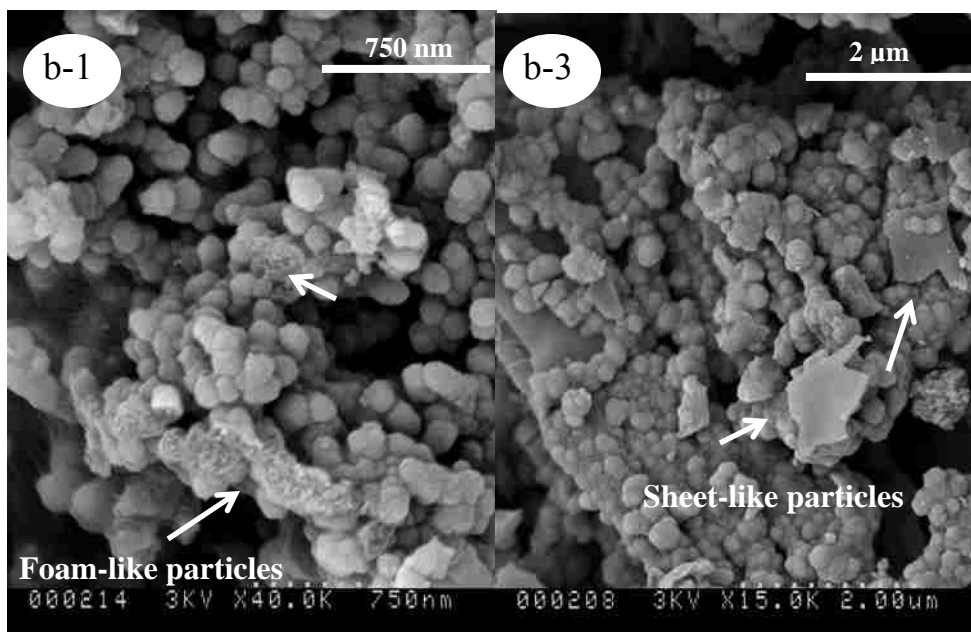
Figure 8.7. Representative SEM images of samples b-1 and b-3.
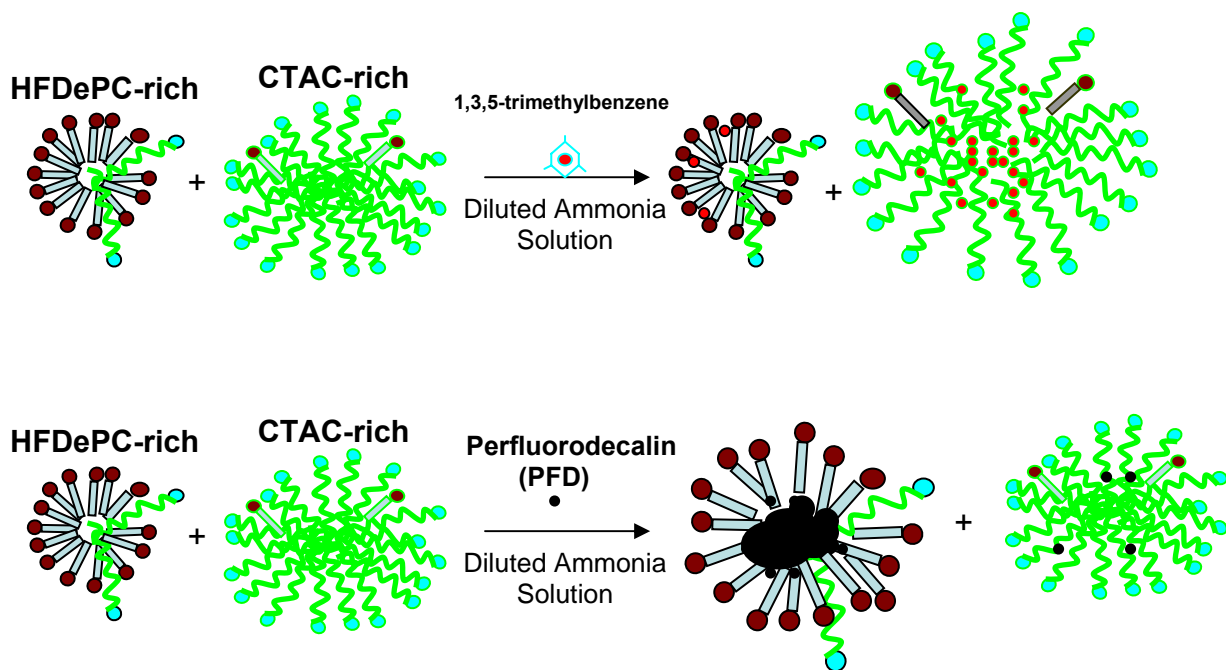
Scheme 8.1. Schematic representation of proposed selective swelling of demixed micelles composed of CTAC-rich and HFDePC-rich surfactant in initial sols

(a)   (b)
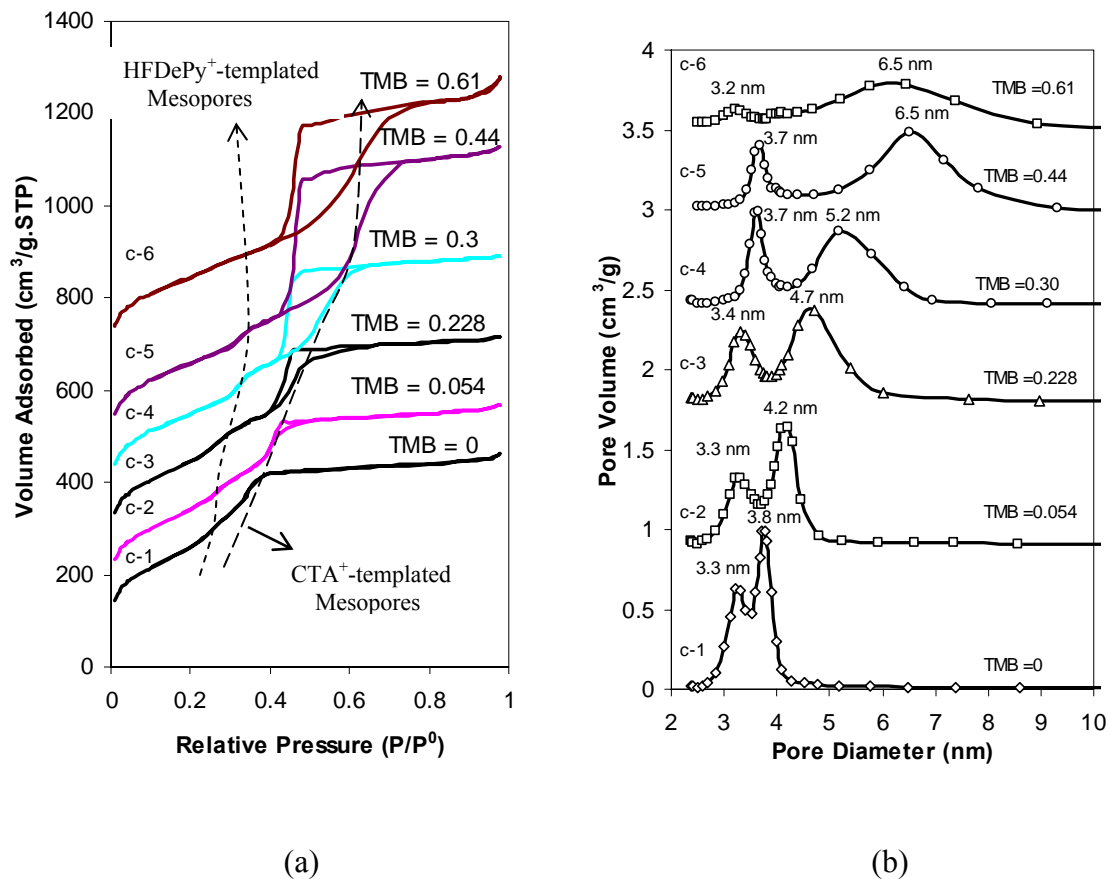
Figure 8.8. (a) Nitrogen adsorption isotherm plots of a series of samples c-1, c-2 (upshifted 100 cm^3/g), c-3 (upshifted 200 cm^3/g), c-4 (upshifted 300 cm^3/g), c-5 (upshifted 400 cm^3/g) and c-6 (600 cm^3/g) made with addition of different amount of TMB. The dash lines indicate the shift of capillary condensation steps corresponding to CTA$^+$-templated mesopores and HFDePy$^+$-templated mesopores. (b) Pore size distributions of this series of samples after extraction, calculated using the KJS method assuming cylindrical pore geometry.
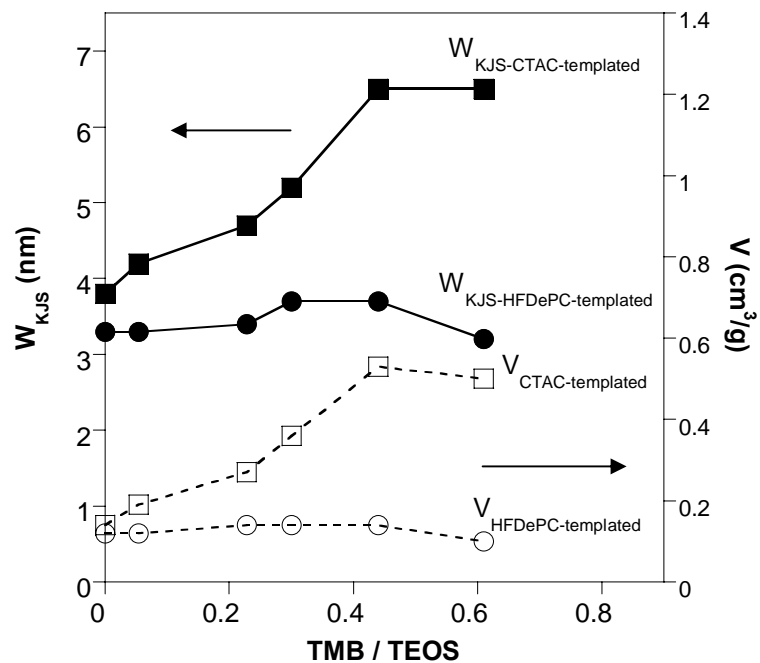
Figure 8.9. Calculated W_{KJS} and V as a function of the amount of TMB added to samples c-1 through c-6.
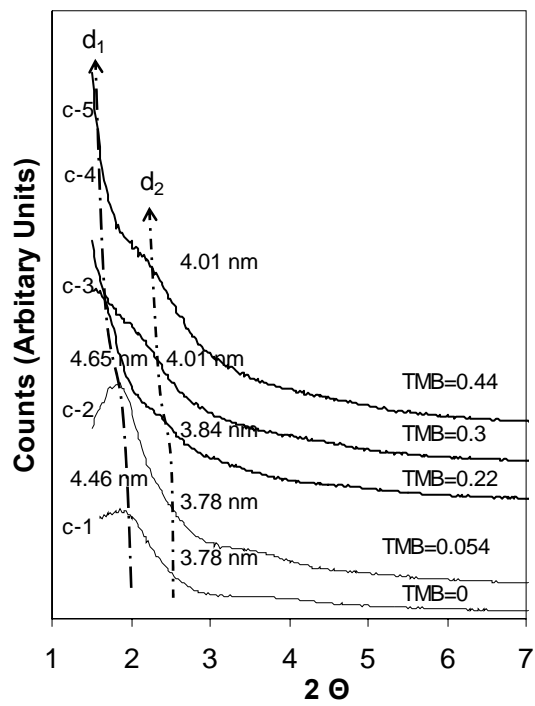
Figure 8.10. XRD results for a series of extracted sample c-1 through c-5.

c-5 · Large pore region · Small pore region · 20 nm

c-5 · 20 nm
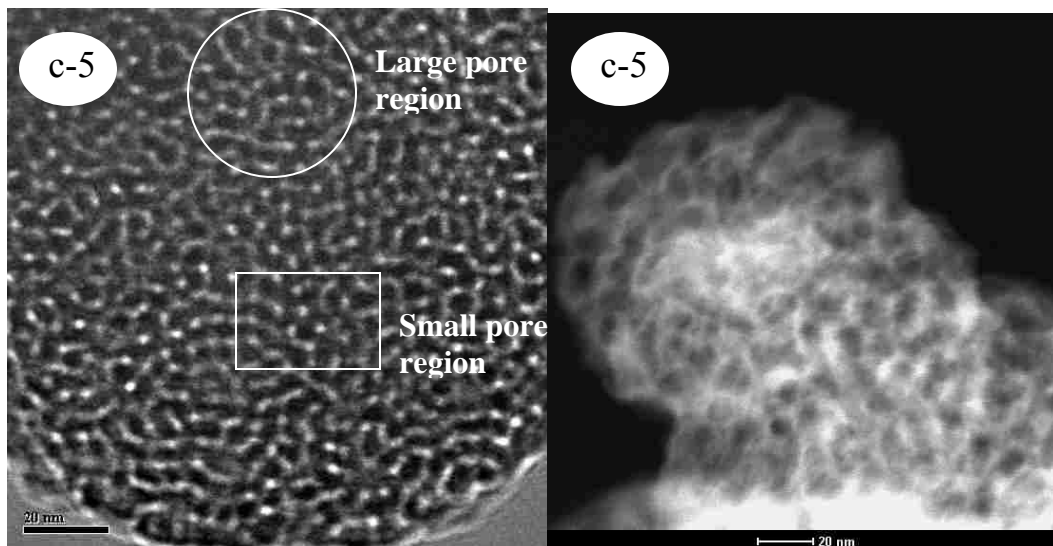
(a)   (b)

Figure 8. 11. Representative TEM image (a) and STEM image

(b) for extracted sample c-5.
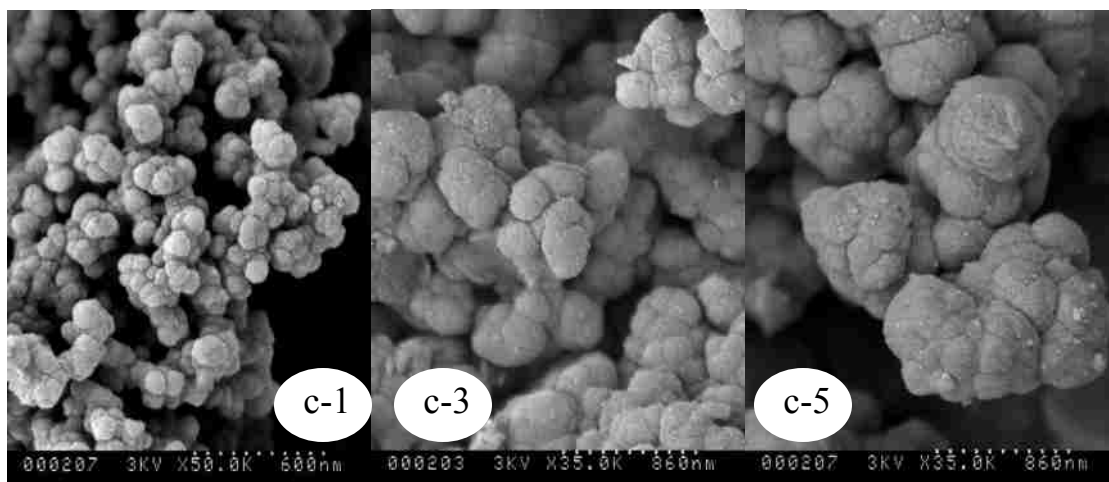
Figure 8. 12. Representative SEM images for extracted
samples c-1, c-3 and c-5.

(a)   (b)
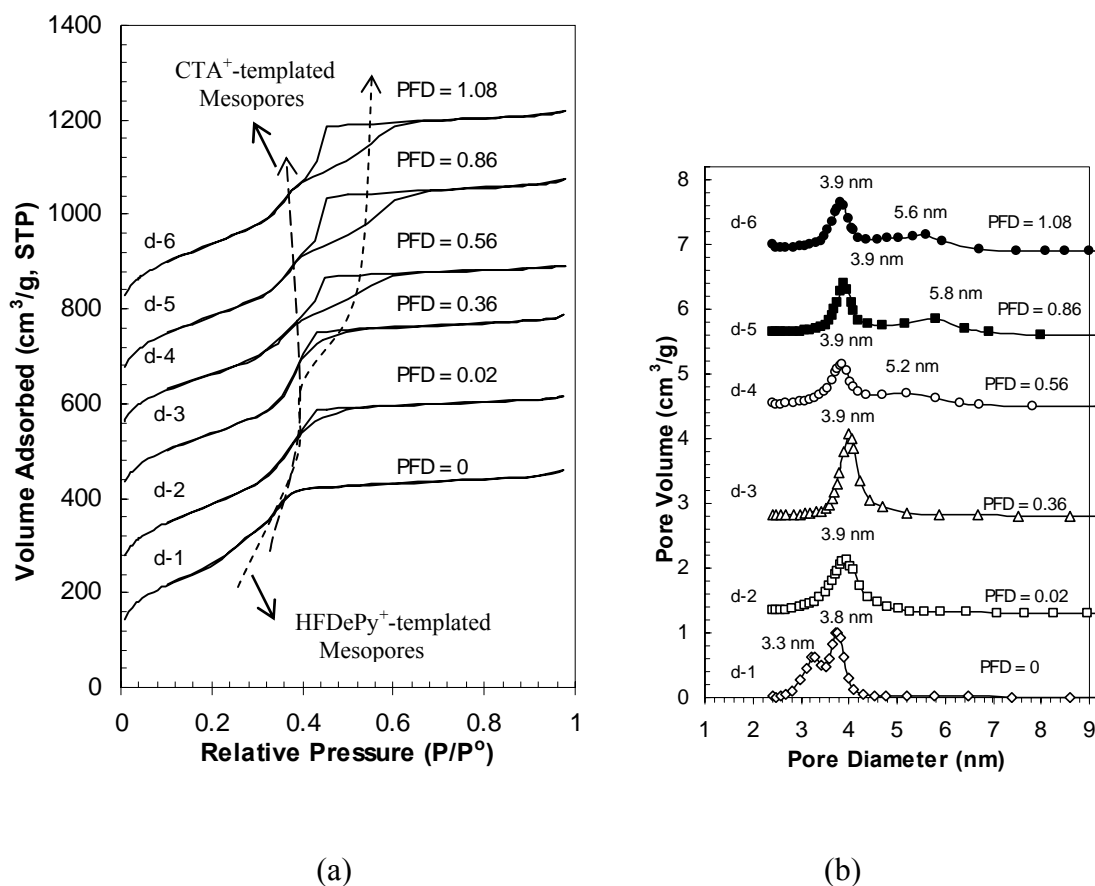
Figure 8.13. (a) Nitrogen adsorption isotherm plots of a series of samples d-1, d-2 (upshifted 150 cm^3/g), d-3 (upshifted 300 cm^3/g), d-4 (upshifted 450 cm^3/g), d-5 (upshifted 550 cm^3/g) and d-6 (upshifted 700 cm^3/g) made with addition of different amount of PFD. The dash lines indicate the shift of capillary condensation steps corresponding to CTA^+-templated mesopores and $HFDePy^+$-templated mesopores. (b)Pore size distributions of this series samples after extraction, calculated using the KJS method assuming cylindrical pore geometry.
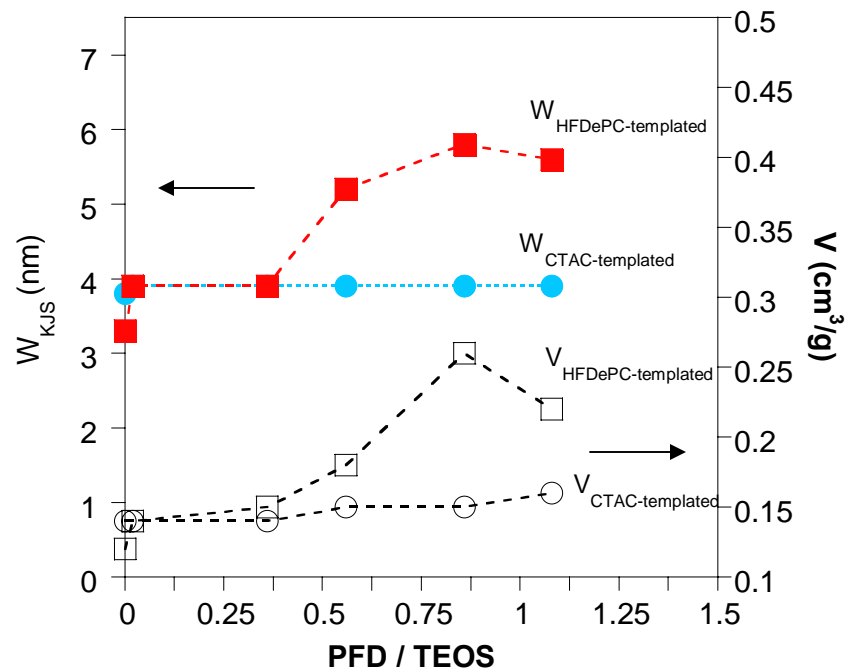
Figure 8. 14. Calculated W_{KJS} and V as a function of amount PFD added to samples d-1 through d-6.
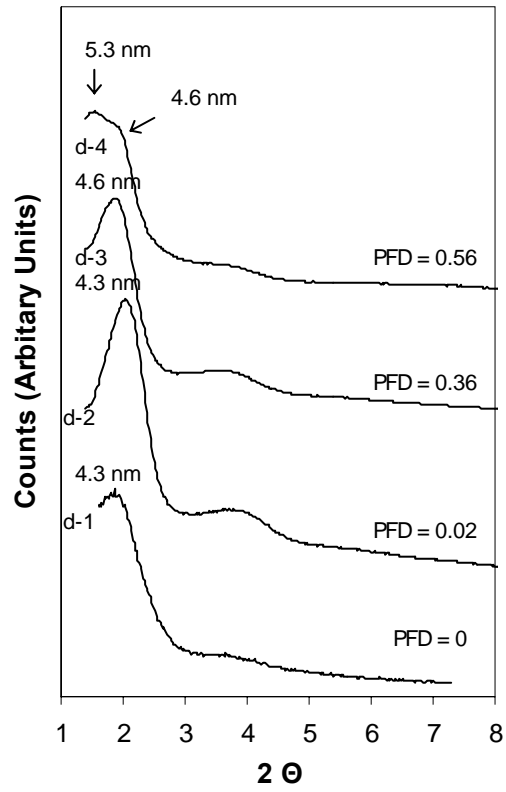
Figure 8.15. XRD patterns of the samples d-1 through d-5 after extraction.
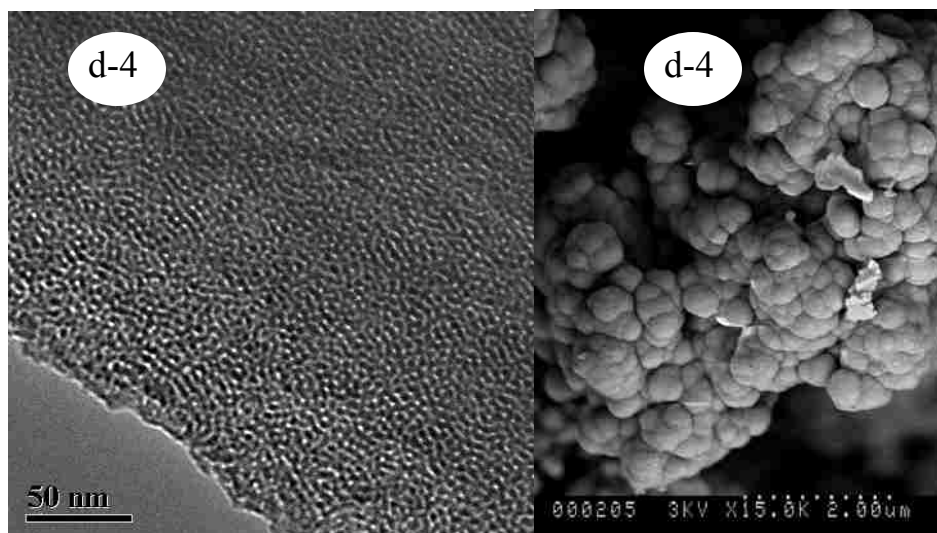
Figure 8. 16. Representative TEM and SEM images for extracted sample d-4.
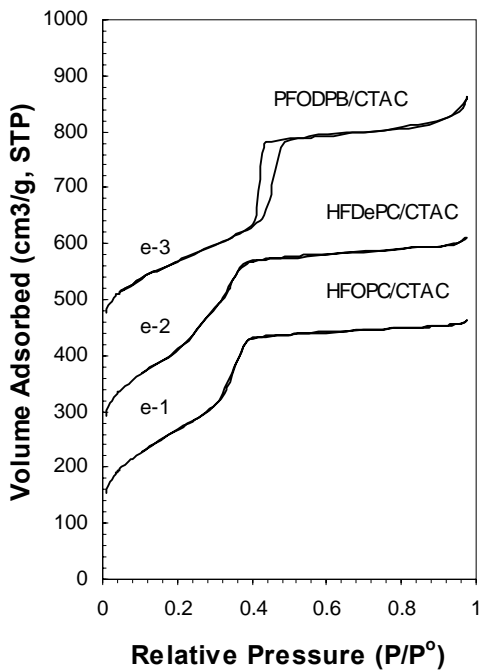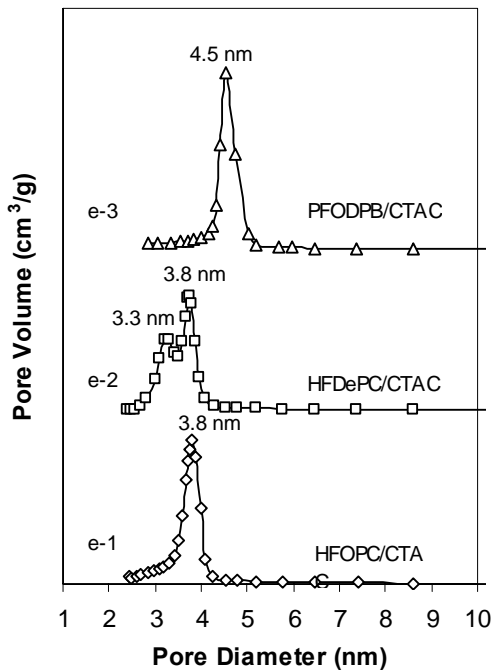
Figure 8.17. (a) Nitrogen adsorption isotherm plots of a series of samples e-1, e-2 (upshifted 150 cm^3/g) and e-3 (upshifted 300 cm^3/g) made with different length of fluorocarbon surfactants. (b) Pore size distributions of this series of extracted sample calcualted using the KJS method assuming cylindrical pore geometry.
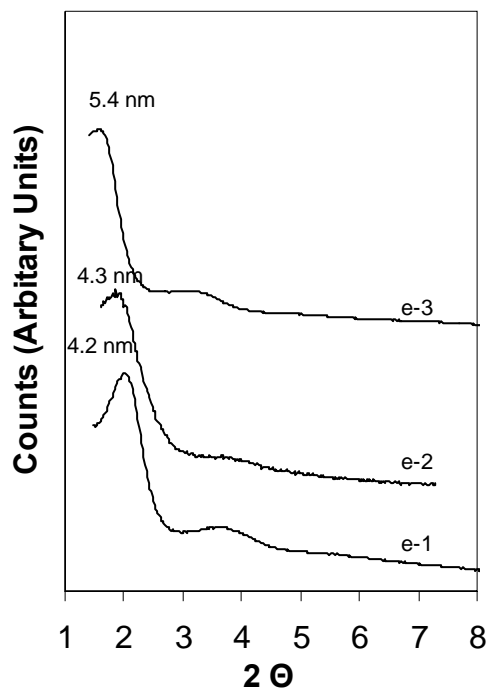
Figure 8.18. XRD results for a series of extracted samples e-1 through e-3.
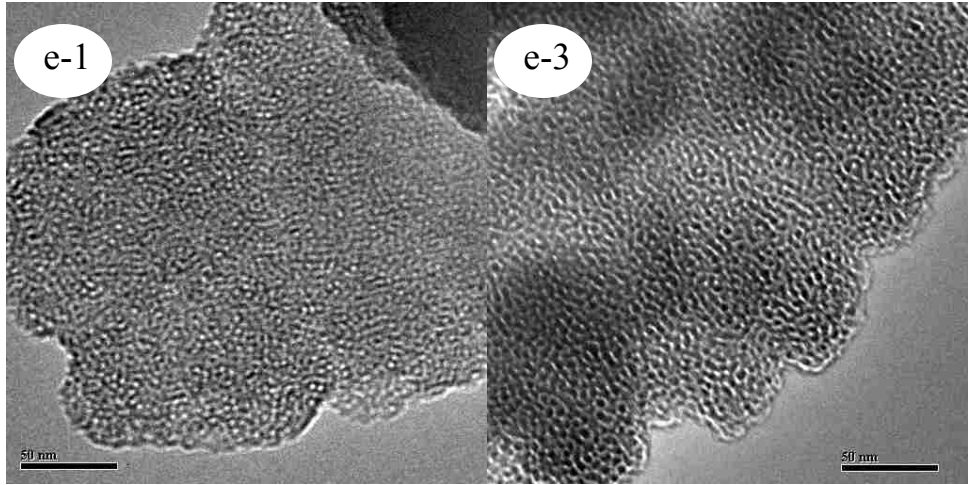
Figure 8.19. Representative TEM images for extracted samples e-1 and e-3.
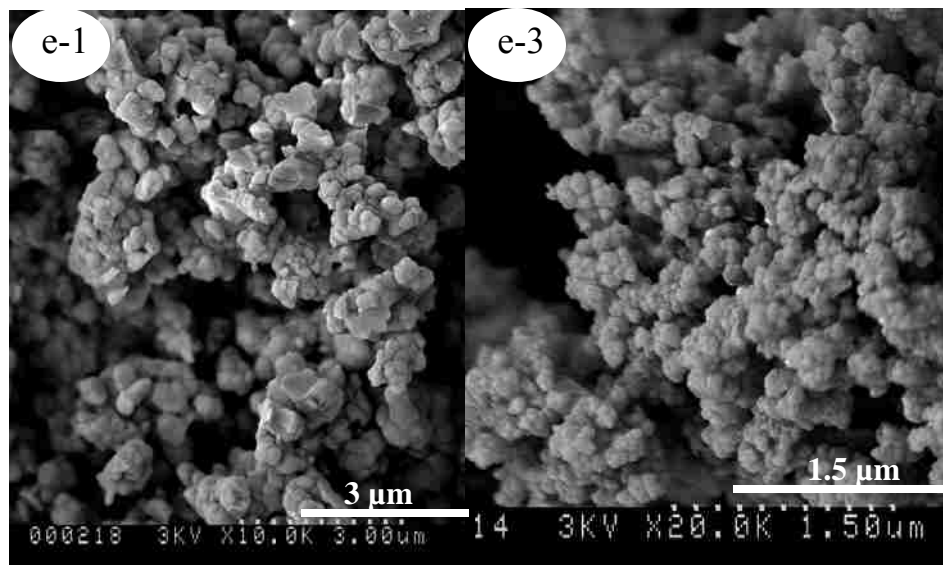
Figure 8.20. Representative TEM images for extracted samples e-1 and e-3.

Chapter 9. Synthesis of Protein-Accessible Hollow Spherical Silica Particles with Inter-Connected Bimodal Mesoporous Shells

9.1. Introduction

The synthesis of hollow spherical silica particles (HSSP) with mesoporous shells has received increasing interest for potential applications in encapsulation, adsorption, catalysis, chromatography, drug storage and controlled drug delivery.[1,2,3,4,5] A large number of studies have demonstrated that supramolecular templating is an effective and simple approach to prepare HSSP. For example, HSSP have been synthesized by using block copolymer or surfactants as mesopore templates in the presence of macropore templates such as vesicles[6,7,8,9] polyelectrolyte nanoparticles[10], or oil/water emulsion droplets[11,12,13]. Recently, additional methods have been developed for hollow core templating. For example, Shiomi et al.[14] described the tunable synthesis of protein/silica hollow particles by a combination of protein catalysis and sonochemical treatment. The morphologies of the products can be controlled by changing the protein concentration. Xia et al.[15] reported the synthesis of hollow spheres of metal oxide with crystalline walls via nanocasting of mesoporous carbon hollow shells. In addition, Chen et al.[5] synthesized hollow spherical silica nanoparticles by using $CaCO_3$ nanoparticles as an inorganic template that could be removed by acidic washing. In spite of the desirable particle structure they create, such technologies often suffer from diadvantages – for example, some require extremely strict and carefully-controlled reaction conditions, and some produce particles with broad size distributions.

While many methods have been reported for the synthesis of hollow spherical particles, dual surfactant/latex templating is a very effective and simple way to prepare hollow spherical silica particles with independently controlled hollow cores and mesoporous shells. In this method, the surfactant co-assembles with silica precursors to form mesoporous shells, while the latex microspheres control void formation. For example, Tan et al.[16] described dual latex/cetyltrimethylammonium bromide (C_{16}TAB) surfactant templating of hollow spherical silica particles with hexagonally ordered mesoporous shells in concentrated ammonia solution. The procedure developed allows independent control of core size, shell thickness and mesopore size in silica particles.[16] However, the pore

channels in the shells run mainly parallel to the surface of the particles, which is expected to prevent large guest molecules from entering into the hollow cores. This will restrict their applications, especially in the field of drug delivery, which requires the diffusion of drug molecules into the cores during loading and out of the cores during delivery. To illustrate the importance of this for small-molecule drug delivery, Zhu et al.[2] recently reported dual polyvinylpyrrolidone (PVP)/CTAB templating to synthesize HSSP in highly alkaline NaOH solution. Penetration of pores across the shells of these HSSP give them a large storage capacity of drug molecules like Ibuprofen. Similarly, HSSP with Ia3d cubic mesoporous shells prepared by a two-step procedure store significantly more drug molecules than ordinary MCM-48 mesoporous particles due to their hollow core.[17] For these two cases, the pore channels in the shells are inter-connected to permit core access, but the small pore size limits their applications for adsorption or selective drug delivery of large molecules such as proteins. HSSP with larger pores will be a significant advance. Also, HSSP with shells having interconnected bimodal mesopores are desirable for reducing transport limitations of guest molecules in applications like catalysis and drug delivery.

In this chapter, we present a facile two-step pathway for the synthesis of HSSP with expanded inter-connected bimodal mesoporous shells. In the first step, latex/surfactant templating generates HSSP with ordered uniform mesopores that run parallel to the particle surfaces, denoted as HSSP-P. In the second step, interconnected bimodal mesoporous shells (HSSP-I) are obtained by micelle expansion through ammonia hydrothermal post-synthesis treatment at 100 °C. The micelle expansion is enhanced by using a pyridinium surfactant rather than a more commonplace trimethylammonium surfactant.[18] The effects of key parameters on the formation of HSSP-I, such as the concentrations of both templates, latex size and post-synthesis temperature, are investigated in detail. The accessibility of the hollow cores of HSSP-P and HSSP-I to small-molecule dyes and green fluorescent protein are compared by laser scanning confocal microscopy.

9.2. Experimental section

9.2.1 Materials

Aqueous latex microspheres with diameters of 0.202 μm, 0.356 μm, 0.495 μm and 0.535 μm (1 wt% polystyrene in water, Polysciences, Inc.), tetraethoxysilane (TEOS, 98%, Sigma), cetylpyridinium chloride ($C_{16}PyCl$, > 99%, Sigma), aqueous ammonia (29 wt%, Merck), sulforhodamine B (SRB, Molecular Probes), and recombinant enhanced green fluorescent protein (EGFP, Bio Vision) were purchased and used as received.

9.2.2 HSSP-I materials synthesis

The two-step procedure for the synthesis of HSSP-I materials is shown in Scheme 9.1. The first step is based on the dual-templating procedure developed by Tan et al.[16] and is expected to yield spherical latex beads coated with silica shells containing hexagonal micelles running parallel to their surfaces. The synthesis of the base sample is described here, and the procedure is the same for all other samples except that one synthesis parameter is changed as described in the results and discussion section. First, 0.90 g of aqueous polystyrene latex (0.356 μm), 0.2 g of $C_{16}PyCl$ and 9.0 g of aqueous ammonia were mixed together with vigorous stirring for 30 min. Then, 0.47 g of TEOS was added slowly with continued stirring. The solution was stirred and aged at room temperature for another 2 hr. The precipitates were then recovered by filtration and washed with deionized water. The as-made samples (HSSP-P) were dried at 50 °C for 24 hr. In the second step, 0.4 g of the as-made HSSP-P were added to a solution of 1.7 ml of concentrated ammonia (28 wt%) and 26 ml water, sealed in a Teflon-lined autoclave, and heated in an oven at 100 °C for 3 days. The final products were filtered, washed with water and dried at 50 °C, and then calcined in air at 550 °C for 5 hr to remove the templates. The hydrothermal stability of HSSP-I particles was evaluated by treating them in boiling water for 120 hr. The thermal stability of HSSP-I particles was evaluated by heating them in air at 800 °C for 24 hr.

9.2.3 Characterization methods

Powder X-ray diffraction patterns were obtained at a scan rate of 0.1 °/min using a Siemens 5000 diffractometer with 0.154098 nm Cu K_α radiation and a graphite monochromator. Nitrogen adsorption-desorption isotherms were collected at -196 °C using a Micromeritics Tristar 3000 automated adsorption instrument. The samples were degassed at 120 °C for 4 hr prior to analysis. For transmission electron microscopy (TEM), solid samples were dispersed by sonication in iso-propanol solvent and loaded

onto lacey carbon grids for analysis using a JEOL 2010F instrument at a voltage of 200 kV. Scanning electron microscopy (SEM) was performed with a Hitachi S-3200 microscope. Solid SEM samples were loaded on PELCO carbon tabs and coated with gold under vacuum. FTIR spectra were obtained with a desiccated and sealed ThermoNicolet Nexus 470 infrared spectrometer with a DTGS detector. Samples were finely ground and diluted to 1 wt% with KBr powder before being pressed into translucent pellets with a hand press. Confocal fluorescence images were collected with a Leica laser scanning confocal microscope. Both argon laser (green fluorescence) and krypton (red fluorescence) were used for phase microscopy.

9.3. Results and discussions

9.3.1 Characterization of representative HSSP

The low angle XRD patterns of representative samples of as-made HSSP-P, calcined HSSP-P and HSSP-I are shown in Figure 9.1. While only one reflection can be resolved in the pattern of as-made HSSP-P, calcining the HSSP-P sample reveals four well-resolved Bragg diffraction peaks, which can be indexed to the (100), (110), (200) and (210) reflections of a hexagonal columnar phase (HCP). The unit cell parameter of calcined HSSP-P calculated from the XRD data is 4.2 nm. However, after ammonia hydrothermal post-synthesis, the (100) reflection becomes weak and shifts to lower angle while the higher-angle reflections disappear, showing a significant modification of the pore structure in HSSP-I besides lattice expansion, similar to the previous report by Yuan et al.[18] with only $C_{16}PyCl$ surfactant as the template.

The nitrogen sorption isotherm and calculated pore size distribution of calcined HSSP-I are shown in Figure 9.2. The adsorption and desorption isotherms exhibit a behavior which is characteristic of mesoporous materials.[19] Two distinct capillary condensation steps can be clearly observed at 0.4 and 0.65 of P/P_o, indicating a bimodal pore size distribution. The pore size distribution was calculated from the adsorption branch with the modified Kelvin equation and the Harkins-Jura equation for film thickness (also known here as KJS pore size distributions).[20] The pores are assumed to be cylindrical for these calculations. The PSD of HSSP-I has one sharp peak centered at 4.4 nm and another broad peak in the region of 6-14 nm with a maximum at ~10 nm, confirming the formation of bimodal mesoporous shells. To learn more about the

structure, we calculate other structure parameters based on the nitrogen adsorption measurements of calcined HSSP-I materials with the method developed by Sayari et al.[21] We also calculate a BET surface area of 604.8 m^2/g and a pore volume of 1.25 cm^3/g at $P/P_o = 0.98$ for PSSD-I as shown in Table 9.1.

Representative TEM images of calcined HSSP-P and HSSP-I are shown in Figure 9.3. Figure 9.3a and 9.3b show images of sample HSSP-P at different magnifications. We observe that the morphology of HSSP-P is predominantly spherical and the particles are uniform in size with most have a diameter around 500-600 nm. Image contrast between the cores and shells can be observed, suggesting that the spherical particles are hollow. All of the hollow cores appear intact, showing that the particles are stable during calcination. In addition, the shells of hollow particles are 100-120 nm thick and contain HCP mesopores as shown in the high magnification image of this sample. The stripe patterns at the center of each particle and hexagonal patterns near the edges indicate that the mesopores in the shells lie parallel to the particle surfaces. Detailed characterization of HSSP-P has been reported previously.[13] Figures 9.3c and 9.3d show images of base sample HSSP-I with different magnifications. After ammonia post-treatment, the spherical morphology of particles is preserved. The shells of the particles are 150-200 nm thick and contain inter-connected wormhole-like pore networks. The disappearance of the stripe pattern at the center of each particle as well as the loss of the HCP patterns near the edges indicate that a secondary pore system is generated in the shells, which presumably act as penetrating pore channels across the shells. Figure 9.4 shows a representative SEM image of HSSP-I. The particles are almost spherical, and the average size of the particles is approximately 500-600 nm, which is consistent with TEM results.

The hydrothermal stability of both HSSP-P and HSSP-I has been tested by the treatment of respective calcined samples in boiling water for different time intervals. The XRD results show a loss of HCP order in HSSP-P after only 12 hr of heating in boiling water. However, TEM results show that the particles of HSSP-I are still stable and unbroken after even 120 hr in boiling water. Moreover, nitrogen sorption isotherms still clearly show two-step capillary condensation for sample HSSP-I, indicating that the bimodal mesopores are preserved after hydrothermal treatment. These results show that

the ammonia hydrothermal post-synthesis improves the hydrothermal stability of HSSP-P materials.

Generating secondary mesopores in MCM-41 materials by means of ammonia hydrothermal post-synthesis treatment was first reported by Yuan et al.[18] They hypothesized that the modification of the pore structure was due to combined physical and chemical changes, but presented no direct evidence. In order to learn more about the changes during the second synthesis step, we analyze samples by FTIR. Figure 9.5a shows the infrared spectra of the base sample. In the uncalcined samples HSSP-P and HSSP-I, two intense bands at 2850 cm^{-1} and 2922 cm^{-1} are observed, which are attributed to CH_2 symmetric and asymmetric stretching[22], respectively. These two bands may come from both $C_{16}PyCl$ and polystyrene latex templates. The bands around 1486 cm^{-1} are associated with deformation modes of $C_{16}PyCl$.[23] Weak bands in the region between 3000 cm^{-1} and 3100 cm^{-1} (expanded Figure 9.5b) are attributed to aromatic C-H stretching in $C_{16}PyCl$ and the polystyrene latex (discussed later). After calcination, these bands disappear. The spectrum of calcined HSSP-I is similar to that of fumed silica, indicating complete removal of both templates. The bands at 963 cm^{-1} and 783 cm^{-1} in HSSP-P are attributed to Si-OH streching[24]. They both shift to higher frequencies (969 cm^{-1} and 798 cm^{-1}) after hydrothermal treatment, and even further (to 970 cm^{-1} and 805 cm^{-1}) after calcination. All three samples have a broad band associated with Si-O-Si stretching in the region from 1020 cm^{-1} to 1090 cm^{-1}.[25] The position of this band shifts to higher wavenumber upon hydrothermal treatment (from 1048 cm^{-1} to 1087 cm^{-1}), suggesting enhanced sol-gel condensation. The band at 1209 cm^{-1} disappears after ammonia treatment, indicating that some chemical change occurs during the second synthesis step.

In order to clearly show the differences caused by ammonia hydrothermal treatment, the region from 2700 cm^{-1} to 3200 cm^{-1} is expanded in Figure 9.5b. For comparison, the spectra of $C_{16}PyCl$ and dried latex particles are also shown. The bands in the range from 3000 cm^{-1} to 3200 cm^{-1} are associated with aromatic C-H stretching[26]. The bands at 3026 cm^{-1}, 3060 cm^{-1} and 3082 cm^{-1} are from aromatic C-H stretching of polystyrene, and the bands at 3008 cm^{-1}, 3048 cm^{-1}, 3085 cm^{-1} and 3129 cm^{-1} are from aromatic C-H stretching of the pyridinium headgroup in $C_{16}PyCl$.[26] The spectrum of HSSP-P includes

both sets of bands, which indicates that, as expected, $C_{16}PyCl$ and latex are both incorporated into the sample. After ammonia treatment, the bands associated with $C_{16}PyCl$ disappear, indicating pyridinium ring decomposition. Since $C_{16}PyCl$ has a low thermal stability and a melting point of 86 °C, it is likely to decompose under hydrothermal conditions (> 100 °C). Decomposition of the pyridinium should release uncharged, low molecular weight volatile species[27], which would enhance the generation of secondary pores in the shells. Although IR shows the loss of pyridinium during hydrothermal treatment, the distribution of decomposition products cannot be clearly determined from the IR spectrum.

9.3.2 Effect of $C_{16}PyCl$/latex ratio

A series of five samples has been prepared to investigate the effect of the $C_{16}PyCl$/latex ratio on the particle morphology and pore size distribution in the shells. The mass ratio of $C_{16}PyCl$:latex solution is 0.6:0.9, 0.5:0.9, 0.4:0.9, 0.2:0.9 and 0.1:0.9 for samples from $HSSP-I-S_1$ to $HSSP-I-S_5$, respectively. Sample $HSSP-I-S_4$ is the base sample discussed in the previous section. For all samples, we observe white precipitates immediately after slowly adding TEOS. All precipitates are easily recovered by filtration to give high yields of HSSP-P. After ammonia treatments at 100 °C, all of the calcined HSSP-Is are predominantly composed of spherical particles, but the porous networks and morphology of the silica shells exhibit different features. Some representative TEM images are shown in Figure 9.6. Sample $HSSP-I-S_1$, prepared with largest amount of $C_{16}PyCl$, consists of spherical particles with uniform 160 ± 10 nm thick shells in the low magnification of TEM micrographs. However, some broken shells are observed by high magnification TEM. The shells are composed of a mixture of straight and coiled silica nanotubes with an almost uniform pore diameter of ~ 6 nm. The length of nanotubes can reach as long as 120 nm. These nanotubes entangle with each other and construct a loosely-arranged network. Sample $HSSP-I-S_5$, prepared with the least amount of $C_{16}PyCl$, shows broken hollow spherical particles with very thin shells. The shell thickness decreases dramatically as $C_{16}PyCl$ content decreases, indicating that $C_{16}Py^+$/silica aggregates are the species which add to the surface of the latex particles to form the hollow particles. Paintbrush-like mesoporous silica regions or arrays of silica nanotube bundles are observed at the broken edges of the particles.

Nitrogen sorption isotherms and calculated pore size distributions of this series of calcined samples are compared in Figure 9.7. Except for sample HSSP-I-S_5, these samples show two inflections and large hysteresis loops in their isotherms, indicating that the samples are bimodal mesoporous silica. The calculated pore size distributions confirm the formation of bimodal mesopores. Sample HSSP-I-S_5 even has a trimodal pore size distribution with pore sizes of 3.5, 4.2 and 8.6 nm. With increasing C_{16}PyCl/latex ratio, the primary mesopore size in this series of samples increases from 3.5 nm to 4.7 nm and remains constant, but the width of the primary mesopore peak broadens. Similarly, the secondary mesopore size increases from 9 nm to 12 nm as C_{16}PyCl content increases, suggesting that the swelling extent of mesopores is determined by the amount of C_{16}PyCl used in the templates. In fact, the generation and expansion of secondary mesopores appears to be achieved at the expense of primary (small) mesopores.

This series of samples show the C_{16}PyCl/latex mass ratio significantly affects the structural stability of hollow silica spheres. The C_{16}PyCl content affects both the shell thickness and pore size distribution of final particles. If excessive C_{16}PyCl is used, decomposition of C_{16}PyCl releases so much volatile molecules that a fraction of the shells break during ammonia treatment. If too little C_{16}PyCl is used, less C_{16}Py$^+$/silica aggregates attach to the latex surface, leading to thin shells in the HSSP-P sample, which are unstable and easily broken during ammonia treatment. We conclude that an appropriate amount of C_{16}PyCl is crucial for the formation HSSP-I with stable, structured shells. In addition, nanotube-like silica aggregates are found under both low and high C_{16}PyCl content, although the mechanism of forming these tubes requires more study.

9.3.3 Effect of latex size

A series of samples has been prepared with different sizes of unmodified latex microspheres. The size of the latex is 0.202 μm, 0.356 μm, 0.495 μm and 0.535 μm for samples from HSSP-I-L_1 through HSSP-I-L_4. Sample HSSP-I-L_2 is the base sample. Some representative TEM images are shown in Figure 9.8. All samples are uniformly sized spherical particles with hollow cores and inter-connected mesoporous shells similar to the base sample. Sample HSSP-I-L_1, prepared with the smallest size of latex microspheres, consist of uniform hollow particles with shells ~120 ± 10 nm thick (Figure 9.8a). Inter-connected mesoporous networks in the shells of hollow particles can be

discerned in the high magnification TEM image (Figure 9.8b). The original hexagonal and stripe patterns in sample HSSP-P-L1 (not shown) are replaced by the inter-connected mesopore channels due to the generation of secondary mesopores across the shells of hollow particles after ammonia treatment. Sample HSSP-I-L_4, prepared with the largest latex microspheres, also consists of hollow spheres. However, in contrast to sample HSSP-I-L_1, the thickness of the shells increases to 230 ± 10 nm. The increasing shell thickness as the latex size increases may be attributed to the decrease of number density of microparticles for larger particles.

Nitrogen sorption isotherms and pore size distributions for this series of samples are compared in Figure 9.9a. All samples show two-step capillary condensation with large hysteresis loops in the isotherms, consistent with hollow particles and bimodal mesoporous shells. The pore size distributions (Figure 9.9b) are indeed bimodal. A surprising trend is observed as the latex size increases from HSSP-I-L_1 through HSSP-I-L_4: the primary mesopore sizes increases slightly from 4.4 nm to 4.7 nm, while the secondary mesopore size gradually decreases from 11 nm to 8.5 nm. The contrary changes in the sizes of primary and secondary mesopores are related to the variation of shell thickness. Large latex microspheres lead to thicker shells than small latex microspheres. Thicker shells provide greater resistance to secondary mesopores generation during ammonia treatment. As a result, the decomposition of $C_{16}PyCl$ during ammonia treatment only causes swelling of primary mesopores when large microspheres are used, while secondary pores are effectively generated with smaller microspheres. In addition, as the latex size decreases, the primary mesopore size distribution broadens and the total pore volume decreases slightly.

This series of samples illustrates the complex relationship between hollow core template size, shell thickness, and mesopores structure. Under the same conditions, the use of smaller latex as template leads to the formation of thinner shells, which is favorable for the generation of secondary mesopores after ammonia treatment.

9.3.4 Effects of hydrothermal treatment conditions

In order to know more about the changes occurring during the second synthesis step, we conduct a systematic investigation of the effects of ammonia hydrothermal conditions on the pore size distribution of HSSP-I.

9.3.4.1 Effect of ammonia concentration during hydrothermal treatment

A series of samples has been prepared to examine the effect of ammonia concentration on the pore size distributions of HSSP-I. For 0.4 g of as-made HSSP-P, different amounts of concentrated ammonia solution (28 wt %) are added to 26 ml of deionized water. The volumes of ammonia used are 3.5 ml, 1.7 ml, 0.9 ml and 0 ml for samples HSSP-I-N_1 through HSSP-I-N_4. Just like the base sample (HSSP-I-N_2), all samples have been hydrothermally treated at 100 °C for 3 days.

Nitrogen sorption isotherms and pore size distributions of this series of samples are shown in Figure 9.10. All samples display type IV isotherms with hysteresis loops. For samples HSSP-I-N_1 through HSSP-I-N_3, two inflections can be observed in the isotherms, consistent with a hollow, bimodal mesopore structure. Sample HSSP-I-N_4, treated with deionized water only, shows one sharp inflection in the isotherm, suggesting the need for the addition of ammonia to generate secondary mesopores. The calculated pore size distribution of sample HSSP-I-N_4 confirms the formation of unimodal mesopores. The pore size of sample HSSP-I-N_4 also is smaller than the primary mesopores in the other three samples. The expansion of the primary mesopores during ammonia treatment in this sample is only 0.3 nm, which is much smaller than the 1.1 nm expansion observed in the other three samples. The other three samples, treated with different ammonia concentration in the second step, have similar sizes of both primary and secondary mesopores, 4.4 nm and 9.0 nm, respectively. Other structure parameters are listed in Table 9.1. As can be seen, with increasing ammonia concentration, the total pore volume increases, but the BET surface area (S_{BET}) gradually decreases.

This series of samples shows that the presence of ammonia is necessary for the introduction of secondary mesopores in the shells of HSSP-I. The size of the pores is not proportional to the amount of ammonia used, but the pore volume can be increased by using more ammonia.

9.3.4.2. Effect of hydrothermal aging time

A series of samples has been prepared to investigate the effects of the aging time during the second (hydrothermal) synthesis step. As made HSSP-P samples are treated at 100 °C in the same concentration of ammonia solution (prepared with 1.7 ml of concentrated ammonia). The aging time is 5 days, 3 days and 1 day for samples HSSP-I-

T_1 through HSSP-I-T_3. HSSP-I-T_2 is the base sample. The TEM images of samples HSSP-I-T_1 and HSSP-I-T_3 are basically similar to that of the base sample, except that the particle size of sample HSSP-I-T_3 is slightly smaller than that of other two samples (not shown). Nitrogen sorption isotherms and calculated pore size distributions of this series of samples are shown in Figure 9.11. All samples display hysteresis loops. Samples HSSP-I-T_1 and HSSP-I-T_2 have two inflections, while a secondary capillary condensation step in sample HSSP-I-T_3 is barely visible. Both HSSP-P-T_1 and HSSP-I-T_2 have similar primary and secondary pores, 4.4 nm and 10.0 nm, respectively. The primary mesopore size of sample HSSP-I-T_3 slightly decreases to 4.2 nm after ammonia treatment.

This series of samples shows that an aging time of 3 days is enough to produce bimodal mesoporous shells with well-defined mesopores in the HSSP-I materials. One day of aging is not enough to produce the secondary pores, and a longer time does not seem to change the pore size distribution (although the pore volume decreases somewhat after five days).

9.3.4.3. Effect of hydrothermal temperature

A series of samples has been prepared to investigate the effects of hydrothermal treatment temperature. As-made HSSP-P samples are ammonia-treated for 3 days at 80 °C, 100 °C, 120 °C and 150 °C to produce samples HSSP-I-Temp$_1$ through HSSP-I-Temp$_4$. Sample HSSP-I-Temp$_2$ is the base sample. Nitrogen sorption isotherms and calculated pore size distributions are shown in Figure 9.12. Sample HSSP-I-Temp$_1$, treated at the lowest temperature, shows one adsorption step with a type H2 hysteresis loop, indicating the formation of inkbottle-like mesopores. Increasing the treatment temperature to 100 °C in sample HSSP-I-Temp$_2$ leads to an isotherm with two capillary condensation steps and a type H3 hysteresis loop, indicating that bimodal mesopores are formed in the shells of hollow particles. At this temperature, the decomposition of $C_{16}PyCl$ occurs, which induces the generation of secondary mesopores across the shells. Further increasing the temperature to 120 °C in sample HSSP-I-Temp$_3$, causes the first inflection to become very weak, which indicates a loss of primary mesopore volume. At the highest temperature (150 °C), a type II isotherm is observed, indicating that the original mesopore channels of HSSP-P are completely destroyed by reorganization of the silica walls during ammonia treatment. The calculated pore size distributions confirm that

treatment at 100-120 °C for three days allows secondary mesopore generation, while a lower temperature has little effect and a higher temperature destroys the pore structure.

The observed temperature effect is consistent with a secondary mesopore formation mechanism driven by the decomposition of $C_{16}PyCl$. The temperature must be high enough to allow this chemical reaction to occur, but not so high that excessive decomposition or rearrangement of the silica network occurs. The hydrothermal temperature can be used to tune the pore size and distributions within a moderate range.

9.3.5. Particle accessibility tests

HSSP-I particles are designed to be applied to large solutes in applications for drug delivery, adsorption, or catalysis. Accessibility testing has been conducted and compared for HSSP-P and HSSP-I samples by using two different probe molecules, SRB and GFP. SRB is a low molecular weight dye molecule showing red fluorescence, with molecular dimensions along the short and long axes of 11.5 Å and 19 Å, respectively.[28] GFP is a green-fluorescing protein composed of 238 amino acids. GFP has a cylindrical structure with a diameter of ~30 Å and a length of ~40 Å.[29] In our study, confocal fluorescent microscopy is used to conduct the accessibility test. The conditions for the microscopy are selected so that fluorescence is visible when the solute diffuses inside of the shell and core of the particles.

Our results show that SRB can diffuse inside of both HSSP-P and HSSP-I, but that GFP molecules can diffuse into the hollow cores of only HSSP-I, and not HSSP-P. Figure 9.13 shows representative scanning confocal fluorescence (SCF) micrographs collected during the accessibility test of HSSP particles using both SRB and GFP molecules as probes. Figure 9.13a shows a series of SCF images collected across a single HSSP-P particle as a function of focusing depth. As we can see that the SRB molecule can completely diffuse inside the hollow core, in spite of the mesopores being aligned parallel to the shell walls in this sample. This indicates either that the shells contain a significant number of defects, or that the SRB is able to diffuse directly through the micropores that may be present in the silica walls. Figure 9.13b shows the SCF images of a cluster of HSSP-I particles immersed in either SRB or GFP aqueous solutions. Both SRB and GFP molecules are able to diffuse completely inside the core of HSSP-I particles. The observation of green fluorescence indicates that the GFP proteins retain their activity

during diffusion and are not denatured due to interactions with the silica particles. A similar experiment with GFP shows that it is not able to diffuse into the cores of HSSP-P particles prepared without pore expansion by hydrothermal treatment. Preliminary tests also indicate that the diffusion rates of SRB and GFP into the hollow core of HSSP-I differ substantially. It takes less than 1 min for SRB from 0.1 mM solution to completely diffuse into the hollow cores, but at least 5 min for GFP molecules to diffuse in from a 1 mg/ml solution. In addition, the solvent also makes a difference. For example, when acetone is used in stead of water, the diffusion rates of both SRB and GFP molecules are greatly enhanced. Further investigations of diffusion kinetics of SRB and GFP into and out of the hollow cores will be required for potential applications in adsorption and controlled drug release.

9.4. Conclusions

In this chapter, we described a facile two-step procedure for the synthesis of hollow spherical silica particles with inter-connected bimodal mesoporous shells. Latex microspheres were used as templates for the hollow cores of the particles, and a cationic surfactant was used to generate well-defined mesoporosity in the shells. The generation of secondary mesopores was caused by the decomposition of the surfactant template $C_{16}PyCl$ during ammonia hydrothermal treatment in the second step. The HSSP-I samples after hydrothermal treatment show higher hydrothermal stability than the corresponding HSSP-P samples before hydrothermal treatment due to enhanced condensation by ammonia solution. Key factors such as latex/$C_{16}PyCl$ ratio, latex size and ammonia hydrothermal conditions were investigated to learn more about the two-step synthetic processes, and to optimize the experimental conditions for controlled synthesis of HSSP-I with desired bimodal pore size distributions. All results are consistent with pore expansion during ammonia hydrothermal treatment through a combination of physical swelling of micelles and decomposition of the pyridinium templates in a way that can be controlled by the time and temperature of treatment. Accessibility tests were conducted by using scanning confocal microscopy to show that under the proper conditions, hydrothermal pore expansion provides large channels with a pathway into the hollow core of the particles that is large enough for the diffusion of both sulforhodamine B and green fluorescent protein molecules. In contrast, the shells of HSSP-P admit only

the rhodamine dye but exclude the protein from the hollow core of the particles. Thus, the particles reported here have potential use for protein adsorption and release.

Table 9.1. Pore structure parameters of prepared HSSP-I[a]

Sample name	S_{BET} (m^2/g)	V_p @P/P$_0$=0.98 (cm^3/g)	$W_{KJS(primary)}$ (nm)	$W_{KJS(secondary)}$ (nm)
HSSP-I-base	604.8	1.25	4.4	10.0
HSSP-I-S$_1$	406.7	1.35	4.7	12.0
HSSP-I-S$_2$	462.8	1.28	4.7	11.0
HSSP-I-S$_3$	527.6	1.17	4.7	10.4
HSSP-I-S$_5$	547.8	1.07	3.5, 4.2	8.6
HSSP-I-L$_1$	726.1	1.38	4.4	11.0
HSSP-I-L$_3$	562.8	1.28	4.5	9.5
HSSP-I-L$_4$	564.8	1.31	4.7	8.5
HSSP-I-N$_1$	598.6	1.28	4.4	10.0
HSSP-I-N$_3$	657.9	1.20	4.4	10.0
HSSP-I-N$_4$	695.0	0.97	3.6	-
HSSP-I-T$_1$	566.3	1.28	4.2	~ 8
HSSP-I-T$_3$	527.6	1.07	4.4	10
HSSP-I-Tem$_1$	74.6	0.45	-	-
HSSP-I-Tem$_2$	343.7	1.31	4.4	18
HSSP-I-Tem$_4$	888.6	1.21	4.2	-

a. S_{BET} = BET surface area,[30] the adsorbed volume $V_{p/po=0.98}$, W_{KJS} = pore diameter at peak of KJS pore size distribution.
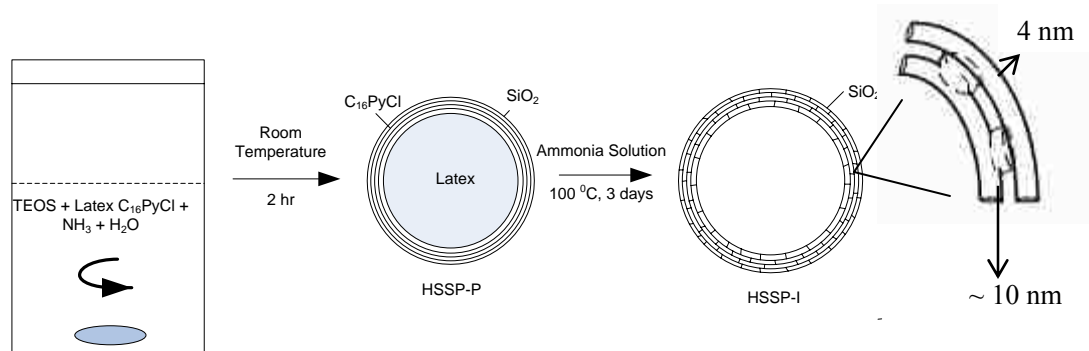
Scheme 9.1. Experimental procedure for the two-step preparation of HSSP-I with interconnected bimodal porous shells.
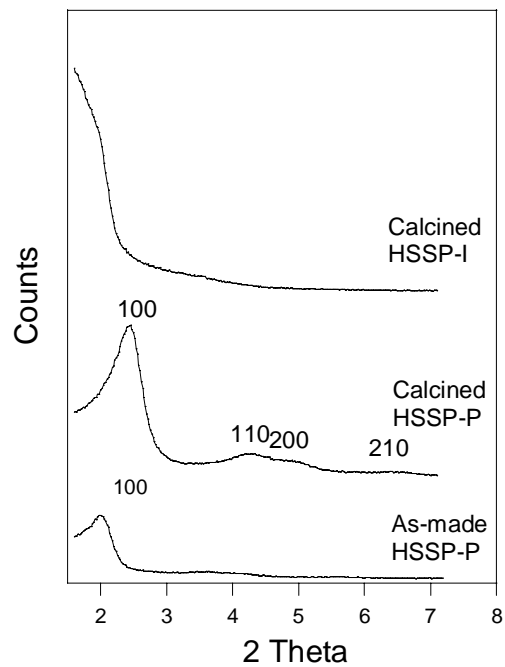
Figure 9.1 Representative XRD results for the base sample obtained at different stages.
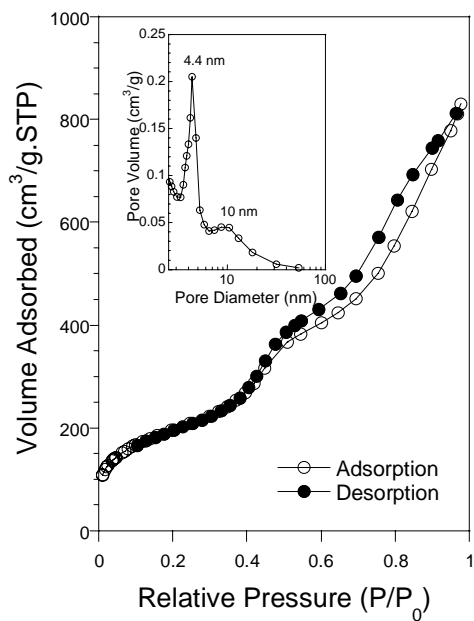
Figure 9.2. Nitrogen sorption isotherms and calculated pore size
distribution of the base sample.
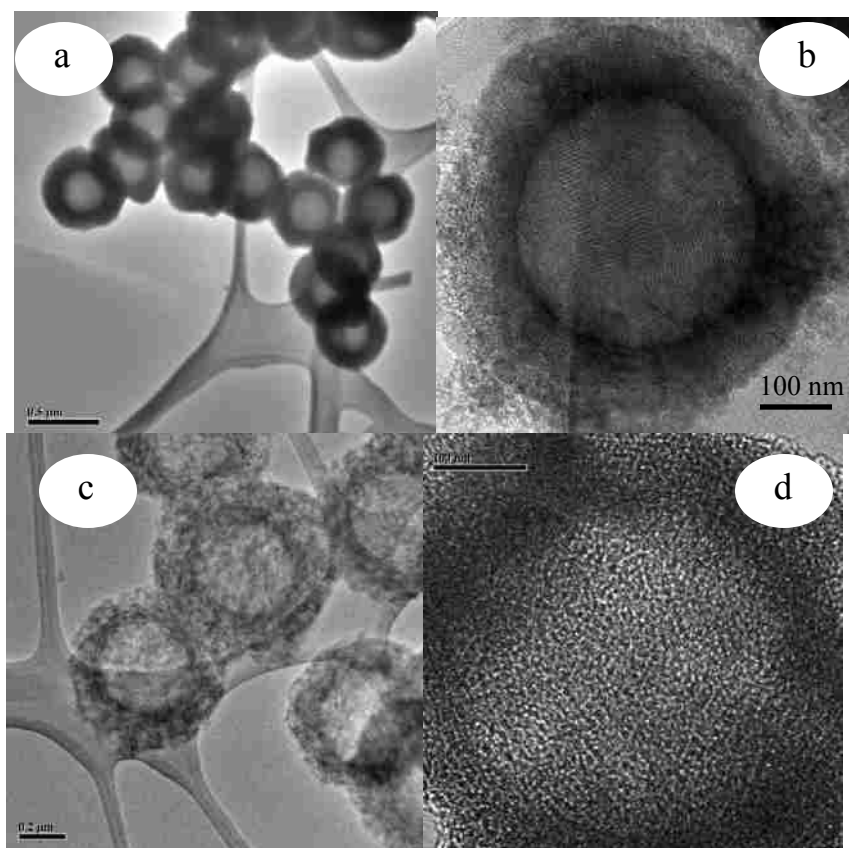
Figure 9.3. Representative TEM images for the base sample. (a) low magnification of HSSP-P, (b) high magnification of HSSP-P, (c) low magnification of HSSP-I, (d) high magnification of HSSP-I. The latex size used is 0.356 μm.
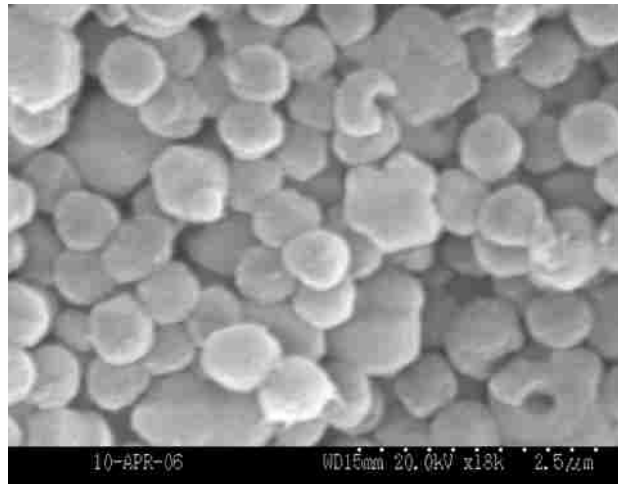
Figure 9.4. Representative SEM images of the base sample HSSP-I.
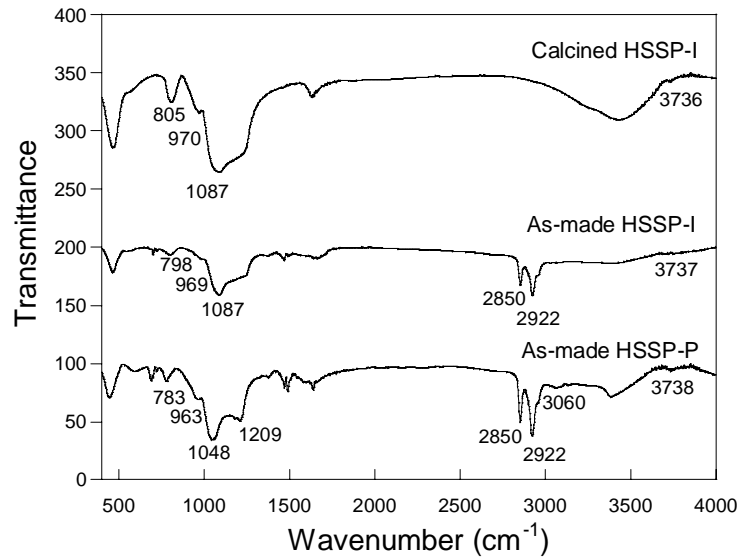
(a)
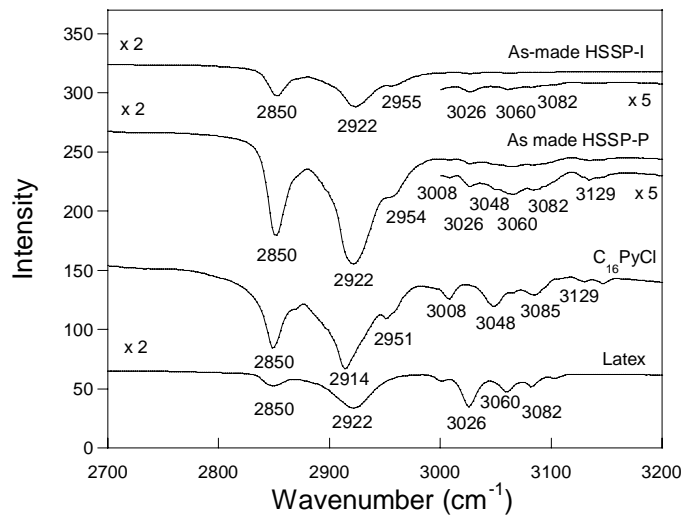
(b)

Figure 9.5. (a) FTIR spectra of KBr pellets pressed with 1 wt% of the base sample obtained at different stages. (b) Expanded FTIR spectra in the wavenumber range from 2700 cm^{-1} through 3200 cm^{-1}.
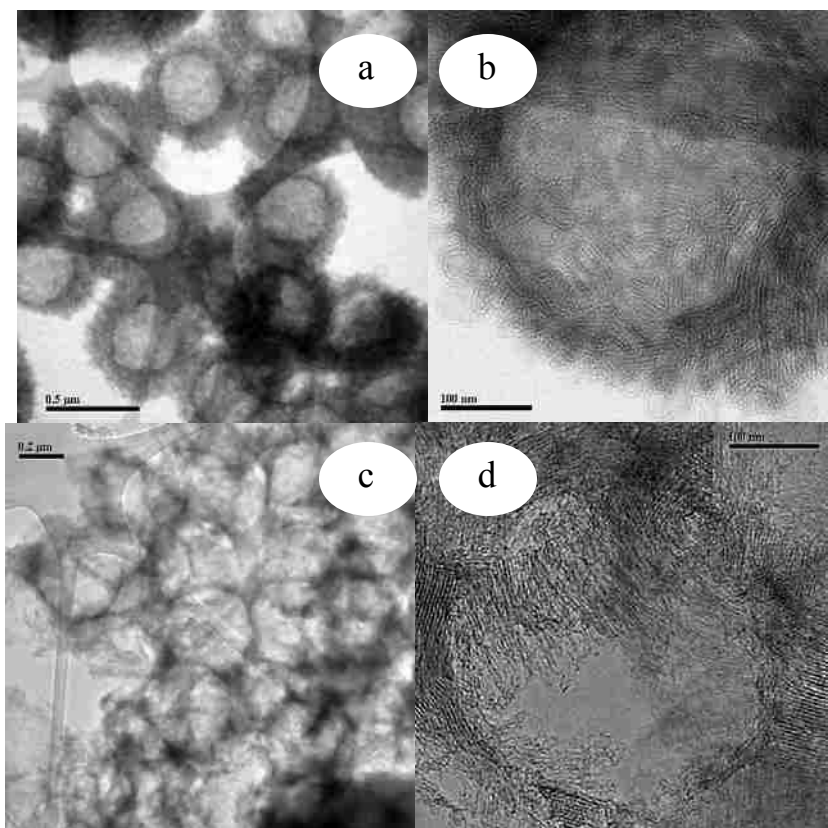
Figure 9.6. Representative TEM images for calcined samples. (a) low magnification of sample HSSP-I-S$_1$, (b) high magnification of HSSP-I-S$_1$, (c) low magnification of HSSP-I-S$_5$, and (d) high magnification of HSSP-I-S$_5$.
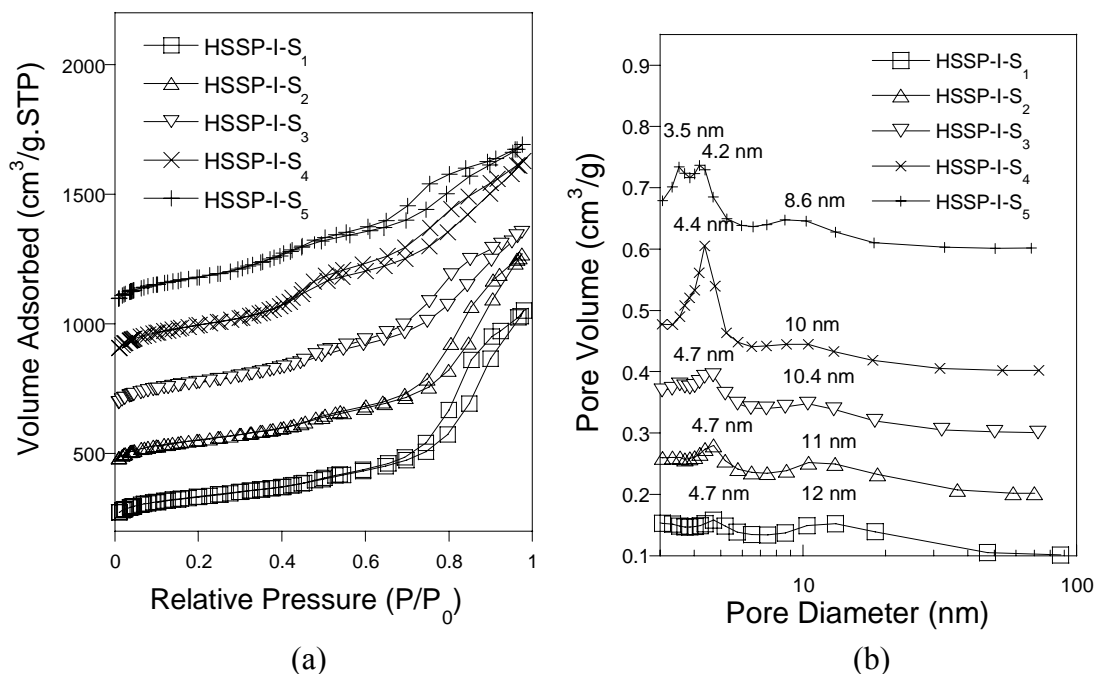
Figure 9.7. (a) Nitrogen adsorption isotherm plots of the series of samples HSSP-I-S$_1$ (upshifted 200 cm^3/g), HSSP-I-S$_2$ (upshifted 400 cm^3/g), HSSP-I-S$_3$ (upshifted 600 cm^3/g), HSSP-I-S$_4$ (upshifted 800 cm^3/g) and HSSP-I-S$_5$ (upshifted 1000 cm^3/g) made with different mass ratios of C$_{16}$PyCl to latex. (b) Pore size distributions of this series of calcined samples calculated using the modified KJS method assuming cylindrical pore geometry.

273
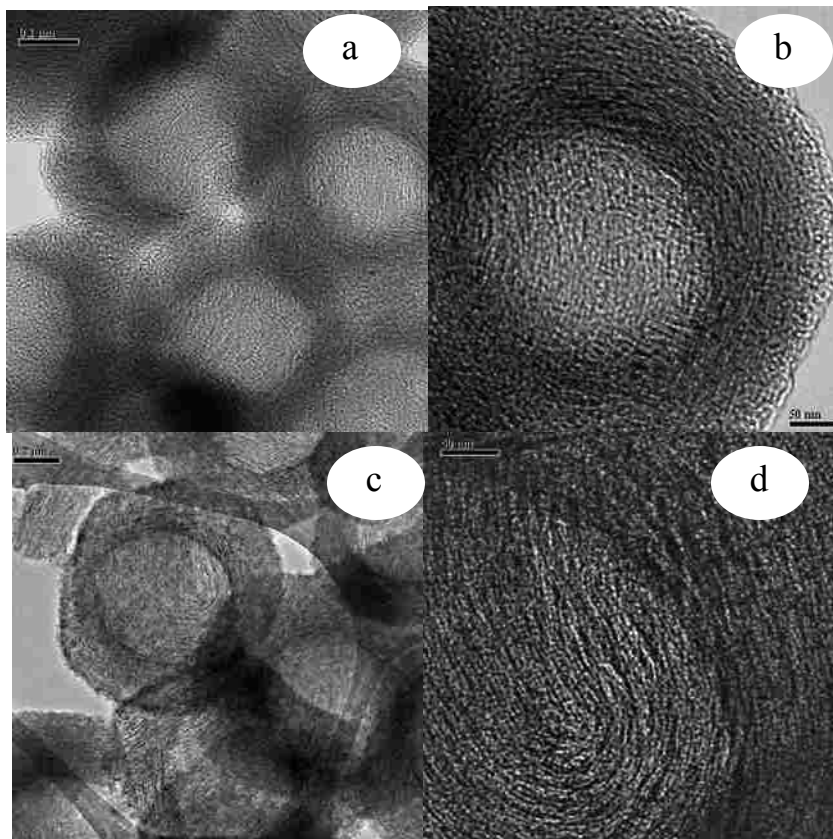
Figure 9.8. Representative TEM images for calcined samples (a) HSSP-I-L$_1$ at low magnification, (b) HSSP-I-L$_1$ at high magnification, (c) HSSP-I-L$_4$ at low magnification, (d) HSSP-I-L$_4$ at high magnification.
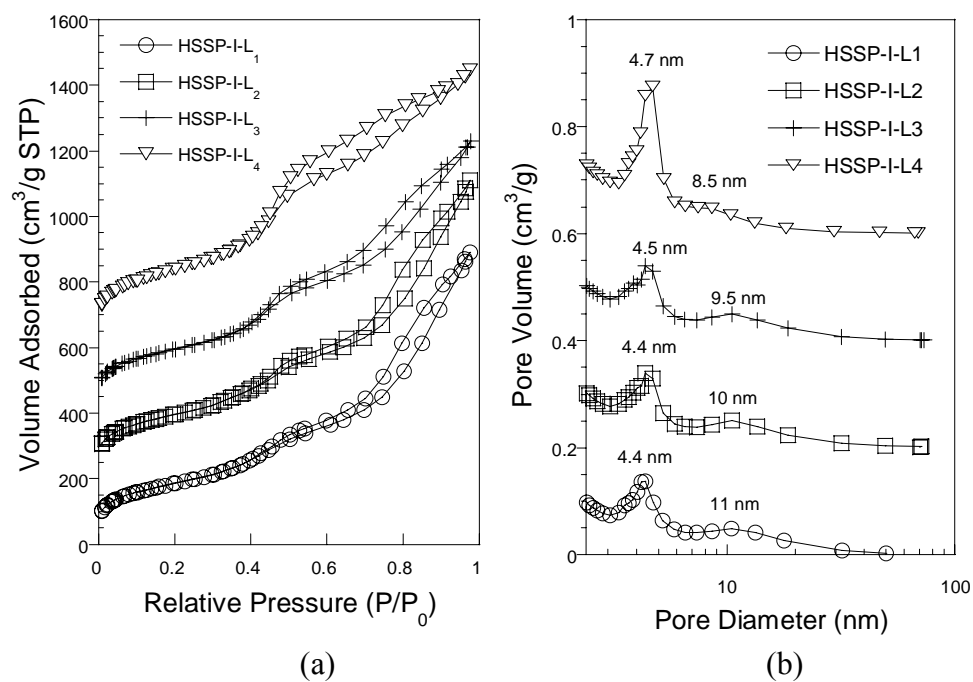
Figure 9.9. (a) Nitrogen adsorption isotherm plots of a series of samples HSSP-I-L$_1$, HSSP-I-L$_2$ (upshifted 200 cm^3/g), HSSP-I-L$_3$ (upshifted 400 cm^3/g) and HSSP-I-L$_4$ (upshifted 600 cm^3/g) made with different latex sizes. (b) Pore size distributions of this series of calcined samples calculated using the modified KJS method assuming cylindrical pore geometry.
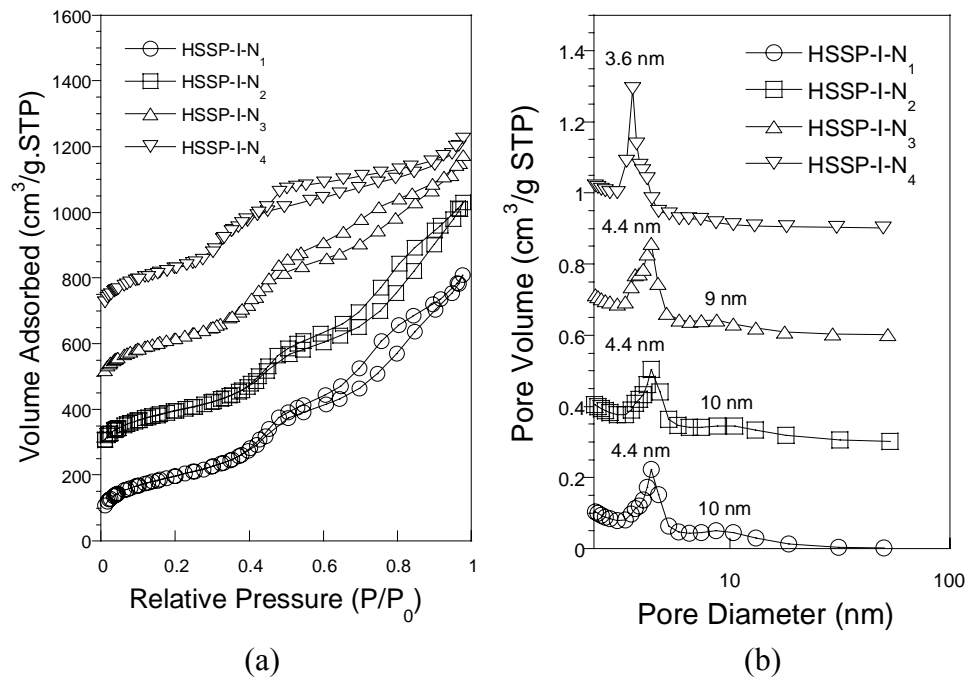
Figure 9.10. (a) Nitrogen adsorption isotherm plots of a series of samples HSSP-I-N_1, HSSP-I-N_2 (upshifted 200 cm^3/g), HSSP-I-N_3 (upshifted 400 cm^3/g) and HSSP-I-N_4 (upshifted 600 cm^3/g) treated post-synthesis with different amounts of ammonia. (b) Pore size distributions of this series of calcined samples calculated using the modified KJS method assuming cylindrical pore geometry.
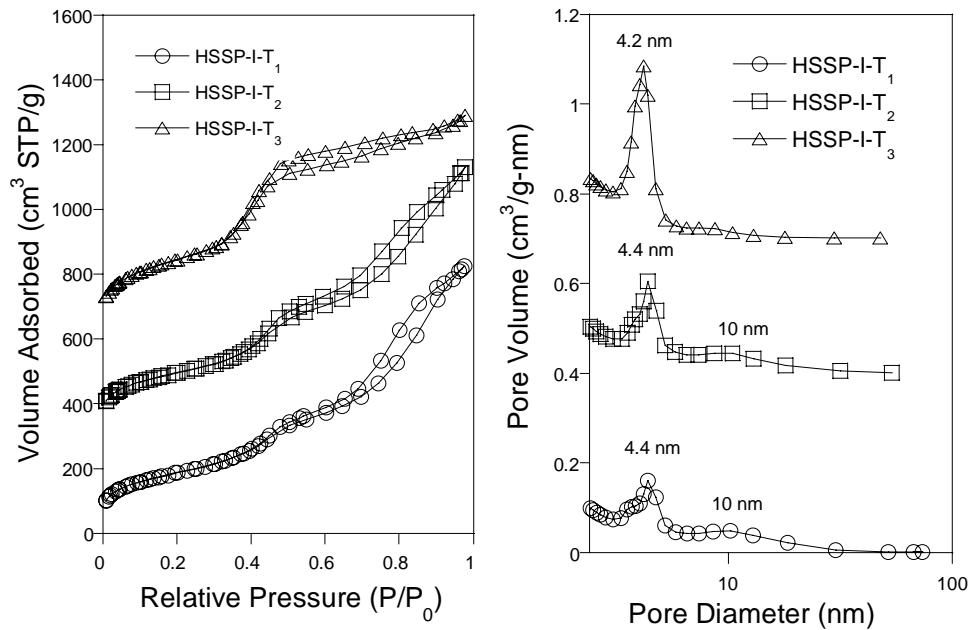
Figure 9.11. (a) Nitrogen adsorption isotherm plots of a series of samples HSSP-I-T_1, HSSP-I-T_2 (upshifted 300 cm^3/g) and HSSP-I-T_3 (upshifted 600 cm^3/g) treated post-synthesis with dilute ammonia for different times. (b) Pore size distributions of this series of calcined samples calculated using the modified KJS method assuming cylindrical pore geometry.
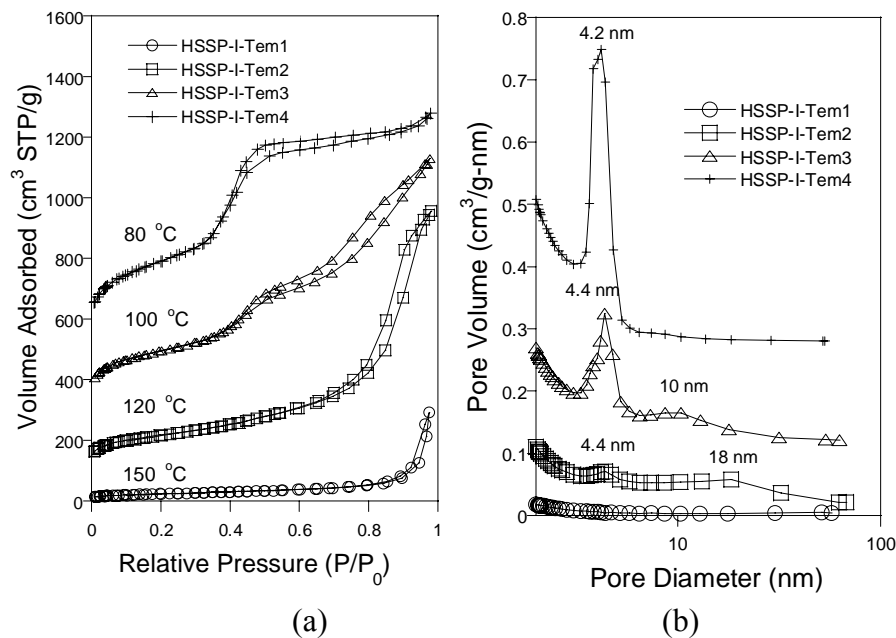
Figure 9.12. (a) Nitrogen adsorption isotherm plots of a series of samples HSSP-I-Temp$_1$, HSSP-I-Tem$_2$ (upshifted 100 cm^3/g), HSSP-I-Tem$_3$ (upshifted 300 cm^3/g) and HSSP-I-Tem4 (upshifted 500 cm^3/g) treated post-synthesis with dilute ammonia at different temperatures. (b) Pore size distributions of this series of calcined samples calculated using the modified KJS method assuming cylindrical pore geometry.

0.1 mM SRB solution
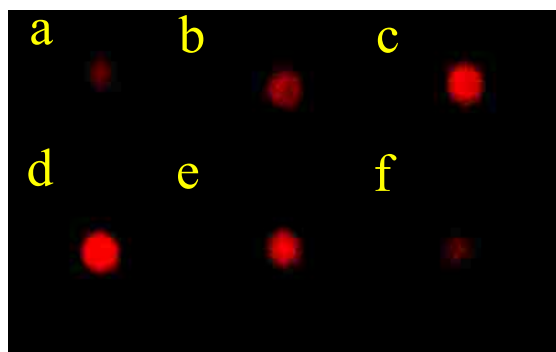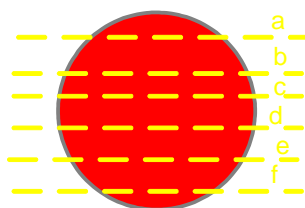
(a) a single HSSP-P particle

0.1 mM SRB   1.0 mg/ml GFP
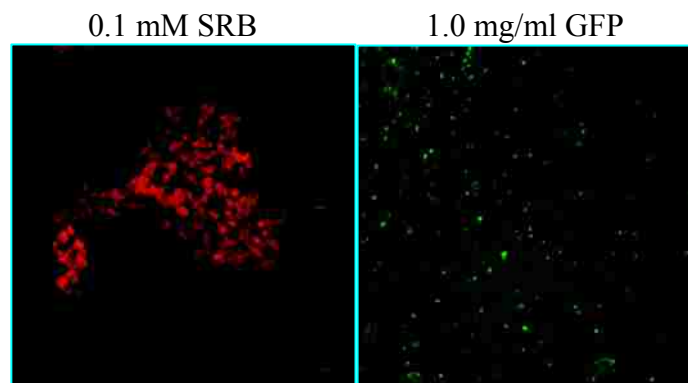
(b) a cluster of HSSP-I particles.

Figure 9.13. Representative confocal scanning fluorescent (CSF) images of SRB and GFP molecules inside the hollow core of HSSP.

Chapter 10. Conclusions and Future Work

10.1. Conclusions based on this dissertation

This thesis addresses two research areas. The first set of chapters (1 through 3) focuses on the investigation of adsorption kinetics and self-assembly behavior on hydroxylated germanium of an anionic fluorinated surfactant, tetraethylammonium perfluorooctylsulfonate (TEA-FOS).   Its adsorption at the solid/liquid interface is measured using a combination of attenuated total reflection Fourier transform infrared spectroscopy (ATR-FTIR) and atomic force microscopy (AFM). The second set of chapters (4 through 9) addresses engineering the synthesis of novel organic/inorganic mesostructured silica composites and mesoporous silica with diverse phase structure, rich particle morphology and well-defined pore size distributions by using a dual templating approach. The research areas are related by the participation of aggregates of surfactants at the solid-liquid interface. The former area (adsorption) involves a 2-dimensional interface on which surfactants are free to assemble, diffuse and aggregate, while the latter area (materials synthesis) involves the formation of 3-dimensional aggregates with a dynamically evolving material. Common issues are the relationship between micelle structure in bulk solution vs. at the solid-liquid interface and how to tune the aggregate shape and size, for instance by adding salts.

In chapters 2 and 3, the ATR-FTIR technique was used in situ to investigate the adsorption kinetics, adsorption isotherms and structural orientation of adsorbed TEA-FOS molecules deposited from an aqueous solution onto hydroxylated germanium under different conditions. We concluded that the adsorption kinetics and average orientation of adsorbed surfactant are strongly dependent of bulk concentration, solution pH and salt concentration. At pH ~ 6, the adsorption kinetics show three stages with clearly different time scales. The first two stages of adsorption lead to the formation of admicelles, which are favored by strong counter-ion binding of TEA^{+}. A surprising acceleration of adsorption rate in the third stage of adsorption leads to a heterogeneous multilayer cluster structure at equilibrium. The three-stage, fast-slow-fast kinetic trend is observed for a wide range of bulk solution concentrations, from 10 % of the CMC of the surfactant to at least 5 times the CMC. The addition of a simple salt like NaCl promotes the initial adsorption rate and causes the adsorbed surfactant to pack more closely at the solid

surface. The presence of a low concentration of NaCl (2 mM) reduces the duration of the three stages almost by half.   While the surface excess reached in the second stage increases with the addition of NaCl, the final surface excess decreases. At pH 3.4, the initial adsorption rate accelerates due to favorable charge interactions between anions FOS$^-$ and positive-charged solid surfaces. The equilibrium surface excess passes through a maximum with increase of salt concentrations. At pH 10, the adsorption rate also accelerates compared to pH 6 due to enhanced negative charge density at the Ge surface. The TEA$^+$ cations mediate the adsorption of FOS$^-$ surfactants at the Ge/aqueous solution interface. Similar to pH 3.4, the equilibrium surface excess passes through the maximum with increase of NaCl concentrations. The salt effects can be explained primarily by (1) screening of surfactant-surfactant repulsion at low concentrations, allowing close-packed layers to form and (2) screening of TEA-FOS attraction at high concentrations, which reduces the thickness and size of the multilayer clusters.

The evolution of the average molecular orientation of TEA-FOS was determined from linear dichroism measurements. Generally, surfactants tend to orient more normal to the surface during adsorption, and a preferred orientation somewhat normal to the surface at equilibrium is finally reached. The average orientation angle of adsorbed TEA-FOS depends on bulk solution concentration, solution pH and ionic strength. For example, at pH 6, without NaCl added, the adsorbed TEA-FOS has an average tilt angle of 48° at equilibrium. With 2 mM NaCl added, the average tilt angle decreases to 38°. These angles indicate a flattened adsorbed micelle structure with oriented surfactants near the center of the micelle and randomly oriented surfactants at the edges, rather than a symmetrical adsorbed micelle.

AFM was also used to image the structure of adsorbed layers on the mica surface, which complements our understanding of the surface aggregation mechanism. Based on the combined AFM and ATR-FTIR study, we proposed a mechanism for three-stage multilayer formation to describe the process of TEA-FOS adsorption from aqueous solution onto hydroxylated germanium.

The fundamental investigations of surfactant self-assembly behavior at the solid/liquid interface support our understanding of the interactions between surfactants / solvents and solid surfaces, how these interactions influence surfactant aggregation at

interfaces, and the effects of variables such as bulk solution pH and the addition of salts. This knowledge should be applicable to the formation of surfactant-templated materials. The second part of this dissertation focuses on using interactions between surfactants and polymerizing metal alkoxides precursors to direct their assembly into ordered mesophases and mesoporous materials.

In chapters 5 and 6, we investigated nanocasting using mixtures of a new pair of surfactant types: the cationic surfactant cetyltrimethylammonium bromide (CTAB) and the sugar-based surfactant n-octyl-β-D-glucopyranoside (C_8G_1). As we explained there, the headgroups of the sugar-based surfactant are of long-term interest in our group as models for the types of nonionic functionalities that may be useful for creating selective adsorption and catalytic sites at the pore wall.

In chapter 5, we explored an unusually large level of pore distortion observed while attempting to preserve the structure of dual surfactant-templated materials. We proposed a reactive pore expansion mechanism during ammonia vapor post-treatment of ordered mesoporous silica templated by binary mixtures of CTAB and C_8G_1. We found that ammonia vapor treatment of as-made materials lead to retention or improvement of the long-range pore order. We also observed not only that the pores expanded during ammonia treatment, but also that the degree of expansion could be controlled by adjusting the amount of C_8G_1 in the mixed surfactant system. Based on a series of investigations with other nonionic surfactants, we concluded that the large degree of pore expansion is driven not only by a change in the physical interactions between silica and the surfactants, but also by the occurrence of the Maillard reaction between C_8G_1 and ammonia vapor at the surface of silica. It is possible that silica catalyzes the sugar transformation reaction.

In chapter 6, the ternary phase diagram of CTAB/C_8G_1/water was developed by using polarized optical microscopy. We found a very large range where mixed C_8G_1 and CTAB form 2D hexagonal columnar phase (HCP) in water. Narrow cubic, lamellar and solid surfactant phases form at compositions spanning the phase diagram from binary C_8G_1/water to binary CTAB/water. The main hypothesis that we tested in this chapter was that this ternary phase diagram could be utilized as guidance to synthesize ordered thick mesoporous silica films by replacing the water in the liquid crystal with an

equivalent volume of silica. We found that the compositions over which different type of mesostructured materials are prepared correspond very well with those of the ternary phase diagram. The only complication was that for samples containing too little silica, the walls were too fragile to allow the structure to be preserved after surfactant removal. However, our success with predicting the mesostructure from the ternary phase diagram suggests that we can use phase studies to find a surfactant system that will give a stable mesoporous product.

In chapters 7 and 8, we investigated synergistic sol-gel induced precipitation using mixture of cetyltrimethylammonium chloride (CTAC) and 1H, 1H, 2H, 2H-perfluorodecylpyridinium chloride (HFDePC), to study the micelle mixing and demixing behavior of this system in the context of materials synthesis.

In chapter 7, we synthesized a series of mesoporous silica materials with diverse phase and pore structure using mixture of CTAC and HFDePC as dual templates. Many parameters were investigated not only to verify mixing and demixing, but also to control the demixed micelle architectures. The parameters included the molar ratio of CTAC to HFDePC, ammonia concentration, the amount of NaCl, ethanol addition and the synthesis temperature. Demixing can be observed in precipitated silica under a wide range of molar compositions of the combined surfactants used for materials synthesis. The phase structure of the final materials changes from 2D HCP to wormhole-like to disordered to random mesh phase as the molar fraction of HFDePC increases in the mixture. Addition of a large amount of ammonia to an aqueous solution of an equimolar mixture of mixed CTAC/HFDePC surfactants causes the formation of co-existing domains of distinct meso-structured silica particles due to micelle demixing. This leads to an ordered biphasic 2D HCP/ mesh mesophase material with well-defined bimodal mesoporosity. In addition, the addition of an appropriate amount of salt NaCl or ethanol can promote the formation of bimodal mesoporous materials with wormhole-like mesopores. The increase of synthesis temperature favors the formation of very small nanoparticles, which sinter together to form secondary large mesopores. These results could be explained by the effects of synthesis conditions on the interactions between surfactants and silica, micellization, and the relative rates of precipitation of particles precipitated by fluorinated and hydrogenated surfactants.

In chapter 8, we investigated the effects of different type of salts, organic additives and alkyl chain length on the pore properties and particle morphology of silica particles prepared using mixture of CTAC and partially fluorinated alkylpyridinium chloride as dual templates. We found that particle morphology and pore size distributions are strongly dependent of the type of salts added and chain length of surfactants. The effect of the cation in the salt could be correlated with the ionic volume of the cation, while the anion effect followed the Hofmeister series. Adding lipophilic or fluorophilic solvents was shown to selectively swell hydrocarbon or fluorocarbon micelles, respectively, thus enabling fine tuning of the bimodal pore size distributions of the final silica particles. Preliminary results suggest that the dual surfactant-templated particles can be used for preparation of bi-functional catalysts by selective deposition of metal complexes within different pores.

In chapter 9, we described a facile two-step procedure for the synthesis of hollow spherical silica particles with inter-connected bimodal mesopore shells (HSSP-I). In the first step, cetylpyridinium chloride and latex microparticles jointly template spherical mesostructured particles with latex cores. Hydrothermal treatment causes decomposition of the pyridinium and the formation of large secondary mesopores. Enhanced condensation of the walls of HSSP-I during hydrothermal treatment causes it to exhibit higher hydrothermal stability than the corresponding HSSP-P sample isolated and calcined before hydrothermal treatment. Key factors such as latex/cetylpyridium chloride ($C_{16}PyCl$) mass ratio, latex size and ammonia hydrothermal conditions were investigated to learn more about the two-step synthetic processes, and to optimize the experimental conditions for controlled synthesis of HSSP-I with desired bimodal pore size distribution. Accessibility tests were conducted by using scanning confocal fluorescent microscopy to show that hydrothermal pore expansion provides a pathway of large channels into the hollow core of the particles that is large enough for the diffusion of both sulforhodamine B (SRB) and green fluorescent protein molecules. In contrast, the shells of HSSP-P admit only the SRB dye but exclude the protein from the hollow core of the particles. This result is immediately relevant for applications such as enzyme stabilization and protein adsorption.

To summarize, this thesis addressed fundamental physical aspects of the aggregation of new types of fluorinated and mixed surfactants at solid-liquid interfaces. These included TEA-FOS adsorption at the solid-liquid interface and templating of sol-gel derived mesoporous silica materials using dual templates. Effects of parameters such as reagent concentrations, salt addition, and solvent addition in all of these processes could be explained based on changes in surface forces and the kinetics of reactions occurring during these processes. The surfactant adsorption results have direct application for cleaning, fluorinated surfactant recovery, and surface modification by fluorinated surfactants. The methods developed to tune the mesopores structure of the materials have potential applications in adsorption, catalysis and drug delivery.

10.2. Future work

While we have described many achievements derived from the study of surfactant aggregation during adsorption from solution and materials templating, this dissertation also revealed areas where further fundamental studies are warranted, and suggested new directions for applications of porous materials.

During TEA-FOS adsorption at the solid/liquid interface, we have observed unusual three stage adsorption kinetics and quantified the influence on the kinetics and adsorbed layer structure of factors including surfactant concentration, solution pH and salts. However, more remains to be learned about the nature of the adsorption process and the dynamics of the adsorbed layer of TEA-FOS. This information includes the surfactant exchange rate with the solution, the distribution of TEA^+, water displacement and the nature of the surface. This information would allow us to address some questions that we are still not quite sure about right now. For example, why is the adsorption so slow compared with normal hydrocarbon surfactants? What kind of reorganization process (if any) is happening at the solid/liquid interface during the second, slowest, adsorption stage? What kind of surfactant orientation is favorable for the third stage to happen? To answer these questions, some innovative experimental techniques are required, such as small angle neutron scattering (SANS), neutron reflectivity and atomic force microscopy (AFM). Because SANS and neutron reflectivity are not easily accessible, AFM is a good choice if a germanium substrate with low roughness is available. We can match the adsorption kinetics with appropriate time scale to capture images, and develop force-

distance curve at specific points on the sample surface to obtain depth-resolved structure information about the adsorbed surfactant layer. In addition, some other factors such as the influence of counter-ions and temperature effects need to be quantified. The long-term goal will be to establish a model for the three-stage adsorption kinetics. In addition, this research area can be extended to a study of the kinetics of self-assembly and exchange of mixed hydrocarbon and fluorocarbon surfactant systems at the solid/liquid interface.

In terms of dual templating of porous silica, we have performed some of the groundwork that will make the mesoporous materials we prepared applicable to different fields. For example, we have investigated the effect of ammonia treatment on the pore structure of the silica materials, and developed the cetyltrimethylammonium bromide (CTAB)/water/n-octyl-β-D-glucopyranoside (C_8G_1) ternary phase diagram, and showed that it can be used for predictive mesoporous materials synthesis. This groundwork will make it possible to begin introducing more components to functionalize the materials to move towards our long-term goal of creating designed sites on the pore walls. We can introduce organic functionality and transition metals into the pore walls of the materials by using precursors complexed to the sugar headgroups of a surfactant such as C_8G_1. The functionalized materials can be used for different applications such as selective adsorption, sensors and catalysis. It remains to be seen how far this approach can be extended, in terms of the types of surfactants whose materials templating can be predicted and the degree of well-defined functional group incorporation possible.

In contrast to mixed CTAB/C_8G_1 pore templates, the mixed CTAC/HFDePC system has unique properties that are both useful and of fundamental interest. We have successfully used the sol-gel process to verify mixing or demixing in concentrated mixtures of surfactants in precipitated silica, and demonstrated the ability to control the demixed micelle architectures, pore size distribution and particle morphology in combined CTAC/HFDePC templated mesoporous materials. We found facile methodologies to synthesize long-range ordered biphasic materials, which act as well-defined bimodal porous materials. The groundwork we did brings out many significant findings which provide a better understanding of mixing and demixing behavior of binary incompatible surfactants in sol-gel reaction induced precipitation. In the future, more work needs to be

286

done to gain deeper insight into the fundamental factors that underlie the formation of novel biphasic and hierarchical structures, as well as morphology control of the precipitated particles. In addition, we have showed that the two populations of segregated micelles can be independently swollen by adding a lipophilic oil (TMB) to swell the hydrogenated cores of CTA^+ micelles or a fluorophilic oil (PFD) to swell the fluorinated cores of $HFDePy^+$ micelles. The swollen micelles can serve as templates during the hydrolysis of TEOS in aqueous ammonia to form silica particles with controlled bimodal mesoporosity. The long-term goal is to make controlled deposition of different types of metal oxides into different channels for bi-functional catalyst applications. A preliminary study shows that the hydrogenated metal complex $Cr(acac)_3$ can be preferentially deposited within CTA^+-rich micelle templated channels. Attempts with hexafluoro-acac complexes showed that they were not deposited as selectively, most likely because they are not fluorophilic enough. To find a fluorinated metal complex with strong fluorophilicity will be important. For the CTAC/HFDePC system, we have shown that the materials templated by using this pair of surfactants in solution show demixed micelle architectures over a range of compositions when the total concentration is below 10 wt%. More work still needs to be done to know the mixing and demixing phase behavior of this pair of surfactants in the liquid crystal state (by developing a ternary phase diagram) and for materials prepared by nanocasting. Preliminary studies have shown that this pair can form mixed crystals and acid-catalyzed silica materials with diverse phase structure such as 2D hexagonal columnar phase (HCP), lamellar and $Pm\bar{3}n$ cubic phases over a wide range of ternary compositions of CTAC/HFDePC/water. Small domains of demixed phases were also found. To investigate the organization of hydrocarbon and fluorocarbon surfactants in mixed or demixed micelles will be useful for applications in controlled functionalization of mesoporous materials.

Using dual templating with cetylpyridinium chloride ($CP_{16}yCl$) and latex, we have shown that hollow silica particles with protein-accessible pore shells can be prepared. This was a preliminary study focusing only on pore structure. In future, protein adsorption and release from and to the hollow cores need to be quantified for potential application in drug delivery. Functionalizing the surface will be desirable for controlling surfactant adsorption, infiltration, and release. A pH-responsive protein release system would be quite valuable for drug delivery. Furthermore, the dual templating of hollow particles also provide a

facile methodology for introducing independent functional groups or transition metals within the hollow cavities and within the shells, which would serve as a new type of nanometer-resolved multifunctional material.

There were some directions that we pursued but which did not reach completion. For example, we tried to use anionic fluorinated surfactants to make ordered materials. These are the most readily available surfactants commercially, so using anionic surfactants would make application of fluorinated surfactant templating more accessible to other research groups. Two methods were investigated. At high concentration of surfactant (> 10 wt%), we investigated nanocasting using different anionic fluorinated surfactants, such as lithium perfluorooctylsulfonate (LiFOS), TEA-FOS, lithium perfluorooctanonate (LiPFO), ammonium perfluorooctanonate (NH_4PFO), lithium perfluorodecanoate (LiPFD) and tetramethylperfluorodecanoate ($N(CH_3)_4PFD$). While some surfactants, such as $N(CH_3)_4PFD$ and LiPFD, form ordered liquid crystal phases over a wide range of concentration in their phase diagram, the materials we prepared always had a disordered pore structure. When using LiFOS and TEAFOS as templates, only lamellar mesophase structure could be obtained. Our results showed that with the synthetic approaches we took, the phase diagram of anionic fluorinated surfactants could not be used as a guide for predictive materials synthesis. This may be caused by the rapid kinetics of polymerization compared to the time required for ordering of a liquid crystal. Another complicating factor is the strong repulsion between anionic surfactants and negatively charged silicates above the isoelectric point of silica. At low concentrations (<10 wt%), we investigated synergistic precipitation using the same anionic fluorinated surfactants by changing the synthetic conditions (temperature, composition, addition of ethanol and solution pH). Unfortunately, the materials we prepared had lamellar or disordered structure.

Another direction pursued was an effort to prepare long-range ordered intermediate phase structures using the cationic fluorinated surfactant HFDePC. The phase diagram of HFDePC shows an intermediate phase over a relative wide range of concentration at the temperature of 50 °C. We expected to make order mesoporous materials with intermediate phase by the nanocasting method. However, the materials we prepared using HFDePC alone always had poorly ordered structure with one broad peak in XRD pattern.

We found that the ordering of the final materials could be improved by increasing the relative amount of CTAC. We come to conclusion that the nanocasting method is more suitable for hydrocarbon surfactants than fluorinated surfactants. Any explanation for this observation would be the subject for future studies, but some studies with TEA-FOS supply a hypothesis that can be tested in the future. During polarized microscopy studies with TEA-FOS, isotropic phases were formed even in concentrated solutions, and it took an extraordinarily long time to begin to see anisotropic phases forming. A sample that accidentally began drying, however, showed hexagonal phase formation very quickly. Therefore, it seems that some fluorinated surfactants assemble slowly into ordered phases (this is consistent with the slow adsorption and exchange dynamics observed in this dissertation). Comparing samples prepared by rapid drying (such as coatings) to samples made by slow reaction and evaporation (nanocasting) would allow this to be tested.

The list of future prospects could continue, but it should be clear by now that this area of research is still open to further fundamental insights and application developments. It is our hope that the work reported here will provide inspiration for further investigation and discovery.

References:
Chapter 1:
(1) J. S. Beck, R. J. Stokes, D. F. Evans. Fundamentals of Interfacial Engineering; Wiley-VCH Publisher, **1997**.

(2) J. Umemura, D. G. Cameron, H. H. Mantsch. *J. Phys. Chem.* **1980**, 84, 2272.

(3) M. J. Citra, P. H. Axelsen, *Biophys. J.* **1996**, 71, 1796.

(4) F. Picard, T. Buffeteau, B. Desbat, M. Auger, M. Pézolet. *Biophys. J.* **1999**, 76, 539.

(5) J. N. Israelachvili, B. W. Mitchell, B.Ninham. *J. Chem. Soc. Faraday Trans.* 2 **1976**, 72, 1525.

(6) M. P. Krafft, J.G. Riess, *Biochimie* **1998**, 80,489.

(7) E. Kissa, Fluorinated Surfactants. New York, Marcel Dekker, **1994**.

(8) S. E. Rankin, B. Tan, H.J. Lehmler and B.L. Knutson. Materials Research Society Symposium Proceedings **2003**, 775, 47.

(9) J. J. Lehmler, P. M. Bummer, *Chemtech* **1999**, 29, 7.

(10) N. P. Hankins, J. H. O'Haver, J. H. Harwell. *Ind. Eng. Chem. Res.* **1996**, 35, 2844.

(11) M. A. Yeskie, J. H. Harwell, *J. Phys. Chem.* **1988**, 92, 2346.

(12) R. Atkin, V. S. J. Craig, S. Biggs. *Langmuir* **2001**, 17, 6155.

(13) F. Tiberg, B. Jönsson, B. Lindaman. *Langmuir* **1994**, 10, 3714.

(14) C. Ström, P. B. Jönsson, O. Söderman. *Langmuir* **2000**, 16, 2469.

(15) S. Manne, V. Hansson, *Prog. Colloid Polym. Sci.* **1997**, 103, 226.

(16) M. L. Fielden, P. M. Claesson, R. E. Verrall, *Langmuir*, **1999**, 15, 3924.

(17) B. G. Sharma, S. Basu, M .M. Sharma, *Langmuir*, **1996**, 12, 6506.

(18) T. Svitova, R. M. Hill, C. J. Radke, *Colloids and Surfaces A: Physicochem. Eng. Aspects*, **2001**, 183-185, 607.

(19) J. F. Liu, W. A. Ducker. *J. Phys. Chem. B* **1999**, 103, 8558.

(20) T. W. Davey, G. G. Warr, M. Almgren, T. Asakawa, *Langmuir*, **2001**, 17, 5283.

(21) B. Y. Zhu, P. Zhang, L. Wang, Z.-F. Liu, *J. Colloid Interface Sci.* **1997**, 185, 551.

(22) R. E. Lamont, W. Ducker. *J. Colloid Interface Sci.* **1997**, 191, 303.

(23) G.G. Warr. *Curr. Opinion in Colloid Int. Sci.* **2000**, 5, 88.

(24) A. R. Rennie, E. M. Lee, E. A. Simister, R. K. Thomas, *Langmuir* **1990**, 6, 1031.

(25) D. C. McDermott, J. McCarney, R. K. Thomas. *J. Colloid Interface Sci.* **1994**,162, 304.

(26) P. J. K. Paterson, *Mater. Forum* **1987**, 10, 144.

(27) R. P. Sperline, S. Muralidharan, H. Freiser. *Langmuir* **1987**, 3, 198.

(28) K. S. Rochester, C. H. *J. Chem. Soc., Faraday Trans.* 1 **1988**, 84, 3641.

(29) S. Cheng, K. K. Chittur, C. N. Sukenik, L. A. Culp, K. Lewandowska. *J. Colloid Interface Sci.* **1994**, 162, 135.

(30) P. K. Singh, J. J. Adler, Y. I. Rabinovitch, B.M. Moudgil. *Langmuir* **2001**, 17, 468.

(31) D. J. Neivandt, M. L. Gee, M. L. Hair, C. P. Tripp. *J. Phys. Chem. B* **1998**, 102, 5107.

(32) W.-H. Jang, J. Miller. *J. Phys. Chem.* **1995**, 99, 10272.

(33) A. R. Hind, S. K. Bhargava, S. C. Grocott. *Langmuir* **1997**, 13, 3483.

(34) R. P. Sperline, S. Muralidharan, H. Freiser. *Langmuir* **1987**, 3, 198.

(35) N. J. Harrick. Internal Reflection Spectroscopy; Interscience Publisher: New York, **1967**.

(36) Crystal Reference Guide from Nicolet.

(37) H. G. Tompkins. *Applied spectroscopy.***1974**, 28, 335.

(38) A. Ulman. In Fourier Transform Infrared Spectroscopy in Colloid and Interface Science; S. R. Ed: Scheuing, American Chemical Society: Washington, DC, **1990** 144.

(39) R. Z. Zbinden. In Infrared Spectroscopy of High Polymers; Academic Press: New York, **1964**.

(40) S. Fray, L.K. Tamm. *Biophys. J.* **1991**, 60, 922.

(41) G. Binnig, C. F. Quate, Ch. Gerber. *Phys. Rev. Lett.* **1986**, 12, 930.

(42) AFM manual notebook for multimode III.

(43) S. Manne, J.P. Cleveland, H.E. Gaub, G.D. Stucky, P.K. Hansma. *Langmuir* **1994**, 10, 4409.

(44) S. Manne, H. E. Gaub. *Science* **1995**, 270, 1480.

(45) C.-L. Lai, J. H. Harwell, E. A. O'Rear, S. Komatsuzaki, J. Arai, T. Nakakawaji, Y. Ito. *Colloids Surf. A* **1995**, *104*, 231.

Chapter 2:

(1) M. Sprik, U. Röthlingsberger, M. L. Klein. *Molec. Phys.* **1999**, *97*, 355.

(2) U. Röthlingsberger, K. Laasonen, M. L. Klein, M. Sprik. *J. Chem. Phys.* **1996**, *104*, 3692.

(3) H. J. Lehmler, P. M. Bummer, M. Jay. *Chemtech* **1999**, *29*, 7.

(4) K. Harrison, J. Goveas, K. P. Johnston, E. A. O'Rear. *Langmuir* **1994**, *10*, 3536.

(5) E. Kissa, *Fluorinated Surfactants*. New York, Marcel Dekker. **1994**.

(6) A. Emmer, M. Jansson, J. Roeraade. *J. Chromatogr.* **1991**, *547*, 544.

(7) P. Boivin, R. K. Kobos, S. L. Papa, W. H. Scouten. *Biotechnol. Appl. Biochem.* **1991**, *14*, 155.

(8) S. Yamada, J. Israelachvili. *J. Phys. Chem. B* **1998**, *102*, 234.

(9) S. E. Rankin, B. Tan, H. J. Lehmler, K. P. Hindman, and B. L. Knutson. *Micropor. Mesopor. Mater.* **2004,** *73*, 197.

(10) B. Tan, A. Dozier, H. J. Lehmler, B. L. Knutson, S. E. Rankin. *Langmuir* **2004**, *20*, 6981.

(11) B. Tan, H. J. Lehmler, S. M. Vyas, B. L. Knutson, S. E. Rankin. *Chem. Mater.* **2005**, *17*, 916.

(12) J. L. Blin, P. Lesieur, M. J. Stébé. *Langmuir* **2004**, *20*, 491

(13) M. P. Krafft, J. G. Riess. *Biochimie* **1998**, *80*, 489.

(14) J. C. Ravey, M. Stébé. *J. Colloids Surf.*, A **1994**, *84*, 11.

(15) K. Shinoda, M. Hatō, T. J. Hayashi. *Phys. Chem.* **1972**, *76*, 909.

(16) R.J. Stokes, D. F. Evans. *Fundamentals of Interfacial Engineering*; Wiley-VCH Publisher, **1997**.

(17) J. Umemura, D. G. Cameron, H. H. Mantsch. *J. Phys. Chem.* **1980**, *84*, 2272.

(18) T. J. Lenk, V. M. Hallmark, C. L. Hoffmann, J. F. Rabolt, D. G. Castner, C. Erdelen, H. Ringsdorf. *Langmuir* **1994**, *18*, 8085.

(19) C.-L. Lai, J. H. Harwell, E. A. O'Rear, S. Komatsuzaki, J. Arai, T. Nakakawaji, Y. Ito. *Colloids Surf. A* **1995**, *104*, 231.

(20) R. Banga, J. Yarwood, A. M. Morgan, B. Evans, J. Kells. *Thin Solid Films* **1996**, *284-285*, 261.

(21) R. Lamont, W. Ducker. *J. Coloid. Interface Sci.* **1997**, *191*, 303.

(22) L. Evenäs, I. Furó, P. Stilbs, R. Valiullin. *Langmuir* **2002**, *18*, 8096.

(23) O. J. Rojas, L. Macakova, E. Blomberg, A. Emmer, P. M. Claesson. *Langmuir* **2002**, *18*, 8085.

(24) R. Atkins, V. S. J. Craig, E. J. Wanless, S. Biggs. *Adv. Colloid Interface Sci.* **2003**, *103*, 219.

(25) D. W. Fuerstenau. *J. Colloid Interface Sci.*, **2002**, 256, 79.

(26) D. K. Schwartz. *Annu. Rev. Phys. Chem.* **2001**, *52*, 107.

(27) W. A. Hayes, D. K. Schwartz. *Langmuir* **1998**, *14*, 5913.

(28) I. Doudevski, W. A. Hayes, D. K. Schwartz. *Phys. Rev. Lett.* **1998**, *81*, 4927.

(29) L. S. Penn. H. Huang, M. D. Sindkhedkar, S. E. Rankin, K. Chittenden, R. P. Quirk, R. T. Mathers, Y. Lee. *Macromolecules* **2002**, *35*, 7054.

(30) A. Knoblich, M. Matsumoto, K. Murata, Y. Fujiyoshi. *Langmuir* **1995**, *11*, 2361.

(31) D. P. Bossev, M. Matsumoto, M. Nakahara. *J. Phys. Chem. B* **1999**, *103*, 8251.

(32) D. P. Bossev, M. Matsumoto, T. Sato, H. Watanabe, M. Nakahara. *J. Phys. Chem. B* **1999**, *103*, 8259.

(33) M. Matsumoto, C. E. McNamee, D. P. Bossev, M. Nakahara, T. Ogawa. *Colloid Polym. Sci.* **2000**, *278*, 619.

(34) M. J. Citra, P. H. Axelsen. *Biophys. J.* **1996**, *71*, 1796

(35) F. Picard, T. Buffeteau, B. Desbat, M. Auger, M. Pézolet. *Biophys. J.* **1999**, *76*, 539

(36) R. Arkin, V. S. J. Craig, S. Biggs. *Langmuir* **2001**, *17*, 6155.

(37) F. Tiberg, B. Jönsson, B. Lindman. *Langmuir* **1994**, *10*, 3714.

(38) C. Ström, P. B. Jönsson, O. Söderman. *Langmuir* **2000**, *16*, 2469.

(39) D. J. Neivandt, M. L. Gee, C. P. Tripp, M. L. Hair. *Langmuir* **1997**, *13*, 2519.

(40) K. S. Kung, K. F. Hayes. *Langmuir* **1993**, *9*, 263.

(41) R. P. Sperline, Y. Song, H. Freiser. *Langmuir* **1992**, *8*, 2183

(42) P. W. Hoffmann, M. Stelzle, J. F. Rabolt. *Langmuir* **1997**, *13*, 1877.

(43) J. T. Woodward, I. Doudevski, H. D. Sikes, D. K. Schwartz. J. Phys. Chem. B **1997**, 101, 7535.

(44) H. G. Tompkins. *Appl. Spec.* **1974**, *28*, 335.

(45) M. W. Tsao, C. L. Hoffmann, J. F. Rabolt. *Langmuir* **1997** 13, 4317

(46) C. A. Alves, M. D. Porter. *Langmuir* **1993** 9, 3507

(47) C. Naselli, J. D. Swalen, J. F. Rabolt. *J. Chem. Phys.* **1989** 90, 3855

(48) Y. Ren, M. Asanuma, K. Iimura, T. Kato. *J.Chem. Phys.* **2001** 114, 8, 923

(49) T. J. Lenk, V. M. Hallmark, C. L. Hoffmann, J. F. Rabolt. *Langmuir* **1994** 10, 4610

(50) R. B. Bird, W. E. Stewart, E. N. Lightfoot. *Transport phenomena*, John Wiley & Sons, Inc. New York, **2002**; p520

(51) K. A. Peterlinz, R. Georgiadis. *Langmui*r, **1996**, 12, 4731

(52) J. R. Rahn, R.B. Hallock. *Langmui*r, **1995**, 11, 650.

(53) K. A. Peterlinz, R. Georgiadis. *Langmuir* **1996**, *12*, 4731.

(54) Y. Gao, J. Du, T. Gu. *J. Chem. Soc. Faraday Trans. I.* **1987**, *83*, 2671.

(55) A. Carre, F. Roger, C. Varinot. *J. Colloid Interface Sci.* **1992**, *154*, 174.

(56) N. P. Hankins, J. H. O'Haver, J. H. Harwell. *Ind. Eng. Chem. Res.* **1996**, *35*, 2844.

(57) H. Hoffmann. Würtz, J. *J. Molec. Liquids.* **1997**, *72*, 191.

(58) D. J. Neivandt, M. L. Gee, M. L. Hair, C. P. Tripp. *J. Phys. Chem. B* **1998**, *102*, 5107.

(59) J. F. Scamehorn, R. S. Schechter, W. H. Wade. *J. Colloid Interface Sci.* **1982**, *85*, 463.

(60) P. Somasundaran, D. W. Fuerstenau. *J. Phys. Chem.* **1966**, *70*, 90.

(61) P. K. Singh, J. J. Adler, Y. I. Rabinovitch, B. M. Moudgil. *Langmuir* **2001**, *17*, 468.

(62) M. A. Yeskie, J. H. Harwell. *J. Phys. Chem.* **1988**, *92*, 2346.

(63) E. Johannessen, H. Walderhaug, B. Balinov. *Langmuir*, **2004**, *20*, 336.

Chapter 3:

(1) M. Drach, A. Andrzejewska, J. Narkiewicz-Michalek, W. Rudziński, L. Koopal. *Phys. Chem. Chem. Phys.* **2002**, 4, 5846.

(2) R. Atkin, V. S. Craig, S. Biggs. *Langmuir* **2001** 17, 6155.

(3) R. Atkin, V. S. J. Craig, S. Biggs. *Langmuir* **2000**, 16, 9374.

(4) E. J. Wanless, W. A. Ducker. *J. Phys. Chem.* **1996**, 100, 3207.

(5) L. K. Koopal, E. M. Lee, Bönmer. *J. Colloid Interface Sci.* **1995**, 170, 85.

(6) D. M. Nevskaia, A. Guerrero-Ruíz, J. López-González, de-D. *J. Colloid Interface Sci.* **1998**, 205, 97.

(7) A. N. Davis, S. A. Morton, R. M. Counce, D. W. DePaoli, M. Z. C. Hu. *Colloids and Surfaces A.* **2003**, 221. 69.

(8) E. J. Wanless, W. A. Ducker. *Langmuir*, **1997**, 13, 1463.

(9) S. B. Velegol, B. D. Fleming, S. Biggs, E. J. Wanless, R. D. Tilton. *Langmuir*, **2000**, 16, 2548.

(10) S. C. Biswas, D. K. Chattoraj. *J. Colloid Interface Sci.* **1998**, 205, 12.

(11) P. C. Pavan, E. L. Crepaldi, G. Gomes, Valim, *J. Colloid and Surf. A* **1999**, 154, 399.

(12) P. Somasundaran, D. W. Fuerstenau. *J. Phys. Chem.* **1966**, 70, 90.

(13) D. J. Neivandt, M. L. Gee, M. L. Hair, C. P. Tripp. *J. Phys. Chem. B* **1998**, 102, 5170.

(14) R. Windsor, D. J. Neivandt, P. B. Davies. *Langmuir* **2001**, 17, 7306.

(15) R. E. Lamont, W. Ducker. *J. Am. Chem. Soc.* **1998**, *120*, 7602.

(16) H. Hoffmann, J. Würtz.. *J. Molec. Liquids.* **1997**, *72*, 191.

(17) K. Wang, G. Karlsson, M. Almgren. *J. Phys. Chem. B* **1999**, 103, 9237.

(18) M. Matsumoto, C. E. McNamee, D. P. Bossev, M. Nakahara, T. Ogawa, *Colloid Polym. Sci.* **2000**, *278*, 619.

(19) W. Schorr, H. Hoffmann, *J. Phys. Chem.* **1981**, 85, 3160.

(20) P. Lianos, R. Zana, *J. Phys. Chem.* **1980**, 84, 3339.

(21) M. S. Vethamuthu, M. Almgren, G. Karlsson, P. Bahadur, *Langmuir* **1996**, 12, 2173.

(22) T. Imae, R. Kamiya, S. Ikeda, *J. Colloid Interface Sci.* **1985**, 108, 215.

(23) G. Porte, J. Appell, Y. Poggi, *J. Phys. Chem.* **1980**, 84, 3105.

(24) T. Asakawa, H. Hisamatsu, S. Miyagishi. *Langmuir* 1995, 11, 478.

(25) K. Tamori, K. Kihara, K. Esumi, K. Meguro. *Colloid Polym. Sci.* **1992**, 270, 927.; T. Asakawa, T. Fukita, S. Miyagishi. *Langmuir* **1991**, 7, 2112.

(26) R. E. Lamont, W. Ducker. *J. Colloid Interface Sci.* **1997**, 191, 303.

(27) C.-L. Lai, J. H. Harwell, E. A. O'Rear, S. Komatsuzaki, J. Arai, T. Nakakawaji, Y. Ito. *Colloids Surf. A* **1995**, *104*, 231.

(28) V. Glöckner, K. Lunkwitz, D. Prescher. *Tenside Surfactants Detery* **1989,** 26, 376.

(29) A. Knoblich, M. Matsumoto, K. Murata, Y. Fujiyoshi *Langmuir* **1995**, *11*, 2361.

(30) D. P. Bossev, M. Matsumoto, M. Nakahara. *J. Phys. Chem. B* **1999**, *103*, 8251.

(31) D. P. Bossev, M. Matsumoto, T. Sato, H. Watanabe, M. Nakahara. *J. Phys. Chem. B* **1999**, *103*, 8259.

(32) K. S. Kung, K. F. Hayes. *Langmuir* **1993**, 9, 263.

(33) A. Carre, F. Roger, C. Varinot. *J. Colloid Interface Sci.* **1992**, 154, 174.

(34) S. A. Sukhishvili, S. Granick. *J. Chem. Phys.* **1998**, 109, 6861.

(35) M. R. Böhmer, O. A. Evers, J. M. H. M. Scheutjens. *Macromolecules*, **1990**, 23, 2288.

(36) H. G. M. Van de Streeg, M. A. Cohen Stuart, A. De Keizer, B. H. Bijstebosch. *Langmuir* **1992**, 8, 2538.

(37) F. Fang, I. J. Szleifer. *J. Chem. Phys.* 2003, 119 (2), 1053.

(38) J. N. Israelachvili. Intermolecular and Surface Forces, 2nd edition; Academic Press: New York, **1991**.

(39) S. A. Sukhishvili, S. J. Granick. *J. Phys. Chem. B* **1999**, 103, 472.

Chapter 4:

(1) C. T. Kresge, M. E. Leonowicz, W. J. Roth, J. C. Vartuli, J. S. Beck, *Nature* **1992**, 359, 710.

(2) A. Stein, Adv. Mater. **2003**, 15, 763.; M. Hartmann. *Chem. Mater.* **2005**, 17, 4577.

(3) A. Monnier, F. Schüth, Q. Kumar, D. Margolese, R. S. Maxwell, G.D. Strucky, M. Krisnamurthy, P. Petroff, A. Firouzi, M. Janicke, B.F. Chmelka, *Science* **1993**, 261, 1299.

(4) P. T. Tanev, T. J. Pinnavaia, *Science* **1995**, 10, 865.

(5) G. S. Attard, J. C. Glyde, C. G. Göltner, *Nature* **1995**, 378, 366.

(6) B. Echchahed, M. Morin, S. Blais, A.-R. Badiei, G. Berhault, L. Bonneviot, *Micropor. Mesopor. Mater.* **2001**, 44-45, 53.

(7) S. A. Bagshaw. *J. Mater. Chem.* **2001**, 11, 831.

(8) S. E. Rankin, B. Tan, H.-J. Lehmler, K. P. Hindman, B. L. Knutson, *Micropor. Mesopor. Mater.* **2004,** *73*, 197.

(9) B. Tan, A. Dozier, H.-J. Lehmler, B. L. Knutson, S. E. Rankin, *Langmuir* **2004**, *20*, 6981.

(10) B. Tan, H.-J. Lehmler, S.M. Vyas, B. L. Knutson, S. E. Rankin, *Chem. Mater.* **2005**, *17*, 916.

(11) Q. Huo, D. I. Margolese, U. Ciesla, P. Feng, T. E. Gier, P. Sieger, R. Leon, P. M. Petroff, F. Schüth, G. D. Stucky. *Nature*, **1994**, 368. 317.; J. Fan, L. Wang, B. Tu, D. Zhao, Y. Sakamoto, O. Terasaki, *J. Am. Chem. Soc.* **2001**, 123, 12113.

(12) P. T. Tanev, T. J. Pinnavaia, *Science* **1996**, 271, 1267.

(13) T. Yokoi, H. Yoshitake, T. Tatsumi. *Chem. Mater.* **2003**, 15, 4536.

(14) B. Tan, S. E. Rankin, *J. Phys. Chem. B* **2004** 108, 20122.

(15) S. E. Friberg, C. C. Yang, J. Sjöblom, *Langmuir* **1992**, 8, 372.

(16) Y. Takasawa, M. Ueno, T. Sawamura, K. Meguro. *J. Colloid Interface Sci.* **1981**, 84, 196.; N. Funasaki, S. Hada. *J. Phys. Chem.* **1979**, 83, 2471.

(17) D.-G. Nilsson, B. Lindman. *J. Phys. Chem.* **1984**, 88, 5391.

(18) J. M. Corkill, J. F. Goodman, J. R. Tate. *Trans. Faraday Soc.* **1964**, 60, 986.; K. J. Mysels, R. J. Otter. *J. Colloid Interface Sci.* **1961**, 16, 462.

(19) A. Malliaris, W. Binana-limbele, R. Zana. *J. Colloid Interface Sci.* **1986**, 110, 114.

(20) E. W. Kaler, K. L. Herrington, A. K. Murthy. *J. Phys. Chem.* **1992**, 96, 6698.

(21) J. Penfold, E. J. Staples, I. Tucker, L. J. Thompson, R. K. Thomas. *Physica B*. **1998**, 248, 223.

(22) Q. Huo, D. I. Margolese, G. D. Stucky, *Chem. Mater.* **1996**, 8, 1147.

(23) Y. Liang, M. Hanzlik, R. Anwander. *J. Mater. Chem.* **2006**, 16, 1238.

(24) R. Ryoo, S. H. Joo, J. M. Kim. *J. Phys. Chem. B* **1999**, 103, 7435.

(25) M. Song, J. Kim, S. Cho, J. Kim, *Langmuir* **2002** 18, 6110.; D. Kushalani, A. Kuperman, G. A. Ozin, K. Tanaka, J. Garces, M. M. Olken, *Adv. Mater.* **1996**, 7, 842.; L. D. Dai, T. W. Wang, L. T. Bu, G. Chen, *Colloids Surf. A* **2001**, 181, 151.; R. Ryoo, C. H. Ko, I.-S. Park, *ChemComm.* **1999**, 1413.

(26) A. Lind, B. Spliethoff, M. Lindèn, *Chem. Mater.* **2003**, 15, 813.; H.-P. Hentze, S. R. Raghavan, C. A. McKelvey, E. W. Kaler. *Langmuir* **2003**, 19, 1069

(27) J. Pang, J. E. Hampsey, Q. Hu, Z. Wu, V. T. John, Y. F. Lu, *ChemComm.* **2004,** 682.

(28) F. Chen, L. Huang, Q. Li, *Chem. Mater.* **1997,** 9, 2685. ; D. Chen, Z. Li, C. Yu, Y. Shi, Z. Zhang, B. Tu, D. Y. Zhao, *Chem. Mater.* **2005**, 17, 3228.; L. Kong, S. Liu, X. Yan, Q. Li, H. He, *Micropor. Mesopor. Mater.* **2005**, 81, 251.; S. Zhai, J. Zheng, J. Zou, D. Wu, Y. Sun, *Journal of Sol-gel Science and Technology*. **2004**, 30, 149.

(29) D. Chen, Z. Li, Y. Wan, X. Tu, Y. Shi, Z. Chen, W. Shen, C. Yu, B. Tu, D. Zhao, *J. Mater. Chem.* **2006**, 16, 1511. D. H. Chen, Z. Li, C. Z. Yu, Y. Shi, Z. Zhang, B. Tu, D. Zhao, *Chem. Mater.* **2005**, 17, 3228.

(30) F. X. Chen, L. M. Huang, Q. Z. Li, *Chem. Mater.* **1997**, 9, 2685.; A. Lind, J. Anderson, S. Karlsson, P. Agren, P. Bussian, H. Amenitsch, M. Linden, *Langmuir* **2002**, 18, 1380. A. Lind, B. Spliethoff, M. Linden, *Chem. Mater.* **2003**, 15, 813.

(31) F. Portet, P. L. Desbene, C. Treiner, *J. Colloid Interface Sci.* **1996**, 184, 216.

(32) K. Tamori, K. Esumi, K. Meguro. *J. Colloid Int. Sci.* **1991**, 142, 236.

(33) K. Shinoda, T. Nomura. *J. Phys. Chem.* **1980**, 84, 365.

(34) T. Asakawa, K. Johten, S. Miyagishi, M. Nishida, *Langmuir* **1985**, 1, 347.; N. Funasaki, S. Hada, *Chem. Lett.* **1979**, 717.

(35) P. Mukerjee, A. Y. S. Yang, *J. Physical Chemistry* **1976**, 80, 1388.

(36) K. L. Mysels, *J. Colloid Interface Sci.* **1978**, 66, 331.

(37) T. Asakawa, K. Johten, S. Miyagishi, M. Nishida, *Langmuir* **1985**, 1, 347.; T. Asakawa, H. Hisamatsu, S. Miyagishi, *Langmuir* **1995**, 11, 478.

(38) R. E. Pagano, N. L. Gershfeld, *J. Phys. Chem.* **1972**, 76, 1238. J. Nishida, A. Brizard, B. Desbat, R. J. Oda, *Colloid and Interface Sci.* **2005**, 284, 298. T. Imae, T. Takeshita, M. Kato, *Langmuir* **2000**, 16, 612.

(39) Y. Muto, K. Esumi, K. Meguro, R. J. Zana, *Colloid Interface Sci.* **1987**, 120, 162.; T. W. Davey, G. G. Warr, T. Askawa, *Langmuir* **2003**, 19, 266. T. Asakawa, H. Hisamatsu, S. Miyagishi, *Langmuir* **1996**, 12, 1204. P. Barthelemy, V. Tomao, J. Selb, Y. Chaudier, B. Pucci, *Langmuir* **2002**, 18, 2557.

(40) K. Yoda, K. Tamori, K. Esumi, K. Meguro, *J. Colloid Interface Sci.* **1989**, 131, 282.; R. D. Lisi, A. Inglese, S. Milioto, A. Pellerito, *Langmuir* **1997**, 13, 192.

(41) P. Barthelemy, V. Tomao, J. Selb, Y. Chaudier, B. Pucci, *Langmuir* **2002**, 18, 2557. S. Rossi, G. Karlsson, S. Ristori, G. Martini, K. Ewards, *Langmuir* **2001**, 17, 2340.

(42) P. Barthelemy, V. Tomao, J. Selb, Y. Chaudier, B. Pucci, *Langmuir* **2002**, 18, 2557.

(43) M. Almgren, V. M. Garamus, *J. Phys. Chem. B* **2005**, 109, 11348.

(44) K. Esumi, T. Arai, K. Takasugi, Colloid Surf. A. **1996**, 111, 231. N. Funasaki, S. Hada, *J. Phys. Chem.* **1980**, 84, 736. N. Funasaki, S. Hada, *J. Phys. Chem.* **1983**, 87, 342. T. Arai, K. Takasugi, K. Esumi, *J. Colloid Interface Sci.* **1998**, 197, 94.; K. Nagai, K. Esumi, *Colloids Surf. A.* **1995**, 94, 97.

(45) D. Li, Y. Han, J. Song, L. Zhao, X. Xu, Y. Di, F.-S. Xiao. *Chem. Eur. J.* **2004**, 10, 5911.

(46) M. Groenewolt, M. Antonietti, *Langmuir* **2004**, 20, 7811.; S. Areva, C. Boissiere, D. Grosso, T. Asakawa, C. Sanchez, M. Linden, *Chem. Comm.* **2004**, 1630.

(47) Y. Han, J. Y. Ying, *Angew. Chem. Int. Ed.* **2005**, 44, 288.

(48) K. Wang, G. M. Orädd, Almgren, T. Asakawa, B. Bergenståhl, *Langmuir* **2000**, 16, 1042.

(49) H. Djojoputro, X. F. Zhou, S. Z. Qiao, L. Z. Wang, C. Z. Yu, G. Q. Lu, *J. Am. Chem. Soc.* **2006**, 128, 6320.

(50) Y. Han, J. Y. Ying, *Angew. Chem. Int. Ed.* **2004**, 44, 288.

(51) T. Asakawa, H. Hisamatsu, S. Miyagishi, *Langmuir* 1995, 11, 478; M. Kadi, P. Hansson, M. Almgren, I. Furó,. *Langmuir*, **2002**, 18, 9243; M. Almgren, V. M. Garamus, *J. Phys. Chem. B,* **2005**, 109, 11348

(52) P. Yang, T. Deng, D. Zhao, P. Feng, D. Pine, B. F. Chmelka, G. M. Whitesides, G. D. Stucky. *Science* **1998**, 282, 2244.

(53) H. Maekawa, J. Esquena, S. Bishop, C. Solans, B. F. Chmelka. *Adv. Mater.* **2003**, 15, 591.

(54) W. Ogasawara, W. Shenton, S. A. Davis, S. Mann. *Chem. Mater.* **2000**, 12, 2835. V. Pedroni, P. C. Schulz, M. E. G. de Ferreira, M. A. Morini. *Colloid Polym. Sci.* **2000**, 278, 964.

(55) J.-H. Smått, S. Schunk, M. Lindén. *Chem. Mater.* **2003**, 15, 2354.

(56) T. Sen, G. J. T. Tiddy, J. L. Casci, M .W. Anderson. *Chem. Commun.* **2003**, 2182. F. Carn, A, Colin, M. F. Achard, H. Deleuze, E. Sellier, M. Birot, R. Backov. *J. Mater. Chem.* **2004**, 14, 1370.

(57) D. Zhao, P. Yang, B. F. Chmelka, G. D. Stucky. *Chem. Mater.* **1999**, 11, 1174. H. Nishihara, S. R. Mukai, D. Yamashita, H. Tamon. *Chem. Mater.* **2005**, 17, 683.

(58) S.A. Davis, S. L. Burkett, N. H. Mendelson, S. Mann. *Nature* **1997**, 385, 420.

(59) J. Yu, J. C. Yu, M. K.-P. Leung, W. Ho. B. Cheng, X. Zhao, J. Zhao. *J. Catal.* **2003**, 217, 69. N. Tsubaki, Y. Zhang, S. Sun, H. Mori, Y. Yoneyama, X. Li, K. Fujimoto. *Catal. Commun.* **2001**, 2, 311.

(60) Y. Zhou, M. Antonietti. *Chem. Commun.* **2003**, 2546

(61) J. R. Bellare, H. T. Davis, W. G. Miller, L. E. Scriven, *J. Colloid Interface Sci.* **1990** 136, 305.

(62) A. Firouzi, F. Atef, A. G. Oertli, G. D. Stucky, B. F. Chmelka, *J. Am. Chem. Soc.* **1997** 119, 3596.

Chapter 5:

(1) J. S. Beck, J. C. Vartuli, W. J. Roth, M. E. Leonowicz, C. T. Kresge, K. T. Schmitt, C. T-W. Chu, D. H. Olson, E. W. Sheppard, S. B. McCullen, J. B. Higgins, J. L. Schlenker, *J. Am. Chem. Soc.* **1992**, 114, 10834.

(2) C. T. Kresge, M. E. Leonowicz, W. J. Roth, J. C. Vartuli, J. S. Beck, *Nature* **1992**, 359, 710.

(3) A. Corma, D. Kumar, in Mesoporous Molecules Sieves 1998, L. Bonneviot, F. Béland, C. Danumah, S. Giasson, and S. Kaliaguine (eds.), *Studies Surface Sci. Catal.* **1998**, 117, 201.

(4) X. S. Zhao, G. Q. Lu, G. J. Millar, *Ind. Eng. Chem. Res.* **1996**, 35, 2075.

(5) C. G. Guizzard, A. C. Julbe, A. Ayral, *J. Mater. Chem.*, **1999**, 9, 55.

(6) U. Ciesla, F. Schüth, *Micropor. Mesopor. Mater.* **1999**, 27, 131.

(7) S. Inagaki, S. Guan, T. Ohsuna, O. Terasaki, *Nature* **2002**, 416, 304.

(8) Q. Huo, D. I. Margolese, U. Ciesla, D. G. Demuth, P. Feng, T. E. Gier, P. Sieger, A. Firouzi, B. F. Chmekla, F. Schüth, G. D. Stucky, *Chem. Mater.* **1994**, 6, 1176.

(9) Y. Zhou, M. Antonietti, *Adv. Mater.* **2003**, 15, 1452.

(10) Y. Wei, J. Xu, H. Dong, J.H. Dong, K. Qiu, S.A. Jansen-Varnum, *Chem. Mater.* **1999**, 11, 2023.

(11) C. Stubenrauch, *Curr. Opinion in Colloid Int. Sci.* **2001**, 6, 160.

(12) B. Hoffmann, G. Platz, *Curr. Opinion in Colloid Int Sci.* **2001**, 6, 171.

(13) C. Pinel, P. Loisil, P. Gallezot, *Adv. Mater.* **1997**, 9, 582.

(14) J. H. Jung, M. Amaike, S. Shinkai, *Chem. Commun.* **2000**, 2343.

(15) M. A. Markowitz, P. R. Kust, G. Deng, P. E. Schoen, J. S. Dordick, D. S. Clark, B. P. Gaber, *Langmuir* **2000**, 16, 1759.

(16) P. Sakya, J. M. Seddon, R. H. Templer, *J. Phys. II France 4* **1994**,1311.

(17) F. Nilsson, O. Söderman, *Langmuir* **1006**, 12, 902.

(18) U. Lavrenčič-Štangar, N. Hüsing, *Silicon Chem.* **2003**, 2, 157.

(19) G. Persson, H. Edlund, H. Amenitsch, P. Laggner, G. Lindblom, *Langmuir* **2003**, 19, 5813.

(20) A. B. Cortés, M. Valiente, *Colloid Polym. Sci.* **2003**, 281, 319.

(21) J. C. Vartuli, K. D. Schmitt, C. T. Kresge, W. J. Roth, M. E. Leonowicz, S.B. McCullen, S. D. Hellring, J. S. Beck, J. L. Schlenker, D.H. Olson, E.W. Sheppard, *Chem. Mater.* **1994**, 6, 2317.

(22) P. T. Tanev, T.J. Pinnavaia, *Science* **1995**, 10, 865.

(23) D. Zhao, Q. Huo, J. Feng, B. F. Chmelka, G. D. Stucky, *J. Am. Chem. Soc.* **1998**, 120, 6024.

(24) A. Firouzi, D. Kumar, L. M. Bull, T. Besier, P. Sieger, Q. Huo, S. A. Walker, J.A. Zasadzinski, C. Glinka, J. Nicol, D. Margolese, G. D. Stucky, B. F. Chmelka, *Science* **1995**, 267, 1138.

(25) A. Monnier, F. Schüth, Q. Huo, D. Kumar, D. Margolese, R. S. Maxwell, G. D. Stucky, M. Krishnamurty, P. Petroff, A. Firouzi, M. Janicke, B. F. Chmelka, *Science* **1993**, 261, 1299.

(26) S. E. Friberg, C. C. Yang, J. Sjöblom, *Langmuir* **1992**, 8, 372.

(27) G. S. Attard, J. C. Glyde, C. G. Göltner, *Nature* **1995**, 378, 366.

(28) C. G. Göltner, M. Antonietti, *Adv. Mater.* **1997**, 9, 431.

(29) C. G. Spickermann, Top. *Curr. Chem.* **2003**, 226, 29.

(30) Y. Zhou, M. Antonietti, *Chem. Mater.* **2004**, 16, 544.

(31) C. J. Brinker, Y. F. Lu, A. Sellinger, H.Y. Fan, *Adv. Mater.* **1999**, 11, 579.

(32) C. G. Göltner, B. Smarsly, B. Berton, M. Antonietti, *Chem. Mater.* **2001**, 13, 1617.

(33) H. P. Hentze, E. Krämer, B.Berton, S. Förster, M. Antonietti, *Macromolecules* **1999**, 32, 5803.

(34) S. A. Bagshaw, E. Prouzet, T.J. Pinnavaia, *Science* **1995**, 269, 1242.

(35) S. Polarz, B. Smarsly, L. Bronsterin, M. Antonietti, *Angew. Chem. Int. Ed.* **2001**, 40, 4417.

(36) M. Antonietti, B. Berton, C. Göltner, H. Hentze, *Adv. Mater.***1998**, 10, 154.

(37) M. Groenewolt, M. Antonietti, *Langmuir* **2004**, 20, 7811.

(38) P. Feng, X. Bu, D. J. Pine, *Langmuir* **2000**, 16, 5304.

(39) M. G. Song, J. Y. Kim, S. H. Cho, J. D. Kim, *Langmuir* **2002**, 18, 6110.

(40) G. M. Wu, J. Wang, J. Shen, Q. Y. Zhang, B. Zhou, Z. S. Deng, B. Fan, D. P. Zhou, F. S. Zhang, *J. Phys. D-Appl. Phys.* **2001**, 34, 1301.

(41) H. P. Lin, C. Y. Mou, S. B. Liu, C. Y. Tang, C. Y. Lin, *Micropor. Mesopor. Mater.* **2001**, 44-45, 129.

(42) Z. Y. Yuan, J. L. Blin, B. L. Su, *Chem. Comm.* **2002**, 504.

(43) A. Sayari, Y. Yang, M. Kruk, M. Jaroniec, *J. Phys. Chem. B* **1999**, 103, 3651.

(44) K. S.W. Sing, D. H. Everett, R. A.W. Haul, L. Moscou, R. A. Pierotti, J. Rouquérol, T. Siemieniewska, *Pure Appl. Chem.* **1985**, 57, 603.

(45) E. P. Barrett, L. G. Joyner, P. Halenda, *J. Am. Chem. Soc.* **1951**, 73, 373.

(46) M. Kruk, M. Jaroniec, *Langmuir* **1997**, 13, 6267.

(47) A. Sayari, P. Liu, M. Kruk, M. Jaroniec, *Chem. Mater.* **1997**, 9, 2499.

(48) M. Jaroniec, M. Kruk, *Langmuir* **1999**, 15, 5410.

(49) S. Polarz, Antonietti, M. *Chem. Comm.* **2002**, 2593.

(50) M. Kruk, M. Jaroniec, Chem. Mater. **2001**, 13, 3169.

(51) A. R. Hind, S.K. Bhargava, S.C. Grocott, *Langmuir* **1997**, 13, 6255.

(52) D. C. Calabro, E.W. Valyocsik, F.X. Ryan, *Micropor. Mater.* **1996**, 7, 243.

(53) D. R. Scheuing, J.G. Weers, *Colloids Surf.* **1991**, 55, 41.

(54) P. J. Innocenzi, *Non-Cryst. Solids* **2003**, 316, 309.

(55) T. M. Parrill, *J. Mater. Res.* **1992**, 7, 2230.

(56) N. R. B. Coleman, G.S. Attard, *Micropor. Mesopor. Mater.* **2001**, 44-45, 73.

(57) H. P. Lin, C.Y. Mou, S.B. Liu, *Adv. Mater.* **2000**, 12, 103.

(58) D. Khushalani, A. Kuperman, G. Ozin, K. Tanaka, J. Garces, M. Olken, N. Coombs, *Adv. Mater.* **1995**, 7, 842.

(59) K. Ishida, *Bull. Chem. Soc.* Japan **1958**. 31, 143.

(60) G. Grygierczyk, W. Fischer, M. Sajewicz, P. Kuś, R. Wrzalik, M. Czaja, M. Dziadek, T. J. Kowalska, *Planar Chrom.* **2002**, 15, 449.

(61) J. E. Hodge, Ag. *Food Chem.* **1953**, 1, 928.

(62) C. G.A. Davies, B. L. Wedzicha, C. Gillard, *Food Chem.* **1997**, 60, 323.

(63) Z.Y. Yuan, B. L. Su, *Colloids Surfaces A: Physicochem. Eng. Aspects* **2004**, 241, 95.

(64) C. K. Shu, B. M. Lawrence, in Maillard Reactions in Chemistry, Food and Health, B.M. Labuza, G. A. Reineccius, V. Monnier, J. O'Brien, J. Baynes, (eds), Royal Society of Chemistry, Cambridge **1994**, 140.

(65) S. D. Kinrade, R. J. Hamilton, A. S. Schach, C. T. G. Knight, *J. Chem. Soc. Dalton Trans.* **2001**, 961.

(66) S. Brunauer, P. H. Emmett, E. J. Teller, *Am. Chem. Soc.* **1938**, 60, 309.

Chapter 6:
(1) J. S. Beck, J. C.Vartuwli, W. J. Roth, M. E. Leonowicz, C. T. Kresge, K. T. Schmitt, C. T-W. Chu, D. H. Olson, E. W. Shwppard, S. B. McCullen, J. B. Higgins, J. L. Schlenker, *J. Am. Chem. Soc.* **1992**, 114, 10834.

(2) C. T. Kresge, M. E. Leonowicz, W. J. Roth, J. C. Vartuli, J. S. Beck, *Nature* **1992**, 359, 710.

(3) A. Corma, D. Kumar, *Studies in surface Science and Catalysis* **1998**, 117, 201.

(4) X. S. Zhao, G. Q. Lu, G. Millar, J. *Ind. Eng. Chem. Res.* **1996**, 35, 2075.

(5) C. G. Guizzard, A. C. Julbe, A. Ayral, *J. Mater. Chem.* **1999**, 9, 55.

(6) U. Ciesla, F. Schuth, *Micropor. Mesopor. Mater.* **1999**, 27, 131 .

(7) S. Inagaki, S. Guan, T. Ohsuna, O. Terasaki, *Nature* **2002**,416, 304.

(8) Q. Huo, D.I. Margolese, U. D. Ciesla, G. Demuth, P. Feng, T. E.Gier, P. Sieger, A. Firouzi, B. F. Chmekla, F. Schuth, G. D. Stucky, *Chem. Mater*. **1994**, 6, 1176

(9) Y. Zhou, M. Antonietti, *Adv. Mater.* **2003**, 15, 1452.

(10) P. T. Tanev, T. Pinnavaia, J. *Science* **1996** 271, 1267.

(11) D. Zhao, J. Feng, Q. Huo, N. Melosh, G. H. Fredrichson, B. F. Chmelka, G. D. Stucky, *Science*, **1998**, 279, 548.

(12) J. Fan, L. Wang, B. Tu, D. Zhao, Y. Sakamoto, O. Terasaki, *J. Am. Chem. Soc.* **2001**, 123, 48, 12113.

(13) S. E. Rankin, B. Tan, H.-J. Lehmler, K. P. Hindman, B. L. Knutson, *Micropor. Mesopor. Mater.* **2004,** *73*, 197.

(14) B. Tan, A. Dozier, H.-J. Lehmler, B. L. Knutson, S. E. Rankin, *Langmuir* **2004**, *20*, 6981.

(15) B. Tan, H.J. Lehmler,S.M. Vyas, B. L. Knutson, S. E. Rankin, *Chem. Mater.* **2005**, *17*, 916.

(16) A. Firouzi, D. Kumar, L. Bull, M. T. Besier, P. Sieger, Q. Huo, S.A. Walker, J. A. Zasadzinsk, I. Glinka, C. J. Nicol, D. Margolese, G. D. Stucky, B. F. Chmelka, *Science* **1995**, 267, 1138.

(17) A. Monnier, F. Schuth, Q. Huo, D. Kumar, D. Margolese, R. S. Maxwell, G. D. Stucky, M. Krishnamurty, P. Petroff, A. Firouzi, M. Janicke, B. F. Chmelka, *Science* **1993**, 261,1299.

(18) J. Xu, Z. Luan, H. He, W. Zhou, L. Kevan, *Chem. Mater.*, **1998**, 10, 3690.

(19) G. S. Attard, J. C. Glyde, C. G. Goltner, *Nature* **1995**, 378, 366.

(20) C. G. Goltner, M. Antonietti, *Adv. Mater.* **1997**, 9, No. 5, 431.

(21) C. G. Spickermann, *Top. Curr. Chem.* **2003**, 226, 29.

(22) Y. Zhou, M. Antonietti, *Chem. Mater.* **2004**, 16, 544.

(23) C. J. Brinker, Y. F. Lu, A. Sellinger, H. Y. Fan, *Advanced Materials* **1999**, *11*, 579.

(24) M. Song, J. Kim, S. Cho, J. Kim, *Langmuir* **2002** 18, 6110

(25) D. Kushalani, A. Kuperman, G. A. Ozin, K. Tanaka, J. Garces, M. M. Olken, *Adv. Mater.* **1996**, 7, 842.

(26) L. D. Dai, T. W. Wang, L. T. Bu, G. Chen, *Colloids Surf. A* **2001**, 181, 151.

(27) R. Ryoo, C. H. Ko, I.-S. Park, *ChemComm.* **1999**, 1413.

(28) A. Lind, B. Spliethoff, M. Lindẻn, *Chem. Mater.* **2003**, 15, 813.

(29) J. Pang, J. E. Hampsey, Q. Hu, Z. Wu, V. T. John, Y. F. Lu, *ChemComm.* **2004,** 682.

(30) F. Chen, L. Huang, Q. Li, *Chem. Mater.* **1997,** 9, 2685.

(31) D. Chen, Z. Li, C. Yu, Y. Shi, Z. Zhang, B. Tu, D. Y. Zhao, *Chem. Mater.* **2005**, 17, 3228.

(33) L. Kong, S. Liu, X. Yan, Q. Li, H. He, *Micropor. Mesopor. Mater.* **2005**, 81, 251.

(34) S. Zhai, J. Zheng, J. Zou, D. Wu, Y. Sun, *Journal of Sol-gel Science and Technology*. **2004**, 30, 149.

(35) M. Antonietti, B. Berton, C. Göltner, H. Hentze, *Adv. Mater.* **1998**, 10, 154.

(36) M. Groenewolt, M. Antonietti, *Langmuir* **2004**, 20, 7811.

(37) P. Feng, X. Bu, D. J. Pine, *Langmuir*, **2000**, 16, 5304.

(38) Y. Wei, J. Xu, H. Dong, J. H. Dong, K. Qiu, S. A. Jansen-Varnum, *Chem. Mater.* **1999**, *11*, 2023.

(39) C. Stubenrauch, *Current Opinion Colloid Interface Sci.* **2001**, *6*, 160-170.

(40) B. Hoffmann, G. Platz, *Current Opinion Colloid Interface Sci.* **2001**, *6*, 171-177.

(41) C. Pinel, P. Loisil, P. Gallezot, *Adv. Mater.* **1997**, 9, 582.

(42) J. H. Jung, M. Amaike, S. Shinkai, *Chem. Commun.* **2000**, 2343.

(43) M. A. Markowitz, P. R. Kust, G. Deng, P. E. Schoen, J. S. Dordick, D. S. Clark, B. P. Gaber, *Langmuir* **2000**, 16, 1759.

(44) P. Sakya, J. M. Seddon, R. H. Templer, *J.Phys. II France 4* **1994**, 1311.

(45) F. Nilsson, O. Söderman, *Langmuir* **1996**, 12, 902.

(46) Lavrenčič-Štangar, U.; Hüsing, N. *Silicon Chemistry*, **2003**, 2(3-4), 157.

(47) G. Persson, H. Edlund, H. Amenitsch, P. Laggner, G. Lindblom, *Langmuir* **2003**, 19, 5813.

(48) A. B. Cortés, M. Valiente, *Colloid Polym. Sci.* **2003** 281, 319.

(49) M. Klotz, A. Ayral, C. Guizard, L. Cot, *J. Mater. Chem.* **2000**, 10, 663.

(50) P. C. Alberius, K. L. Frindell, R. C. Hayward, E. J. Kramer, G. D. Stucky, B. F. Chmelka, *Chem. Mater.* **2002**, 14, 3284.

(51) J. R. Bellare, H. T. Davis, W. G. Miller, L. E. Scriven, *J. Colloid Interface Sci.* **1990** 136, 305.

(52) A. Firouzi, F. Atef, A. G. Oertli, G. D. Stucky, B. F. Chmelka, *J. Am. Chem. Soc.* **1997** 119, 3596

(53) A. R. Hind, S. K. Bhargava, S. C. Grocott, *Langmuir*, **1997**,13,6255.

(54) D. C. Calabro, E. W. Valyocsik, F. X. Ryan, *Microporous Materials.* **1996**, 7, 243.

(55) K. S. Sing, D. H. Everett, R. A. W. Haul, L. Moscou, R. A. Pierotti, J. Rouquérol, T. Siemieniewska, *Pure& Appl. Chem.* **1985**, 57, 603.

(56) E. P. Barrett, L. G. Joyner, P. Halenda, *J. Am. Chem. Soc.* **1951**, 73, 373.

(57) M. Kruk, M. Jaroniec, *Langmuir*, **1997**, 13, 6267.

(58) A. Sayari, P. Liu, M. Kruk, M. Jaroniec, *Chemistry of Materials* **1997**, 9, 2499.

(59) M. Jaroniec, M. Kruk, *Langmuir* **1999**, 15, 5410.

(60) R. Xing, S. E. Rankin, *Micropor. Mesopor. Mater.* **2007**, doi: 10.1016/ j.micromeso.2007.03.028

(61) H. Lin, C. Mou, S. Liu, C. Tang, C. Lin, *Micropor. Mesopor. Mater.* **2001**, 44-45, 129.

Chapter 7:

(1) H. Hoffmann, J. Würtz, *J. Molec. Liquids.* **1997**, *72*, 191.

(2) E. Kissa, Fluorinated Surfactants and Repellents; A. T. Hubbard, Ed.; Marcel Dekker: New York, **2001**.

(3) U. Röthlingsberger, K. Laasonen, M. L. Klein, M. Sprik, *J. Chem. Phys.* **1996**, *104*, 3692.

(4) M. Sprik, U. Röthlingsberger, M. L. Klein, *Molec. Phys.* **1999,** *97*, 355.

(5) J. C. Ravey, M. J. Stébé, J. Prog. Colloid Polym. Sci. **1987**, 73, 127.

(6) G. Mathis, P. Leempoel, J. C. Ravey, C. Selve, J. J. Delpuech, *J. Am. Chem. Soc.* **1984**, 106, 6162.

(7)   T. Sen, G. J. T. Tiddy, J. L. Casci, M. W. Anderson, *Chem. Mater*. **2004**, 16, 2044.

(8)   K. Valle, P. Belleville, F. Pereira, C. Sanchez, *Nature Mater.* **2006**, 5, 107.

(9)   S. Liu, L. Kong, X. Yan, Q. Li, A. He, *Stud. Surf. Sci. Catal.,* **2005**, 156, 379.

(10)   M.-G. Song, J-K. Kim, S-H. Cho, J-D. Kim, *Langmuir* **2002**, 18, 6110.

(11)   Q. Zhang, K. Ariga, A. Okabe, T. Aida, *Stud. Surf. Sci. Catal,* **2003,** 146, 465.

(12)   F. Chen, L. Huang, Q. Li, *Chem. Mater.* **1997,** 9, 2685.

(13)   J. Pang, J. E. Hampsey, Q. Hu, Z. Wu, V. T. John, Y. F. Lu, *Chem. Comm.*, **2004,** 682.

(14)   V. Castelletto, I. W. Hamley, *Current Opinion Solid State Mater. Sci.*, **2004, 8**, 426; M. A. Hillmayer, T. P. Lodge, *J. Polym. Sci. A: Polym. Chem*. **2002,** 40, 1.

(15)   J. L. Blin, N. Henzel, M. J. Stébé, *J. Colloid Interface Sci*., **2006,** 302, 643.

(16)   K. Wang, G. M. Orädd, Almgren, T. Asakawa, B. Bergenståhl, *Langmuir* **2000**, 16, 1042.

(17)   D. Li, Y. Han, J. Song, L. Zhao, X. Xu, Y. Di, F.-S. Xiao. *Chem. Eur. J.* **2004**, 10, 5911.

(18)   M. Groenewolt, M. Antonietti, *Langmuir* **2004**, 20, 7811.

(19)   S. Areva, C. Boissiere, D. Grosso, T. Asakawa, C. Sanchez, M. Linden, *Chem. Comm*. **2004**, 1630.

(20)   H. Djojoputro, X. F. Zhou, S. Z. Qiao, L. Z. Wang, C. Z. Yu, G. Q. Lu, *J. Am. Chem. Soc*. **2006**, 128, 6320.

(21)   Y. Han, J. Y. Ying, *Angew. Chem. Int. Ed*. **2005**, 44, 288.

(22)   T. Asakawa, H. Hisamatsu, S. Miyagishi, *Langmuir* 1995, 11, 478; M. Kadi, P. Hansson, M. Almgren, I. Furó,. *Langmuir*, **2002**, 18, 9243; M. Almgren, V. M. Garamus, *J. Phys. Chem. B,* **2005**, 109, 11348

(23)   K. Tamori, K. Esumi, K. Meguro *J. Colloid Interface Sci*. **1991**, 142, 236; J.C. Ravey, A. Gherbi, M.J. Stébe, *Progr. Colloid Polym. Sci*. **1989**, 79, 272.

(24)   B. Tan, A. Dozier, H.-J. Lehmler, B. L. Knutson, S. E. Rankin, *Langmuir*, **2004**, 20, 6981.

(25)   A. R. Hind, S. K. Bhargava, S. C. Grocott, *Langmuir* **1997**, 13, 6255.

(26)   D. C. Calabro, E. W. Valyocsik, F. X. Ryan, *Microporous Materials*. **1996**, 7, 243.

(27)   M. W. Tsao, C. L. Hoffmann, J. F. Rabolt, *Langmuir* **1997**, 13, 4317.

(28)   P. J. Innocenzi, *Non-Cryst. Solids* **2003**, 316, 309.

(29)   D. R. Scheuing, J. G. Weers, *Colloids Surf.* **1991**, 55, 41.

(30)   B. Tan, H.-J. Lehmler, S. M. Vyas, B. L. Knutson, S. E. Rankin, *Adv. Mater.* **2005**, 17, 2368.

(31)   B. Tan, S. M. Vyas, H.-J. Lehmler, B. L. Knutson, S. E. Rankin, *J. Phys. Chem. B*, **2005**, 109, 23225.

(32)   K. Ikari, K. Suzuki, H. Imai, *Langmuir*, **2004**, 20, 7811.

(33)   J. C. Vartuli, K. D. Schmitt, C. T. Kresge, W. J. Roth, M. E. Leonowicz, S. B. McCullen,S. D. Hellring, J. S. Beck, J. S. Schlenker, J. L. Schlenker, D. H. Olson, E. W. Scheppard, *Chem. Mater.* **1994**, 6, 2317.

(34)   M. L. Peńa, Q. Kan, A. Corma, F. Rey, *Micropor. Mesopor. Mater.* **2001**, 44-45, 9.

(35)   K. S. W. Sing, D.H. Everett, R.A.W. Haul, L. Moscou, R.A. Pierotti, J. Rouquérol, T. Siemieniewska, *Pure Appl. Chem.* **1985**, 57, 603.

(36)   E. P. Barret, L. G. Joyner, P. P. Halenda, *J. Am. Chem. Soc.* **1951**, 73, 373.

(37)   M. Kruk, M. Jaroniec, *Langmuir* **1997**, 13, 6267.

(38)   A. Sayari, P. Liu, M. Kruk, M. Jaroniec, *Chem. Mater.* **199**7, 9, 2499.

(39)   M. Jaroniec, M. Kruk, *Langmuir* **1999**, 15, 5410.

(40)   B. Echchahed, M. Morin, S. Blais, A. Badiei, G. Berhault, L. Bonneviot. *Micropor. Mesopor. Mater.* **2001**, 44-45, 53.

(41)   R. Ryoo, J. M. Kim, C. H. Ko, C. H. Shi, *J. Phys. Chem.* **1996**, 100, 17718.

(42)   T. Imae, S. Ikeda, *Colloid Pol. Sci.* **1987**, 265, 1090.

(43)   L. Magid, Z. Han, G. Warr, M. Cassidy, P. Bulter, W. Hamilton, *J. Phys. Chem. B* **199**7, 101, 7919.

(44)   M. Matsumoto, C. E. McNamee, D. P. Bossev, M. Nakahara, T. Ogawa. *Colloid Polym. Sci.* **2000**, 278, 619.

(45)   J. Yu, J.-L. Shi, H.-R. Chen, J.-N. Yan, D.-S. Yan, *Micropor. Mesopor. Mater.* **2001**, 46, 153.

(46)   T. Asakawa, H. Hisamatsu, S. Miyagishi, *Langmuir,* **1996**, 12, 1204.

(47)   T. Asakawa, T. Fukita, S. Miyagishi. *Langmuir,* **1991**, 7, 2112.

(48)   L.S. Romsted. *Langmuir,* **2007**, 23. 414.

(49)   M. T. Anderson, J. E. Matin, J. G. Odinck, P. P. Neweomer, *Chem. Mater.* **1998**, 10, 311.

(50)   S. Liu, P. Cool, O. Collart, P. V. D. Voort, E. F. Vansant, O. I. Lebedev, G. V. Tendeloo,M. Jiang, *J. Phys. Chem. B.* **2003**, 107, 10405.

(51)   C. C. Landry, S. H. Tolbert, K. W. Gallis, A. Monnier, G. D. Stucky, P. Norby, J. C. Hanson, *Chem. Mater.* **2001**, 13.1601.

(52)   P. Ågren, M. Linden, J. B. Rosenholm, R. Schwarzenbacher, M. Kriechbaum, H. Amenitsch, P. Laggner, J. Blanchard, F. Schüth, *J. Phys. Chem. B.* **1999**, 103, 5943.

(53)   J. E. Haskouri, D. O. Zárate, C. Guillem, J. Latorre, *Chem. Commun.* **2002**, 330.

(54)   S. Brunauer, P. H. Emmett, E. J. Teller, Am. Chem. Soc. **1938**, 60, 309.

Chapter 8:

(1) J. F. Scamehorn, J. H. Harwell, Surfactant-based separations. The American Chemical Society, Washington, **2000**.

(2) A. Monnier, F. Schüth, Q. Kumar, D. Margolese, R. S. Maxwell, G. D. Strucky, M. Krisnamurthy, P. Petroff, A. Firouzi, M. Janicke, B. F. Chmelka, *Science* **1993**, 261, 1299.

(3) S. A. Bagshaw, Chem. Comm. 1999, 1785.; D. Zhao, P. Yang, B. F. Chmelka, G. D. Stucky. *Chem. Mater.* **1999**, 11, 1174.

(4) R. Ryoo, S. J. Jun, *Phys. Chem .B* **1997**, 101, 317.; D. Das, C.-M. Tsai, S. Cheng. *Chem. Commun.* **1999**, 473.

(5) J. M. Kim, S. Jun, R. J. Ryoo, *Phys. Chem. B.* **1999**,103, 6200.

(6) R. Ryoo, J. M. Kim, C. H. Ko, C. H. Shin, *J. Phys. Chem.* **1996**, 100, 17718.

(7) J. Yu, J.-L. Shi, H.-R. Chen, J.-N. Yan, D.-S. Yan, *Micropor. Mesopor. Mater.* **2001**, 46, 153.5. C. Yu, B. Tian, J. Fan, G. D. Stucky, D. Zhao, *J. Am. Chem. Soc.* **2002**, 124, 4556.

(8) H.-P. Lin, C.-Y. Mou, *Micropor. Mesopor. Mater.* **2002**, 55, 69.

(9) C. Yu, B. Tian, J. Fan, G. D. Stucky, D. Y. Zhao, *Chem. Comm.* **2001**, 2726.

(10) B. L. Newalkar, S. Komarneni, *Chem. Mater.* **2001**, 13, 4573.

(11) F. D. Renzo, F. Testa, J. D. Chen, H. Cambon, A. Galarneau, D. Plee, F. Fajula, *Micropor. Mesopor. Mater.* **1999**, 28, 437.

(12) Q. Huo, D. I. Margolese, U. Ciesla, P. Feng, T. E. Gier, P. Sieger, R. Leon, P. M. Petroff, F. Schüth, G. D. Stucky, *Nature* **1994**, 368, 317.

(13) A. Firouzi, D. Kumar, L. M. Bull, T. Besier, P. Sieger, Q. Huo, S. A. Walker, J. A. Zasadzinski, C. Glinka, J. Nicol, *Science* **1995**, 267, 1138.

(14) A.-R. Badiei, S. Cantournet, M. Morin, L. Bonneviot, *Langmuir*, 14, 7087.

(15) A.-R. Badiei, L. Bonneviot, *Inorg. Chem.* **1998**, 37, 4142.

(16) H.-P. Lin, C.-P. Kao, C.-Y. Mou, *Micropor. Mesopor. Mater.* **2001**, 48, 135.

(17) R. R. Holmes. *Chem. Rev.* **1990**, 90, 17.

(18) Z. W. He, X. Q. Liu, J. Gou, Y.Y. Wang. *Mater. Sci. Eng. B.* **2006**, 128, 168.

(19) P. Schmidt-Winkel, P. Yang, D. I. Margolese, B. F. Chmelka, G. D. Stucky. Adv. Mater. **1999**, 11, 303.

(20) W. J. Kim, J. C. Yoo, D. T. Hayhurst. *Micropor. Mesopor. Mater.* **2002**, 49, 125.

(21) A. Okabe, T. Fukushima, K. Ariga, M. Niki, T. Aida. *J. Am. Chem. Soc*. **2004**, 126, 9013.

(22) K. J. Edler, J. W. White, *Chem. Mater.* **1997**, 9, 1226.

(23) E. Leontidis, *Curr. Opin. Colloid Interface Sci.*, **2002**, 7, 81.

(24) H. O. Pastore, M. Munsignatti, D. R. S. Bittencourt, M. M. Rippel, *Micropor. Mesopor. Mater.* **1999**, 32, 211.

(25) A. Corma, Q. Kan, N. T. Navarro, J. Pérez-Pariente, F. Rey, *Chem. Mater.* **1997**, 9, 2123.

(26) B. Echchahed, M. Morin, S. Blais, A.-R. Badiei, G. Berhault, L. Bonneviot, *Micropor. Mesopor. Mater.* **2001**, 44-45, 53.

(27) T. Asakawa, H. Hisamatsu, S. Miyagishi. *Langmuir*, **1996**, 12, 1204.

(28) T. Asakawa, T. Fukita, S. miyagishi. *Langmuir* **1991**, 7, 2112.

(29) M. H. Ropers, M. J. Stébé, *Langmuir* **2003**, 19, 3137.

(30) D. Zhao, J. Feng, Q. Huo, N. Melosh, G. H. Fredrickson, B. F. Chmelka, G. D. Stucky, *Science* **1998**, 279, 548.

(31) T. Kimura, Y. Sugahara, K. Kuroda, *J. Mater. Chem.* **1998**, 8, 569.

(32) M. F. Ottaviani, A. Moscatelli, D. Desplantier-Giscard, F. DiRenzo, P. Kooynab, A. Galarneau, *J. Phys. Chem. B* **2004**, 108, 12123.

(33) C. Boissière, M. A. U. Marines, M. Tokumoto, A. Larbot, E. Prouzet, *Chem. Mater.* **2003**, 15, 509.

(34) T. Kimura, Y. Sugahara, K. Kuroda, *Chem. Commun.* **1998**, 559.

(35) A. Sayari, M. Kruk, M. Jaroniec, I. L. Moudrakovski, *Adv. Mater.* **1998**, 10, 1376.

(36) X. Cui, J.-H. Ahn, W.-C. Zin, W.-J. Cho, C.-S. Ha, *Studies in Suface and Catalysis*, **2003**, 146, 117.

(37) N. Ulagappan, C. N. R. Rao, *Chem. Commun.* **1996**, 2759.

(38) J. L. Blin, C. Otjacques, G. Herrier, B.-L. Su, *Langmuir* **2000**, 16, 4229.

(39) J. L.Blin, B.-L. Su, *Langmuir* **2002**, 18, 5303.

(40) H. Kunieda, K. Ozawa, K. L. Huang, *J. Phys. Chem. B* **1998**, 102, 831.

(41) D. Li, Y. Han, J. Song, L. Zhao, X. Xu, Y. Di, F.-S. Xiao. *Chem. Eur. J.* 2004, 10, 5911.; Y. Han, D. Li, L. Zhao, J. Song, X. Yang, N. Li, Y. Di, C. Li, S. Wu, X. Xu, X. Meng, K. Lin, F.-S. Xiao. *Angew. Chem.* 2003, 42, 3633.

(42) J. C. Ravey, M. J. Stébé, S. Sauvage, *Coll. Surf. A: Physicochem. Eng. Aspects* 1994, 91, 237.

(43) G. Mathis, P. Leempoel, J. C. Ravey, C. Selve, J. J. Delpuech, *J. Am. Chem. Soc.* **1984**, 106, 6162.

(44) J .C. Ravey, M. J. Stébé, *Prog. Coll. Polym. Sci.* **1987**, 73. 127.

(45) J. L. Blin, M. J. Stébé, *J. Phys. Chem. B* **2004**, 108, 11399.

(46) J. L. Blin, M. J. Stébé, *Micro. Mesopor. Mater.* **2005**, 87, 67.

(47) Y. Di, X. Meng, S. Li, F.-S. Xiao, *Micropor. Mesopor. Mater.* **2005**, 82, 121.

(48) B. Tan, A. Dozier, H.-J. Lehmler, B. L. Knutson, S. E. Rankin, *Langmuir,* **2004**, 20, 6981.

(49) J. N. Israelachvili. Intermolecular and Surface Forces, 2nd ed.; Academic Press, London, **1991**.

(50) Y. Marcus, Ion properties; Marcel Dekker Inc: New York, **1997**.

(51) T. Imae, T. Kohsaka, *J. Phys. Chem. B* **1992**, 96, 10030.

(52) M. A. Cassidy, G. G. Warr, *J. Phys. Chem.* **1996**, 100, 3237.

(53) T. Asakawa, H. Hisamatsu, S. Miyagishi, *Langmuir* **1995**, 11, 478; M. Kadi, P. Hansson, M. Almgren, I. Furó, *Langmuir,* **2002**, 18, 9243; M. Almgren, V. M. Garamus, *J. Phys. Chem. B,* **2005**, 109, 11348.

(54) K. S. W. Sing, D. H. Everett, R. A. W. Haul, L. Moscou, R. A. Pierotti, J. Rouquérol, T. Siemieniewska, *Pure Appl. Chem.* **1985**, 57, 603.

(55) K. Shinoda, T. Nomura. *J. Phys. Chem.* **1980**, 84, 365.

(56) C. Tanford. The Hydrophobic Effect; Wiley-Interscience Publication: New York, **1980**.

(57) T. Asakawa, K. Amada, S. Miyagishi. *Langmuir,* **1997**, 13, 4569.

(58) S. Brunauer, P.H. Emmett, E. J. Teller, *J. Am. Chem. Soc.* **1938**, 60, 309.

(59) A. Sayari, P. Liu, M. Kruk, M. Jaroniec, *Chem. Mater.* **199**7, 9, 2499.

Chapter 9:

(1) K. F. Lam, K. L. Yeung, G. McKay, *J. Phys. Chem. B,* **2006**, 110, 2187.

(2) Y. Zhu, J. Shi, W. Shen, H. Chen, X. Dong, M. Ruan, *Nanotechnology*, **2005**, 16, 2633.

(3) C. Lai, B. G. Trewyn, D. M. Jeftinija, K. Jeftinija, S. Xu, S. Jeftinija, V. S. Y. Lin, *J. Am. Chem. Soc.* **2003**, 125, 4451.

(4) Y. Zhu, J. Shi, Y-S. Li, H.-R. Chen, W.-H. Shen, X.-P. Dong, *J. Mater. Res.* **2005**, 20, 54.

(5) J.-F. Chen, H.-M. Ding, J.-X. Wang, L. Shao, *Biomaterials*, **2004**, 25, 723.

(6) P. T. Tanev, Y. Liang, T.J. Pinnavaia, *J. Am. Chem. Soc.* **1997**, 119, 8616.

(7) S. S. Kim, W. Z. Zhang, T. J. Pinnavaia. *Science* **1998**, 282, 1302.

(8) D. H. W. Hubert, M. Jung, A. L. German. *Adv. Mater.* **2000**, 12, 1291.

(9) B. Tan, H.-J. Lehmler, S. M. Vyas, B. L. Knutson, S. E. Rankin, *Adv. Mater.* **2005**, 17, 2368.

(10) F. Caruso. *Chem. Eur. J.* **2000**, 6, 413.

(11) S. Schacht, Q. Huo, I. G. Voigt-Martin, G. D. Stucky, Schüth. *Science*, **1996**, 273, 768.

(12) W. Li, X. Sha, W. Dong, Z. Wang, *Chem. Commun.* **2002**, 2434.

(13) J. Wang, Y. Xia, W. Wang, R. Mokaya, M. Poliakoff, *Chem. Commun.*, **2005**, 210.

(14) T. Shiomi, T. Tsunoda, A. Kawai, H. Chiku, F. Mizukami, K. Sakaguchi, *Chem. Commun.*, **2005**, 5325.

(15) Y. Xia, R. Mokaya, *J. Mater. Chem.*, **2005**, 15, 3126.

(16) B. Tan, S. E. Rankin, *Langmui*r, **2005**, 21, 8180.

(17) Y.-F. Zhu, J.-L. Shi, Y.-S. Li, H.-R. Chen, W.-H. Shen, X.-P. Dong, *J. Mater. Res.,* **2005**, 20, 54.

(18) Z. Y. Yuan, J. L. Blin, B.L. Su, *Chem. Comm.* **2002** ,   504.

(19) K. S. Sing, D. H. Everett, R. A. W. Haul, R. A.Pierotti, J. Rouquerol, T. Siminiewska, *Pure Appl. Chem.* **1985**, 57, 603.

(20) M. Kruk, M. Jaroniec, *Langmuir* **1997**, 13, 6267.

(21) A. Sayari, P. Liu, M. Kruk, M. Jaroniec, *Chem. Mater.* **1997**, 9, 2499.

(22) A. R. Hind, S. K. Bhargava, S. C. Grocott, *Langmuir* **1997**, 13, 6255.

(23) D. C. Calabro, E. W. Valyocsik, F. X. Ryan, *Microporous Materials.* **1996**, 7, 243.

(24) P. Innocenzi, *J. Non-Cryst. Solids,* **2003**, 316, 309.

(25) D. R. Scheuing,; J. G. Weers, *Colloids Surf.* **1991**, 55, 41.

(26) R. M. Silverstein, F. X. Webster, *Spectrometric Indentification of Organic Compounds*; Wiley-VCH: Singapore, **1997**.

(27) C. G. A. Davies, B. L. Wedzicha, C. Gillard, Food Chem. **1997**, 60, 323

(28) K. Ray, H. Nakahara. *J. Phys. Chem. B* **2002**, 106, 92.

(29) F. Yang, L. G. Moss, G. N. Phillips, Jr. *Nature Biotechnology.* **1996**, 14, 1246.

(30) S. Brunauer, P. H. Emmett, E. J. Teller, Am. Chem. Soc. **1938**, 60, 309.

Vita

Date of Birth: 04/18/1973   **Place of Birth:** Henan, China

Education:

07/2002, Master, Chemical Engineering, East China University of Science& Technology, Shanghai, P. R. China   Advisor: Prof. Wende Xiao

07/1996, Bachelor, Chemical Technology of Coal, East China University of Science & Technology, Shanghai, P. R. China   Advisor: Prof. Xingzhong Sha

07/1996, Minor, English for Science & Technology, East China University of Science & Technology, Shanghai, P. R. China

Professional Experience:

11/1997-08/1999, Chemical Engineer, Nissei Group (China) Co., Ltd.
07/1996-11/1997, Process Engineer, Yizheng Chemical Fibre. Co. Ltd.

Selected Publications:

- R. Xing, S. E. Rankin, "Use of the Ternary Phase Diagram of a Mixed Cationic/Glucopyranoside Surfactant System to Predict Meso-structured Silica Synthesis", *J. Colloid. Interface. Sci.* 2007, submitted.

- R. Xing, S. E. Rankin, "Reactive Pore Expansion during Ammonia Vapor Post-Treatment of Ordered Mesoporous Silica with Mixed Glycopyranoside and Cationic Surfactants," *Micropor. Mesopor. Mater.* 2007, doi:10.1016/j.micromeso.2007.03.028.

- R. Xing, S. E. Rankin, "Three-Stage Multilayer Formation Kinetics during Adsorption of an Anionic Fluorinated Surfactant onto Germanium. 1. Concentration Effect", *J. Phys. Chem. B*, 2006, 110, 295.

- Z. Zhou, R. Xing, W. Shen, B. Dou, X. Sha, "Ni-based Multifunctional Cleaner of High Temperature Coal Gas", *Gas & Heat*, 2003, 23, 3.

- W. Shen, R. Xing, G. Zhao, X. Shao, "Study of Operating Condition for Catalytic Conversion of Organic Sulphur in Hot Coal Gas**"** *Gas & Heat*, 2000, 20, 327.

- W. Shen, B. Dou, R. Xing, X. Sha, "Removal of Alkali Meta Vapor from Hot Coal Gas", *Gas & Heat*, 2000, 6, 403.

- W. Shen, J. Lu, B. Dou, R. Xing, X. Sha, G.. Zhao, H. Li, "Ammonia Removal in Hot Coal Gas. II. Kinetic Study on Ammonia Catalytic Decomposition", *Ranliao Huaxue Xuebao*, 1999, 27, 462.

- C. Wan, X. Sha, W. Shen, R. Xing, S. Tang, "High-temperature Coal Gas Desulfurization Using Cu-Mn-O-Based Absorbent. I. Sulfidation of Cu-Mn-O Based Sorbent", *Ranliao Huaxue Xuebao*, 1998, 26, 400.